Western Australian School of Mines

Scaled Down Tunnel Testing for Comparison of Surface Support Performance

Ayako Kusui

This thesis is presented for the Degree of
Doctor of Philosophy
of
Curtin University

December 2015

Declaration

To the best of my knowledge and belief this contains no materials previously published by any other person expect where due acknowledgement has been made.

This thesis contains no material which has been accepted for the award of any other degree or diploma in any university.

Signed:……楠井彩子…….

Date:……17 December 2015…….

Abstract

The depth of underground mine has increased as a result of a technology development and high demand for commodities. As the depth increases, the stress surrounding the excavations becomes higher to the point in which it causes failures. Damage occur near the excavation surface and surface support is critical to achieve excavation stability and safe underground access. The work presented in this thesis investigate stress induced failure and surface support performance under high stress.

In order to understand stress induced failures around underground excavations, a number of scaled down tunnels were prepared and tested at Western Australian School of Mines (WASM). Rectangular intact rock blocks with internal circular tunnels were loaded uniaxially at a constant loading rate and its failure mechanisms and behaviour was geotechnically monitored. The test specimens consisted of two different types of sandstone and granite and the circular excavation diameters ranged from 56 to 203 mm. Their mechanical properties of the rock materials were determined and linked with observed tunnel behaviour.

The unsupported tunnel tests revealed distinct failure mechanisms during the loading process. Initially tensile cracks were propagated on top and bottom of the excavation parallel to the loading direction. Seismic activities commenced with crack generation and the load and displacement increased linearly until spalling occurred on the tunnel sidewalls. Extensile crack appeared on the tunnel walls and once it propagated along the entire tunnel geometry, violent material ejection was experienced. Prior to spalling, there were no clear indication of impending failure from the seismic activities and a sudden increase was experienced immediately before material ejection. After spalling occurred, the load increased again until the peak load was reached. Shear failure occurred in the adjacent pillars along with continuous seismic activity until the end of testing. Vertical cracks were generated and propagated within the pillars. Ejection velocities were calculated using high speed filming and a positive correlation was observed with the material strength.

Failure induced stress was evaluated as a function of the intact rock strength. The stress distribution within the specimens was analysed using both linear and elasto-plastic numerical modelling. A ratio of the intact rock strength to maximum tangential stress on excavation boundary at spalling was plotted with respect to the intact rock strength. The results suggest that the strength to induced stress ratio are reduced to the material strength. A similar relationship was observed in the ratio of the intact rock strength to average pillar stress at pillar crushing. The results from laboratory scale tests compare well with data from full scale excavations from a number of mine pillars suggesting that the onset of spalling and pillar crushing are scale independent.

The surface support performance following violent failure was examined using scaled down surface support systems. Ground support materials including reinforcement, mesh and shotcrete were specially designed for this research project and applied onto sandstone specimens in various configurations. Mesh types varied from welded wire mesh to chain link mesh and were installed either underneath, over or both underneath and over a shotcrete layer. Their mechanical corresponded well with observations of full scale size ground support schemes.

Overall, stabilised test specimens with ground support installation, showed more controlled behaviour, i.e. ejection velocities decreased and excavation strength subjected to failure also increased. The results show that the welded mesh showed a stiff behaviour and buckled in compression, while the chain link mesh accommodated internal deformations between reinforcement elements. The difference was significant for reinforced shotcrete. The chain link mesh interacted with the shotcrete layers at a tunnel sidewall failure when it was embedded within a shotcrete. In case of mesh exposed, the shotcrete layers deteriorated at the tunnel sidewalls with spalling propagation and the shotcrete breaking into small pieces. The best performance was achieved by a combination of shotcrete with external and embedded chain link mesh layers. The additional shotcrete layer reduced the internal damage and showed more controlled behaviour while the external mesh minimised shotcrete ejection.

Acknowledgement

This thesis has been made possible due to the assistance of many people who contributed their time and knowledge. Without their support this thesis could not have been achieved.

Firstly, I would like to thank Prof. Ernesto Villaescusa for giving me the opportunity to conduct this research project. For his full support, advice, guidance, enthusiasm and encouragement sharing his tremendous knowledge and experience I am forever grateful. It has been an honour to undertake a PhD program under his supervision.

Appreciation is expressed to Dr. Alan Thompson for advice, valuable comments, and suggestions for experiment design and data analysis.

Immeasurable appreciation and deepest gratitude for their help and support are extended to the following people;

- Mr. Pat Hogan for technical support, sample preparation and data analysis.
- Mr. Lance Fraser for technical advice, providing the assistance for sample preparation and encouragement.
- Mr. James Langdon for preparing the laser scanner and advice for data acquisition and analysis.
- Dr. Takahiro Funatsu for preparing and running the numerical models and research advice.
- Mrs. Myriam Sullivan for preparing the material characterisation test.

I also would like to give my thanks to all of the members of Rock Mechanics WASM and WASM staff for all of the help and support.

Lastly, I would like to thank to my dearest family for their constant support and encouragement over the years.

Author's Statement of Previous Publication

Some results of data analyses and approaches discussed in this thesis have been previously published by the author during the time of thesis preparation. No references to these publications have been made in the body of the thesis, as the ideas and analysis techniques were developed as a part of the thesis background work by the author prior to publication. The following list details the previous publications by the author at the time of submission of this thesis.

Kusui, A., & Villaescusa, E. (2016). Seismic response prior to spalling failure in highly stressed underground. Paper presented at the Seventh International Conference & Exhibition on Mass Mining, MassMin 2016, Sydney. (accepted)

Table of Contents

Declaration i

Abstract ii

Acknowledgement iv

Author's Statement of Previous Publication v

Table of Contents vi

List of Figures xii

List of Tables xxii

Chapter 1 Introduction……1

1.1 Background 2

1.2 Objectives of Research 2

1.3 Outline of Thesis 3

Chapter 2 A Review of a Surface Support Performance……...5

2.1 Introduction 6

2.3 Stress Induced Failure 6

2.4 A Review of Brittle Failure Mechanism Investigation 7

2.4.1 Physical Model Tests 8

2.4.2 Crack Damage Initiation Thresholds 10

2.5 A Review of Surface Support for Massive Rock 14

2.5.1 Excavation Stability Estimation 15

2.5.2 Surface Support Selection 15

2.6 Literature Review Summary 19

Chapter 3 Material Characterisation……21
3.1 Introduction 22
3.2 Uniaxial Testing 23
3.2.1 Uniaxial Compressive Strength 24
3.2.2 Young's Modulus 26
3.2.3 Poison's Ratio 27
3.2.4 Tensile Strength 28
3.3 Triaxial Testing 29
3.3.1 Failure Envelope 29
3.3.2 Cohesive Strength and Friction Angle 30
3.4 Material Property Summary 30

Chapter 4 Model Test Preparation……33
4.1 Practicalities and Limitations 34
4.2 Scaled-down Tunnel Construction 34
4.3 Ground Support System 36
4.4 Reinforcement 36
4.4.1 Rock Bolt Types 39
4.4.2 Encapsulation Material 39
4.4.3 Tensile Loading Test 39
4.5 Surface Support 43
4.5.1 Mesh Type 44
4.5.2 Mesh Material Properties 46
4.5.3 Shotcrete 48

4.6 Ground Support Component Summary 53

Chapter 5 Model Test Configuration……55

5.1 Test Set-up 56

5.2 Loading Method 57

5.3 High Speed Filming 57

5.4 Seismic Data Monitoring 59

5.5 Internal Deformation Measurement by Laser Scanner 60

5.5.1 Laser Displacement Unit 60

5.5.2 Laser Scanner 60

5.5.3 Reference Scan Testing 64

5.6 Test Configuration Summary 67

Chapter 6 Unsupported Tunnel Test Result…….69

6.1 Test Configurations 70

6.2 Load Displacement Relationship 71

6.3 Tunnel Size Effect 76

6.4 Seismic Response 79

6.4.1 Results for Sandstone 79

6.4.2 Results for Granite 80

6.5 Ejection Velocities 82

6.5.1 Observed Spalling Process 82

6.5.2 Ejection Velocities 84

6.6 Unsupported Tunnel Test Summary 89

Chapter 7 Ratio of Intact Rock Strength to Induced Stress……91
7.1 Computer Simulations Using Abaqus 92
7.1.1 Material Properties for Numerical Modelling 92
7.1.2 Linear Elastic Finite Element Modelling 93
7.1.3 Non-linear Elasto Plastic Modelling 96
7.1.4 Numerical Modelling Summary 102
7.2 Spalling Failure 103
7.2.1 Ratio of Intact Rock Strength to Induced Stress 103
7.2.2 Comparison of Model Results with Field Observations 104
7.3 Pillar Crushing Failure 105
7.3.1 Ratio of Intact Rock Strength to Induced Stress 106
7.4 Comparison with Past Physical Model Studies 107
7.5 Application of Test Results to Pillar Design 109
7.5.1 Pillar Stability Graph 109
7.5.2 Failure Envelopes Derived from Model Tests 110
7.5.3 Strain at Spalling and Pillar Crushing 113
7.6 Unsupported Tunnel Test Summary 116

Chapter 8 Ground Support Performance…….....117
8.1 Introduction 118
8.2 Ground Support Test Configurations 118
8.2.1 Patterns Tested 118
8.3 Ground Support Stabilisation 121
8.4 Comparison for Similar Ground Support Schemes 127
8.5 Comparison of Bolting Pattern 131

8.6 Comparison of Mesh Materials 136
8.6.1 Stiff welded vs Chain Link 136
8.6.2 Mesh Material Comparisons with a Shotcrete Layer 139
8.7 Shotcrete Layer 150
8.7.1 Shotcrete Application Followed by Bolts and Stiff Mesh 150
8.7.2 Shotcrete Application Followed by Bolts and Chain Link Mesh 154
8.8 Mesh Reinforced vs Mesh Exposed 157
8.9 A Comparison of Ground Support Schemes 161
8.10 Ejection Velocity and Ground Support 170
8.11 Ground Support and Ratio of Strength to Stress at Failure 171
8.12 Ground Support Performance Summary 172

Chapter 9 Excavation Shape Measures……...175
9.1 Laser Scanning Arrangement 176
9.2 Data Correction 179
9.3 Initial Measurement 183
9.4 Excavation Behaviour before Spalling 186
9.4.1 Kirsch Solution 186
9.4.2 Strain before Spalling 187
9.5 Excavation Behaviour after Failure 192
9.5.1 Three Dimensional View 192
9.5.2 Strain Data 197
9.5.3 Closure at Failure 200
9.5.4 Results Variability 200
9.5.5 Damaged Volume 204

9.6 Tunnel Deformation Summary 205

Chapter 10 Conclusions and Recommendations…….207

10.1 Conclusions 208

10.1.1 Observed Failure Mechanisms 208

10.1.2 The Ratio of Strength to Induced Stress at Failure 208

10.1.3 Rock Behaviour at Failure 208

10.1.4 Comparison with a Full Scale Sized Tunnel 209

10.1.5 Ground Support Performance 209

10.1.6 Integrated Surface Support Performance under High Stress 209

10.2 Recommendations and Future Work 210

References……211

Appendix A Circular Excavation Failure under Compression…..……217

LIST OF FIGURES

Figure 2.1 Stress-driven failure near the boundary of an excavation……6

Figure 2.2 Notch created following stress-driven failure in a hard rock mine……7

Figure 2.3 Summary of physical model tests a)plotted via diameter b)plotted via pillar width and height ratio (after Martin (1993))……..10

Figure 2.4 Excavation behaviour as a function of the ratio of compressive strength to the induced stress (after Barton et al. (1974); Hutchinson and Diederichs (1996))…….15

Figure 2.5 Flexural failure of shotcrete with external welded mesh (Drover & Villaescusa, 2015)……..18

Figure 2.6 Failure in a reinforced shotcrete layer a) chain link mesh b) mild steel welded mesh (Drover & Villaescusa, 2015)……..19

Figure 3.1 Three rock mass blocks used for physical testing, a) moderately strong sandstone, b) strong sandstone and c) very strong granite. 23

Figure 3.2 Drilling configuration for rock mass preparation. 23

Figure 3.3 Normal distribution of the uniaxial compressive strength obtained by the uniaxial compressive testing. 24

Figure 3.4 Example of moderately strong sandstone sample after uniaxial compressive strength test. 25

Figure 3.5 Example of strong sandstone sample after uniaxial compressive strength test. 25

Figure 3.6 Example of granite sample after uniaxial compressive strength test. ... 26

Figure 3.7 Uniaxial compressive strength and Young's modulus for three different types of rock mass samples. 27

Figure 3.8 Summary of Poison's ratio on three rock materials. 28

Figure 3.9 Example of strong sandstone sample after Brazilian test. 28

Figure 3.10 Tensile strength of the Strong sandstone plotted by uniaxial compressive strength. 29

Figure 3.11 The average strength curve obtained from the triaxial compressive strength tests. 30

Figure 4.1 Sandstone block (strong) before the drilling process……35
Figure 4.2 Example of 200 mm core drilling into a sandstone block.....35
Figure 4.3 Typical tunnel and pillar geometry tested (grid size 20 mm x 20 mm)....36
Figure 4.4 Intact rock block rotation system. 37
Figure 4.5 The miniature drilling system. 38
Figure 4.6 Borehole drilling process using a 5mm diamond drill bit.....38
Figure 4.7 The setting for the rock bolt tensile test by Avery loading machine a) a test sample b) bolt head fixed by nut c) pull testing configuration.....40
Figure 4.8 The rock bolts after the critical embedded test for the different anchor length a) 10mm b) 15mm and c) 25mm.....41
Figure 4.9 Configuration used for rock bolt static tensile test. 42
Figure 4.10 The sample specimen with the rock bolt prior to the tensile test.....42
Figure 4.11 Load displacement curve of miniature rock bolt. 43
Figure 4.12 Long view of broken threaded steel bar after tensile testing. 43
Figure 4.13 Various mesh materials used in the laboratory test a) stiff welded mesh b) wide-aperture stiff mesh c) flexible mesh d) chain link mesh.....45
Figure 4.14 Miniature chain link mesh a) a single bended wire b) manual chain link mesh fabrication.....45
Figure 4.15 Example of pull test sample wire from a) stiff welded mesh b) flexible mesh c) chain link mesh.....47
Figure 4.16 Mesh wire tensile strength. 47
Figure 4.17 Broken wires after pull test a) stiff and wide-aperture stiff mesh b) flexible mesh c) chain link mesh.....48
Figure 4.18 An example of a scaled down tunnel before shotcrete application.....50
Figure 4.19 An example of a mesh installed tunnel before shotcrete application.....50
Figure 4.20 Shotcrete application by miniature spray gun.....51
Figure 4.21 Surface smoothing process after the shotcrete spraying. 52
Figure 4.22 A scaled down tunnel with a 5 mm thickness shotcrete layer after curing. 52

Figure 4.23 Re-drilled boreholes after shotcrete application. 53
Figure 5.1 Block sample confinement setting. 56
Figure 5.2 Typical block sample confinement setting (grid size 20 mm x 20 mm).57
Figure 5.3 Typical experimental set up with SRL camera. 58
Figure 5.4 Background grid used for ejection velocity calibration (grid size 10 mm x 10 mm with 0.5 mm thick line). 58
Figure 5.5 Typical specimen sample following testing showing the location of the two AE sensors. 59
Figure 5.6 Laser displacement sensor unit. 60
Figure 5.7 Displacement measurement concept by laser scanner. 61
Figure 5.8 Laser scanner. 62
Figure 5.9 Laser measurement head. 62
Figure 5.10 An example of the laser scanner setting within a specimen sample. 63
Figure 5.11 An example of the laser scanning before a test. 63
Figure 5.12 Reference scan testing using a ceramic tube. 65
Figure 5.13 An example of reference testing data from a single slide. 65
Figure 5.14 Four sets of reference scanning test data. 66
Figure 6.1 Unsupported tunnel geometry. 71
Figure 6.2 Typical unsupported tunnel and pillar geometry tested (grid size 20 mm x 20 mm), before and after failure. 71
Figure 6.3 Example of load displacement curve with unsupported sandstone tunnel behaviour. 73
Figure 6.4 Typical spalling propagation process of unsupported strong sandstone... 74
Figure 6.5 Load-deformation response for the three different tunnel materials. ... 76
Figure 6.6 Load displacement relationships of different tunnel diameter of unsupported tunnel tests in strong sandstone. 77
Figure 6.7 Load displacement relationship of different tunnel diameter of unsupported granite tests. 77
Figure 6.8 Specimens after failure a) strong sandstone (56 mm diameter), b) strong sandstone (103 mm diameter), c) granite (104 mm diameter). 78

Figure 6.9 a) Failure mode and seismic response of an unsupported tunnel in strong sandstone, b) Rate of seismicity and decreasing ratios of strength/induced stress. 80
Figure 6.10 a) Failure mode and seismic response of an unsupported tunnel in granite, b) Rate of seismicity and decreasing ratios of strength/induced stress. 82
Figure 6.11 Spalling failure of moderately strong sandstone. 83
Figure 6.12 Spalling failure of granite. 84
Figure 6.13 An example of measurement scale determination using an image before experiment. 85
Figure 6.14 An example of a moment of material ejection (photos were taken every 0.02 sec). 86
Figure 6.15 Violent ejection development at spalling (50 fps) a) strong sandstone 2.3 m/s, b) strong sandstone 6.9 m/s, c) granite 8.5 m/s. 88
Figure 6.16 Ejection velocities at spalling of different strength of unsupported tunnel. 89
Figure 7.1 Three-dimentional Abaqus model geometry and finite element mesh. 92
Figure 7.2 Minimum principal stress by linear elastic finite element modelling. .. 94
Figure 7.3 Maximum principal stress prior to failure by linear elastic finite element modelling. 95
Figure 7.4 Calculated pillar stress distribution prior to tunnel wall spalling. 96
Figure 7.5 Minimum principal stress by non-linear elasto-plastic modelling before spalling. 97
Figure 7.6 Comparison of maximum principal stress before spalling between linear elastic and non-linear elasto-plastic modelling results. 98
Figure 7.7 Modelling results of shear band creation by non-linear elasto-plastic modelling. 99
Figure 7.8 Modelling results of shear failure during pillar crushing using the program Abaqus. 101
Figure 7.9 Determination of pillar stress distribution. 102
Figure 7.10 Unsupported tunnel spalling as a function of compressive strength and maximum tangential stress. 104

Figure 7.11 Full scale unsupported semi-circular tunnels showing on-set of brittle failure at the centre of the excavation roof due to high horizontal stress. 105
Figure 7.12 On-set of unsupported pillar crushing as a function of compressive strength and average pillar strength. 106
Figure 7.13 A comparison of strength and stress ratio in material strength at spalling with past physical model test results. 107
Figure 7.14 A comparison of strength and stress ratio in excavation diameter at spalling with past physical model test results. 108
Figure 7.15 A comparison of strength and stress ratio in a ratio of pillar width to height at spalling with past physical model test results. 108
Figure 7.16 Progressive failure of unsupported tunnels as a function of compressive strength and average pillar strength. 109
Figure 7.17 Comparison of scaled-down pillar crushing failure results with the full scale Pillar Stability Graph database (after Villaescusa (2014)). 110
Figure 7.18 Section view of pillar stress distribution. Results from non-linear modelling using the program Abaqus. 111
Figure 7.19 Confinement stress provided by lateral steel confinement platens. 111
Figure 7.20 Failure envelopes for the scaled-down unsupported tunnels. 113
Figure 7.21 An example of strain calculation at a) spalling b) pillar crushing. 114
Figure 7.22 a) Strain at the spalling failure for the scaled-down unsupported tunnels, b) a comparison of strain at the spalling failure and pillar crushing for the scaled-down unsupported tunnels. 115
Figure 8.1 Square bolting style pattern. 119
Figure 8.2 Staggered bolting style pattern. 120
Figure 8.3 An example of rock bolt installation a) full encapsulation b) fixation by nut. 121
Figure 8.4 Mesh overlap at the tunnel bottom. 121
Figure 8.5 Observation of failure mechanism of a) unsupported tunnel b) chain link mesh and rock bolt (square pattern) support (Specimen No.9). 123

Figure 8.6 Sidewall after failure a) unsupported tunnel b) chain link mesh and rock bolt (square pattern) support (Specimen No.9). 124
Figure 8.7 Load displacement relationship with recorded AE activities a) unsupported tunnel b) reinforcement and chain link support (Specimen No.9). 126
Figure 8.8 Rock bolt shear failure (after test). 127
Figure 8.9 Ground support scheme consisting of an initial 5 mm shotcrete layer followed by chain link mesh and rock bolt reinforcement. 128
Figure 8.10 Comparison with the same ground support configuration tests, a) 68 MPa (Specimen No.10) b) 76 MPa (Specimen No.11) and c) 83 MPa (Specimen No.12). 129
Figure 8.11 Load relationship curve of the same ground configuration test with AE data a) 68 MPa (Specimen No.10) b) 76 MPa (Specimen No.11) and c) 83 MPa (Specimen No.12). 130
Figure 8.12 Combined load-displacement curve. 131
Figure 8.13 Two different bolting pattern a) square pattern (Specimen No.3) b) staggered pattern (Specimen No.1). 132
Figure 8.14 Performance comparison with different bolting pattern a) square pattern (Specimen No. 3) b) staggered pattern (Specimen No.1). 133
Figure 8.15 Failures on tunnel sidewall a) square bolting pattern b) staggered bolting pattern. 134
Figure 8.16 Load displacement of a) square pattern (Specimen No. 3) b) staggered pattern (Specimen No.1) c) combined plot. 135
Figure 8.17 Failure on tunnel sidewalls a) stiff welded mesh (Specimen No.3) b) chain link mesh (Specimen No.9). 137
Figure 8.18 Load-displacement curve a) stiff welded mesh b) chain link mesh. 138
Figure 8.19 Ground scheme consisting of mesh, shotcrete and rock bolt application. 139
Figure 8.20 Comparison of failure mechanisms a) flexible mesh (Specimen No.5) b) Wide-aperture stiff mesh (Specimen No.7). 141

Figure 8.21 Load-displacement curve a) flexible mesh b) Wide-aperture stiff mesh.. 142
Figure 8.22 Ground support scheme consisting of mesh, rock bolts and shotcrete application. 143
Figure 8.23 Failure on sidewall at spalling and after pillar failure a) stiff welded mesh (Specimen No.4) b) Wide-aperture stiff mesh (Specimen No.6) c) chain link mesh (Specimen No.8). 145
Figure 8.24 Ejected shotcrete materials on the floor at underground mine. 146
Figure 8.25 Tunnel sidewall after pillar failure a) stiff welded mesh b) Wide-aperture stiff mesh c) chain link mesh. 147
Figure 8.26 Comparison of reinforced shotcrete at failure a) scaled sized specimen b) full scale excavation. 148
Figure 8.27 Load displacement curve a) stiff welded mesh b) Wide-aperture stiff mesh c) chain link mesh. 149
Figure 8.28 Failure progression a) stiff welded mesh and rock bolts (Specimen No.1) b) 5 mm shotcrete layer, stiff welded mesh and rock bolts (Specimen No.2). 151
Figure 8.29 Tunnel sidewall after failure a) stiff welded mesh and rock bolts (Specimen No.1) b) 5 mm thick shotcrete layer, stiff welded mesh and rock bolts (Specimen No.2). 152
Figure 8.30 Load displacement curve a) stiff welded mesh and rock bolts b) 5 mm thick shotcrete layer, stiff welded mesh and rock bolts. 153
Figure 8.31 Tunnel sidewall after failure a) chain link mesh and rock bolts (Specimen No.9) b) 5 mm shotcrete layer, chain link mesh and rock bolts (Specimen No.11). 155
Figure 8.32 Load displacement curve failure a) chain link mesh and rock bolts b) 5 mm shotcrete layer, chain link mesh and rock bolts. 156
Figure 8.33 Failure mechanism in different mesh position a) mesh exposed (Specimen No.8) b) mesh embedded (Specimen No.11). 158
Figure 8.34 Tunnel surface after failure a) mesh reinforced (Specimen No.8) b) mesh exposed (Specimen No.11). 159

Figure 8.35 Load displacement curve a) mesh reinforced b) mesh exposed..... 160
Figure 8.36 A comparison of ground support schemes a) mesh, shotcrete and rock bolt b) shotcrete, mesh and rock bolt c) mesh, shotcrete, mesh and rock bolt d) shotcrete, mesh, shotcrete, mesh and rock bolt. 162
Figure 8.37 Material ejection at spalling failure a) mesh, shotcrete and rock bolt b) shotcrete, mesh and rock bolt c) mesh, shotcrete, mesh and rock bolt d) shotcrete, mesh, shotcrete, mesh and rock bolt. 163
Figure 8.38 Ground support performance following tunnel failure a) mesh, shotcrete and rock bolt b) shotcrete, mesh and rock bolt c) mesh, shotcrete, mesh and rock bolt d) shotcrete, mesh, shotcrete, mesh and rock bolt. 165
Figure 8.39 Tunnel sidewalls after failure a) mesh reinforced shotcrete b) mesh exposed shotcrete c) mesh embedded and mesh exposed shotcrete d) mesh reinforced shotcrete with mesh exposed. 166
Figure 8.40 Load-displacement curves for different ground configuration tests with AE data a) mesh reinforced shotcrete b) mesh exposed shotcrete c) mesh embedded and mesh exposed shotcrete d) mesh reinforced shotcrete with mesh exposed. 168
Figure 8.41 The shear failure on the pillar (Specimen No.14). 169
Figure 8.42 Ejection velocity at spalling for unsupported and stabilized tunnel specimens. 171
Figure 8.43 Unsupported and stabilised tunnel spalling as a function of compressive strength and maximum tangential stress (200 mm diameter tunnels). 172
Figure 8.44 Unsupported and stabilised onset of pillar crushing as a function of compressive strength and average pillar strength. 172
Figure 9.1 Stain measurement point of a) Specimen No.11 b) Specimen No.12 c) Specimen No.14. 178
Figure 9.2 Strain measurement point of Specimen No.15 a) the first loading b) the second loading. 179
Figure 9.3 Laser scanner settings. 180
Figure 9.4 Strain measurement by the laser scanner a) before loading b) after failure. 181

Figure 9.5 Laser scanned data scheme a) measurement before loading b) measurement after loading. 182
Figure 9.6 Data correction concept a) measurement data correction method b) measurement data after correction. 182
Figure 9.7 Data correction values from load displacement curve 183
Figure 9.8 Excavation surface and 3D views by laser scanning before testing a) Specimen No.11 b) Specimen No.12 c) Specimen No. 14 d) Specimen No.15. 185
Figure 9.9 Example of an inside sight of 3D view. 186
Figure 9.10 An example of elastic deformation calculated by the Kirsch solution. 187
Figure 9.11 Specimens before spalling a) Specimen No.12 b) Specimen No.15. . 189
Figure 9.12 Three dimensional views before spalling. 190
Figure 9.13 Average strain profile before spalling. 191
Figure 9.14 Comparison of 3D view and excavation surface after failure of Specimen No.11. 193
Figure 9.15 Comparison of 3D view and excavation surface after failure of Specimen No.12. 194
Figure 9.16 Comparison of 3D view and excavation surface after failure of Specimen No.14. 195
Figure 9.17 Comparison of 3D view and excavation surface after failure of Specimen No.15. 196
Figure 9.18 Strain profiles after failure a) Specimen No.11 b) Specimen No.12 c) Specimen No.14 d) Specimen No.15 198
Figure 9.19 Combined average strain profile after failure. 199
Figure 9.20 Excavation closure after failure. 200
Figure 9.21 Excavation surface with a single layer after failure a) Specimen No.11 b) Specimen No.12. 202
Figure 9.22 Excavation surface with a double layer after failure a) Specimen No.14 b) Specimen No.15. 203
Figure 9.23 Normal distribution of strain profiles……..204

Figure 9.24 Damage volume after failure..... 205

List of Tables

Table 3.1 Rock classification regarding to uniaxial compressive strength (Knill et al., 1970)..... 22
Table 3.2 Average material properties of three different rock mass blocks..... 31
Table 6.1 Scaled sized unsupported tunnel test configurations summary..... 70
Table 7.1 Mechanical properties of rock samples and steel platens used for numerical modelling..... 93
Table 7.2 Summary of the pillar stress prior to spalling. 96
Table 7.3 Summary of the pillar stress prior to pillar crushing..... 102
Table 8.1 Ground support configuration summary. 120
Table 8.2 Comparison of the stress and strength ratio at failure with unsupported tunnel test result. 127
Table 8.3 Strength to stress ratio at failure for specimens having the same ground support scheme..... 131
Table 8.4 Strength to stress ratio at failure of different bolting pattern. 136
Table 8.5 Strength to stress ratio at failure of different mesh material. 138
Table 8.6 Strength to stress ratio at failure of different mesh material at failures. 142
Table 8.7 Debris weight collected after failure with different mesh materials 148
Table 8.8 Strength to stress ratio at failure of the three different mesh material at failures..... 150
Table 8.9 Strength to stress ratio at failure of two ground support scheme. 153
Table 8.10 Strength to stress ratio at failure of shotcrete application comparison. 156
Table 8.11 Strength to stress ratio at failure of mesh reinforced and mesh exposed. 160
Table 8.12 Debris weight collected after failure with different ground support schemes. 170
Table 9.1 Strain measurement arrangement. 177
Table 9.2 Normal deviation of strain profiles. 204
Table 9.3 Damaged volume summary after failure. 205

Chapter 1

Introduction

1.1 Background

As underground mining proceeds to depths below the surface approaching or exceeding 1000 m, the ratio of intact rock strength to induced stresses around conventional development excavations is such that failure of the rock mass adjacent at the excavations can occur very soon after construction. At the present time, such conditions have led to the abandonment of mining operations that have reached these depths, resulting in losses of hundreds of millions of dollars. In addition, over the next two decades or so, when the moderate depth resources are likely to be depleted, those conditions are likely to be faced routinely.

The stability and behaviour of the rock masses surrounding an excavation is dependent upon several factors including the rock mass strength, the geometry of the excavation, the induced stresses surrounding the opening, the blasting or construction practices and the amount of water and weathering process (Villaescusa, 2014). In particular, the rock mass strength is a function of the intact rock properties and the geological discontinuities intersecting the rock mass near the boundaries of an excavation. Furthermore, as mining progresses to greater depths, the induced stresses increase relative to the rock mass strength, such that excavation instability becomes increasingly apparent. Violent failures where the seismic source is located within the vicinity of the excavation can be experienced. While large deformations are experienced in tunnels driven within low strength rock, sudden violent failure can also occur in tunnels that are excavated in high strength rock (Barla, 2014). The visible damage on the excavation surface called spalling has become a serious issue (Hoek & Brown, 1980). To ease the internal damage, ground support, especially surface support with high energy absorption capacity has been recognised as essential and their performance has been investigated both in dynamically and statically (Villaescusa, Thompson, & Player, 2015).

1.2 Objectives of Research

In order to investigate stress-driven fracturing around underground excavations, a large number of scaled-down tunnels have been constructed and tested at the WASM Rock Mechanics Laboratory. Dimensions, loading method and ground support

designs were fully controlled and different configurations were compared. Rock block specimens was created from three different material strength. The specimens were drilled with different diameter holes to simulate tunnels. The specimens were loaded uniaxially until failure was experienced. The testing of the scale down tunnels was undertaken for unsupported and supported with ground support.
This research was mainly focusing on following points:

- Observing of failure mechanisms of scaled-down hard rock tunnels under high stress for different material strengths.
- The determination of critical relationships between intact rock strength and induced stress of the rock during a progressive loading.
- Failure mode such as spalling, ejection velocity and pillar crushing were studied in detail.
- The test results were compared with a full scale sized tunnel.
- The ground support component characteristic and their performances in various configurations were determined.
- In particular, a large number of surface support schemes around the tunnels periphery were studied in great detail.

1.3 Outline of Thesis

The outline of the thesis are described in following sections.

Chapter 2 provides an overview of surface support in massive rock. Stress induced failure mechanism and past studies regarding crack initiation stress were reviewed. The chapter also highlights a surface element and its performance controlling dynamic related excavation damage.

Chapter 3 presents the rock material characteristics used in the thesis experiments. The laboratory tests were conducted to investigate the rock properties that could ne related to the observed behaviour under high stress.

Chapter 4 presents the techniques used to construct the experimented specimens. It also introduces the materials used for surface support and reinforcement with their characteristics and fabrication method.

Chapter 5 provides a review of the experimented methods used. The chapter highlights the monitoring techniques such as high speed filming, seismic data monitoring and laser scanning.

Chapter 6 provides the unsupported tunnel test results. The chapter reviews excavation behaviour and failure mechanisms under compression. Rock characteristics and excavation size effect are shown.

Chapter 7 provides a review of rock strength under high compression stress. The chapter highlights the relationship between intact rock strength to induced rock stress at failure.

Chapter 8 provides a comprehensive view of surface support performance subject to violent failure. The chapter provides a comparison of mechanical behaviour of most widely used surface support components and highlights the capability of surface support as an integrated systems with the reinforcing elements.

Chapter 9 introduces a quantitative assessment of surface support performance. Laser scanning data are utilised to provide a review of damage assessment of excavation surface stabilised with conventional and suggested ground support.

Chapter 10 highlights the outcomes of this research and provides some recommendations for future work.

Chapter 2

A Review of Surface Support Performance

2.1 Introduction

A brief review of surface support performance has been conducted. It summarises stress induced failure, a review of brittle failure studies and surface support performance.

2.3 Stress Induced Failure

As mining excavations go deeper, there is an increase in stress magnitude. In addition to structural failure, massive or moderately jointed rock mass faces serious stress driven failure at a great depth (Figure 2.1).

Figure 2.1 Stress-driven failure near the boundary of an excavation.

The nature of rock fracturing mechanism in massive rock is tensile (Ortlepp, 1997). In deep underground mines, increased stresses concentrated on the excavation boundaries induce extension fracture progression. An excavation surface is cleaved

and rock slabs are split at the stress concentration areas. The phenomena is called spalling and frequently observed under a high stress conditions (Hoek & Brown, 1980; Hoek, Kaiser, & Bawden, 1995). When stress is high around an excavation, the restrained energy releases as with spalling and induced violent failure. In addition, it eventually results in an excavation shape change with related instability issue (Figure 2.2).

Figure 2.2 Notch created following stress-driven failure in a hard rock mine.

2.4 A Review of Brittle Failure Mechanism Investigation

Tensile crack initiation within brittle materials have been studied for decades. Griffith (1921) investigated the tensile failure development in brittle materials. He proposed that a tensile crack propagated from the tips of microscopic inherent cracks in parallel to the maximum stress direction as a result of energy release. The tensile failure initiation threshold was expressed in the tensile strength in a biaxial stress condition.

This tensile crack criteria in brittle rock have been developed by a number of researchers (Fairhurst, 1964; Murell, 1958).

Bieniawski (1967) investigated fracture initiation process within rock specimens with stain measurement. Under triaxial compression, fracture initiation was experienced with a volumetric strain increase, which was well corresponded to the applied stress reaching 30 to 50 % of peak strength.

In massive or less jointed rock, a brittle failure initiated before surrounding stress reaches rock peak strength obtained from laboratory test (Hoek & Brown, 1980). The stress around underground excavation which induces failure does not correspond to the maximum stress obtained from laboratory specimen tests. Therefore, the 'actual' rock strength has been investigated using various methods as shown below.

2.4.1 Physical Model Tests

Stresses around a circular excavation has been examined using physical models. Generally the models composed of various intact rock materials with a circular hole were loaded either uniaxially or biaxially. The behaviour of the hole was monitored and its stress state was examined to investigate the failure mechanisms.

Hoek (1965) studies stress distribution around a circular excavation using a physical model composed of intact rock materials. The rectangular chert dyke block (127 mm x 127 mm x 3 mm) with a circular hole (19 mm diameter) was loaded biaxially. The applied horizontal load was decided as 0.15 times of the vertical stress. Deviatoric stress distribution was observed using photoelastic polariscope technics. After loading, a crack initiation was experienced at the top and bottom of the circular hole. It was induced by a tensile stress and further crack propagation was not seen from these points during the experiment. As loading increasing, a stress concentration was seen at the sidewalls of the excavation where predominant failures occurred. It induced a damage on the tunnel boundary and crushed materials detached resulting in a wedge formation.

Furthermore, fractures were continuously propagated within the specimen in a vertical direction.

Haimson and Herrick (1989) investigated the size effect on brittle failure initiation using limestone (average UCS 43 MPa). Boreholes with a diameter from 20 to 120 mm were drilled into rectangular blocks and loaded at a constant loading rate. Acoustic emission (AE) sensors were attached on to model specimens to monitor the fracture propagation process. A tangential stress magnitude at an onset of failure became constant with borehole which the diameter was greater than 75 mm. As for the smaller diameter boreholes, a stress required to cause the failure become higher.

Carter (1992) tested the fracture initiation around a circular excavation using limestone specimens. Diameters of hole ranged from 3.2 to 64 mm and specimen size were selected to ensure avoiding the boundary effect. Specimens were loaded uniaxially and strain gauges were attached to monitor fracture development. The applied stress which induced a failure around excavation at the tunnel boundary increased for the smaller diameter geometries.

Martin (1993) conducted physical model tests using rectangular granite block (average UCS 225 MPa). Circular holes with diameter ranging from 20 to 103 mm were drilled in the centre of the block and an uniaxial loading was applied with strain gauges on the surface. He compared the obtained results with past studies (Figure 2.3). Figure 2.3a shows the ratio of the material strength and tangential stress at the failure initiation with diameter of the hole. As can be seen, the result was affected by a hole diameter. The stress required to induce the stress becomes higher especially when a diameter of less than 75 mm is used (Martin, 1997). The ratio is also seen as affected by the ratio of pillar width to height.

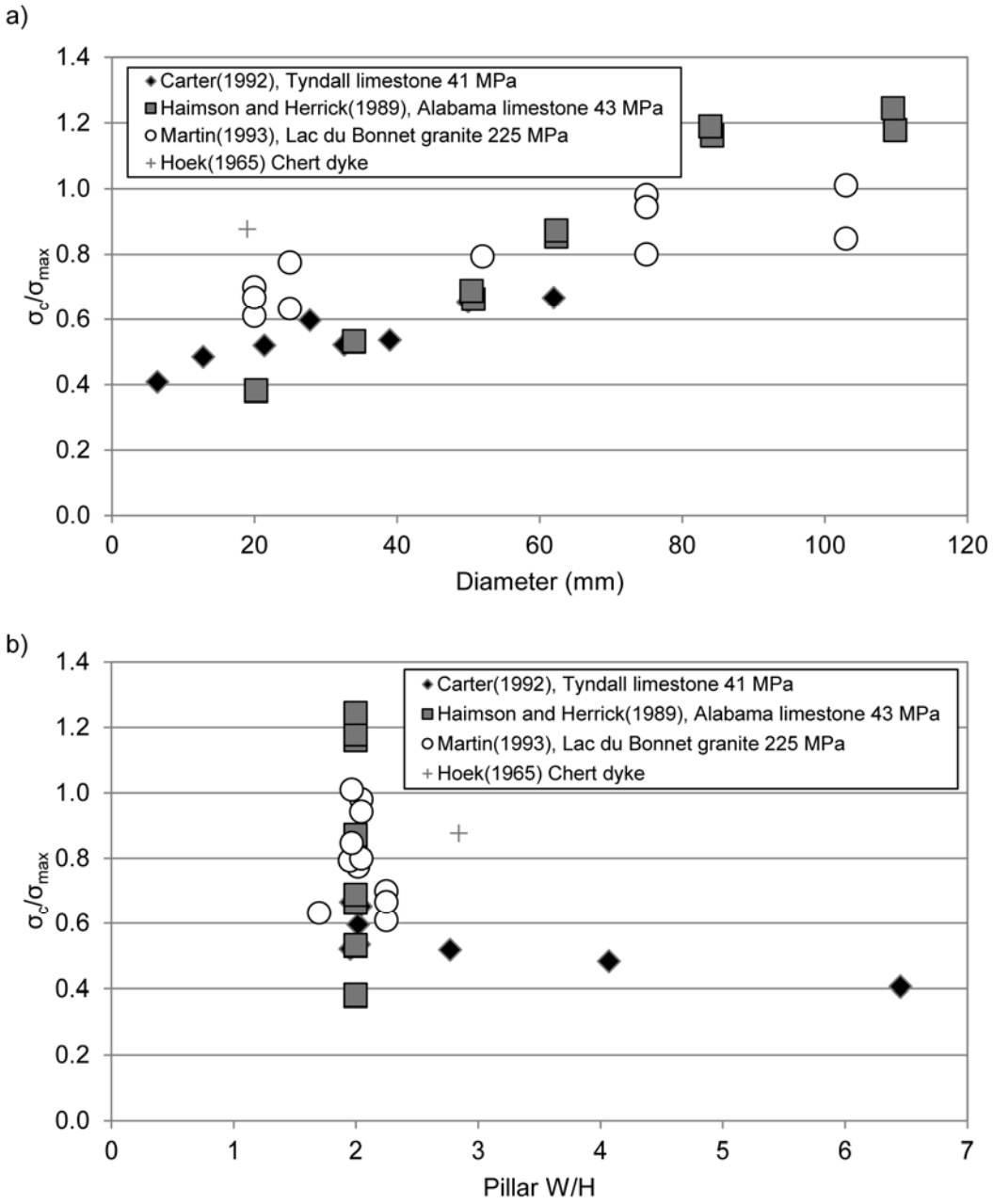

Figure 2.3 Summary of physical model tests a)plotted via diameter b)plotted via pillar width and height ratio (after Martin (1993)).

2.4.2 Crack Damage Initiation Thresholds

An empirical threshold of crack initiation has been investigated using triaxial and uniaxial compressive tests. Either strain measurement or AE measurement can be

undertaken to detect an initiation of crack within specimens. The obtained results were compared with full scale tunnel test and its versatility has been developed.

Martin (1997) investigated the progressive failure undertaking Mine-by experiment at the Underground Research Laboratory of Atomic Energy of Canada Ltd (AECL). A number of boreholes with various diameters from 75 to 1250 mm and a 3.5 m diameter circular tunnel were excavated in the Lac du Bonnet granite (UCS 225 MPa) and their failure mechanism were observed. The material properties of Lac du Bonnet granite was obtained by laboratory compression tests with the strain measurement. Cracks initiation was experienced when the applied stress reach 30 to 40 % of its uniaxial compressive strength. For the in-situ tests, the onset of the failure was observed when the ratio of the rock strength to the maximum tangential stress at the boundary reach 2, which was a lower stress level than the laboratory test result. Martin (1997) presumed that this was affected by its complicated stress path.

Diederichs (1999, 2003) established an empirical damage threshold to predict the damage initiation in massive rock by using a number of laboratory tests and case studies. Crack initiation was experienced when a stress reached 30 to 50 % of its uniaxial compressive strength, depending on deviatoric stress rather than confining stress. Induced cracks were coalesced and specimens became unstable before reaching the peak strength. At a low confinement condition such as near an excavation boundary, extensile crack creation dominated the failure mechanisms, while shear crack formation was experienced for a rock mass instability under high confinement state.

Diederichs, Kaiser, and Eberhardt (2004) conducted detailed research on crack propagation mechanisms. Although the laboratory sample tests crack development was categorised mainly in two distinct phases, crack initiation and damage propagation, at near excavation boundary crack propagates immediately after their initiation. Therefore, at in situ tunnel, crack initiation stress value can be identical to crack propagation.

Diederichs (2007) further developed an empirical damage threshold using various case studies and detailed investigations. He analysed crack propagation process in various stress paths and suggested that a crack initiation occurs when the deviatoric stress reaches 30 to 50 % of UCS. This value was postulated to be independent from rock material characteristics and spalling was induced only at a low confinement condition, i.e. near excavation surface. The empirical damage threshold has been applied and examined with many case studies.

Rojat, Labiouse, Kaiser, and Descoeudres (2009) evaluated the brittle rock mass behaviour at Lötschberg Base Tunnel in Switzerland using the data from AECL. The Steg lateral Adit was excavated with a diameter around 9.4 m in massive to moderately jointed rock mass using tunnel boring machines. Both threshold stress value of crack initiation and crack propagation were obtained by the uniaxial compressive test with the AE monitoring, as 30-50 and 40-80 % of UCS respectively. The in situ tunnel wall stability was assessed and the stress magnitude was estimated using numerical modelling. The results showed a reasonable agreement with AECL data.

Andersson and Martin (2009) conducted the full scaled size tunnel test at the Äspö Hard Rock Laboratory in Sweden (APSE). Two 1.75 m diameter boreholes were excavated 1 m apart and their behaviour were monitored. The boreholes were located within Äspö Diorite, heterogeneous and moderately fractured rock mass which the average UCS was 211 MPa. The crack initiation threshold obtained from the laboratory test was 45 % of UCS. The borehole was monitored by AE sensors and surface damage was observed immediately after the drilling. The stress magnitude was estimated by a numerical modelling and the average in situ spalling induce stress was 125 MPa, 60 % of UCS. The results were similar with Mine-by experiment at AECL and the crack initiation threshold stress was seen as independent from rock mass qualities.

Martin and Christiansson (2009) examined the crack propagation at the AECL and APSE in terms of a factor of safety to evaluate its severities. The crack initiation stress

value obtained from the laboratory tests was used as a rock strength and a spalling induce stress magnitude was estimated by numerical analysis. From two case studies, the spalling initiation stress value was approximately 57 % of UCS and a probabilistic analysis suggested that spalling would occur that when a factor of safety become lower than 1.25.

The reliability of the crack damage threshold estimation method has been verified and discussed by many researchers.

Ghazvinian et al. (2012) reviewed the crack damage threshold values of igneous rock which was obtained at four different laboratories. In each laboratory tests, both AE sensors and strain gauge were undertaken for crack propagation monitoring. The estimated crack damage thresholds were constant among various laboratories results, however, moderate differences were experienced between the values obtained by AE and stain gauge methods.

Nicksiar and Martin (2013) obtained the damage threshold value for various types of materials including igneous, sedimentary and metamorphic rocks by both uniaxial and triaxial compressive tests using the strain measurement. For all types of rocks, crack initiation was experienced at the stress value which was 42-47 % of its peak strength at uniaxial compressive test, while the value became higher when the specimen was confined (50-54%). Crack initiation stress value was concluded to be theoretically independent from rock material property.

Furthermore, Ghazvinian, Diederichs, Labrie, and Martin (2015) studied a sensitivity of fabric orientation on the crack damage threshold values. The crack damage threshold of four different types of brittle rock was investigated by uniaxial compressive testing with strain measurements. For each rock type, laboratory tests were undertaken several times with different core orientations. The results showed that while crack propagation and peak strength differed depending on core orientations, the

onset of crack initiation was constant, i.e. crack initiation threshold can be seen as insensitive to the heterogeneity and anisotropy of micro structure.

Cai and Kaiser (2014) examined an effect of irregularity of excavation boundary surface towards crack initiation. The stress distribution on rough excavation surface was analysed and the result was compared with the smooth surface result. It shows an oversimplified interpretation of excavation shape could lead an underestimation of the in situ rock strength.

In terms of research gaps, the literature review has indicated that experiments that include ground support schemes has never been undertaken before. Since failure cannot be avoided the safety of the excavations and the personnel accessing them relies on the effectiveness of the ground support implemented. The failure around excavations need to be retained by the ground support. Given that the failure in shallow, the performance of the support around the periphery of the excavations is critical.

2.5 A Review of Surface Support for Massive Rock

For ground support design, it is essential to estimate a possible stability problem and select an appropriate ground support design. In massive or moderately jointed rock, high stress condition induces violent failure which is caused by a sudden energy release (Villaescusa, 2014). It is essential to adopt a ground support scheme which has a high energy dissipation capacity.

Thompson, Villaescusa, and Windsor (2012) pointed out that the ground support design procedure can become complicated when a violent failure is expected to happen. In addition to correct damage estimation, ground support with high dynamic capacity need to be selected to increase safety and achieve excavation stability.

2.5.1 Excavation Stability Estimation

The ratio of uniaxial compressive strength σ_c of intact rock to the induced compressive stress tangential to the wall of an excavation σ_{max} has long been recognised as a critical factor controlling excavation stability (Barton, Lien, & Lunde, 1974; Mathews, Hoek, Wyllie, & Stewart, 1980). This ratio has been utilised for rock mass classification and pillar stability graph method as a rock stress factor. Data from many years of numerical modelling and observations of open stoping at Mount Isa Mines (Villaescusa, 2014) have shown that as the ratio decreases below the value of 5, the instability increases markedly (Figure 2.4). The lower the ratio, the more potential for stress induced failure.

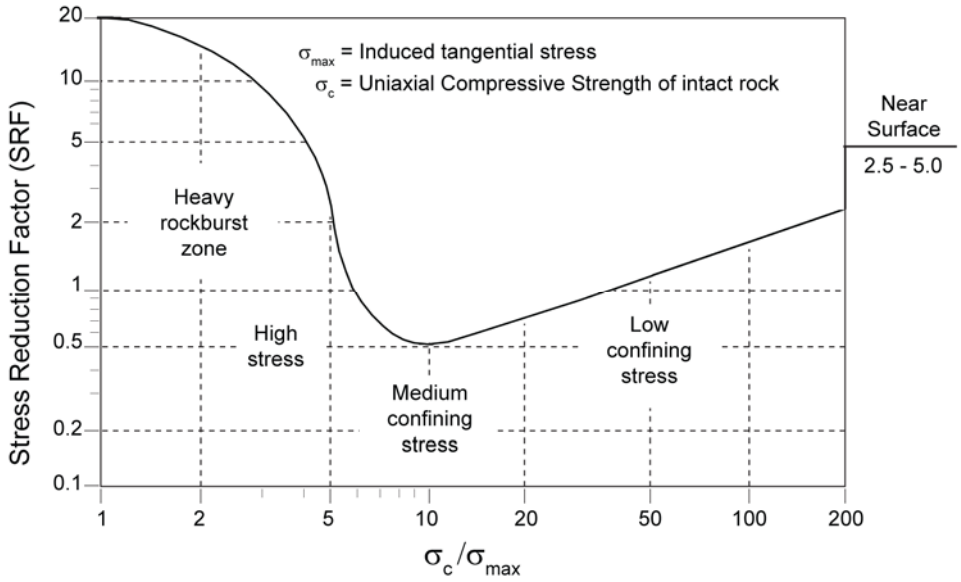

Figure 2.4 Excavation behaviour as a function of the ratio of compressive strength to the induced stress (after Barton et al. (1974); Hutchinson and Diederichs (1996)).

2.5.2 Surface Support Selection

Thompson et al. (2012) stated that a ground support consists of two distinct parts, reinforcement and surface support systems. While reinforcement system contributes to enhance the entire rock mass stability, surface systems restrain excavation surface area between reinforcement spacing (Villaescusa, 2014).Since stress induced failure

occurs near the excavation surface, proper surface support installation become essential to contain the excavation damage.

2.5.2.1 Surface Support

Surface support composes of elements installed on an excavation surface including mesh and shotcrete layers. Unlike reinforcement systems, surface support functions as areal rather than locally between reinforcement spacing (Thompson et al., 2012; Thompson & Windsor, 1992). Loading to surface support is mainly due to the excavation surface movement. In addition to each component characteristics, element selection and configurations of surface systems define a comprehensive surface support performance.

2.5.2.2 Mesh Performance

In underground mines, wire mesh has been installed to restrain deteriorations from excavation surfaces. Welded wire mesh and chain link mesh are widely used in the mining industry in Australia (Villaescusa, Azua, Player, & Morton, 2012).

A large static and dynamic testing of steel mesh were undertaken at WASM to examine their performance (Player, Morton, Thompson, & Villaescusa, 2008). A 1.3 m x 1.3 m size of welded mesh and chain link mesh sheets were loaded in the centre. In addition to load displacement, energy dissipation capacity were obtained from the test results. In the static test, welded mesh ruptured in three different mechanisms, tensile failure, weld failure and failure in heat affected zone. When the latter two cases were experienced, failure occurred before reaching the wire tensile strength. On the other hand, chain link mesh failed at the edge of the loading plate. The test results implied that chain link mesh showed higher performance in all the aspect both in statically and dynamically. Especially, chain link mesh showed higher energy dissipation capacity (Thompson et al., 2012).

2.5.2.3 Shotcrete Performance

Shotcrete is sprayed onto excavation surface directly, therefore it is expected to restrain and supply immediate response to excavation surface movement (Villaescusa, 2014).

Shotcrete performance have been tested using the static testing facilities at WASM (Morton, Thompson, & Villaescusa, 2009). Various configurations of shotcrete mix were tested and the results enabled to compare its force-displacement and energy dissipation capacities. The performance of shotcrete layers reinforced using fibres and mesh were compared. The test results showed that shotcrete had a limited deformability, however, it had flexibility to respond to an immediately movement (Villaescusa, 2014). Compared with fibre reinforced shotcrete. The energy dissipation capacity increased significantly when mesh was embedded.

Drover and Villaescusa (2015) suggested that the total energy dissipation capacities of surface support have improved when mesh is embedded under shotcrete layer rather than mesh exposed outside the shotcrete layer. When mesh was exposed outside the shotcrete layer, each surface support element functioned individually (Figure 2.5). Mesh simply restrained the broken materials and helped to reduce the severity of a failure. Reinforced shotcrete by mesh performed as an integrated systems and showed higher toughness compared with fibre reinforced shotcrete (Figure 2.6).

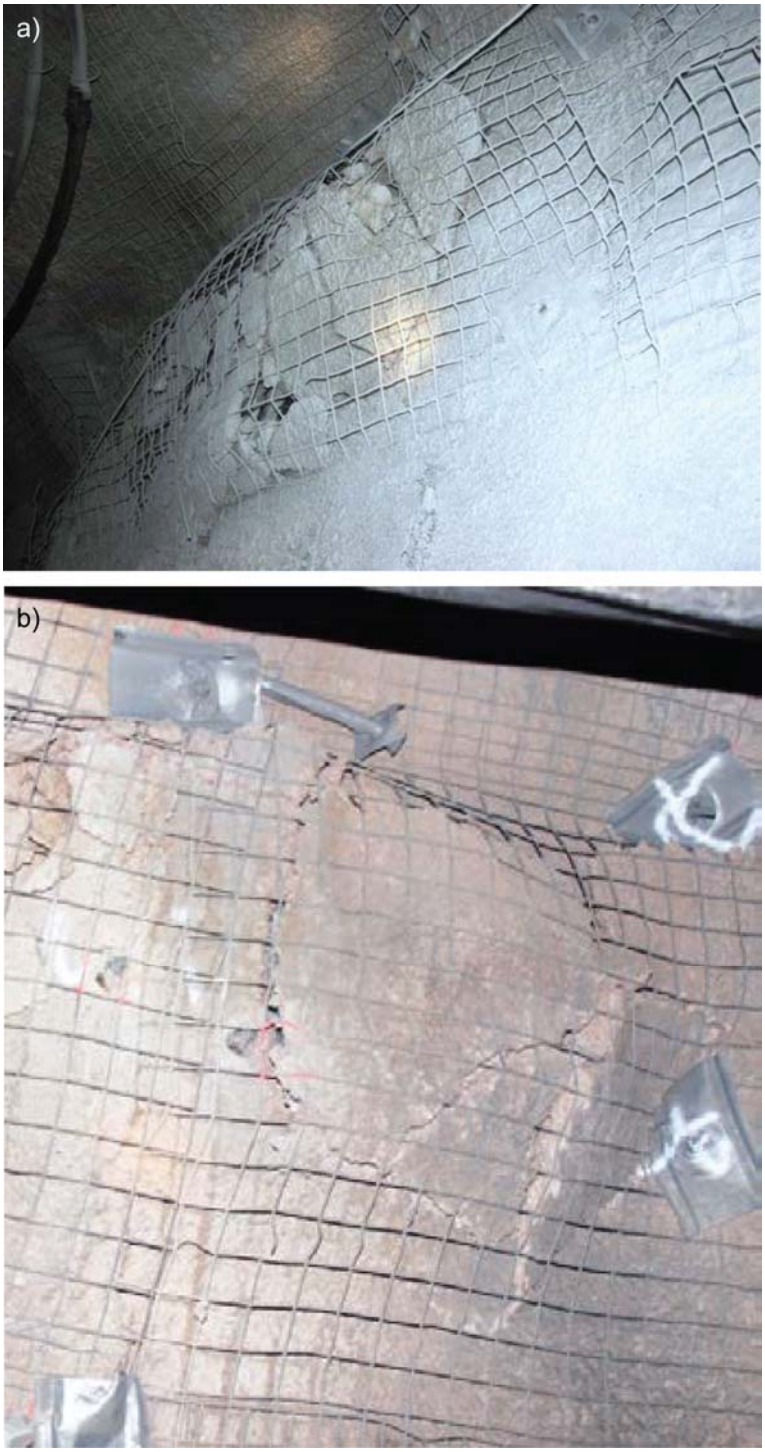

Figure 2.5 Flexural failure of shotcrete with external welded mesh (Drover & Villaescusa, 2015).

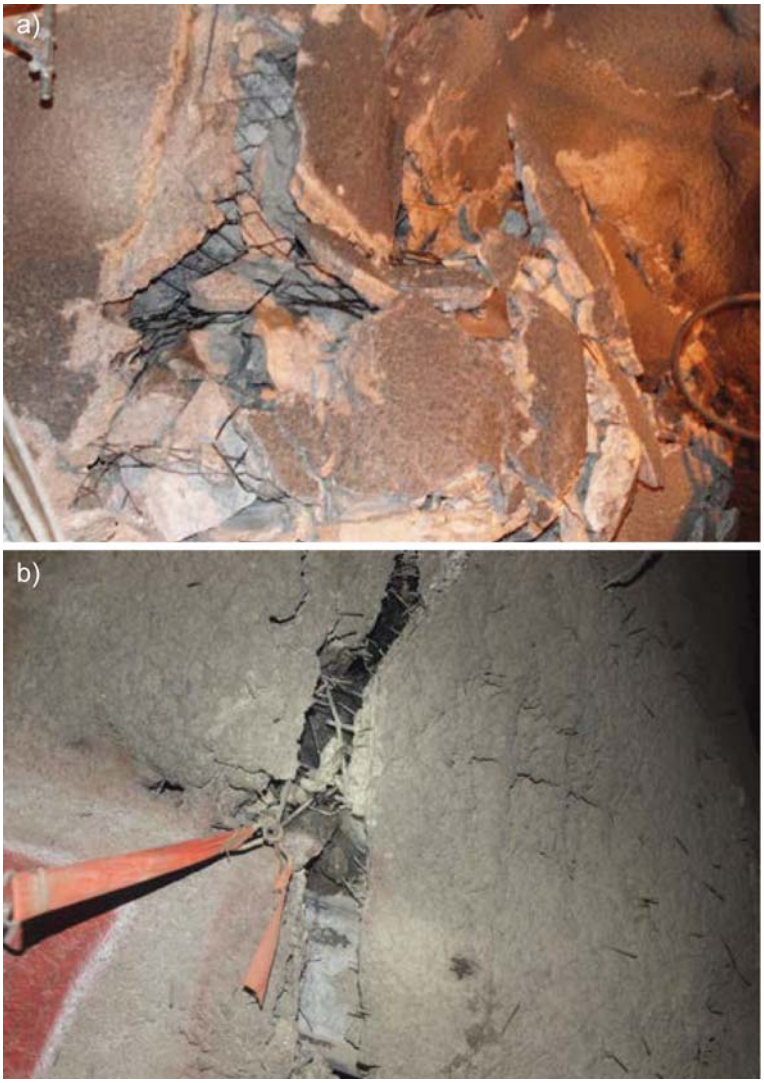

Figure 2.6 Failure in a reinforced shotcrete layer a) chain link mesh b) mild steel welded mesh (Drover & Villaescusa, 2015).

For massive rock, Villaescusa (2014) suggested a surface support installation which consists of a shotcrete reinforced by mesh. A shotcrete layer can accommodate a sudden rock movement and provide the confinement pressure to an excavation surface, with the embedded mesh helping to restrain a larger rock failure.

2.6 Literature Review Summary

It has been recognised that violent failures have become severe issue on excavation surface with an increase in depth. The stress induced failure mechanism within rock

materials have been studied and in situ rock strength have been investigated using physical model and laboratory sample test data. From laboratory sample tests, it implies that failure initiation is experienced when applied stress reach about 40 % of UCS.

It is also necessary to select and install appropriate ground support to contain dynamic failures. However, very few studies has been undertaken to evaluate a surface support performance as an integrated systems. Consequently, there is a need for a better understanding of rock mass demand under high stress and a comprehensive surface support capacity regarding dynamic failure.

Therefore the thesis focuses on the following aspects;

- Understanding of failure mechanisms of circular excavation under high stress.
- Assessment of surface support performance subject to violent failure as an integrated ground support system.

Chapter 3

Material Characterisation

3.1 Introduction

Three different intact rock materials were selected to investigate the effect of the rock strength subjected to an increased stress. Since this research is focusing on the stress driven failure, intact rock without open geological feature were studied. The material consisted of soft and hard sandstone and also granite (see in Figure 3.1). Blocks consisting of sandstone and granite were tested during this research. The material strength was classified according to Knill et al. (1970) as shown in Table 3.1. The sandstone was procured from Queensland and Western Australia and the granite from Western Australia. The sandstone materials consisted of fine and coarse sand particles densely packed to form slightly coloured layers. The granite material consisted of quartz, feldspar and biotite.

In all cases, the intact rock blocks were inspected and arranged such that the subsequent loading was undertaken perpendicular to any bedding or obvious geological weakness. For each block tested, a central core was recovered. This core was subsequently re-drilled to determine the intact rock strength properties. The rock specimens were cored parallel to the loading direction by using a diamond drilling machine (Figure 3.2). The intact rock properties were determined parallel to the vertical direction of loading.

Table 3.1 Rock classification regarding to uniaxial compressive strength (Knill et al., 1970).

Strength (MPa)	Term
- 1.25	very weak
1.25 - 5	weak
5 - 12.5	moderately weak
12.5 - 50	moderately strong
50 - 100	strong
100 - 200	very strong
200 -	extremely strong

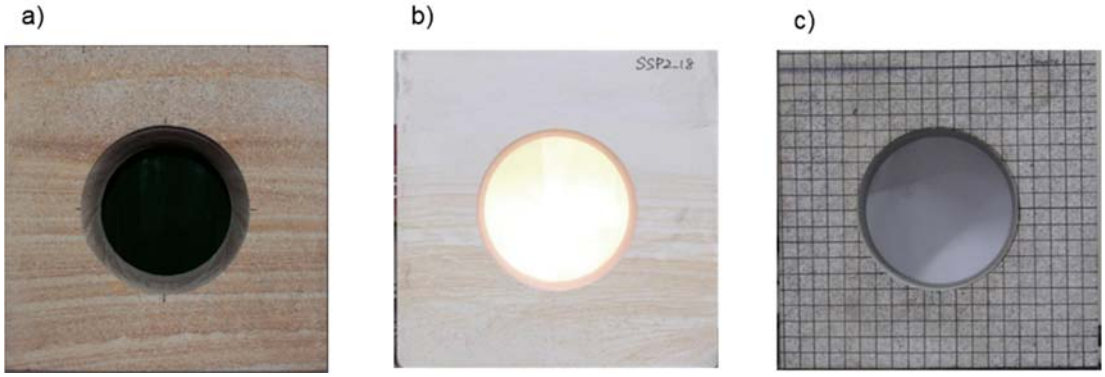

Figure 3.1 Three rock mass blocks used for physical testing, a) moderately strong sandstone, b) strong sandstone and c) very strong granite.

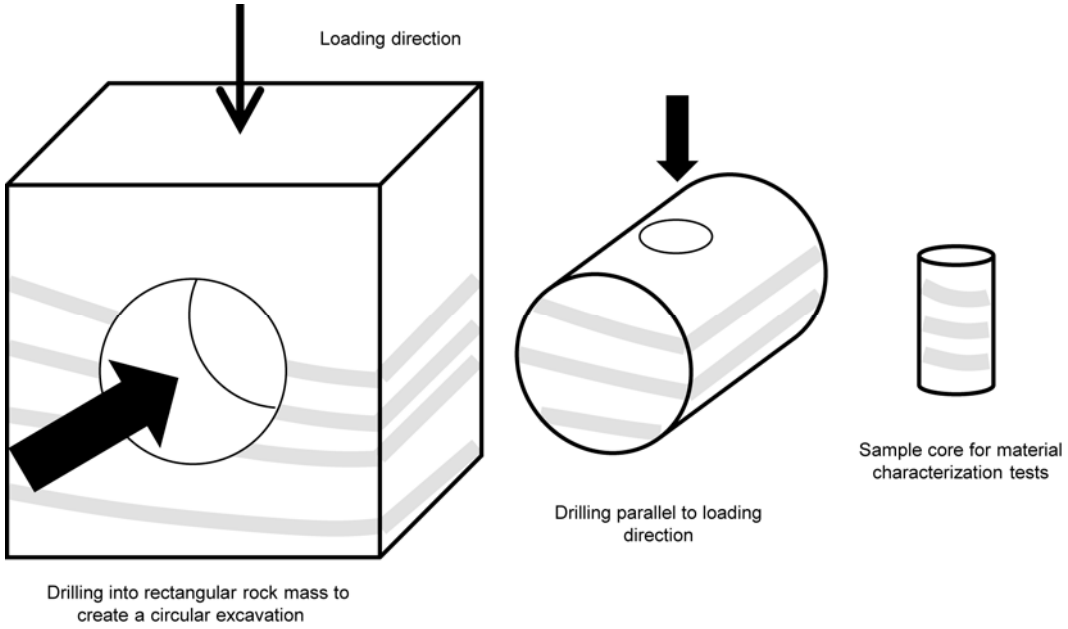

Figure 3.2 Drilling configuration for rock mass preparation.

3.2 Uniaxial Testing

Uniaxial compressive testing was conducted using an INSTRON loading machine. The sample specimens were prepared following ISRM suggested methods (Brown, 1981). The sample cores were drilled to ensure the height / diameter ratio was more than 2.5 and the specimen ends were perfectly grinded perpendicular to the loading direction. Two strain gauges were attached to the middle of the specimen on two opposite sides to measure the axial and lateral strains resulting from the uniaxial

loading. Uniaxial compressive strength, Young's modulus and Poison ratio were determined by the results.

3.2.1 Uniaxial Compressive Strength

The result of uniaxial compressive testing for the three materials is plotted in Figure 3.3. The average uniaxial compressive strength σ_c of the two different types of sandstone is 19 MPa (Figure 3.4) and 82 MPa (Figure 3.5), which is categorised as moderately strong and the strong rock respectively, while the uniaxial compressive strength of granite is 182 MPa (Figure 3.6) which is categorized as very strong rock. As seen on the result, there are some varieties in the strength among the same materials. Violent failure occurred only with strong to very strong materials.

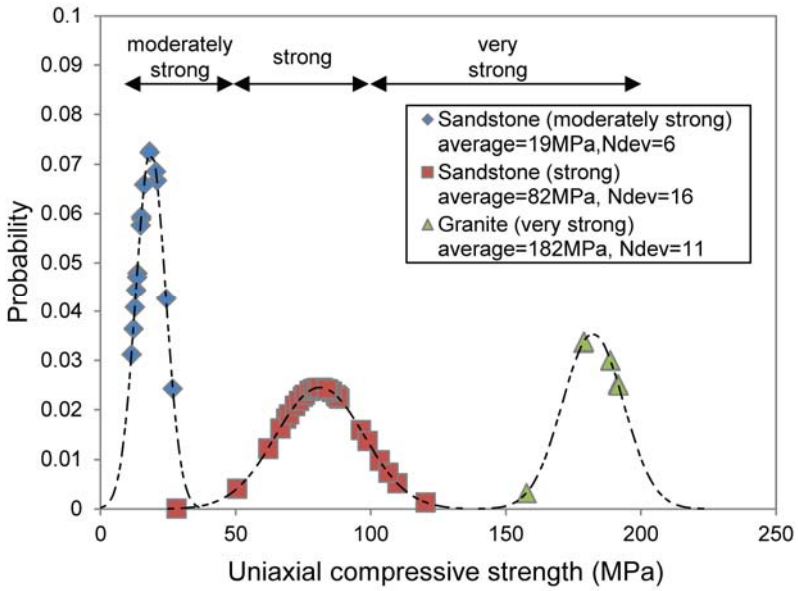

Figure 3.3 Normal distribution of the uniaxial compressive strength obtained by the uniaxial compressive testing.

Figure 3.4 Example of moderately strong sandstone sample after uniaxial compressive strength test.

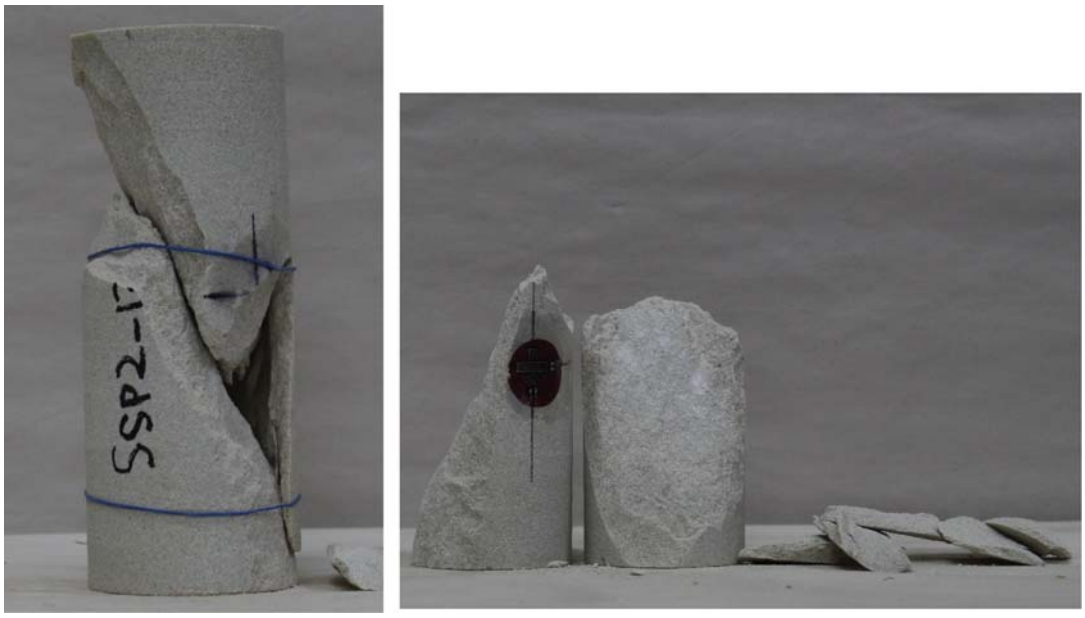

Figure 3.5 Example of strong sandstone sample after uniaxial compressive strength test.

Figure 3.6 Example of granite sample after uniaxial compressive strength test.

3.2.2 Young's Modulus

The Young's modulus E_i was determined from the two strain gauges data. Figure 3.7 shows the relationship between the uniaxial compressive strength and Young's modulus for two types of sandstone and one type of granite. There is a strong positive correlation between these two factors as determined by other earlier research (Li, 2004).

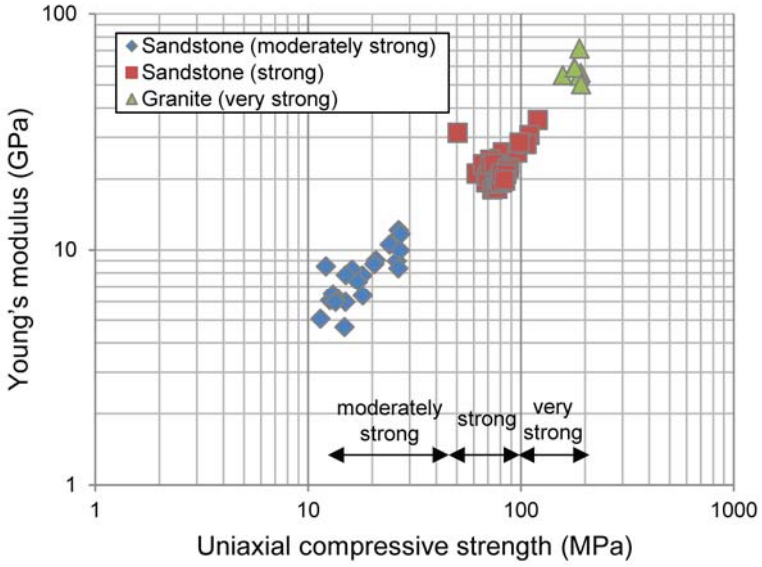

Figure 3.7 Uniaxial compressive strength and Young's modulus for three different types of rock mass samples.

3.2.3 Poison's Ratio

The Poison's ratio was also determined using strain gauge data. The results are shown in Figure 3.8. The Poison's ratio ranges from 0.15 to 0.40 for the two types of sandstone and ranges from 0.20 to 0.30 for the granite. The granite shows less dispersion compared with the sandstone.

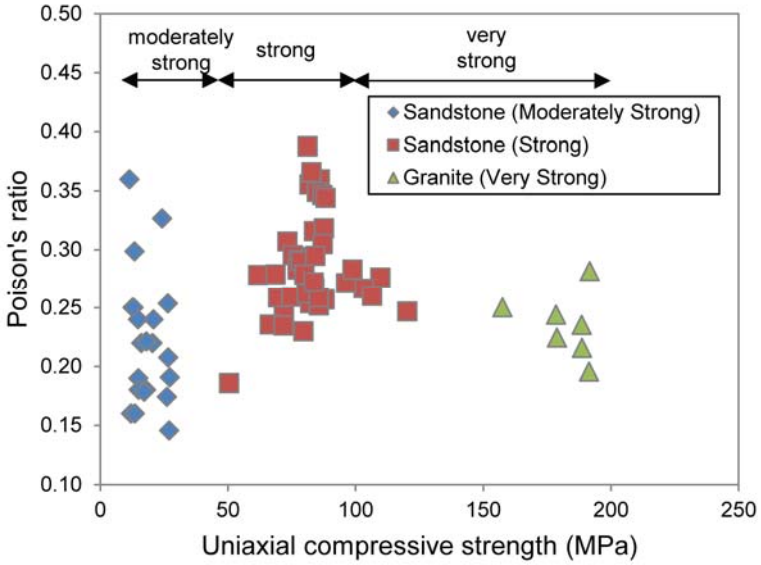

Figure 3.8 Summary of Poison's ratio on three rock materials.

3.2.4 Tensile Strength

The tensile strength of the strong sandstone was investigated by the Brazilian test to obtain the input parameter for subsequent numerical modelling (Figure 3.9). The sample specimens were prepared according to the ISRM suggested method (Brown, 1981). The scatter diagram of the tensile strength and uniaxial compressive strength were plotted in Figure 3.10. The average tensile strength of the Strong sandstone is 4.6 MPa, which is approximately 1 /16 of the average uniaxial compressive strength.

Figure 3.9 Example of strong sandstone sample after Brazilian test.

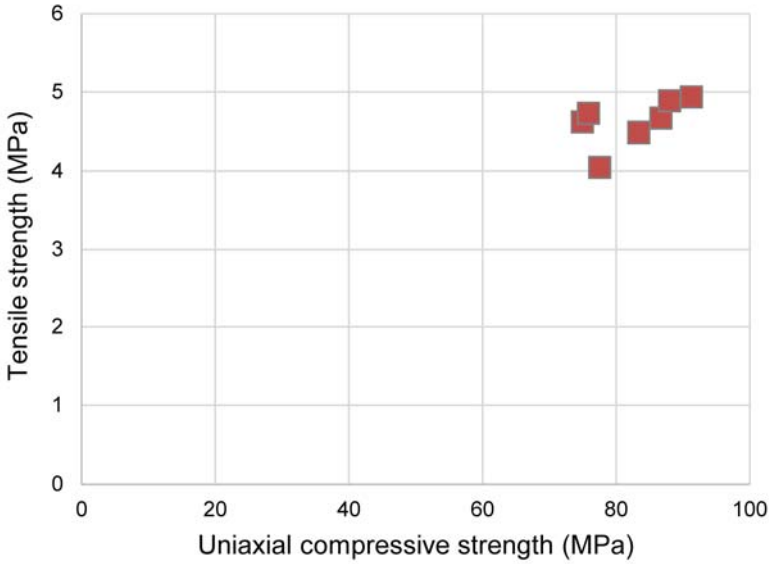

Figure 3.10 Tensile strength of the Strong sandstone plotted by uniaxial compressive strength.

3.3 Triaxial Testing

In addition, triaxial testing was undertaken to obtain the cohesive strengths and friction angles at failure. Three different confining pressures ranging from 1 to 3 MPa for moderately strong sandstone, and 5 to 15 MPa for strong sandstone and granite were used during the triaxial loading respectively. Three sets of tests were conducted for each rock mass type to examine the laboratory test result.

3.3.1 Failure Envelope

The strength curves of each material were determined from the average value of the triaxial test results. Each test result was well fitted to the linear slope lines (see in Figure 3.11). These linear equations are material specific. The tangent of the slope angle is 5 and 8 for sandstone, and 13 for granite. The intercept of the strength curve is in accordance with the average uniaxial compressive strength which was obtained from the previously mentioned uniaxial compressive strength test result (Figure 3.3).

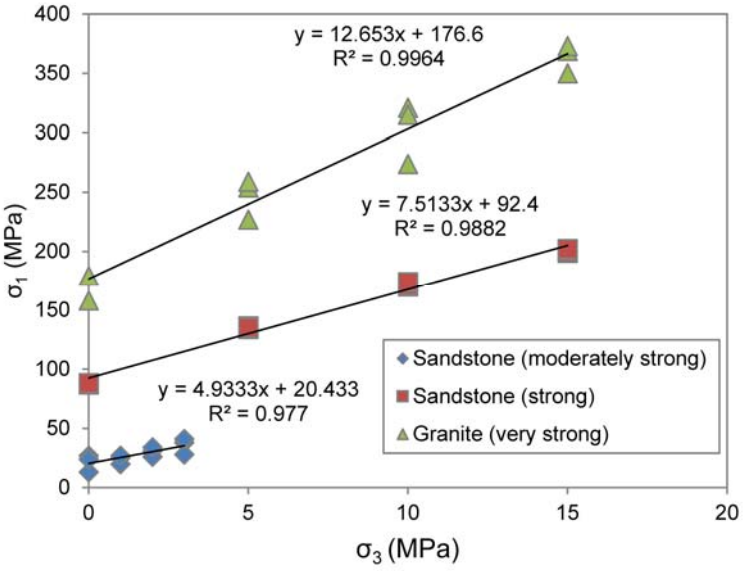

Figure 3.11 The average strength curve obtained from the triaxial compressive strength tests.

3.3.2 Cohesive Strength and Friction Angle

The cohesive strength and friction angle of the three rock types have been determined from the average strength curves. These values were used within subsequent numerical modelling based on the Mohr-Coulomb's failure criterion.

The cohesion values for the sandstone were 5 MPa and 17 MPa for moderately strong and strong material types, respectively. The granite had an average cohesion value of 25 MPa. As for the friction angle value, the moderately strong sandstone showed the lowest angle of 41°, while the strong sandstone and granite had 50° and 59° respectively.

3.4 Material Property Summary

The summary of the three material properties as determined from the uniaxial and triaxial compressive strength tests is given in Table 3.2. Two different types of sandstone showed different material behaviour and were classified as moderately strong and strong respectively based on the uniaxial compressive strength test. Moderately strong sandstone consists of coarser particles interacted with weak

structural layers across the entire block surface. The specimen failed non-violently and the failure surface followed the structure lines. On the other hand, the strong sandstone was composed of the finer sand particles. With coloured layers partially seen in a horizontal direction. The granite block mass showed a much higher strength than two sandstone blocks. It was homogeneous and the heaviest material and showed the least deviation on the laboratory test results amongst the three materials.

Table 3.2 Average material properties of three different rock mass blocks.

Rock type	Strength Category	Unit weight (kN/m^3)	Uniaxial compressive strength (MPa)	Young's modulus (GPa)	Poison's ratio	Cohesive strength (MPa)	Friction angle (°)	Tensile strength (MPa)
Sandstone	MS	21.2	19	8	0.2	5	41	
Sandstone	S	22.6	82	13	0.2	17	50	4.6
Granite	VS	26.0	182	58	0.2	25	59	

Chapter 4

Model Test Preparation

4.1 Practicalities and Limitations

The research is based upon laboratory testing, when the in-situ conditions can never be entirely replicate. There were some practical limitations in the scaled-tunnel construction and the experimental process. First of all, the size of the rock blocks were determined by the space available inside of the available testing machine for this research. The size of the 400 W x 400 H x 400 L mm intact rock blocks were designed to fit into the WASM servo controlled INSTRON loading machine space. The typical size of the tunnel diameter tested was determined to be 200 mm. This allowed the accessibility for scaled down ground support system installations. Because of the rock block dimension, the pillar width was set to 100 mm on either side. This resulted on a pillar size having less than 3 times the tunnel diameter. Consequently, to enhance the pillar strength, a moderate amount of horizontal confining pressure was provided by steel plates restrained by bolts in order to ensure that post-peak strength of the rectangular block was achieved.

In addition to inhomogeneous material properties, the shape of the blocks had some variations in the size ranging between ±5 mm. The block materials were cut to size by a stone masonry and the holes drilled by the author at WASM. The blocks contained some irregularities and errors in squareness and geometry. In addition block materials have heterogeneous characteristics. Sandstones is a sedimentary rock which contains random intrusions and occasional coarse sand particle layer. These varieties in design and material properties appear to affect the failure mechanism, i.e. the tensile crack appearance position, and the asymmetric failure behaviour due to a slightly uneven stress distributions. Blocks which had considerable potential to affect the failure mechanism were eliminated in the process of the sample preparation.

4.2 Scaled-down Tunnel Construction

Figure 4.1 shows the blocks following delivery to WASM. The rectangular blocks were drilling using a diamond drill core as shown in Figure 4.2. Tunnel diameters consisting of 50 mm. 100 mm and 200 mm were compared to examine different pillar strengths. Figure 4.3 shows a completed tunnel following diamond drilling.

Figure 4.1 Sandstone block (strong) before the drilling process.

Figure 4.2 Example of 200 mm core drilling into a sandstone block.

Figure 4.3 Typical tunnel and pillar geometry tested (grid size 20 mm x 20 mm).

4.3 Ground Support System

Scale-down ground support systems which include rock bolts, shotcrete and mesh were installed into the model tunnels. The objective was to replicate a typical 1.5 m x 1.5 m square pattern of rock bolting used in the mining industry. The choice of material properties for the different ground support elements was limited to commercial products at the scale of problem. The choice of materials for the ground support was determined to ensure that failure occurred at the surface support of the scale-down tunnels. That is, the small bolts were designed with a rigid rather than a yielding behaviour.

4.4 Reinforcement

The intact rock block was mounted on a specially developed rotation system which enabled the block to easily rotate 360 degrees to enable a ground support installation (Figure 4.4). The rectangular block was confined with two circular timber plates perpendicular to the tunnel axis. The plates had a hole and four steel brackets inside to hold the block in position and were tightened firmly by four threaded bolts. The block was then set onto a steel stand with four rotors. They were designed to support the

block and to enable smooth rotation with little leverage. Since the intact rock block weighed approximately 60 kg on average, this rotation system helped to increase a material handling capacity and to achieve an elaborate ground support installation.

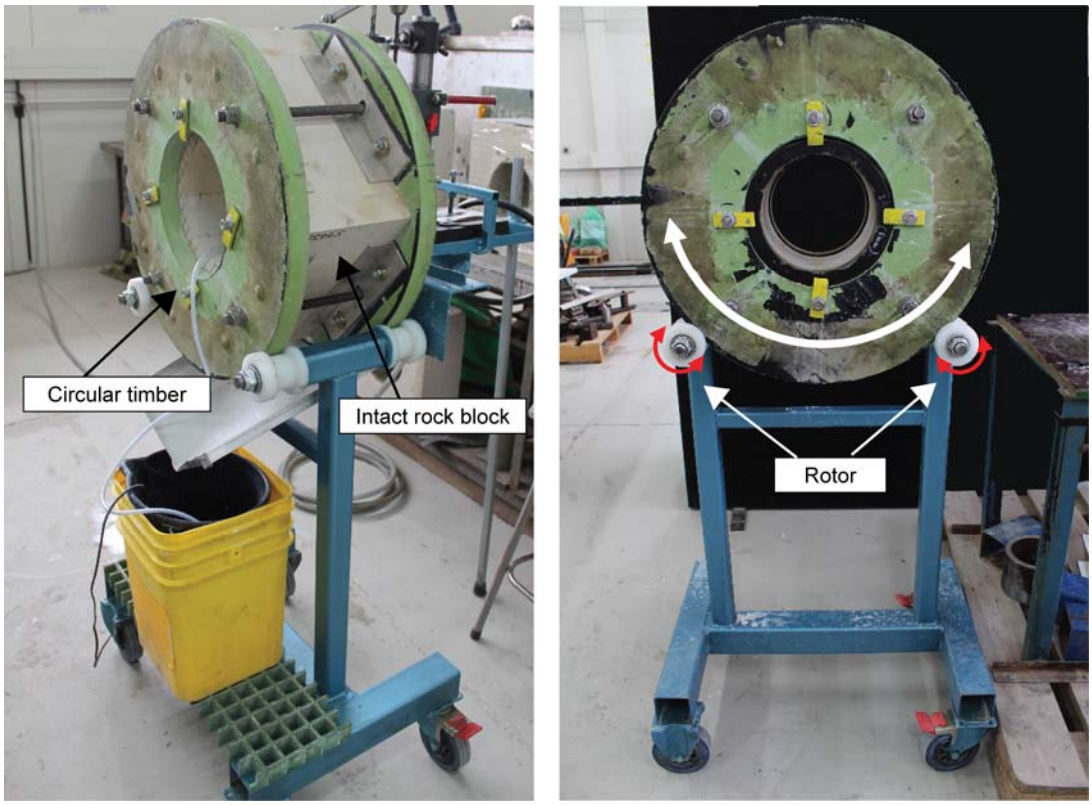

Figure 4.4 Intact rock block rotation system.

Small sized rock bolts were installed as a part of the evaluated ground support schemes. A pneumatic drill was set onto a modified drill press equipment (Figure 4.5). A commercially available drill press was transformed into a drill holding machine to give an offset capacity. The pneumatic drill became adjustable along the tunnel axis and a drill bit penetrated straight and vertically into the intact rock. The drill was pushed through a leverage bar until designed length was reached. A series of 5 mm diameter boreholes were drilled perpendicularly into the intact rock blocks from the tunnel surface using the pneumatic drill (Figure 4.6).To eliminate a friction heat by drilling, the tunnel surface kept wet during the drilling process by using a water pump.

The bolt length was set as 50 mm, and a 2.15 mm diameter threaded steel bar was used to simulate the rock bolt material. The borehole was filled with a high strength adhesive and the rock bolt was inserted to ensure full capsulation to maximize its strength. Once the adhesive was set, the bolt was plated with several washers and fixed by a nut.

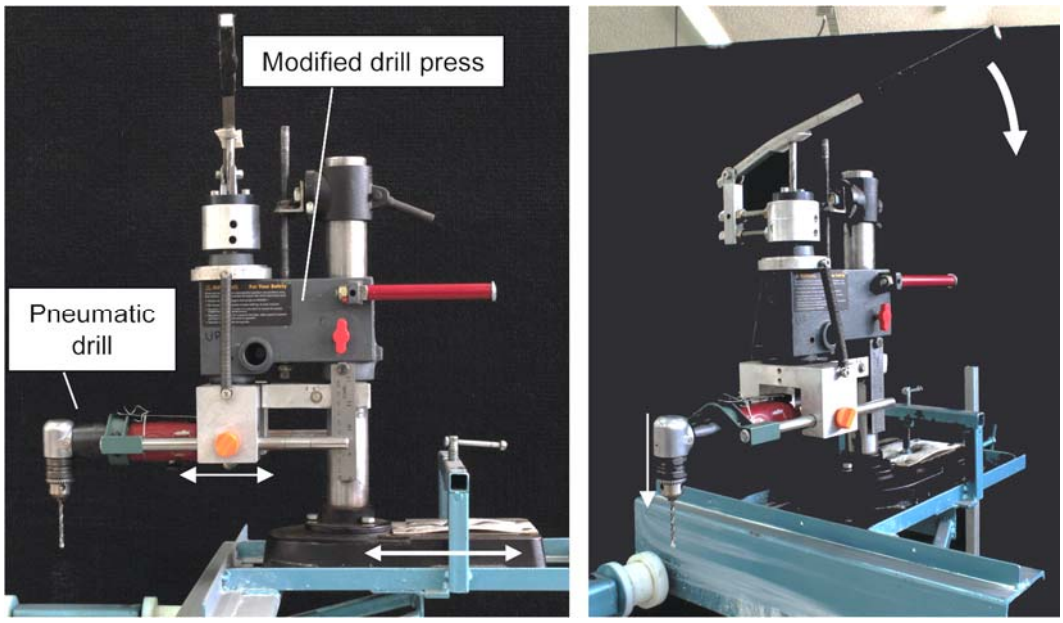

Figure 4.5 The miniature drilling system.

Figure 4.6 Borehole drilling process using a 5mm diamond drill bit.

4.4.1 Rock Bolt Types

The fully threaded rock bolt used had a thread pitch that was uniform for its entire length. This provided continuous mechanical coupling and allowed tension load. The bolt end was fixed by tightening the nut over several washers.

4.4.2 Encapsulation Material

The resin was a liquid epoxy adhesive which intruded into the thread gap and maximised the load transfer capacity.

4.4.3 Tensile Loading Test

Two tensile loading tests were conducted to investigate the miniature rock bolt mechanical properties. The rock bolts were installed into strong sandstone, which was the same material as used in the ground support experiments. The sample core and the end of the rock bolt were confined by a purposely built frame and pulled using a uniaxial Avery machine (Figure 4.7). The face plates were pulled until the bolt failed at the core axis.

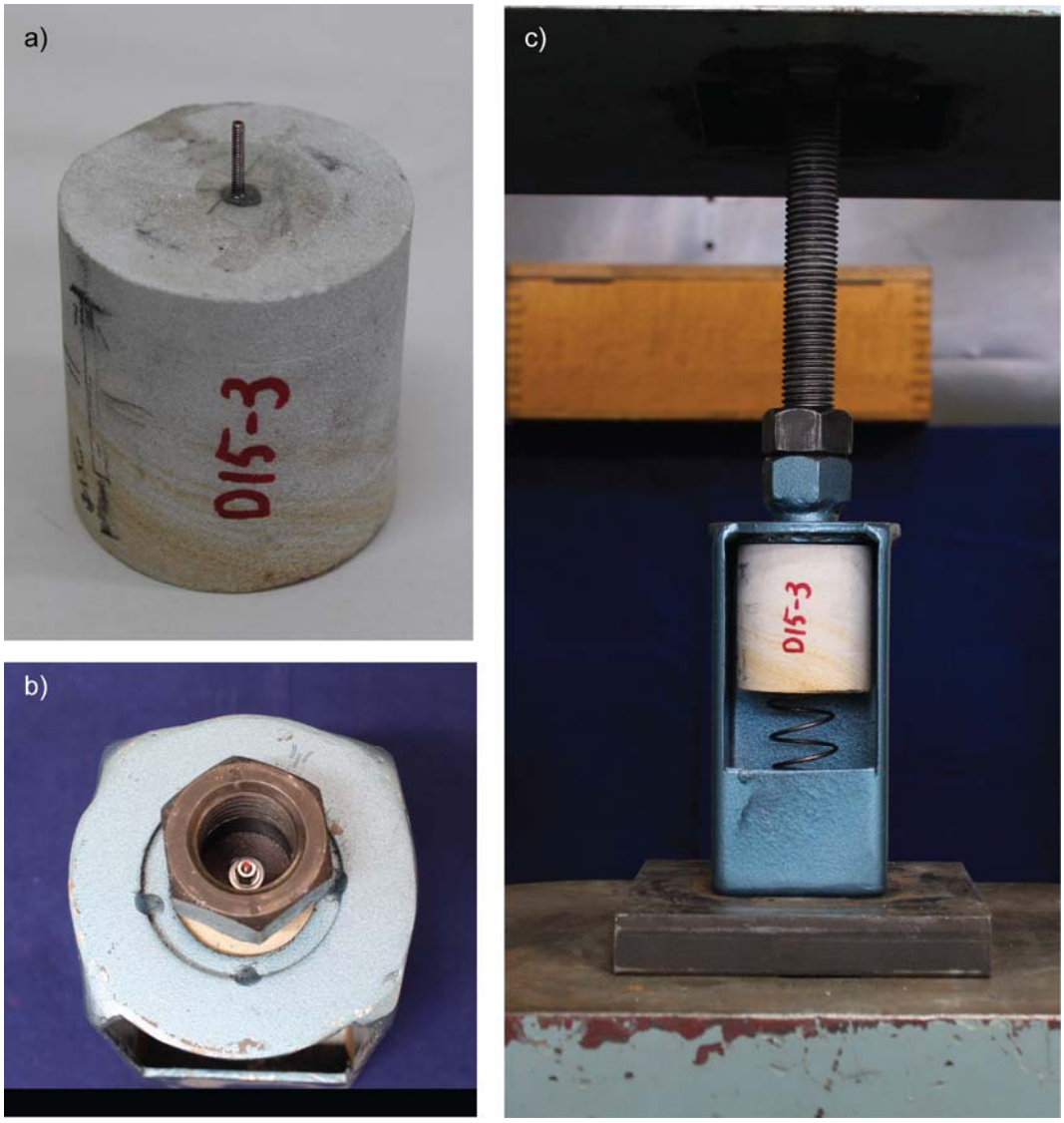

Figure 4.7 The setting for the rock bolt tensile test by Avery loading machine a) a test sample b) bolt head fixed by nut c) pull testing configuration.

4.4.3.1 Embedment Length Test

The load transfer of the miniature bolts was examined by using a tensile test of different embedment lengths. A 5 mm diameter borehole was drilled into a piece of strong sandstone. Borehole lengths having 10 mm, 15 mm and 25 mm were prepared. The rock bolts were encapsulated by adhesive and cured until the adhesive was set. The end of the rock bolt was fixed to the test apparatus by the nut and pulled by the Avery machine until the rock bolts were either pulled out or broken. Figure 4.8 showed

the results of the embedment length testing. The rock bolts with 10 mm embedment length were pulled out from the anchor area. On the other hand the rock bolts which had on embedment length of more than 15 mm were broken within the exposed part of the bolt.

The strength of the adhesive in this experiment had proved to be stronger than the rock bolt strength. The rock bolt failed first when the anchor part length was more than 15 mm. The interaction with the strong sandstone was also confirmed by the experiments.

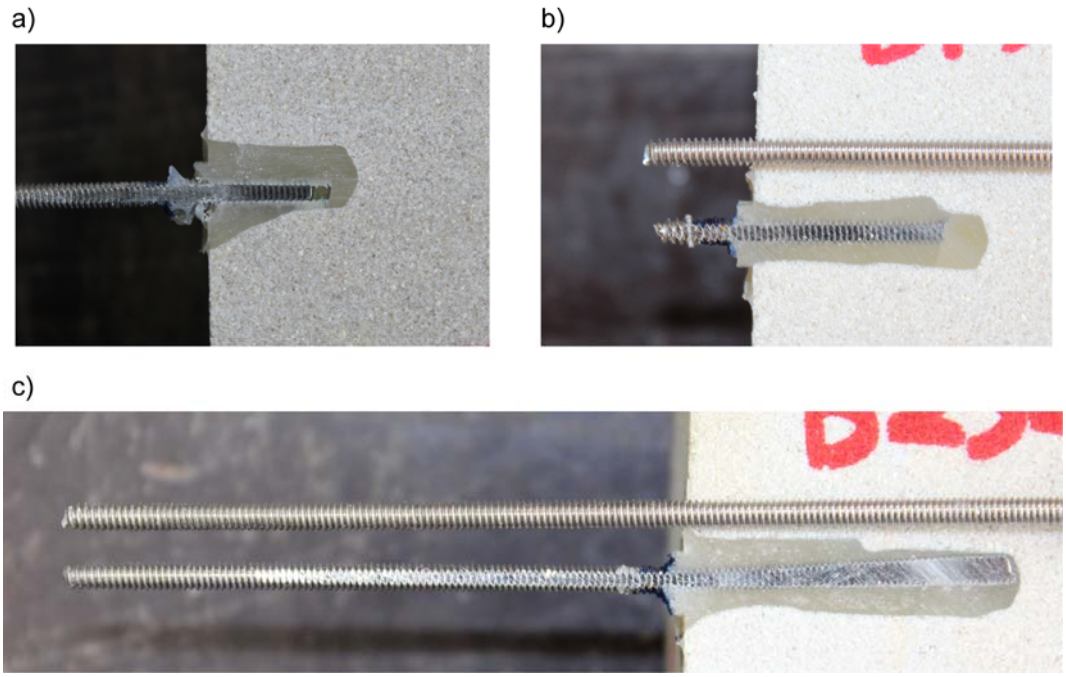

Figure 4.8 The rock bolts after the critical embedded test for the different anchor length a) 10mm b) 15mm and c) 25mm.

4.4.3.2 Tensile Loading Test

The performance of the rock bolt element was examined using a tensile strength test. The fully encapsulated rock bolt was loaded from the washers until the bolt failed by breaking of the element (Figure 4.9). A 5mm borehole was drilled into a sample core using the same method as the embedment length test. As shown in Figure 4.10, a 65 mm length threaded rock bolt was embedded into the rock sample perpendicular to the rock surface. The embedment length was set as 50 mm which was the same design as

the ground support scheme used with the rectangular block mass. The exposed part between the anchor region and the collar part was pulled from the washers until the rock bolt failed.

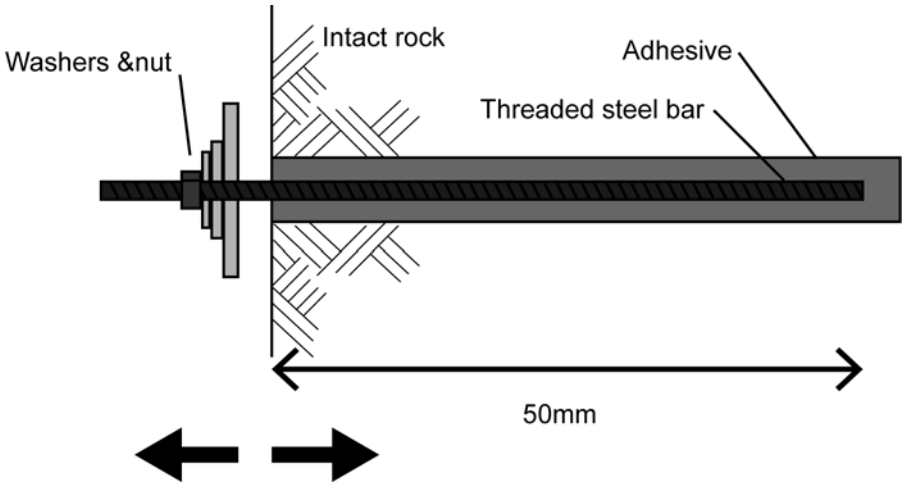

Figure 4.9 Configuration used for rock bolt static tensile test.

Figure 4.10 The sample specimen with the rock bolt prior to the tensile test.

The load-displacement curves are shown in Figure 4.11 and the test results are summarised in Table 4.1. When the load reached its peak, the rock bolt started to yield until the bolt failed. The rock bolts failed at an average load of 2.3 kN. The failure occurred at the rock bolt head as shown in Figure 4.12.

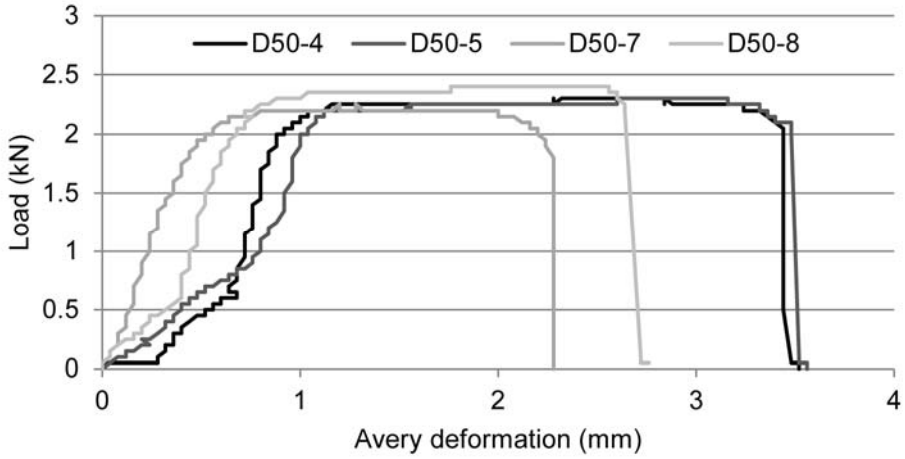

Figure 4.11 Load displacement curve of miniature rock bolt.

Table 4.1 Summary of miniature rock bolt static tensile test result.

Sample No.	Embedment length (mm)	Rock bolt length (mm)	Failure load (kN)	Deformation at failure (mm)	Strain (%)
D50-4	50	65	2.3	3.52	5.42
D50-5	50	65	2.3	3.56	5.48
D50-7	50	65	2.3	2.28	3.51
D50-8	50	65	2.3	2.78	4.25

Figure 4.12 Long view of broken threaded steel bar after tensile testing.

4.5 Surface Support

In the laboratory test, similar to the underground ground support practices wire meshes and shotcrete were used as surface support systems. Various types of wire mesh were selected to examine their performance. A shotcrete mix was also designed for the scaled down tunnels. The practice was to place the mesh sheet onto the tunnel surface or over the shotcrete, and then fixing it by using the miniature rock bolts.

4.5.1 Mesh Type

Four different types of wire mesh were used in the laboratory experiments. The purpose was to investigate the mechanical behaviour of an integrated ground support system and its influence on the resulting excavation surface failure mechanism. The mesh materials were selected based on the tunnel size, the bolting pattern and the material availability.

Welded wire mesh is one of the most common types of surface support materials used in the mining industry. The miniature material used had lateral and transverse wires welded together to create a square aperture. Two different aperture size weld meshes were used in the experiments. A commercially available weld mesh having aperture of 6.5 mm x 6.5 mm (Figure 4.13a) was used as an example of a stiff welded mesh. Another type of the welded mesh was created by modifying the stiff mesh by removing every second wire strand resulting in mesh configuration of 13 mm x 13 mm square aperture mesh as shown in Figure 4.13b.

A commercially available flexible mesh which is shown in Figure 4.13c, consisted of twisted wires which created a hexagonal shape apertures. This type of mesh was more flexible compared with the welded mesh. This material was made of galvanized wire.

The experimental testing also included woven mesh. This material was not commercially available and had to be specially developed by hand by the authour for this thesis work. Figure 4.13d shows the finished product used within the experiments. During construction, the galvanized wires were bent in a zig-zag manner to create a diamond shape by interlocking the wires (Figure 4.14). Mesh sheets of size 200 mm x 640 mm chain link mesh sheet were fabricated by the author. The mesh was designed to create a 20 mm x 9 mm aperture. The biggest advantage of chain link mesh is that it can locally accommodate large deformations compared with weld mesh (Morton, 2009). This is due to the greater flexibility of the woven mesh, which is not permanently fixed by a weld.

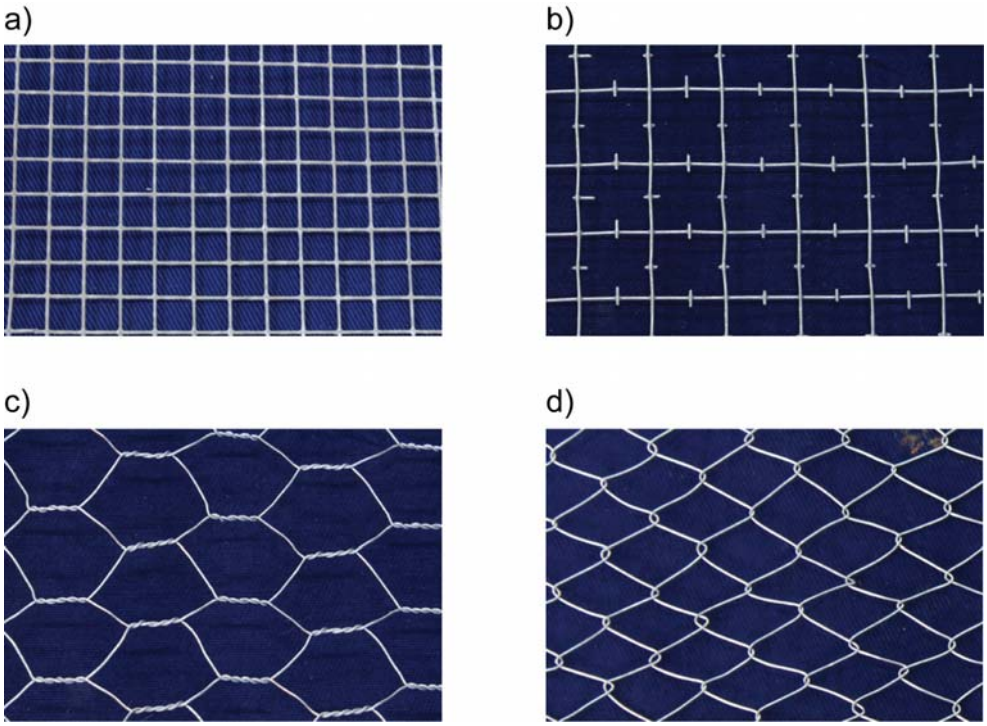

Figure 4.13 Various mesh materials used in the laboratory test a) stiff welded mesh b) wide-aperture stiff mesh c) flexible mesh d) chain link mesh.

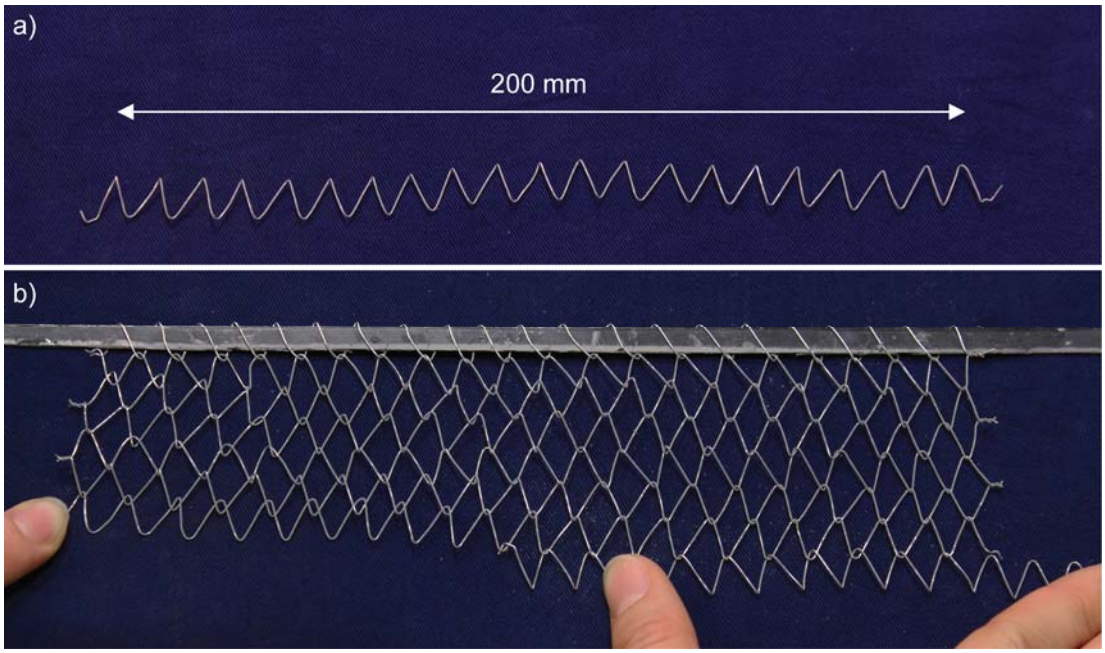

Figure 4.14 Miniature chain link mesh a) a single bended wire b) manual chain link mesh fabrication.

4.5.2 Mesh Material Properties

Pull experiments were conducted to investigate the tensile strength of the mesh wire. The testing focused on the strength of the wires. To achieve this, the wires were trimmed from the mesh sheets and glued on both sides, and then pulled by the Avery machine until the wires were broken. The mesh wire end was anchored by bending the wire before it was fixed. The test results are provided in Figure 4.16 and Table 4.2 showed the summary of the tensile test. Two different failure modes were observed. In the case of the welded mesh, failure occurred at the weld point (Figure 4.17a). Weld failure occurred as the weld strength was weaker than the wire strength (Villaescusa, 1999). The wire from the flexible mesh and the chain link mesh were broken at the maximum tensile strength of wire (Figure 4.17b and c). Even though the welded point weakens the mesh wire strength, the weld mesh wire had the higher tensile strength than the flexible mesh and the chain link mesh used in this experiments. The results show that the ratio of bolt to mesh wire strength ranged from 13 to 23. This is similar to the ratio found for full scale 15 to 25 tonne bolts and 1 tonne wire strength in the mining industry (Villaescusa, 1999). This ratio ensures that failure will likely occur at the mesh support which is the case observed in the full scaled mining situation (Drover & Villaescusa, 2015).

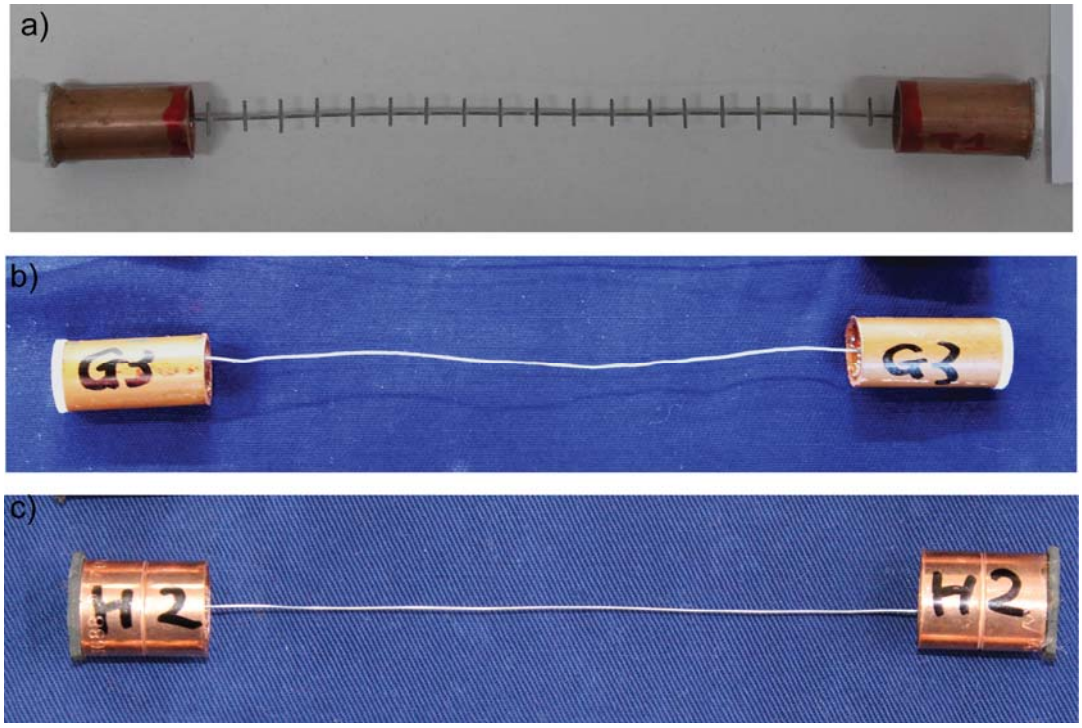

Figure 4.15 Example of pull test sample wire from a) stiff welded mesh b) flexible mesh c) chain link mesh.

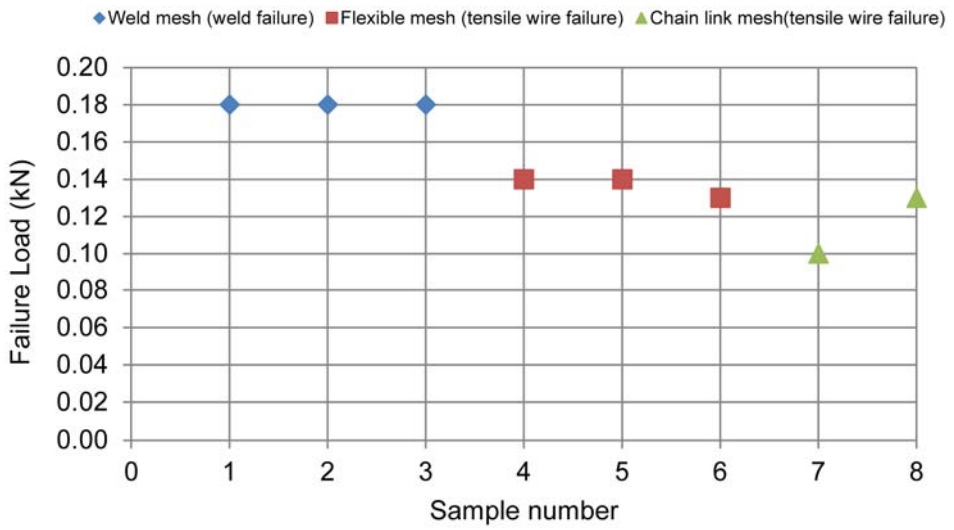

Figure 4.16 Mesh wire tensile strength.

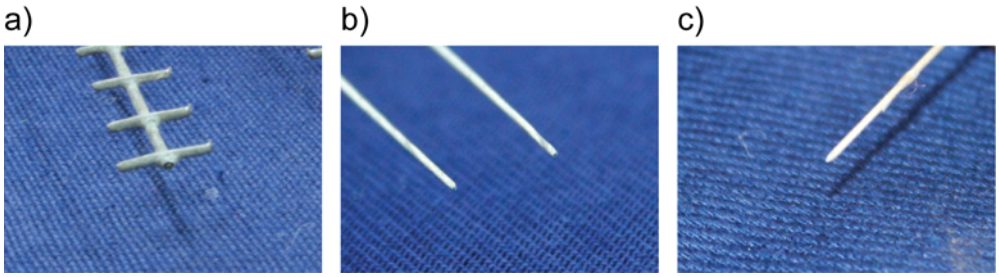

Figure 4.17 Broken wires after pull test a) stiff and wide-aperture stiff mesh b) flexible mesh c) chain link mesh.

Table 4.2 Summary of miniature mesh materials.

Name	Mesh type	Wire material	Grid pattern (mm)	Wire diameter (mm)	Failure load at the tensile test(kN)
Stiff welded mesh	Welded mesh	Galvanized steel	6.5 x 6.5	0.6	0.18
Wide-aperture stiff mesh	Welded mesh	Galvanized steel	13 x 13	0.6	0.18
Flexible mesh	Twisted mesh	Galvanized steel	Hex 13	0.5	0.14
Chain link mesh	Chain link mesh	Galvanized steel	20 x 9	0.44	0.11

4.5.3 Shotcrete

Shotcrete was also used as a part of the surface support investigations. Shotcrete was expected to help with load transfer from broken rock to the reinforcing elements during tunnel stabilisation. The cement mix was applied on to the excavation surface by the pneumatic spray gun to obtain a uniform thickness and cured for approximately 7 days before any testing. Depending on the ground support configuration, the shotcrete was reinforced by the steel mesh or covered by steel mesh after the spraying process.

4.5.3.1 Shotcrete Material and Properties

The shotcrete mix consisted of cement, sand, water and a plasticiser. The mix was designed based on the uniaxial compressive strength after 7 days of curing. A steel sieve was used to separate sand and coarse particles. Particles more than 600 μm were eliminated at the preparation process to optimise the spraying ability. The plasticiser was added to increase the workability of the mix during the application.

The mechanical properties of the shotcrete were obtained by uniaxial compressive strength test. The shotcrete mix was sprayed into a mould and cured under the same circumstance as the scaled down tunnel. The uniaxial test was carried out on the same date, as the rectangular block test. This mix strength was used for ease of workability and placement into the miniature scale tunnels. It represents a weak strength membrane, as it was in about 1/10 of a real shotcrete strength.

Table 4.3 Shotcrete components and uniaxial compressive strength.

W/C (%)	Cement : Sand	Average uniaxial compressive strength (MPa)
170	1:9.434	3.4

4.5.3.2 Shotcrete Application

Since a tunnel surface needed to be wet when boreholes were drilled in order to reduce the friction heat, boreholes were drilled into tunnels before shotcrete application in all cases. Boreholes were filled with a foam material to prevent shotcrete mix penetration (Figure 4.18). Figure 4.19 shows a case of a chain link mesh sheet was applied before shotcrete spraying.

After the preparation, the shotcrete components were mixed evenly and applied to the tunnel surface by a pneumatic spray gun as shown in Figure 4.20. This application method is similar to that used in underground mines. The shotcrete mix was compacted and applied until achieving the proposed thickness. The intact rock was mounted onto the rotation system during the shotcrete application. The shotcrete surface was smoothed after the spraying and the thickness was examined for uniformity (Figure 4.21). The shotcrete layer was cured for 7 days (Figure 4.22). The mesh and rock bolt were installed after or before the shotcrete application, depending upon the ground support scheme being tested. Figure 4.23 shows that boreholes were re-drilled over a shotcrete layer to install rock bolts.

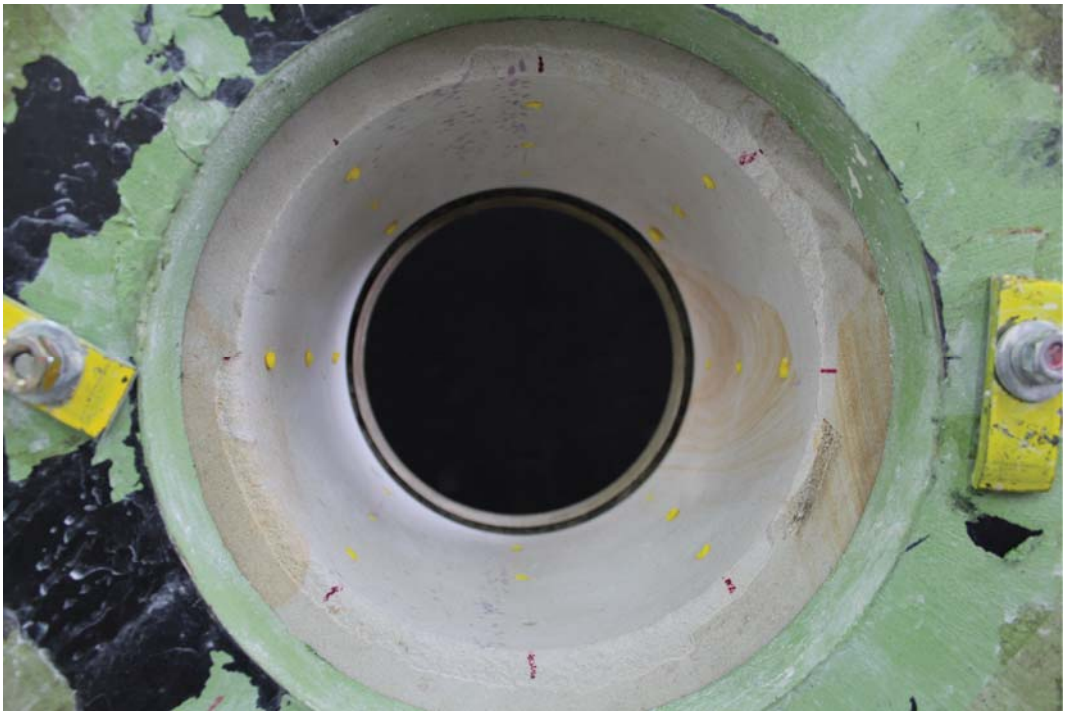

Figure 4.18 An example of a scaled down tunnel before shotcrete application.

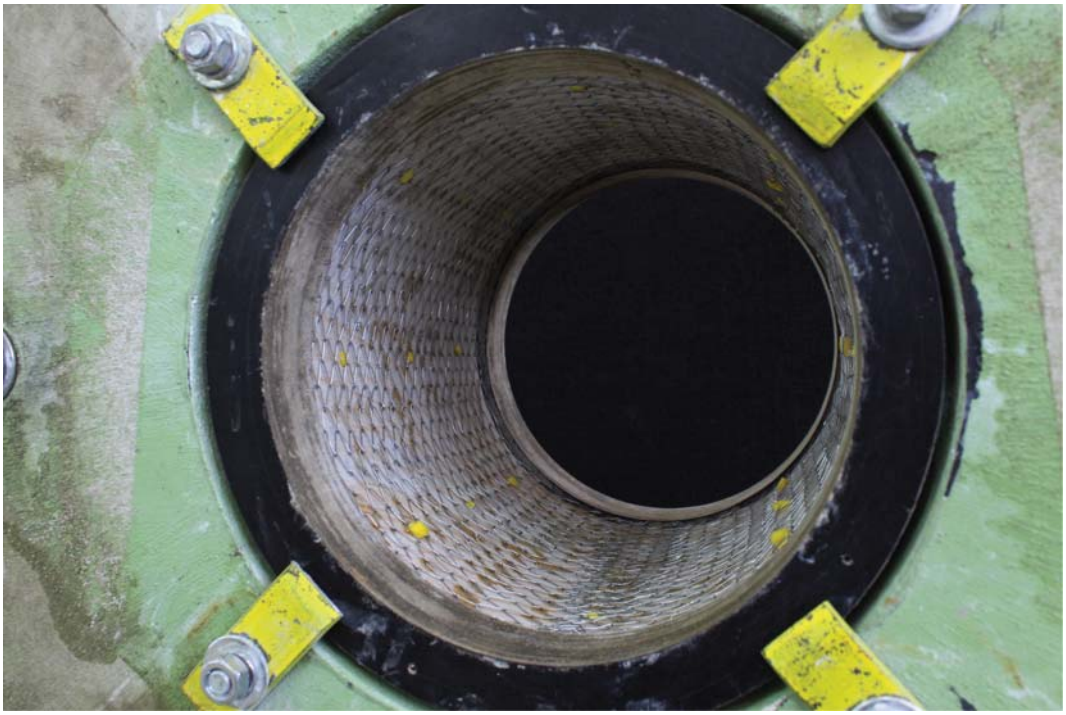

Figure 4.19 An example of a mesh installed tunnel before shotcrete application.

Figure 4.20 Shotcrete application by miniature spray gun.

Figure 4.21 Surface smoothing process after the shotcrete spraying.

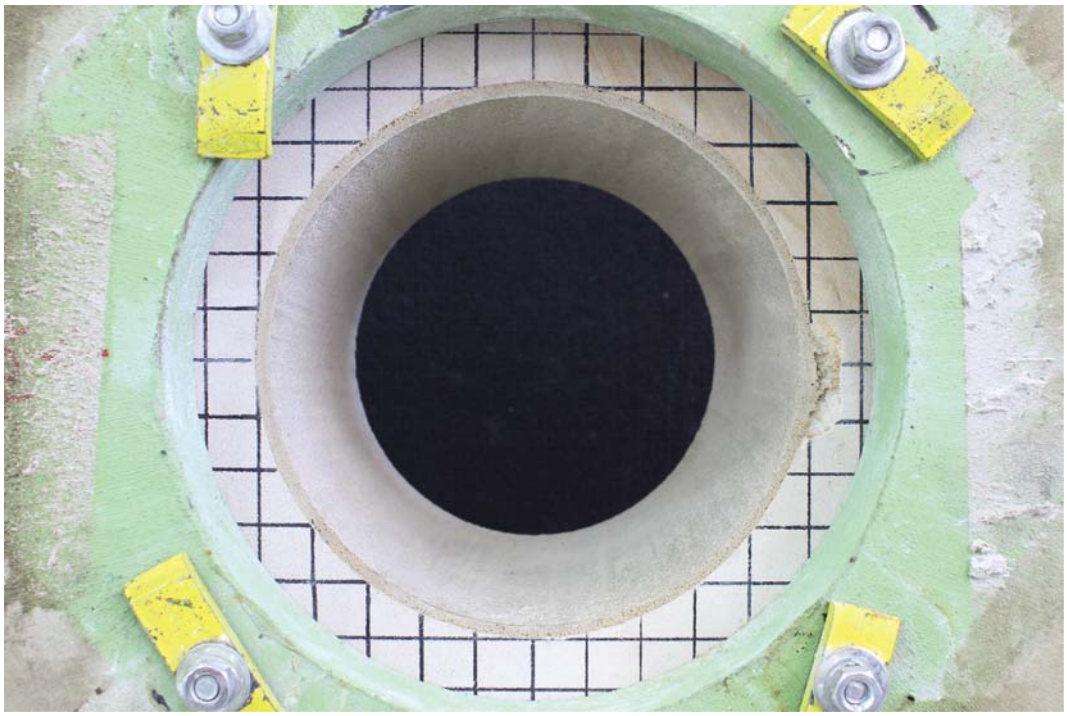

Figure 4.22 A scaled down tunnel with a 5 mm thickness shotcrete layer after curing.

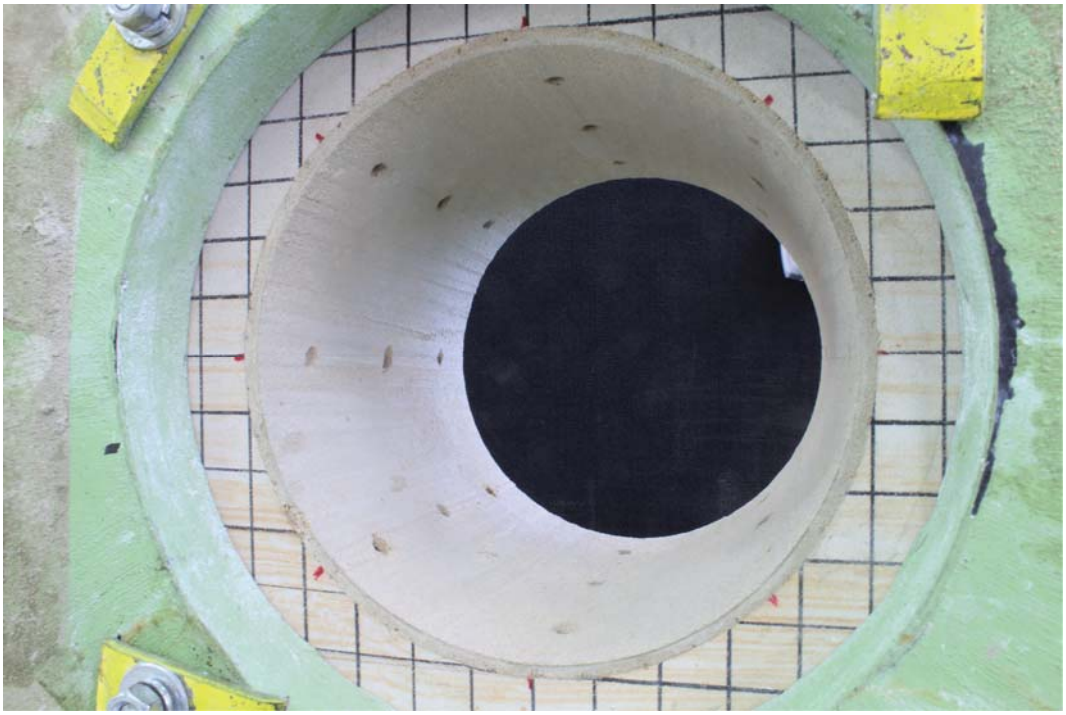

Figure 4.23 Re-drilled boreholes after shotcrete application.

4.6 Ground Support Component Summary

Table 4.4 summarised the material properties of the ground support components used in this experiment.

Table 4.4 Ground support component material properties summary.

	Name	Material	Specification	Material properties
Rock bolt	Rock bolt	Threaded steel bar	ϕ2.15mm ,50mm	Tensile strength 2.3kN
Mesh	Stiff mesh	Galvanized wire	6.5 x 6.5mm aperture	Wire tensile strength 0.18kN
	Wide-aperture stiff mesh	Galvanized wire	13 x 13mmaperture	Wire tensile strength 0.18kN
	Flexible mesh	Galvanized wire	Hex 13mm aperture	Wire tensile strength 0.14kN
	Chain link mesh	Galvanized wire	20 x 9mm aperture	Wire tensile strength 0.11kN
Shotcrete	Shotcrete	cement, sand, water and plasticiser	W/C 170%, C/S 10.6%	Average UCS 3.4MPa

Chapter 5

Model Test Configuration

5.1 Test Set-up

In this experiments, the standard tunnel size was determined as 200 mm, with a pillar width of 100 mm thick on both sides. Figure 5.1 shows the specimen confinement setting scheme. Lateral plates provided a mild amount of confining pressure on to the block sample to ensure the post-peak strength of the sample. The blocks of rock were constrained horizontally by two mild steel plates (16 mm thick) which were held by 4 threaded bars. Prior to testing, the bolts were tightened to a set torque (7 kN) to apply a small initial horizontal stress on the side of the rock block. A Teflon layer was used between the side platens and the rock blocks to reduce the development of vertical shear stresses, as the rock block compressed vertically. Figure 5.2 shows the typical confinement setting of the rectangular blocks tested during this experiments.

A 19 mm thick steel platen was placed at the top and bottom of the specimens. The size of the platen was wider than the sample base and the top area and had an adequate stiffness to transfer the load evenly to the sample from the loading machine. A 1.5 mm thick rubber sheet was placed between the top and bottom steel platens and the specimen in order to reduce the static friction during testing.

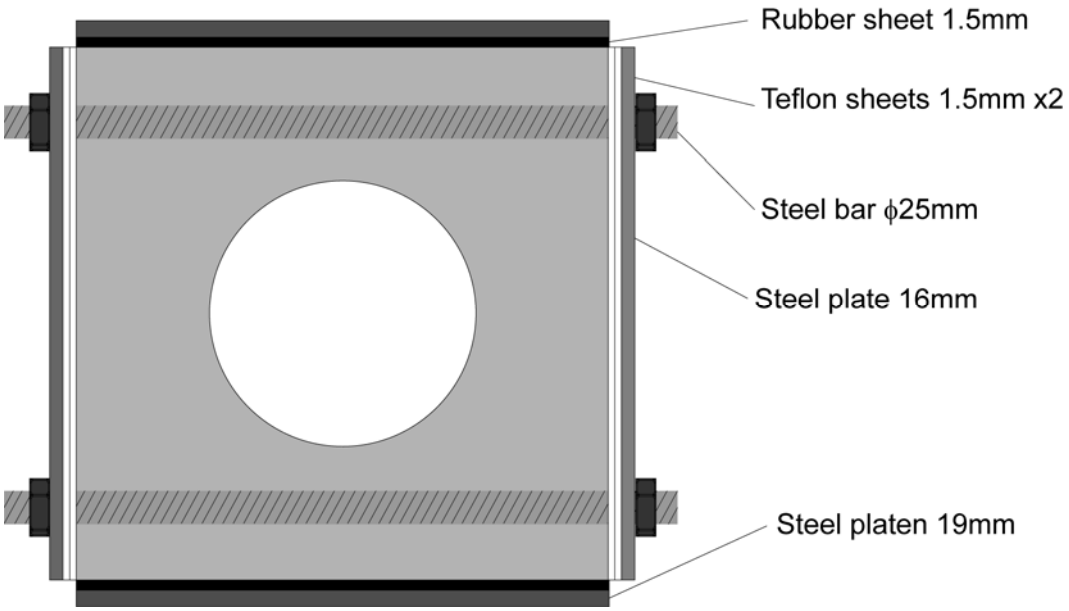

Figure 5.1 Block sample confinement setting.

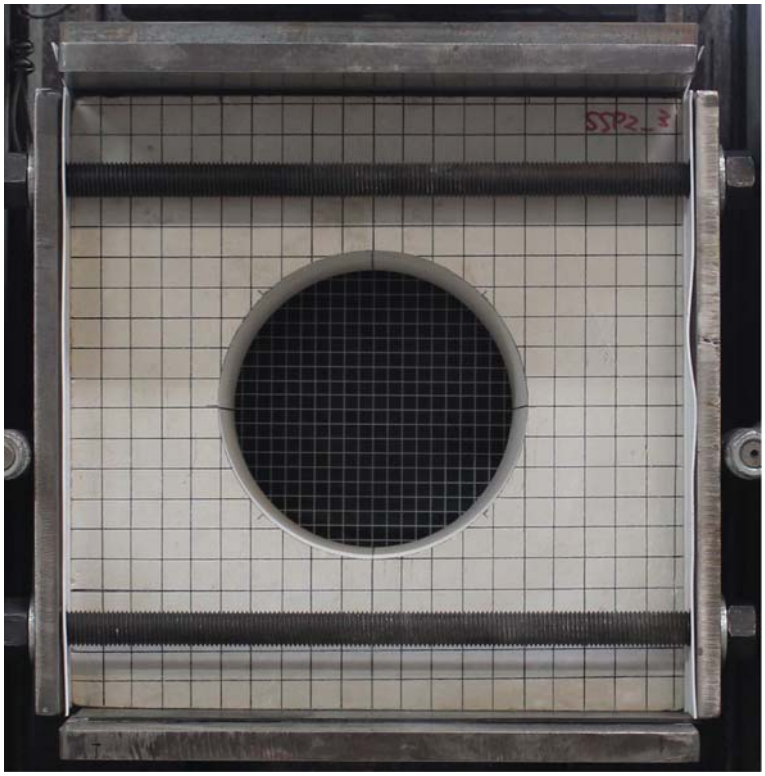

Figure 5.2 Typical block sample confinement setting (grid size 20 mm x 20 mm).

5.2 Loading Method

The tunnels were loaded vertically using a servo controlled 450 tonne capacity INSTRON Machine. The rate of the loading was kept as 0.5mm/min for all the test sets to ensure the initial failure occurred within 3-5 min of loading. The specimen was loaded continuously until pillar crushing and the sample strength was held by the confinement plates. Vertical load and vertical displacement were monitored during tests.

5.3 High Speed Filming

A high speed Canon EOS 650D video camera was used to monitor the tunnel walls during the progressive loading. This digital single-lens reflex camera, was set up in front of the sample and the tunnel behaviour was recorded through a special window within the INSTRON loading machine protective door (Figure 5.3). The camera is capable of capturing up to 50 frames per second. A set of special lights and a suitably

placed background grid (Figure 5.4) were used to estimate the displacement versus time motion of the failure particles that were ejected during the failure.

Figure 5.3 Typical experimental set up with SRL camera.

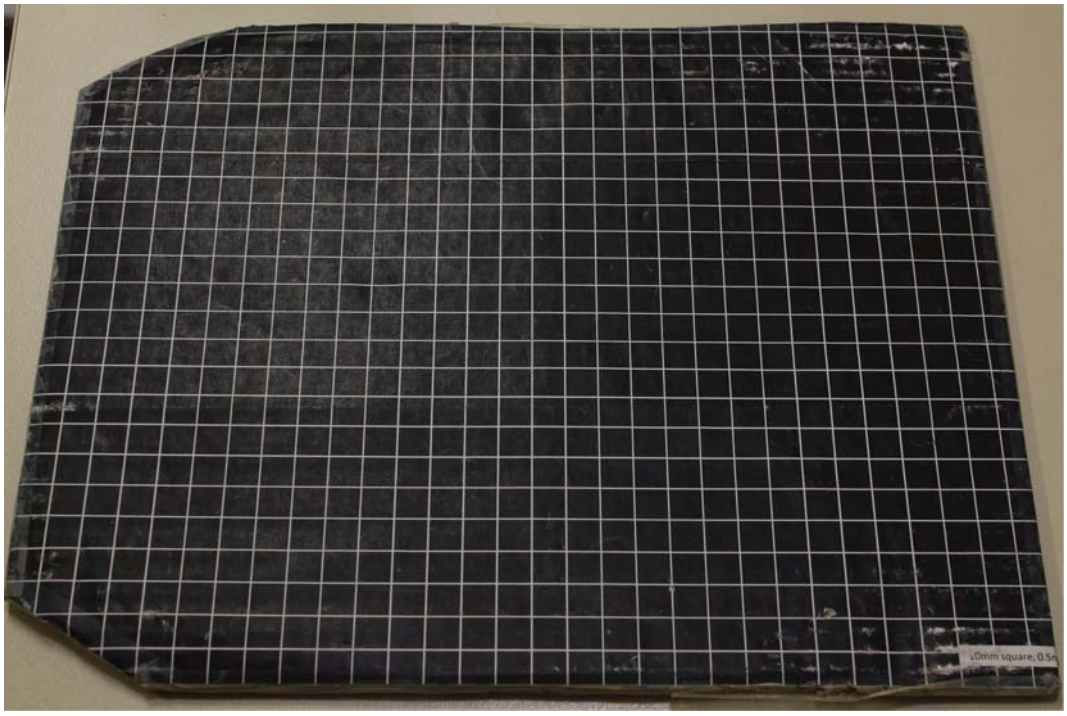

Figure 5.4 Background grid used for ejection velocity calibration (grid size 10 mm x 10 mm with 0.5 mm thick line).

5.4 Seismic Data Monitoring

Acoustic Emission sensors were installed to monitor the seismic response from initial loading to tunnel wall spalling and pillar crushing. Two miniature Nano-30 sensors (8 mm diameter x 8 mm height) with an operating frequency range of 150-400 kHz, manufactured by Physical Acoustic Corporation, were attached to the front face of the test block approximately 70 mm either side of a vertical centre line using an acoustic resin (Figure 5.5). Data from the sensors was amplified by preamplifiers with a 40 dB gain. The amplifiers in turn were connected to a PC running AEwin for PC12 software. All AE data collected by the software included time, duration, counts and amplitude. A lower limit of 24 dB was set to eliminate background noise. Time and AE event rate (events/sec) were monitored visually on a live display for the duration of the test. At the end of the test, the data file was converted to an ASCII file and then imported into spreadsheets. All data was then filtered from 40 dB to 80 dB to remove additional noise and to obtain a better defined responses of the seismic activity. AE event rate and cumulative AE events were superimposed on the load-compression chart to correlate peak seismic activity with the samples failures.

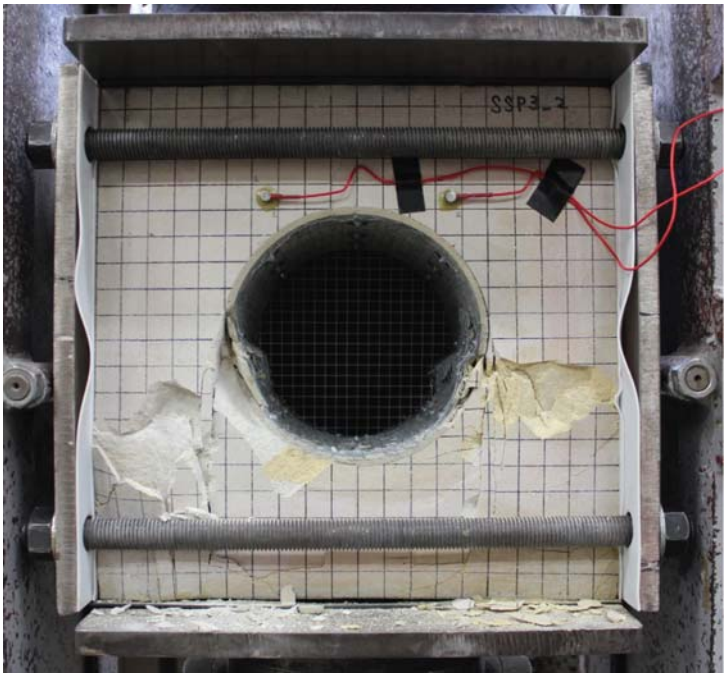

Figure 5.5 Typical specimen sample following testing showing the location of the two AE sensors.

5.5 Internal Deformation Measurement by Laser Scanner

Internal deformation measurements were conducted using a laser scanner. This is a specially designed scanning unit that fit within the scaled-down tunnel geometries. The laser displacement sensor was mounted on a rotating jig and the tunnel surface was scanned before and during the loading process. The laser scanner was operated by a main control unit. The scanning was undertaken mainly for the comparison of the ground support schemes.

5.5.1 Laser Displacement Unit

The laser displacement sensor is a Keyence IL Series Model IL-030 (Figure 5.6). The measurement range from the laser head is 20-45 mm from the sensor. The minimum display is 1μ m with a linearity of +/- 0.1 %. The data was processed through the amplifier unit and sent to the main control unit.

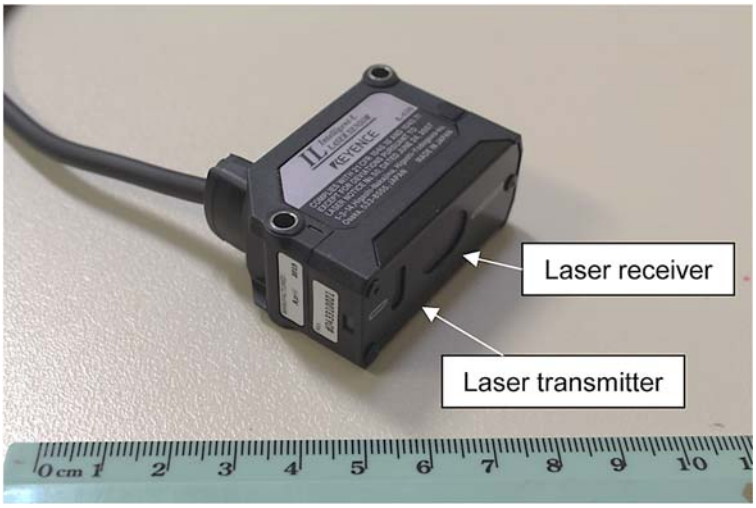

Figure 5.6 Laser displacement sensor unit.

5.5.2 Laser Scanner

A laser unit was mounted onto a rotary axis to scan the tunnels internal surfaces. Figure 5.7 shows a measurement concept. The linear axis was centralised and made parallel to the tunnel axis. The sample measurement parameters were input before the measurements. The laser head was rotated 360 ° and the distance from the linear axis

to the tunnel surface was measured on 4975 points, which means every 0.072 ° for the each scan slice. The measurement was conducted using a 5 mm interval step from the back of the tunnel to the front.

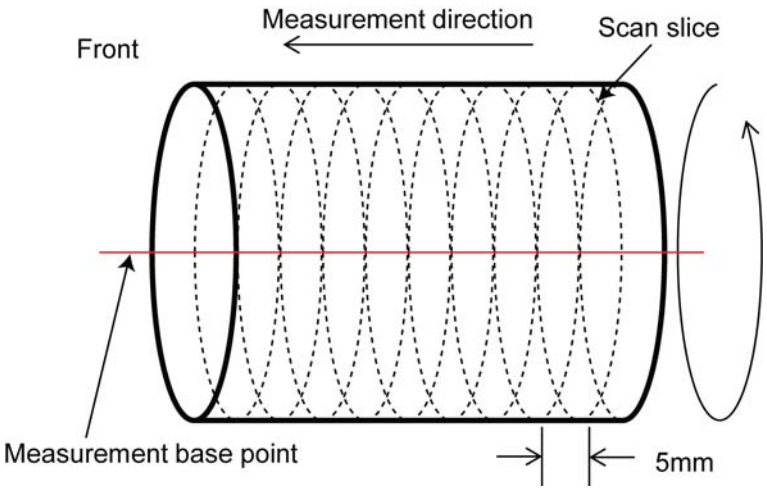

Figure 5.7 Displacement measurement concept by laser scanner.

The scanning unit is mechanical and composed of a linear actuator driven by a step motor to move the laser head a precise amount of distance along the tunnel linear axis (Figure 5.8). At the end of the rotary axis rod is a laser scanning head. The laser was fixed onto the linear axis to enable a measurement range of 100-125 mm from the centre of the linear axis. The laser scanning head was protected from any ejected material during testing (Figure 5.9). The laser scanner unit was mounted on the bottom steel plate and fixed by the magnet switches until the end of the test (Figure 5.10).

It took approximately 20 min for the each scanning process (Figure 5.11). The vertical loading was held at the same loading level when the scanning was conducted during the loading process. The scanned data was sent to a laptop via wireless transmitter.

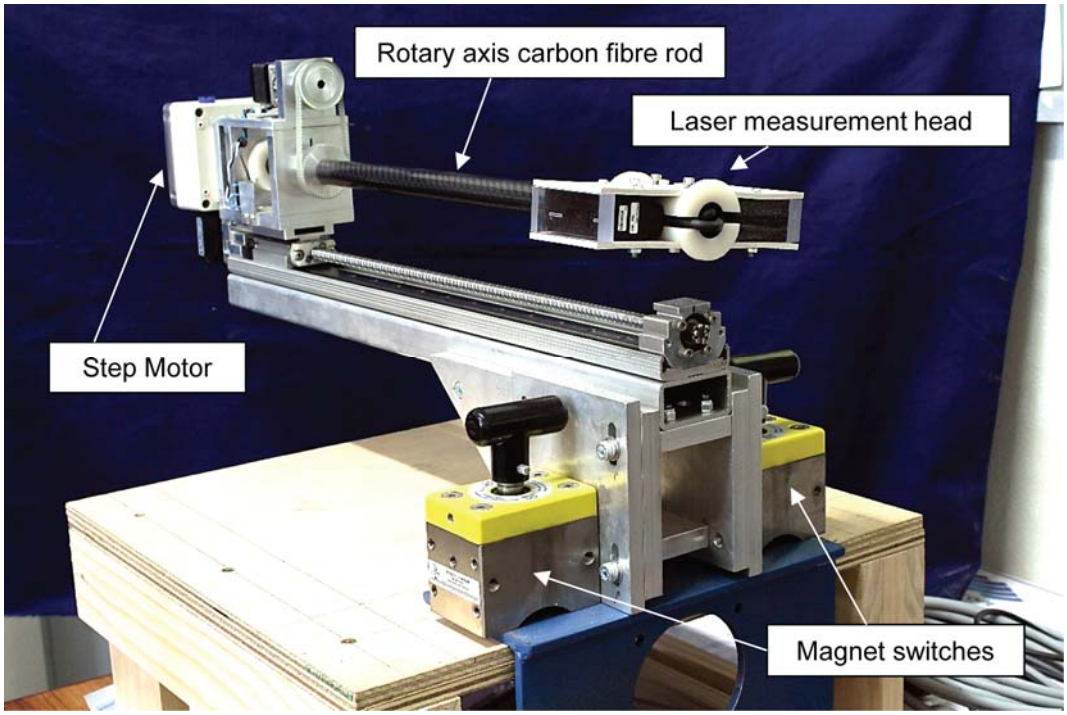

Figure 5.8 Laser scanner.

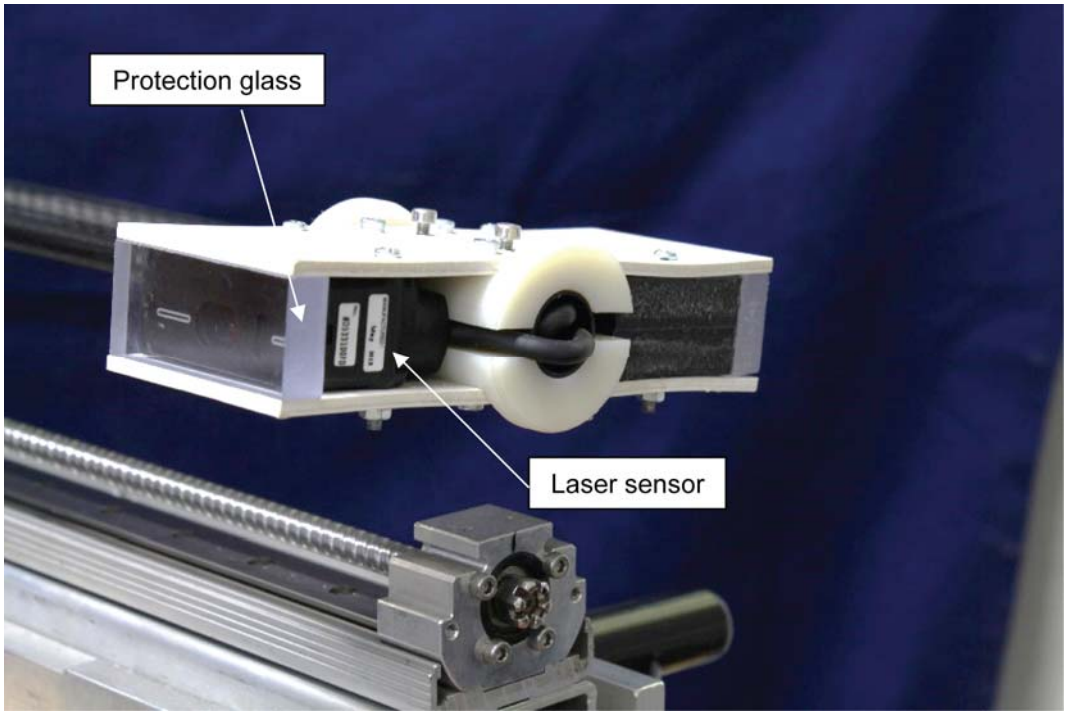

Figure 5.9 Laser measurement head.

Figure 5.10 An example of the laser scanner setting within a specimen sample.

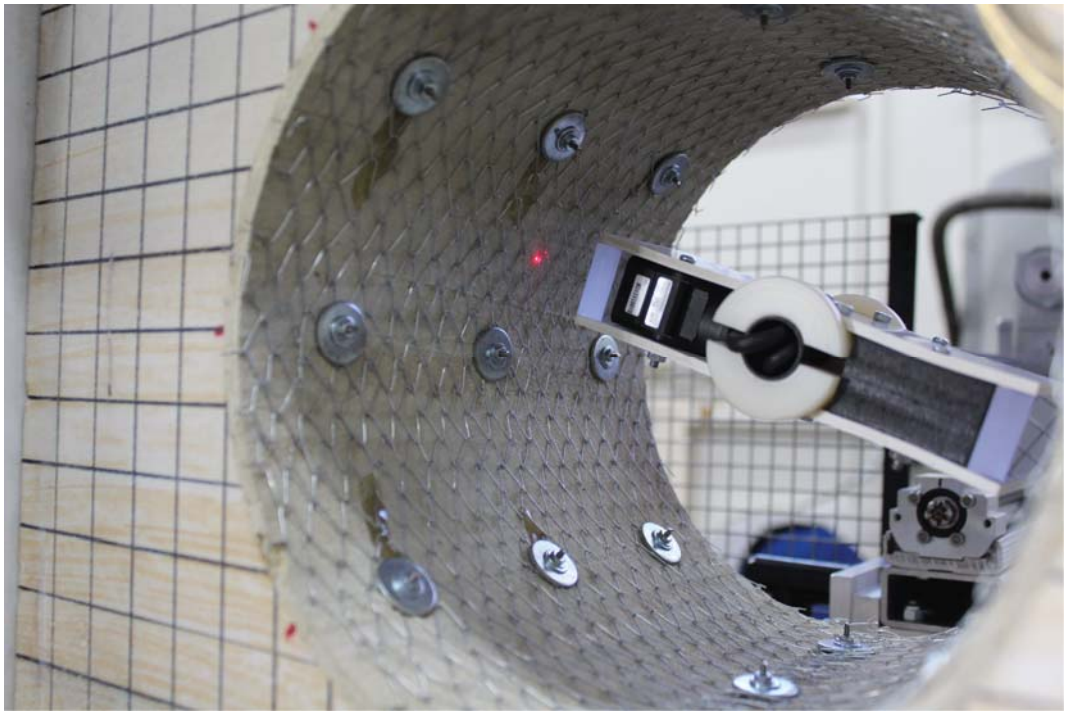

Figure 5.11 An example of the laser scanning before a test.

5.5.3 Reference Scan Testing

A reference scan test was conducted to examine repeatability, resolution and noise of the laser scanner. A number of continuous scans were conducted on a commercially available ceramic tube (Figure 5.12). An error was obtained by subtracting each scan set data for the same points measured.

Figure 5.13 shows an example of an error calculated for a single slice. The long periodic error was a mechanical error. It was caused by a misalignment of the laser scanner. The centre of the laser scanner was moved slightly after each measurement due to a linear actuator slide. The maximum deflection was 0.3 mm, which is equal to 0.15% strain. The blurring of the graph was the electrical back ground noise which is approximately +/- 0.1 mm. It was experienced during all the measurement process. The digitiser integration buffer was seen between 345 to 360 degrees. The laser scanner rotated counter clockwise, i.e. a measurement was conducted from 360 degree to 0 degree for each scanning (see Figure 5.13). After the laser head rotated 360 degrees, it shifted 5 mm ahead parallel to the rotary axis and scans the next slice. During the laser head movement, the digitiser was turned off. The ‘bell shape’ noise was experienced between 340 to 360 degrees after the digitiser was turned on again however reduced into the noise floor.

Figure 5.14 shows four sets of the reference testing results. Each measurement consisted of 23 slices and all the data are shown. In all the cases, both mechanical and digital errors were experienced. Although mechanical errors were most prominent, the error is far smaller than the measurement target range and was subsequently ignored during the data analysis

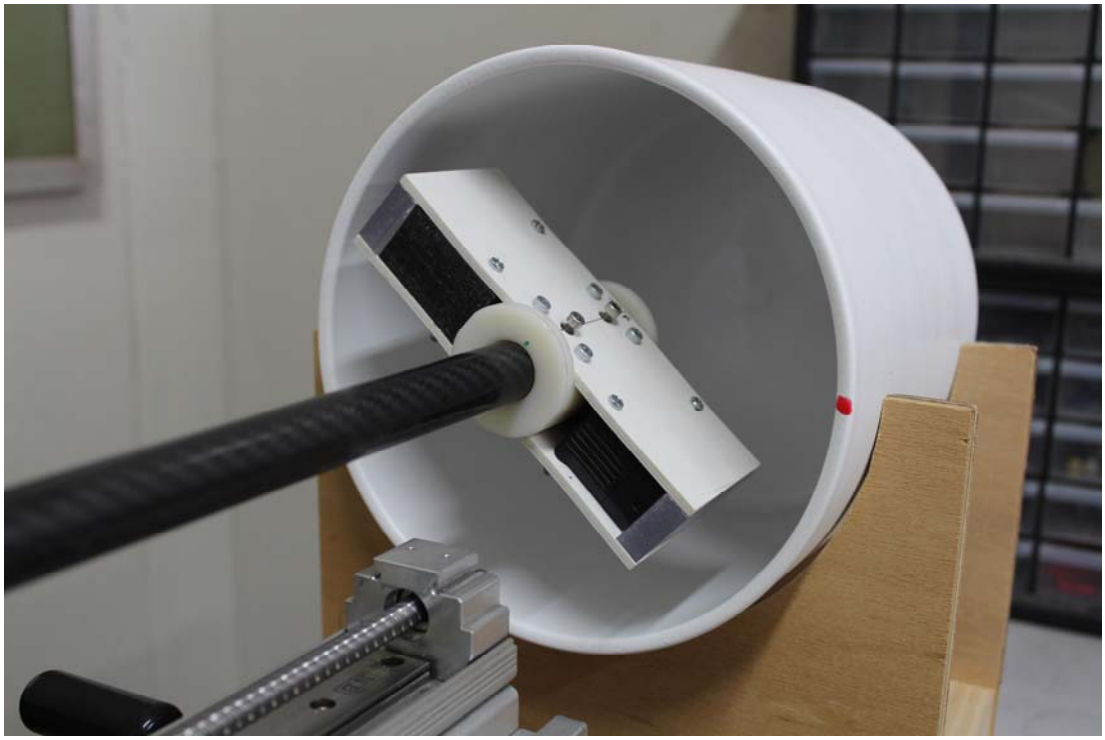

Figure 5.12 Reference scan testing using a ceramic tube.

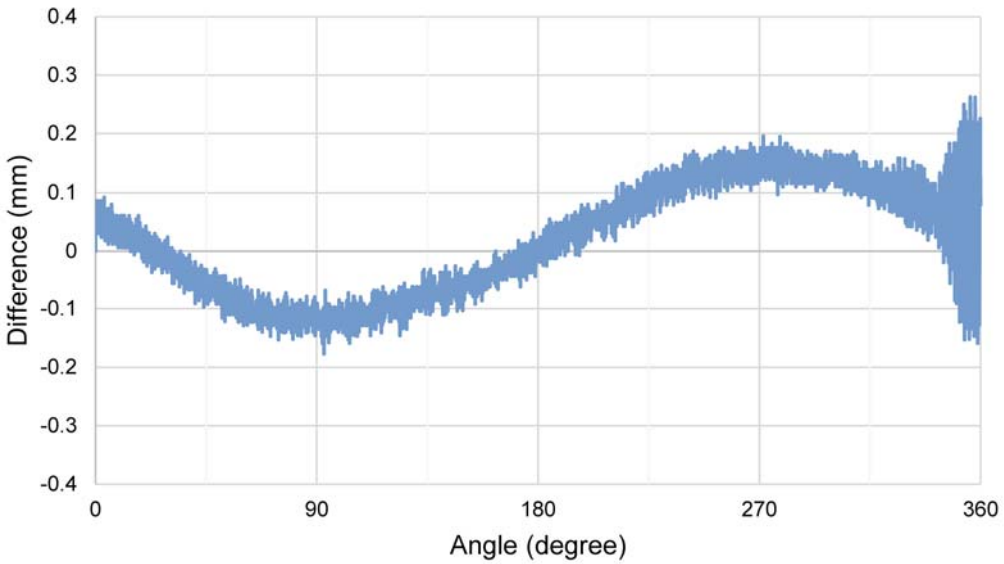

Figure 5.13 An example of reference testing data from a single slide.

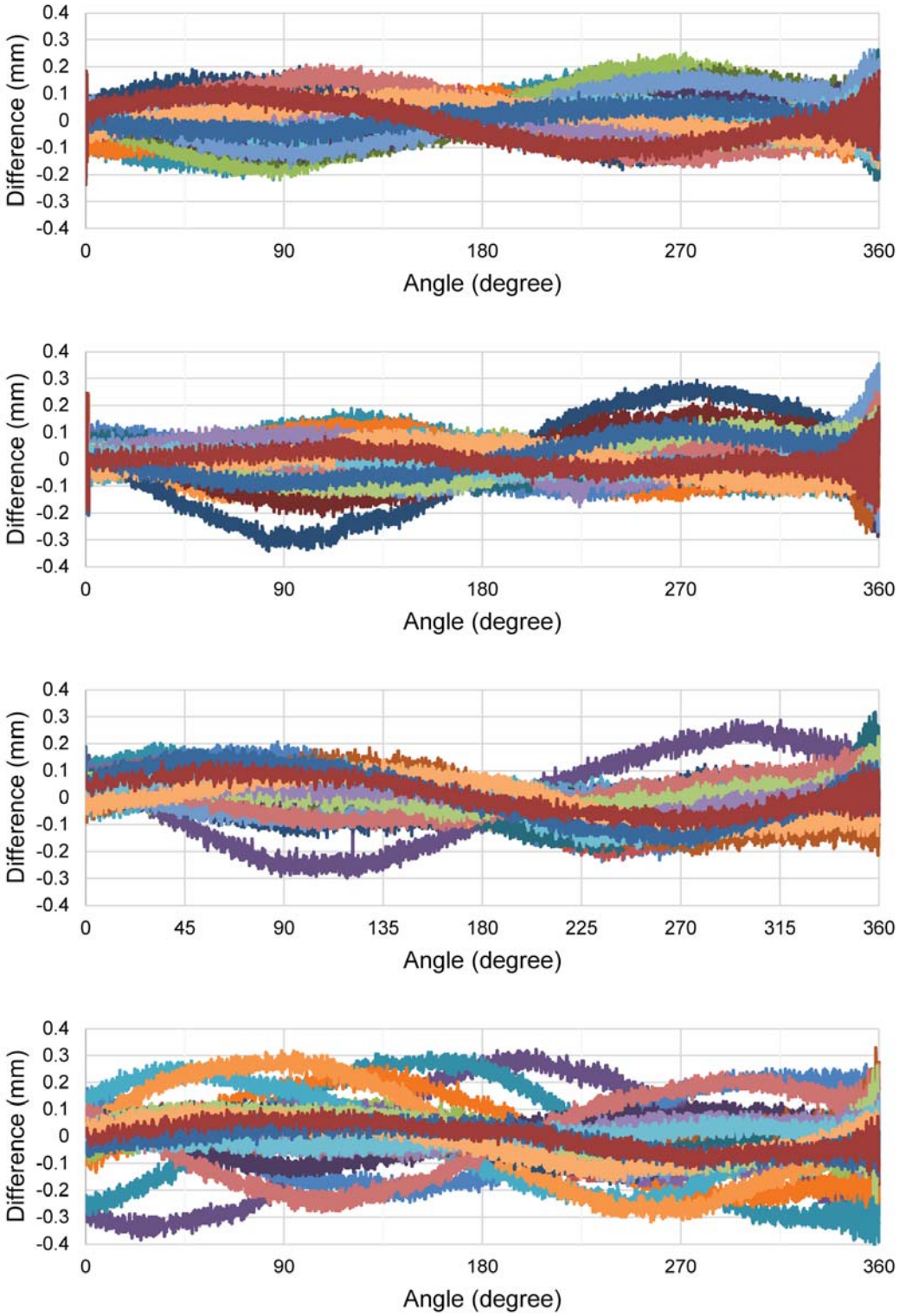

Figure 5.14 Four sets of reference scanning test data.

5.6 Test Configuration Summary

Specimens were assembled before the installation to the INSTRON loading machine. The monitoring devices were set and data were analysed after the test. All the failure behaviour were recorded by the high speed camera and conformed to the loading data. Seismic data monitoring was performed onto a part of the test configurations. Laser measurement was mainly conducted to compare the surface damages resulting from tunnel wall failure.

Chapter 6

Unsupported Tunnel Test Results

6.1 Test Configurations

In order to investigate stress-driven fracturing around underground excavations, a large number of scaled-down tunnels have been constructed and tested at the WASM Rock Mechanics Laboratory. The three types of intact rock ranging in strength from moderately strong to very strong (20 to 200 MPa) were used. The detailed material properties are described in Chapter 2.

Also different size of tunnels were tested to examine the effect of an increased pillar width. The testing included 14 sets of 200 mm diameter tunnels with 100 mm wide pillar, 2 sets of 100 mm diameter tunnel with 150 mm and 1 set of 50 mm tunnel with 175 mm pillar. The unsupported tunnel test configurations are summarised in Table 6.1 and specimen geometry is shown in Figure 6.1

The blocks of rock were loaded vertically using a 450 tonne capacity stiff INSTRON compression testing machine. The rate of loading was 0.5 mm/min for all test specimen. Figure 6.2 shows a typical experimental set-up of 200 mm diameter unsupported tunnel before and after testing. The specimens were loaded until pillar crushing was experiences at the late stages of the failure process.

Table 6.1 Scaled sized unsupported tunnel test configurations summary.

Material	Average UCS (MPa)	Number of samples	Specimen dimension (mm)			Tunnel diameter (mm)	Pillar width (mm)
			Width	Length	Height		
Sandstone (MS)	19	3	400	200	400	200	100
Sandstone (S)	82	1	400	150	400	56	172
		1	400	150	400	103	149
		7	400	200	400	200	100
Granite (VS)	182	1	400	200	400	104	148
		4	400	200	400	200	100

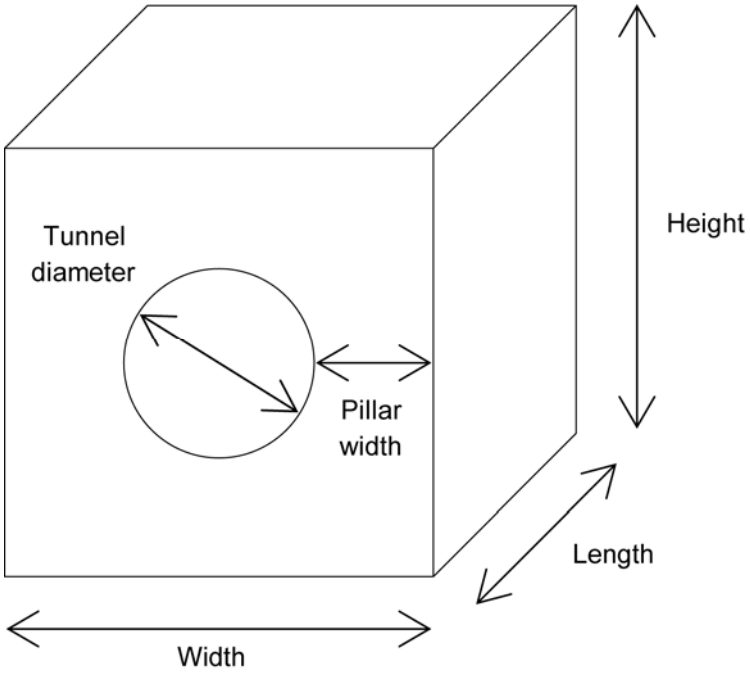

Figure 6.1 Unsupported tunnel geometry.

Figure 6.2 Typical unsupported tunnel and pillar geometry tested (grid size 20 mm x 20 mm), before and after failure.

6.2 Load Displacement Relationship

Figure 6.3 shows an example of the load displacement curve for an unsupported tunnel within strong sandstone. The displacement plotted is a relative displacement

between the loading plates of the top and bottom of the specimen. When the load reached a certain level, spalling was experienced at both sidewall of tunnels with a sudden load decrease. Figure 6.4 shows a typical process of spalling within an unsupported tunnel. The ratio of σ_c/σ_{max} is shown for a number of instability stages on the tunnel was being loaded to failure. When the maximum tangential stress at the tunnel boundary reached a certain level, thin slabs were formed and started to be detached from the tunnel wall surface from either side of the specimen face. The detached slabs fell off to the tunnel bottom with the crack propagating from one end of the tunnel to the other. Once the crack spread through the entire tunnel wall, broken materials were ejected violently from the damaged area. Simultaneously a vertical shear crack was formed on the specimen face which intersected the horizontal spalling area at the edge of the tunnel wall. Slabs were ejected from inside of the tunnel wall and violent ejection occurred at the edge of the specimen face. After spalling occurred in both tunnel sidewalls, the specimen behaved elastically until reaching the peak load. At the peak load, shear cracks formed within the side pillars and eventually it dominated the failure process until the end of the tests. The side confinement plates held the specimen in place after the onset of pillar crushing. The detailed unsupported tunnel failure progression is provided in Appendix A.

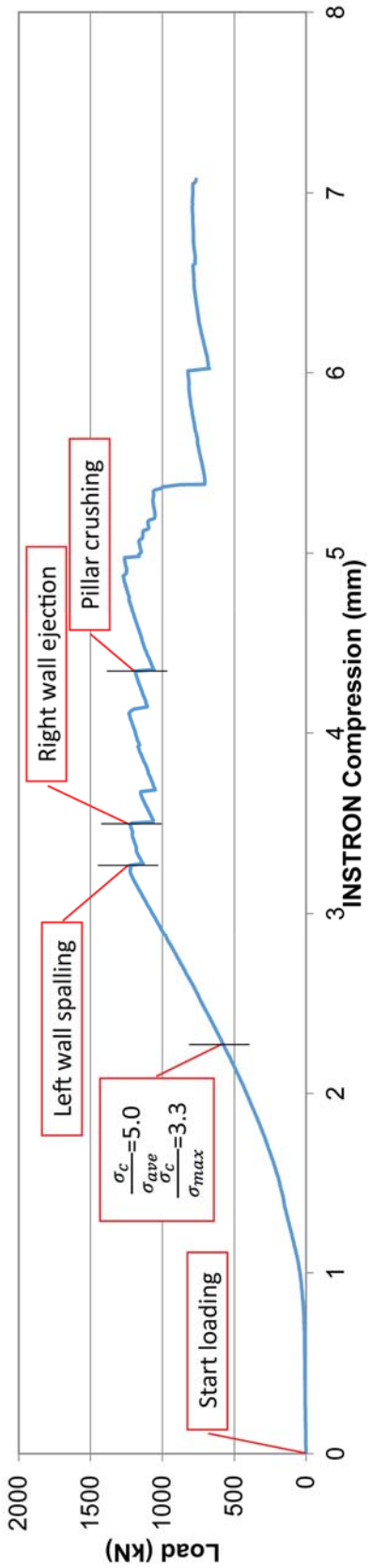

	Start loading (0:00)	$\frac{\sigma_c}{\sigma_{ave}}$=5 (4:37)	Left wall spalling (6:32)	Right wall ejection (7:00)	Pillar crushing (8:41)
Load (kN)	0	600	1227	1214	1191
INSTRON Compression (mm)	0	2.31	3.27	3.50	4.34
$\frac{\sigma_c}{\sigma_{max}}$	-	3.33	1.63	1.65	1.68
$\frac{\sigma_c}{\sigma_{ave}}$	-	5.00	2.45	2.47	2.52
					

Figure 6.3 Example of load displacement curve with unsupported sandstone tunnel behaviour.

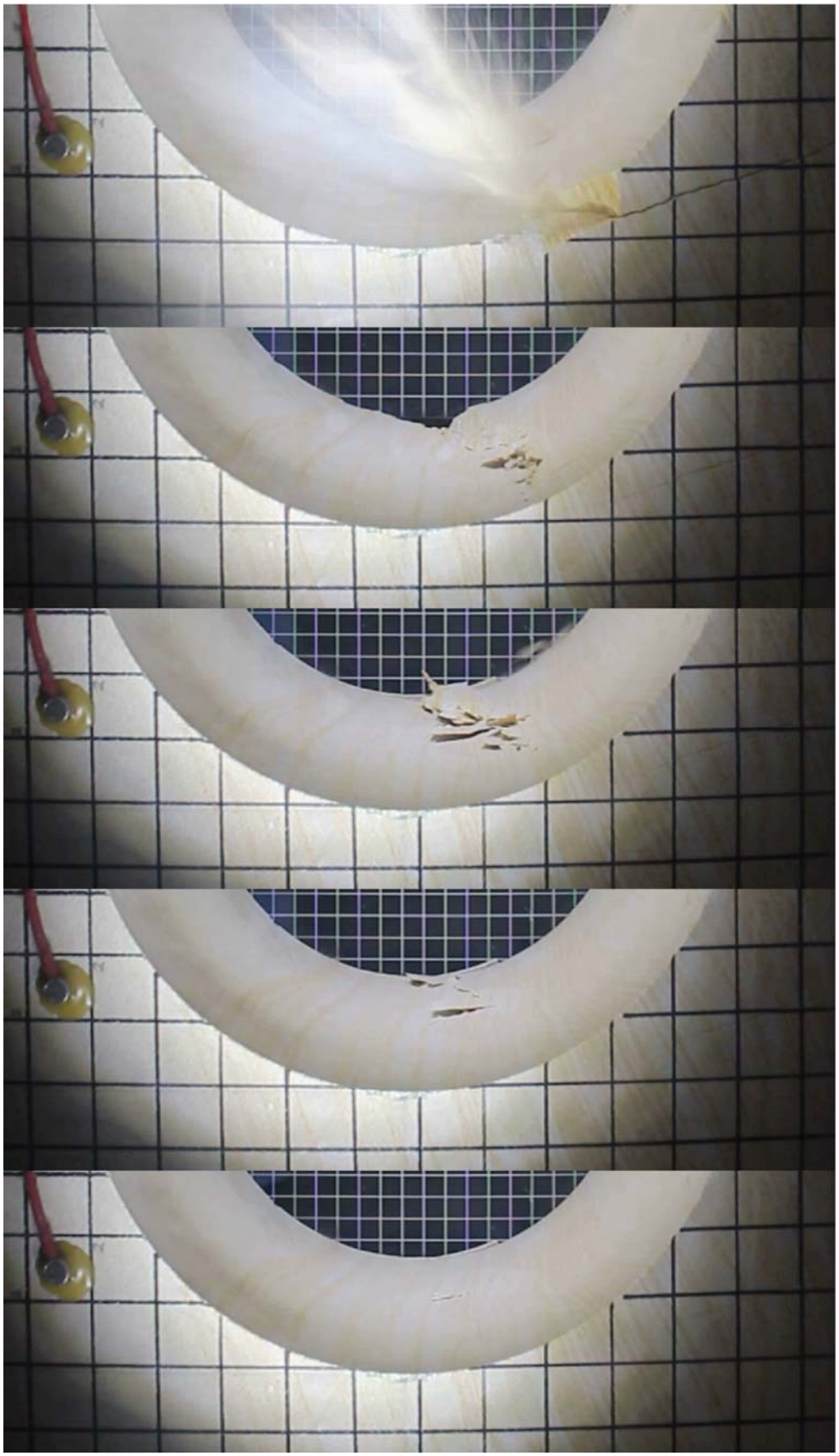

Figure 6.4 Typical spalling propagation process of unsupported strong sandstone.

Figure 6.5 shows the combined load displacement relationship curves of 200 mm diameter unsupported tunnels in which loading was gradually increased from zero until tunnel wall spalling followed by pillar crushing were experienced. All the specimens showed elastic response until spalling occurred on both sides of tunnel walls. Figure 6.2 shows the depth of failure was largely controlled by the presence of potential planes of weakness. This equates to the presence of geological discontinuities in a full scale tunnel.

In the case of moderately strong sandstone (average UCS 19 MPa), the failure showed smoother response compared with a strong sandstone (average UCS 82 MPa). Spalling occurred quietly and the broken material fell off into the tunnel floor without violent ejection. Cracks propagated gradually throughout the entire loading process.

The steepest load increase was seen in granite experiments (average UCS 182 MPa). Violent ejection and significant load drop off was seen at spalling. When shear cracks formed vertically through the pillar from the top to bottom of the specimen, a significant load decrease and a large tunnel convergence was observed in both cases of strong sandstone and granite rocks.

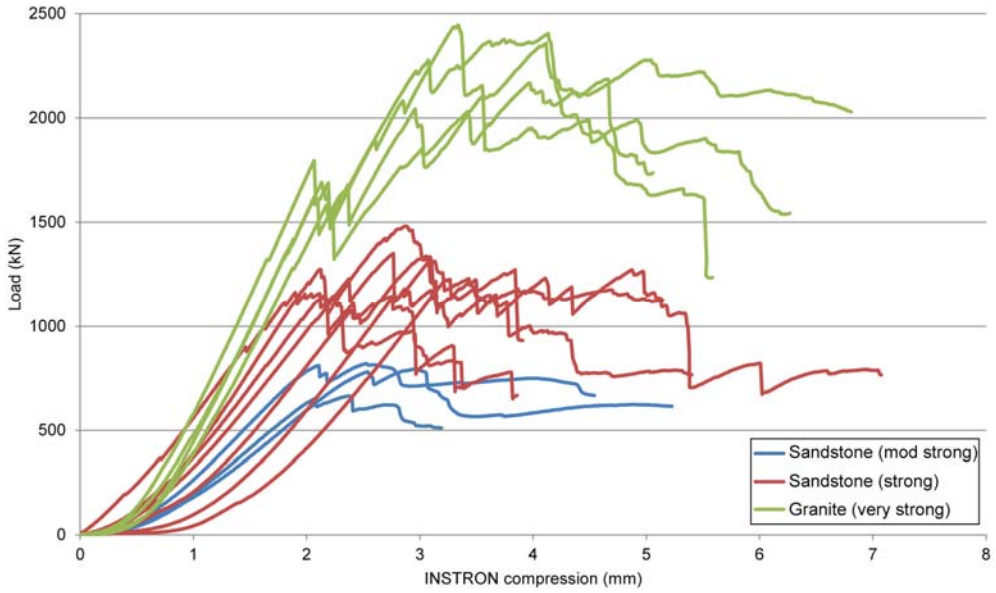

Figure 6.5 Load-deformation response for the three different tunnel materials.

6.3 Tunnel Size Effect

Experiments using different size of tunnel diameter were undertaken to examine the effect of resulting tunnel diameter and pillar width dimensions. Given that all the specimen width was constant at 400 mm for all the configurations, a smaller sized tunnel defined greater pillar widths.

Figure 6.6 shows a comparison of the load displacement curve for different tunnel diameter of unsupported tunnel in strong sandstone. As expected, the large pillar sizes means higher loads, although the rate of load increase remained constant. However the occurrence of spalling and pillar crushing phenomenon was similar for the different sized tunnel.

The results for tunnels in granite having different diameters are presented in Figure 6.7. Spalling was observed before 4000 kN and the load increased again after a sudden drop off. The experiment was terminated when the load reached the maximum loading capacity of the machine (4000 kN).

After failure photos of smaller diameter tunnel are presented in Figure 6.8. Cracks were generated within the upper part of the specimens.

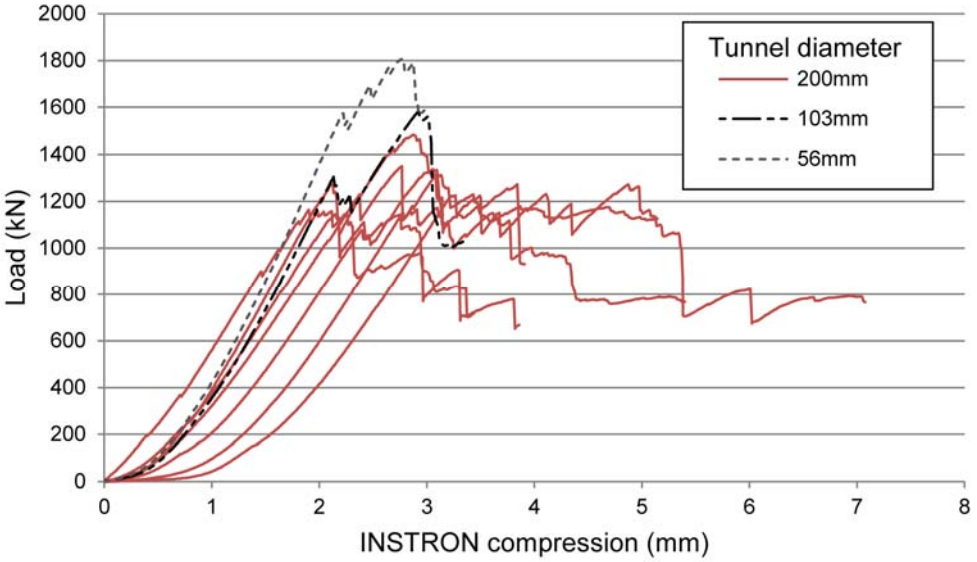

Figure 6.6 Load displacement relationships of different tunnel diameter of unsupported tunnel tests in strong sandstone.

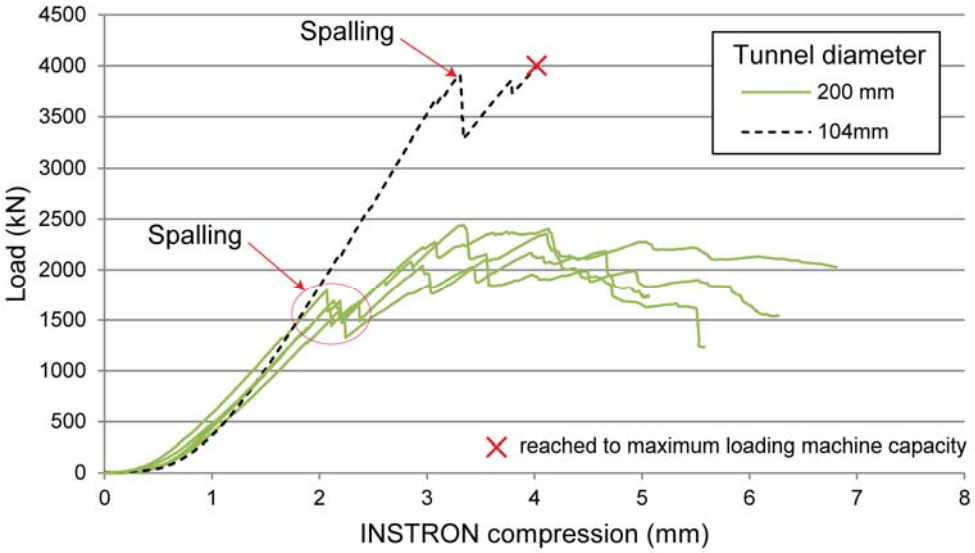

Figure 6.7 Load displacement relationship of different tunnel diameter of unsupported granite tests.

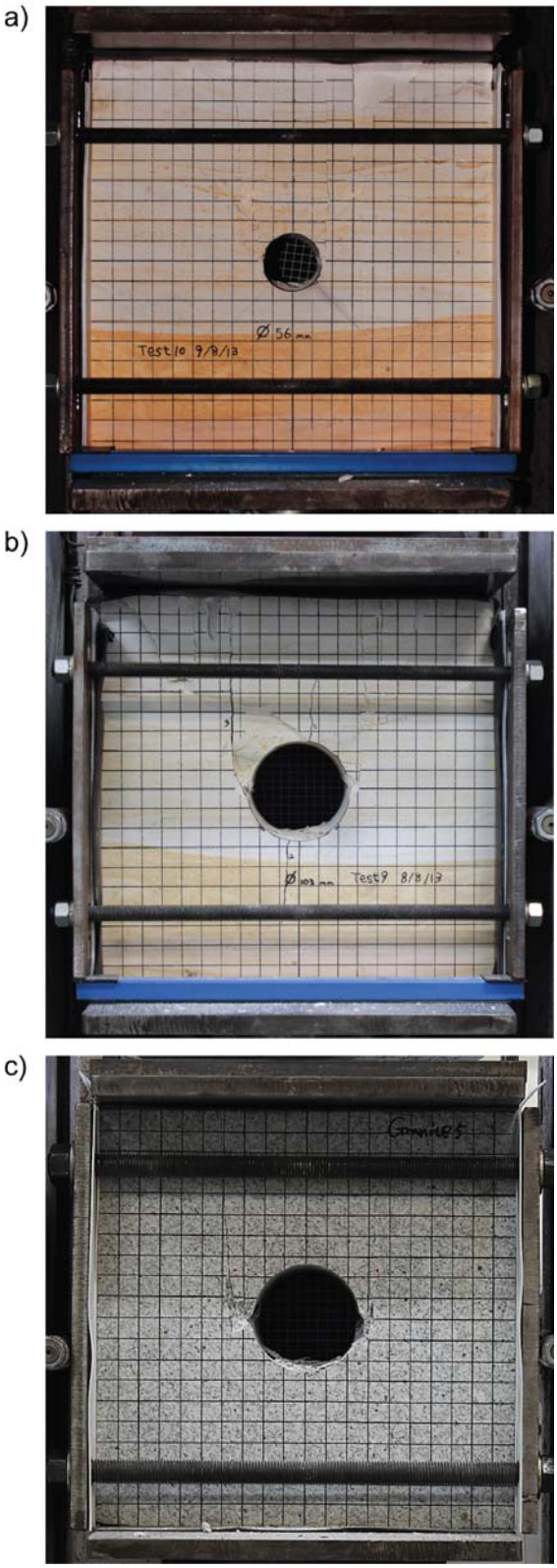

Figure 6.8 Specimens after failure a) strong sandstone (56 mm diameter), b) strong sandstone (103 mm diameter), c) granite (104 mm diameter).

6.4 Seismic Response

6.4.1 Results for Sandstone

Figure 6.9a shows a typical seismic response of an unsupported 200 mm tunnel diameter within strong sandstone. The seismic activity starts with the creation of a vertical tension crack in the floor and roof of the circular opening as predicted by theory (Hoek & Brown, 1980). The rate of seismic activity clearly increased prior to the violent ejection in both walls. Significantly, a relatively quiet period was monitored prior to final rupture and the start of the pillar crushing mode (shear) of failure. Critical levels of strength to induced stress related to the start of any visible instability such as spalling on both walls and the start of pillar have also been identified (Figure 6.9b). A significant decrease in load bearing capacity occurs following the final shear failure of the pillar.

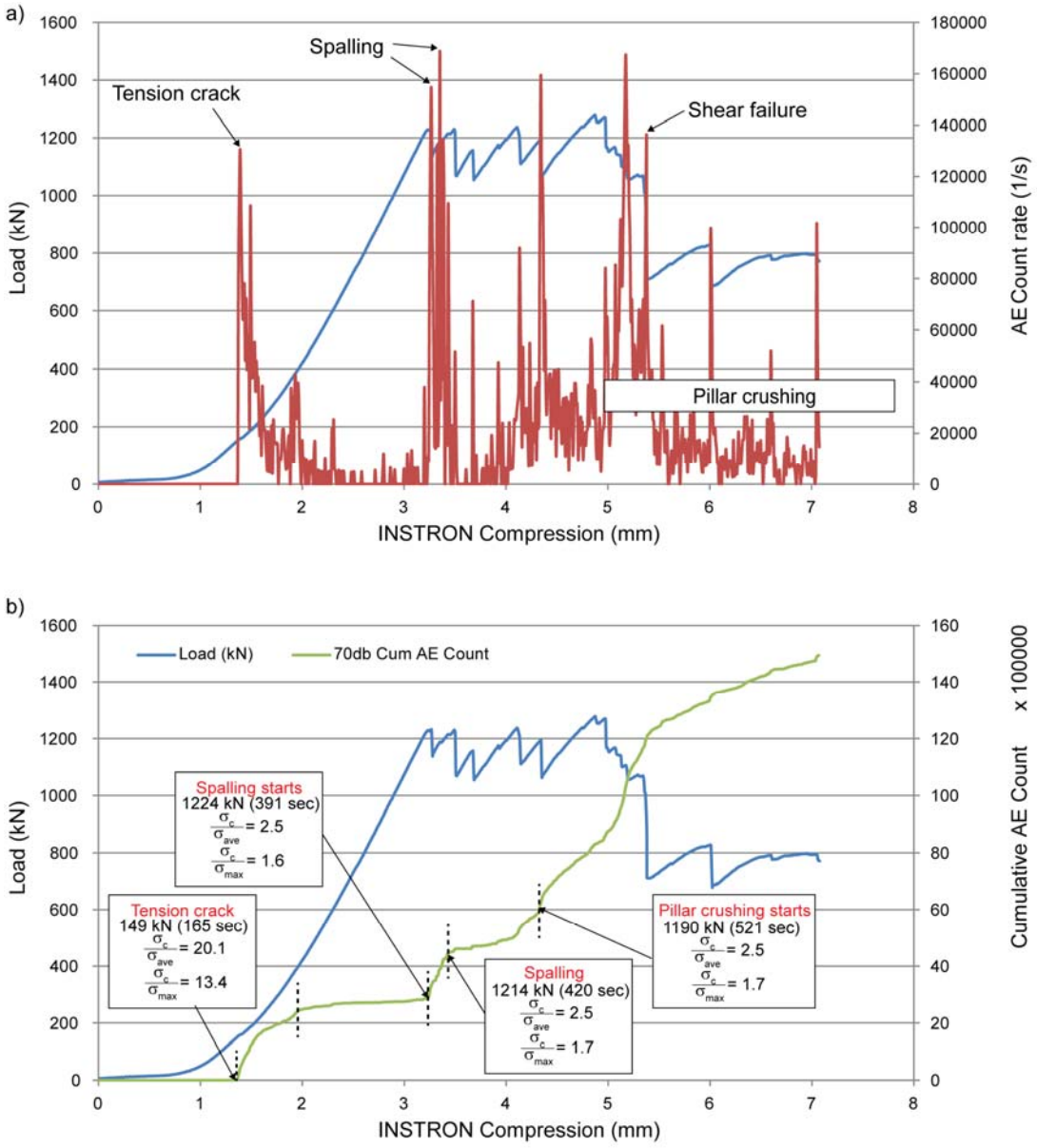

Figure 6.9 a) Failure mode and seismic response of an unsupported tunnel in strong sandstone, b) Rate of seismicity and decreasing ratios of strength/induced stress.

6.4.2 Results for Granite

Figure 6.10 shows the seismic response of an unsupported 200 mm tunnel diameter granite test. Similar to the case of the strong sandstone, the seismic activities initiated after a tension crack appearances at the top and bottom of the excavation (Figure

6.10a). After spalling occurred on both sides of the tunnel, a shear crack propagated on a side pillar and led to continuous pillar crushing failures. The load bearing capacity after the on-set of pillar crushing remained at a high value.

In both material test results, the seismic event was not observed until the tension crack creation. The seismic activities increased after spalling and accumulated towards pillar crushing. Compared with the strong sandstone result, more acoustic activities were recorded in granite.

From both results, there was no clear indication was seen in seismic activities before spalling occurred. When thin slabs were detached from the excavation surface, no relevant activities in seismic response were detected. As can be seen in Figure 6.9 and Figure 6.10, a sudden increase in seismic activities was experienced simultaneously to material ejection. For full scale tunnels, this implies an inability to predict the initial failure using seismic responses.

Seismic data revealed a distinctive difference in each failure mechanism. Although seismic activities at spalling failure was impulsive, pillar crushing failure was accumulative. After spalling occurred on both side of tunnels, seismic activities returned to a low increase rate until an onset of pillar crushing. Frequent seismic activities were recorded and continued until the end of the test.

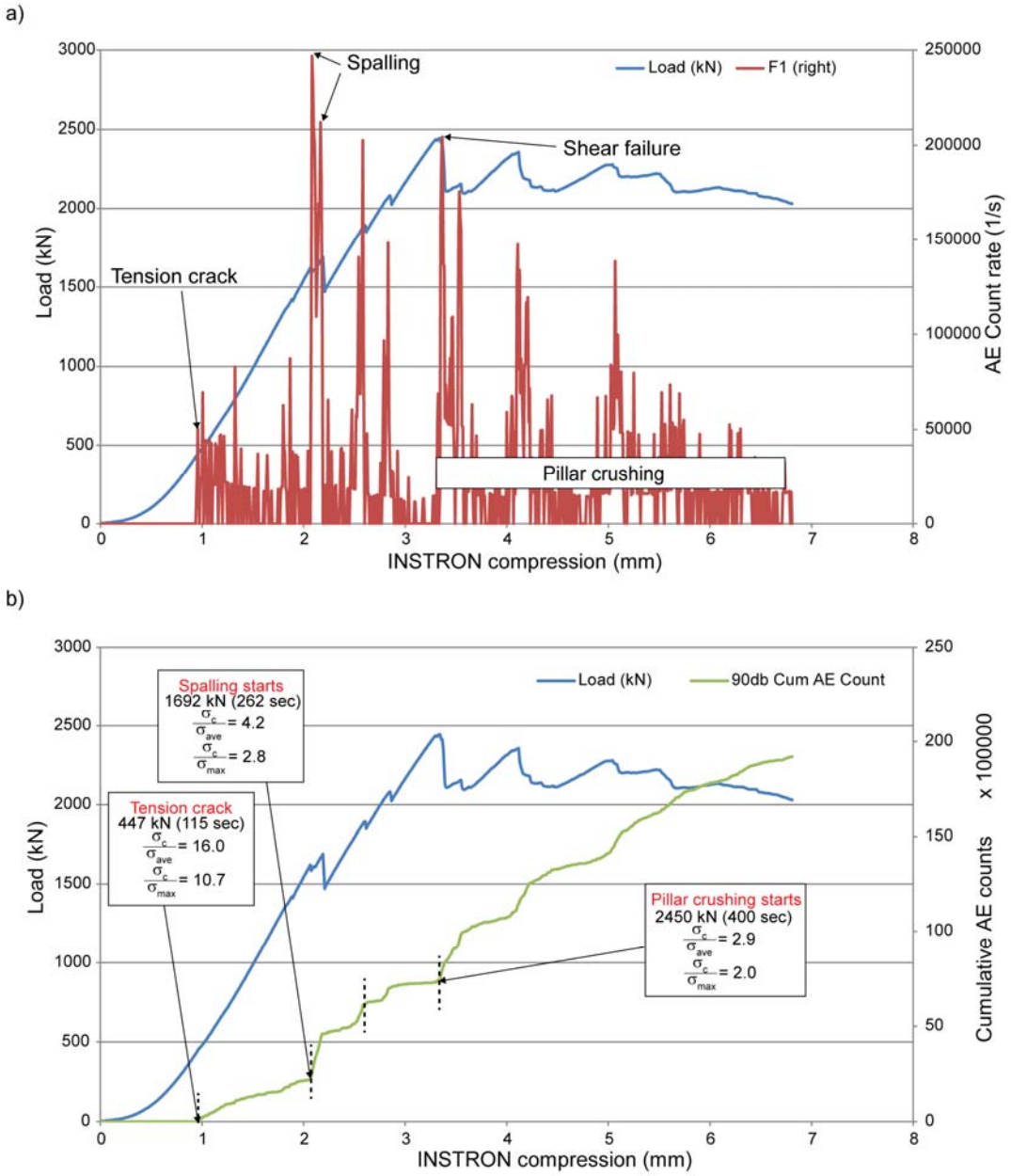

Figure 6.10 a) Failure mode and seismic response of an unsupported tunnel in granite, b) Rate of seismicity and decreasing ratios of strength/induced stress.

6.5 Ejection Velocities

6.5.1 Observed Spalling Process

Stress-driven damage in brittle materials occurs as progressive, often violent, slabbing of the excavation walls and is localised within areas of maximum induced

stress concentrations (Christiansson, Hakala, Kemppainen, Siren, & Martin, 2012; Ortlepp & Stacey, 1994). Within these experiments the broken tunnel wall slabs were ejected to the tunnel floor in what can be described as violent failure.

In the case of the unsupported moderately strong sandstone test, no violent ejection was observed. Once the maximum tangential stress reached certain level, cracks were formed along the entire tunnel wall instantly following the horizontal geological layers (Figure 6.11). The damage was created gradually and the detached materials crumbled.

In the case of granite, violent ejection occurred simultaneously with crack propagation along the tunnel axis. Once slabs were detached from the tunnel surface, they were ejected violently with evident rock failure noise (Figure 6.12).

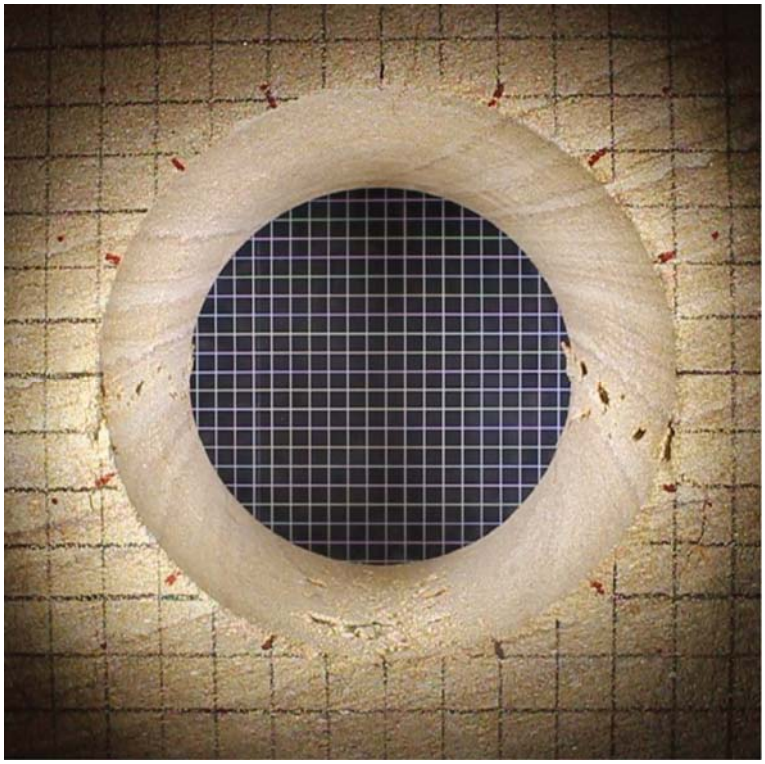

Figure 6.11 Spalling failure of moderately strong sandstone.

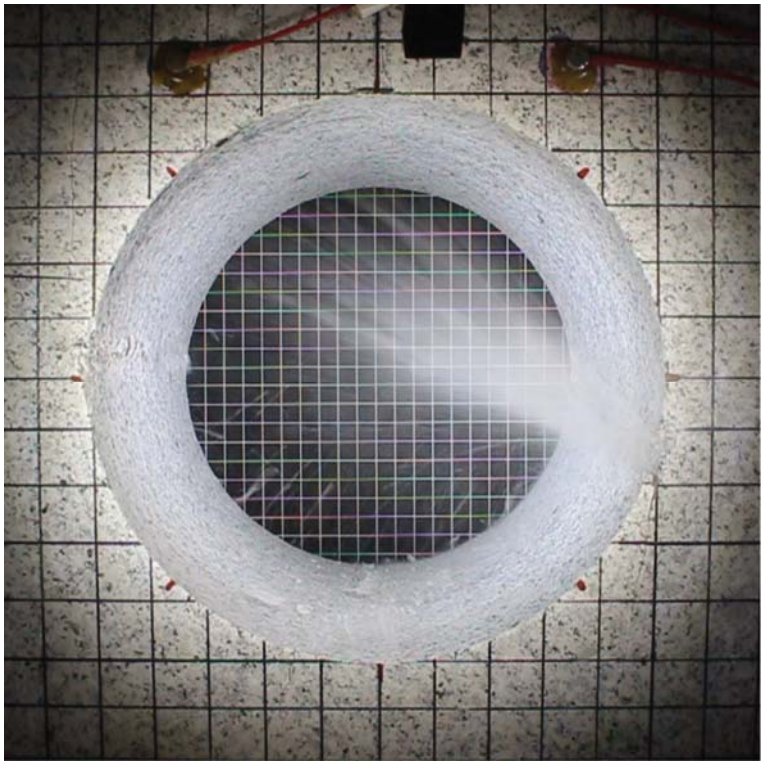

Figure 6.12 Spalling failure of granite.

6.5.2 Ejection Velocities

In the thesis experiments, violent ejection was observed during failure of tunnels in strong sandstone and granite blocks.

Ejection velocities were calculated by image analysis. A spalling moment was captured by examining each image and a travel distance of materials was measured. At recording, a depth of field of images was maximised in order to monitor the tunnel sidewall behaviour. It provided wider vision, however resulted in a perspective exaggeration on images. Therefore a correct measurement scale determination was required for an accurate calculation. Grid drawn on the specimen surfaces (20 mm x 20 mm) and a background grid (10 mm x 10 mm) were used as references. Both front and back measurement scales were calculated from a ratio of a measured length on an image and an actual tunnel diameter before experiment at the front and back of tunnel (Figure 6.13). The appropriate measurement scale was selected depending on a material ejection position.

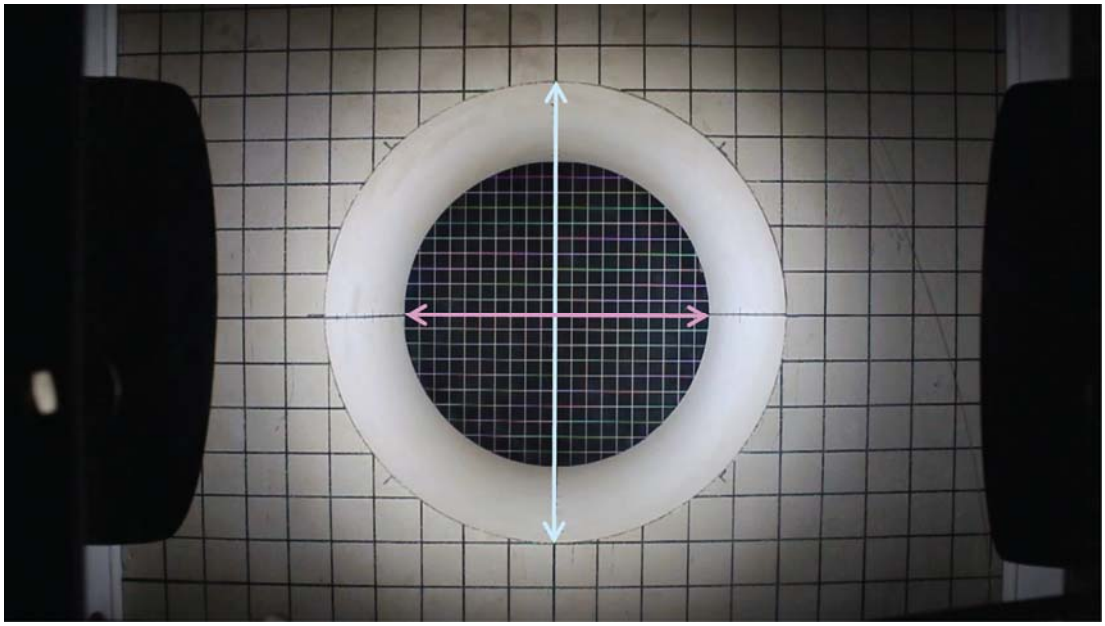

Figure 6.13 An example of measurement scale determination using an image before experiment.

Figure 6.14 shows an example of material ejection calculation. Photos were continuously filmed every 0.02 sec and a material ejection moment was selected Material travel distance was measured on the image and converted using a measurement scale depending on a material ejection position. In Figure 6.14, since material ejection occurred at the front of the tunnel, a front measurement scale was used to obtain the actual travel distance. The calculated distance was divided by the intervals (0.02 sec) and material ejection velocities were determined.

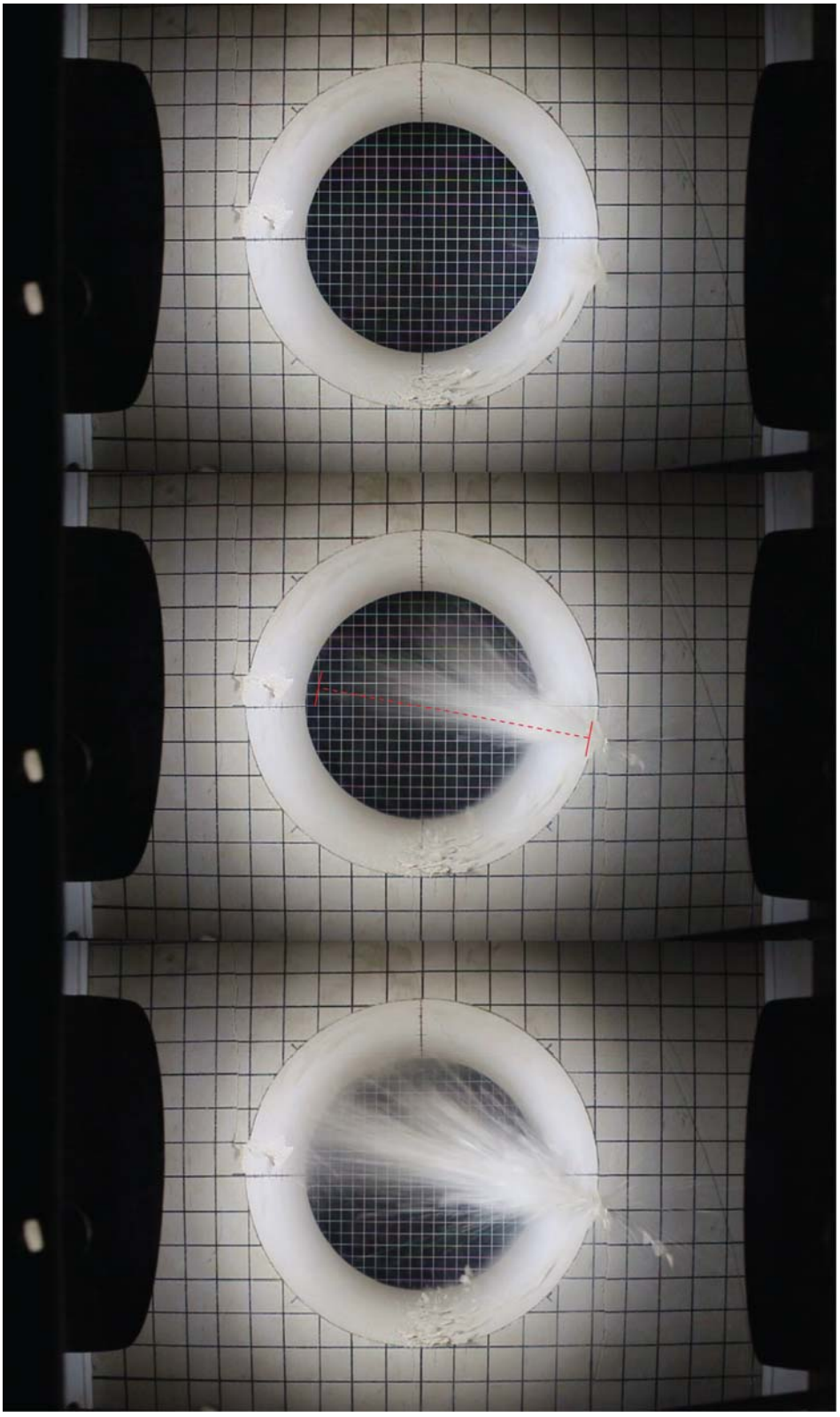

Figure 6.14 An example of a moment of material ejection (photos were taken every 0.02 sec).

A typical ejection development for a wall failure of unsupported tunnel is shown in Figure 6.15. Different ejection velocities of unsupported strong sandstone are shown in Figure 6.15a and b. Figure 6.15a shows a material ejection at lower rate (2.3 m/s). In this case, a horizontal crack propagated along geological weakness areas in the right side of tunnel and detached materials were released from a partial area on the tunnel wall. Figure 6.15b shows aggressive ejection of strong sandstone. Once spalling occurred and crack propagated through the entire tunnel wall, slabs were detached from both the inside of tunnel and specimen face. An ejection velocity of 6.9 m/s can be determined using the background grid. Figure 6.15c shows ejection of unsupported granite block. Ejection occurred immediately after crack formation and finer broken materials were ejected from the tunnel surface. A calculated ejection velocity is 8.5 m/s. Ejected materials hit on the other side of tunnel wall and fell off to the bottom of the tunnel.

Figure 6.16 shows the calculated ejection velocities of 200 mm unsupported tunnel following the uniaxial compressive stress. The ejection velocities ranged from 2.0-10 m/sec. were determined, which validate the back analysis of actual failures in underground mining (Ortlepp, 1993; Ortlepp & Stacey, 1994). Generally the higher the uniaxial compressive strength, the higher were the ejection velocity values. These positive correlation between the intact rock strength and the scale of ejection is consistent with the tunnel observation by Broch and Sørheim (1984). The average ejection velocities are 5.4 m/s and 8.5 m/s for strong sandstone and granite respectively. Similar ejection velocities have been used at WASM during dynamic testing of rock reinforcement systems (Villaescusa, Thompson, Player, & Morton, 2010). Such velocities are capable of damaging most commercially available full scale ground support schemes.

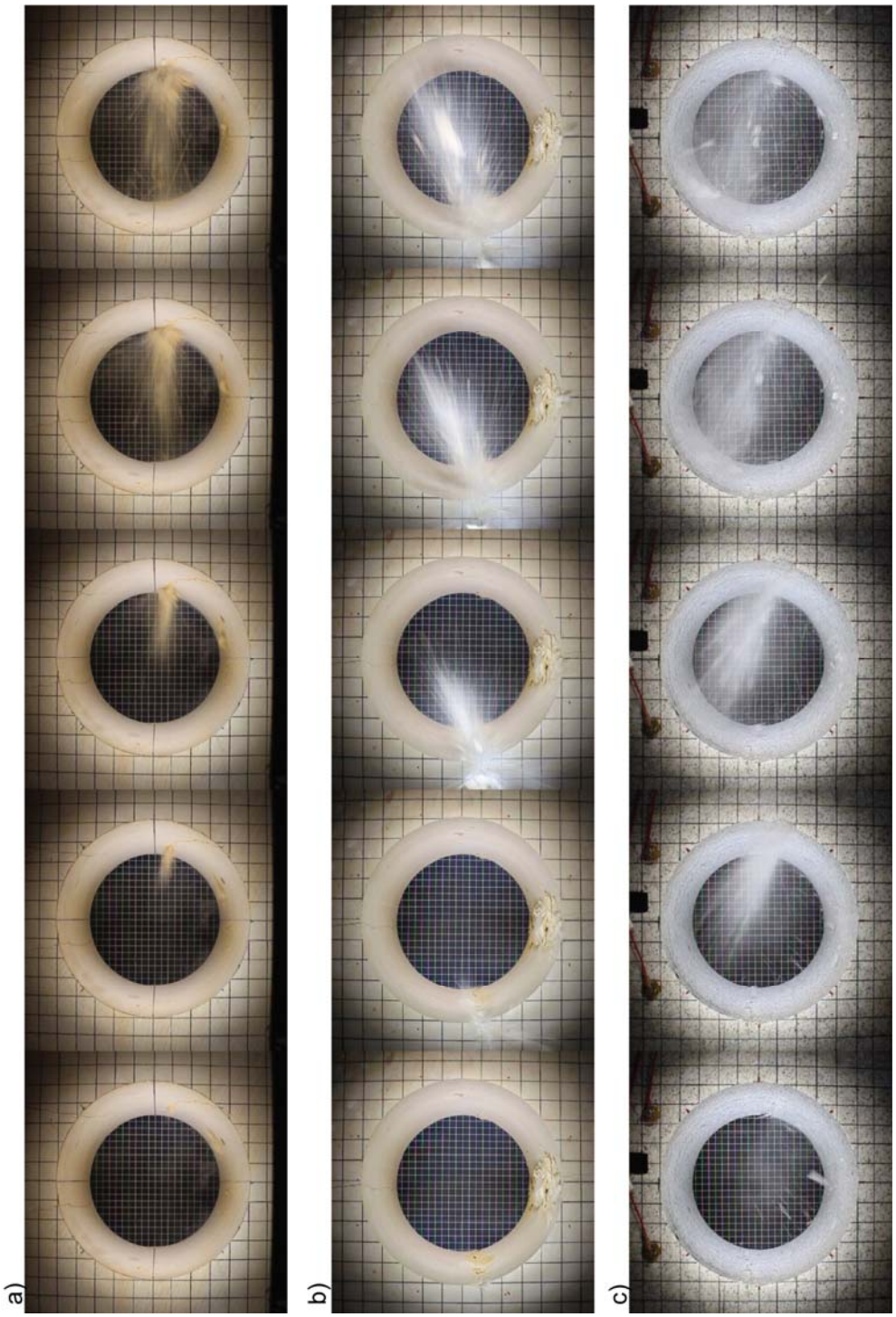

Figure 6.15 Violent ejection development at spalling (50 fps) a) strong sandstone 2.3 m/s, b) strong sandstone 6.9 m/s, c) granite 8.5 m/s.

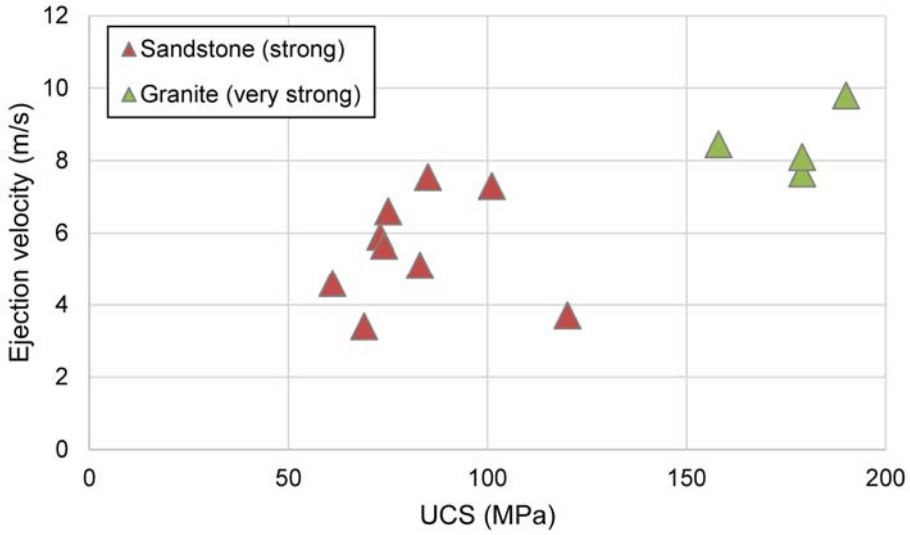

Figure 6.16 Ejection velocities at spalling of different strength of unsupported tunnel.

6.6 Unsupported Tunnel Test Summary

The various unsupported tunnel test results were compared. In all the cases, a load increased elastically until spalling was experienced on both tunnel sidewalls. Pillar crushing started when the specimen reached the peak load and continued until the end of the experiments. The observed behaviour was very similar with different diameter samples. AE sensors were used to monitor the seismic activities. The result showed a clear difference in each failure mechanism and the results were material independent. Violent material ejection occurred on strong sandstone and granite specimens. Ejection velocities were calculated using high speed filming. Higher ejection velocities were determined for stronger material strengths.

Chapter 7

Ratio of Intact Rock Strength to Induced Stress

7.1 Computer Simulations Using Abaqus

In order to better understand the failure processes and to check the three-dimensional calculations, computational modelling was undertaken using the program Abaqus Version 6.12. Analysis was done by both linear elastic model and non-linear elasto-plastic model. Lateral and vertical pressure were applied through steel platens. A finite element mesh used for 3D modelling of the test geometry is shown in Figure 7.1.

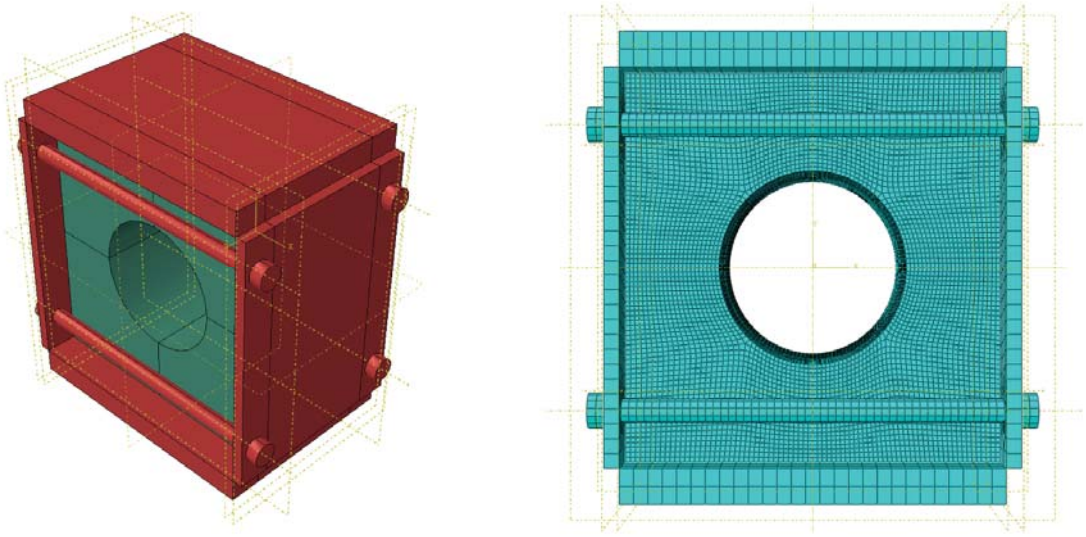

Figure 7.1 Three-dimentional Abaqus model geometry and finite element mesh.

7.1.1 Material Properties for Numerical Modelling

The physical material properties of the rock obtained from the material characterisation test (details are in Chapter 3) and steel materials were used for numerical modelling. The average property value used in the simulation is summarised in Table 7.1.

Table 7.1 Mechanical properties of rock samples and steel platens used for numerical modelling.

	Unite density (kN/m^3)	Young's modulus (GPa)	Poisson's ratio	Cohesion (MPa)	Friction angle (°)	UCS (MPa)	UTS (MPa)
Sandstone (mod strong)	21.6	8	0.2	5	41	19	
Sandstone (strong)	22.6	24	0.3	17	50	89	4.6
Granite (very strong)	26.0	58	0.2	25	59	182	
Steel	77	200	0.3				

Static friction between top/bottom platen and rock (rubber)	1.0
Static friction between side platens and rock (Teflon)	0.04
Static friction between steel and steel	0.5

7.1.2 Linear Elastic Finite Element Modelling

The unsupported tunnel result was modelled by linear elastic finite element modelling. A uniform load was applied in the vertical direction from the bottom platen similar to the laboratory testing. One of the numerical modelling result of unsupported strong sandstone tunnel test is shown in Figure 7.2. Compression is shown as positive value with units of MPa. The figure shows the minimum principal stress distribution when the vertical load was 149 kN, which is the same load level as when a tensile crack creation appeared at the laboratory tests. The numerical modelling result shows that the maximum tensile stress is concentrated at the floor of the tunnel. The tensile stress value is 3.5 MPa, which is close to the average UTS value of a strong sandstone (4.6 MPa).

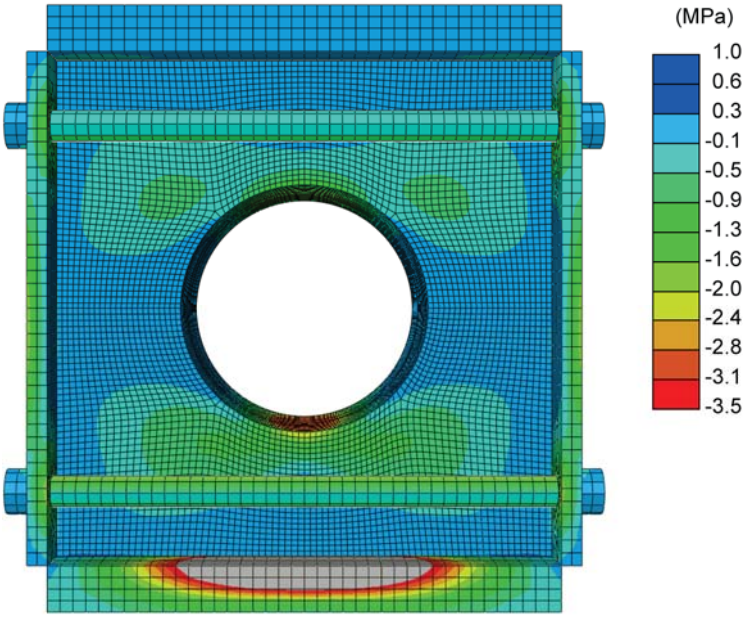

Figure 7.2 Minimum principal stress by linear elastic finite element modelling.

The maximum stress distribution within the specimen was examined before spalling occurred. Figure 7.3 shows the result of linear elastic finite element modelling of unsupported strong sandstone prior to spalling failure. It presents the calculated maximum principal stress value when the vertical stress reached to 15.3 MPa which was the same stress level when the unsupported strong sandstone tunnel (UCS 74 MPa) spalled.

It confirms that the maximum tensile stress occurs at the bottom and top of the tunnel and the maximum stress concentrates at the side of tunnel boundary in elastic modelling. Hoek and Brown (1980) described that in elastic tunnel model, the maximum tangential stress $\sigma_{\max}$ occurred at the side of the tunnel boundary under vertical stress condition and its value can be expressed as below by using the Kirsch solution.

$$\sigma_{\max} = 3\sigma_v - \sigma_h \qquad (7.1)$$

The computational modelling solution for the maximum tangential stress (σ_{max}) has been compared with the Kirsch solution and shown in Figure 7.4 and Table 7.2. Similar values of σ_c/σ_{max} and σ_c/σ_{ave} were determined by the two independent techniques.

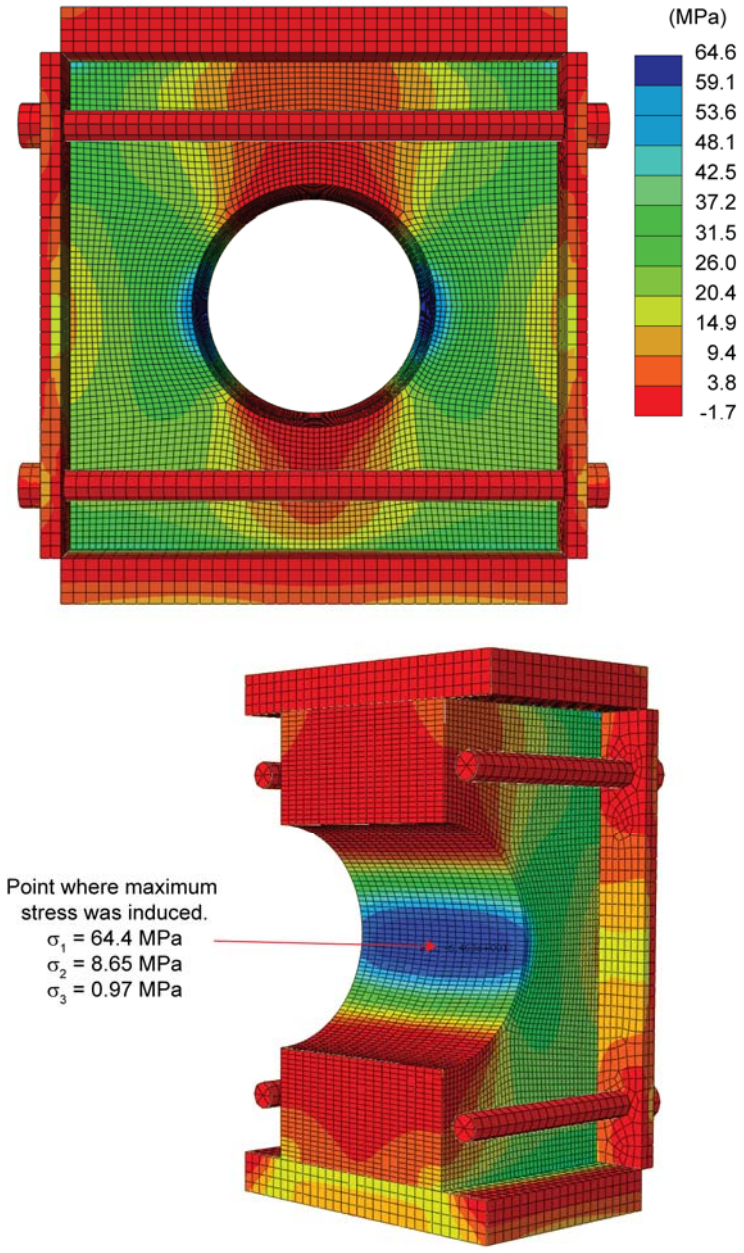

Figure 7.3 Maximum principal stress prior to failure by linear elastic finite element modelling.

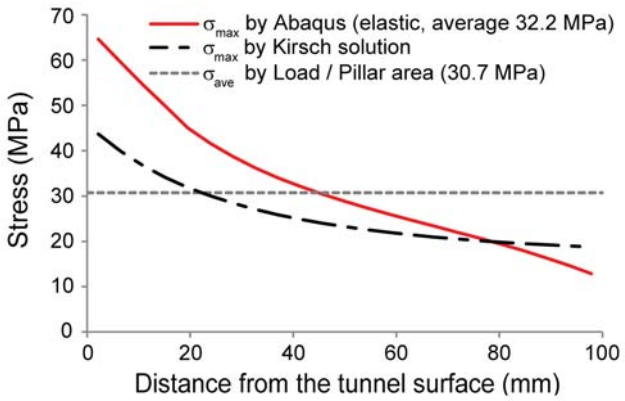

Figure 7.4 Calculated pillar stress distribution prior to tunnel wall spalling.

Table 7.2 Summary of the pillar stress prior to spalling.

		Prior to spalling
Load (kN)/Vertical stress (MPa)		1124/15.3
Maximum principal stress at boundary σ_{max} (MPa)	Abaqus elastic	64.6
	Kirsch solution	46.0
σ_c/σ_{max}	Abaqus elastic	1.1
	Kirsch solution	1.6
Average pillar stress σ_{ave} (MPa)	Abaqus elastic	32.2
	Load / pillar area	30.7
σ_c/σ_{ave}	Abaqus elastic	2.3
	Load / pillar area	2.4

7.1.3 Non-linear Elasto Plastic Modelling

A Mohr-Coulomb model with a tension cut-off was adopted to describe the plastic behaviour of the specimens. During the modelling, the top platen was fixed and a constant displacement rate was applied to the bottom platen. The rate of loading during the simulation was 0.5 mm/min in an upward direction. The simulation lasted 14 minutes.

7.1.3.1 Stress Before Spalling

Figure 7.5 shows the minimum principal stress distribution when the vertical load reached to 412 kN. A tensile stress concentrated on the both of floor and roof of the tunnel. The tensile stress value is 4.5 MPa, which compare very well with the UTS of the sandstone.

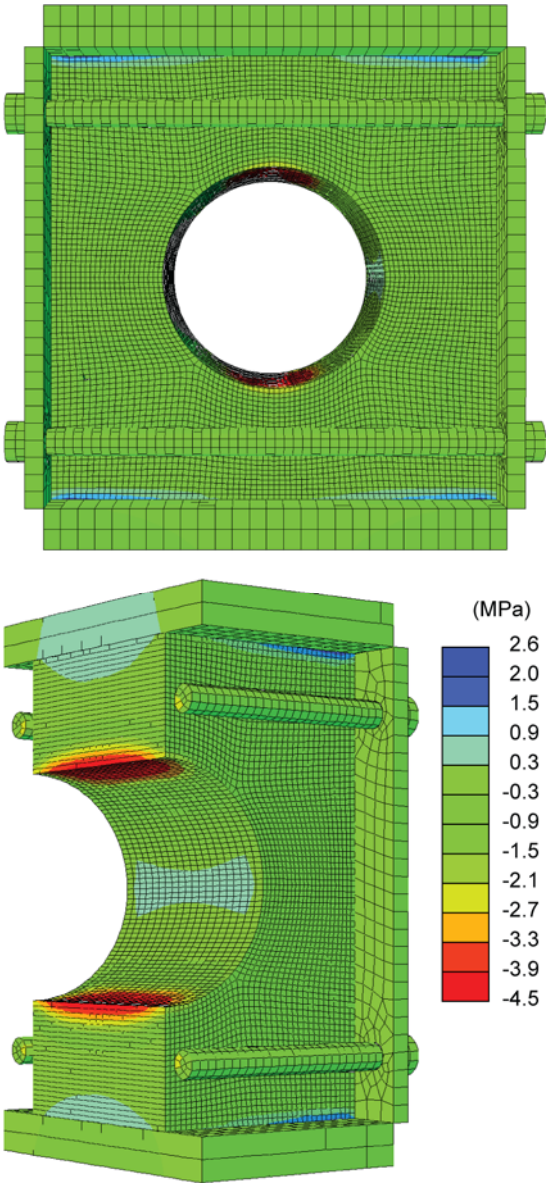

Figure 7.5 Minimum principal stress by non-linear elasto-plastic modelling before spalling.

Figure 7.6 shows both linear elastic and non-linear elasto-plastic modelling results before spalling. The maximum principal distribution are similar which means the tunnel behaves in an elastic manner before spalling occurs.

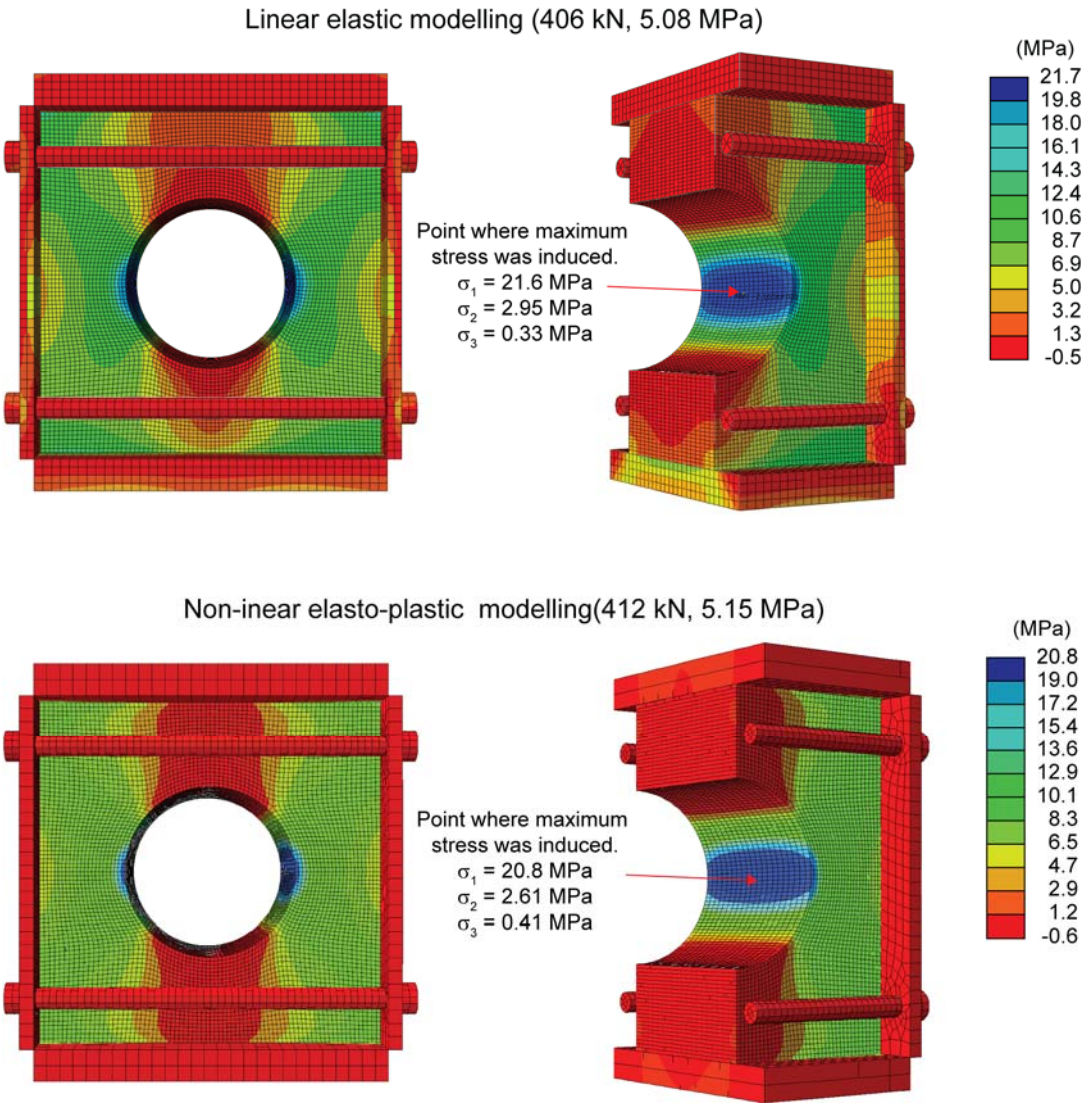

Figure 7.6 Comparison of maximum principal stress before spalling between linear elastic and non-linear elasto-plastic modelling results.

7.1.3.2 Plastic Strain at Sidewall

As the load increased, the plastic strain increased within the tunnel side walls. Figure 7.7 shows the non-linear numerical modelling results in which a shear band was seen to form and grow diagonally from the boundary of the excavation.

The maximum tangential stress still concentrated at the side boundary of the excavation after the plastic strain creation. The plastic strain at the boundary was observed when the maximum tangential stress reached 106 MPa.

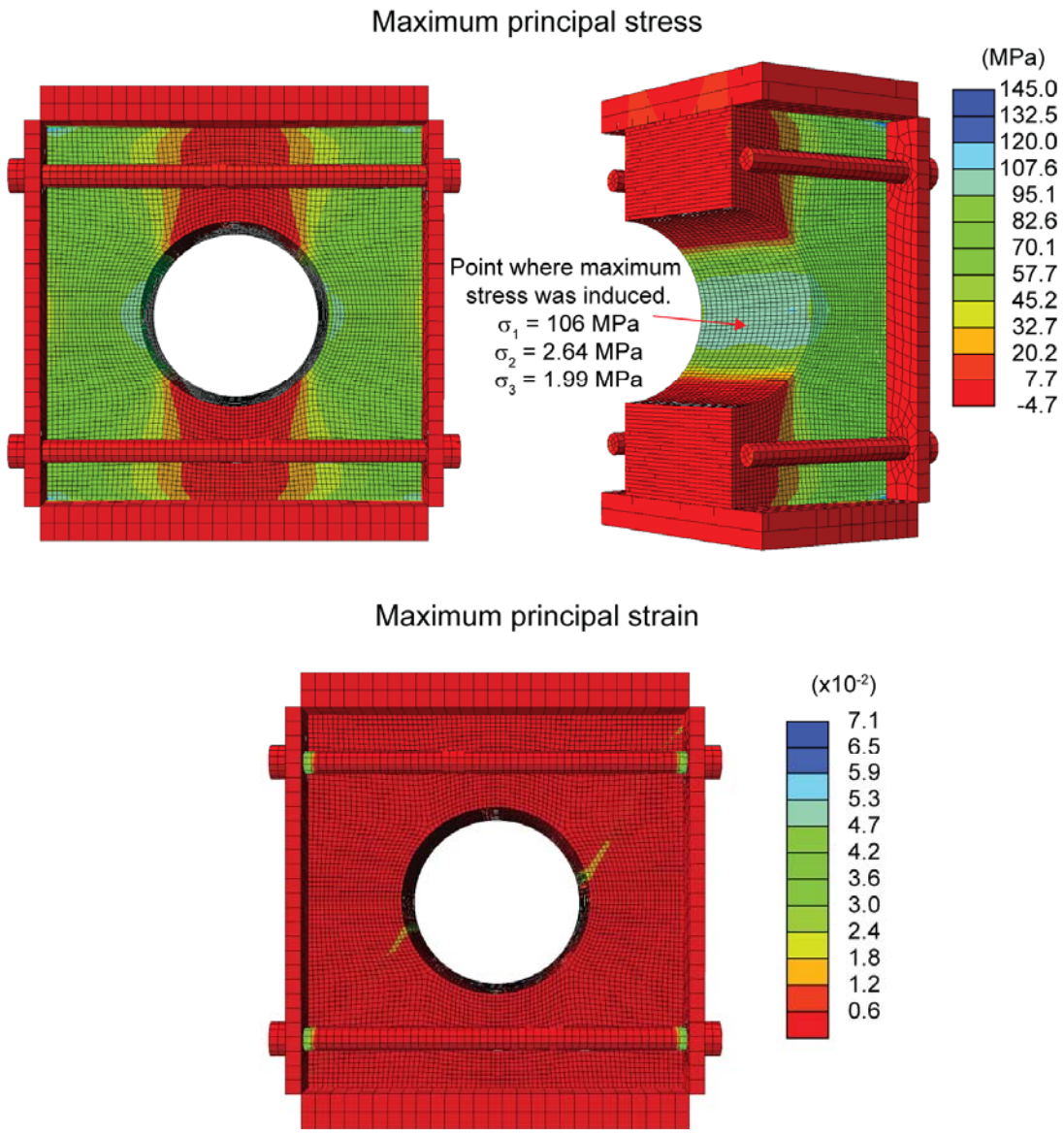

Figure 7.7 Modelling results of shear band creation by non-linear elasto-plastic modelling.

7.1.3.3 Stress at the Final Stages

Figure 7.8 shows the modelling result after 14 mm compression. The plastic strain was extended and a shear band was created as steeply dipping fractures transecting the pillars.

The stress distribution in the final stages of pillar crushing can be seen in Figure 7.8 and summarised in Table 7.3. After the plastic strain increased, a tangential stress on the tunnel boundary decreased compared with the value calculated by the Kirsch solution. The average pillar stress calculated by non-linear numerical modelling and the average stress on the pillar (Load / Pillar area) are very similar. It also shows that the pillar stress value on the side of the specimen are similar, which means the boundary effect by the side confinement plates are not significantly influencing the level of stress used to define the threshold for spalling failure.

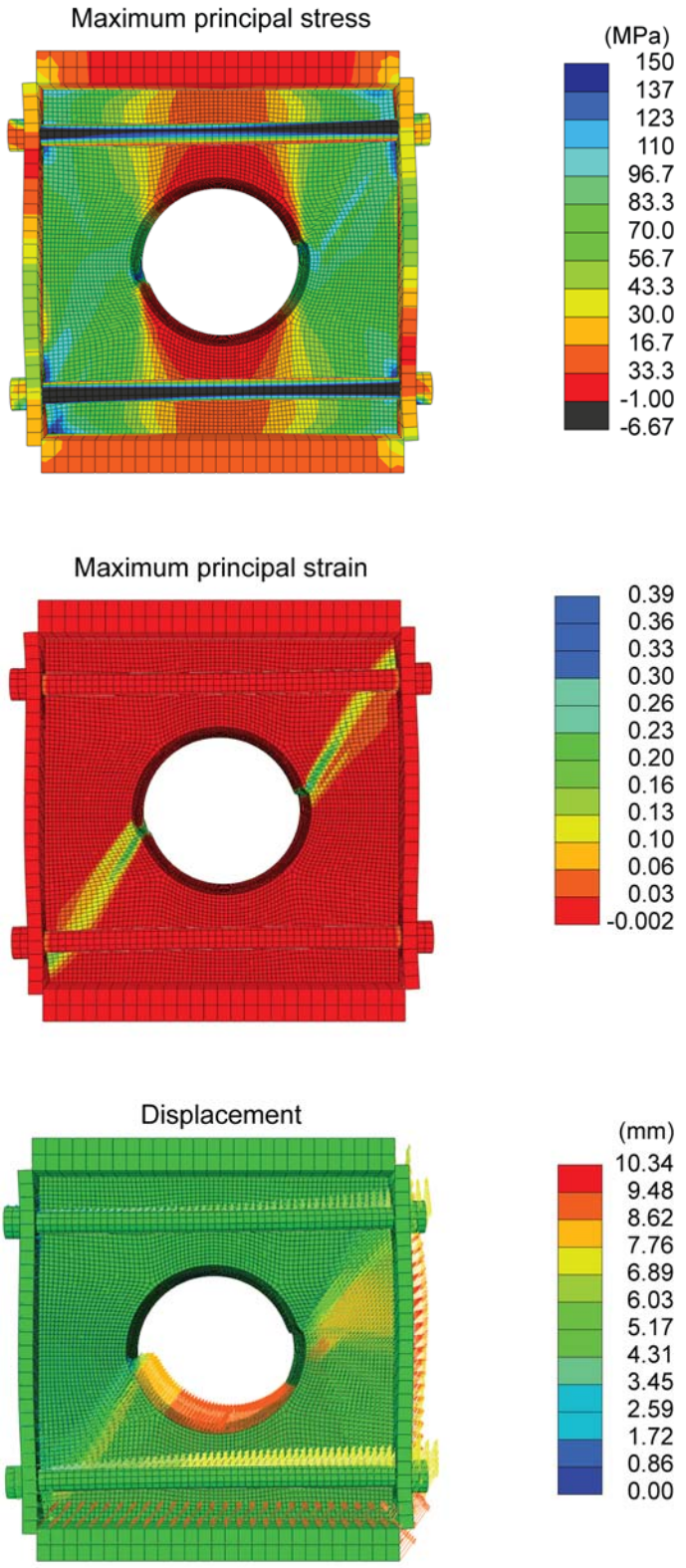

Figure 7.8 Modelling results of shear failure during pillar crushing using the program Abaqus.

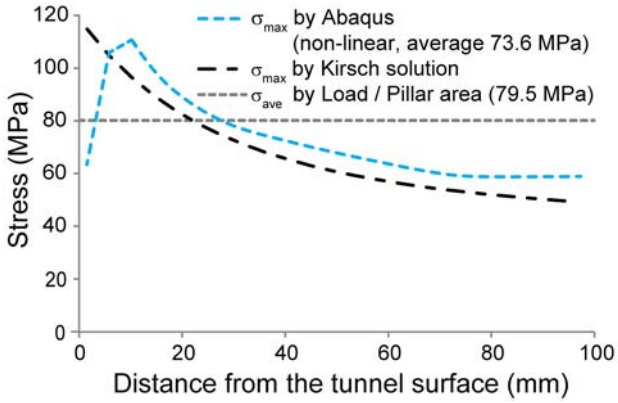

Figure 7.9 Determination of pillar stress distribution.

Table 7.3 Summary of the pillar stress prior to pillar crushing.

		Prior to pillar crushing
Load (kN)/Vertical stress (MPa)		3180 / 39.8
Maximum principal stress at boundary σ_{max} (MPa)	Abaqus Non Linear	62.7
	Kirsch solution	119.2
σ_c/σ_{max}	Abaqus Non Linear	1.2
	Kirsch solution	0.6
Average pillar stress σ_{ave} (MPa)	Abaqus Non Linear	73.6
	Load/Pillar area	79.5
σ_c/σ_{ave}	Abaqus Non Linear	1.0
	Load/Pillar area	0.9

7.1.4 Numerical Modelling Summary

Numerical modelling was conducted using the computer simulation software Abaqus. The results were compared with the Kirsch solution and the average pillar stress calculation results.

The simulation suggest that elastic behaviour before spalling occurs for both the linear and the nonlinear modelling cases. In the non-linear numerical modelling case, the maximum principal stress at the tunnel boundary decreased after spalling.

The computational modelling solution for the maximum tangential stress has been compared with the Kirsch solution. Similar values of σ_c/σ_{max} and σ_c/σ_{max} and were determined by the two independent techniques.

7.2 Spalling Failure

As mentioned in Chapter 6, stress-driven damage in brittle materials such as spalling occurs as progressive, often violent, slabbing of the excavation walls and is localised within areas of maximum induced stress concentrations.

7.2.1 Ratio of Intact Rock Strength to Induced Stress

As mentioned in Chapter 2, the relationship between the rock mass strength and the induced stress at onset of failures have been investigated by a number of researchers using stress-strain data from UCS laboratory tests in the past. (Diederichs, 2007; Lajtai & Dzik, 1996; Martin, 1997). The ratio of uniaxial compressive strength obtained by laboratory test data and the stress magnitude at the initiation of failure has been stabilised between 2 and 3. Martin (1997) also conducted the detailed investigations at underground excavation at AECL in Canada. The crack propagation process started when the strength and stress ratio reached approximately 2.

In this laboratory experiments, as the load was being increased, the ratio of compressive strength to induced stress at sidewall of tunnel was calculated. For the first stage of (spalling), the ratio monitored was the value of compressive strength to maximum tangential stress (i.e. effectively near zero confining stress at the excavation boundary). A total of 17 unsupported laboratory tests for a range of intact rock strengths results are shown in Figure 7.10. The ratio of σ_c to σ_{max} was calculated using the Kirsch solution. The stress value was calculated for both sides of tunnel wall spalling. Similar to previous work, violent ejection from the excavation walls occurred prior to peak intact rock strength (Martin et al. 1997).

The strength / stress ratio and the uniaxial compressive strength appears to be correlated. The value ranges 2 to 3.5 for moderately strong to strong rock. The red dotted line and related equation represents the potential on-set of failure. i.e., the practical safe limits prior to spalling failure. From Figure 7.10, the stress strength ratio at spalling is given by:

$$\frac{\sigma_c}{\sigma_{max}} = -0.00005{\sigma_c}^2 + 0.0232\sigma_c + 0.2767 \qquad (5.2)$$

Li (2004) reported that critical strain value declines with an increase in uniaxial compressive strength of intact rock. The results from unsupported tunnel testing shows that the maximum tangential stresses at spalling failure become lower as the uniaxial compressive strength increases. This trend has full compatibility with the critical strain definition.

Significantly, the tunnels in moderately strong rock (having a compressive strength below 50 MPa) did not experience the violent spalling failure mode.

Data from the smaller tunnel diameter (56-104 mm) are also plotted in Figure 7.10. Most of the data and the comparison shown was for tunnels of similar size (200 mm diameter) and different rock strength.

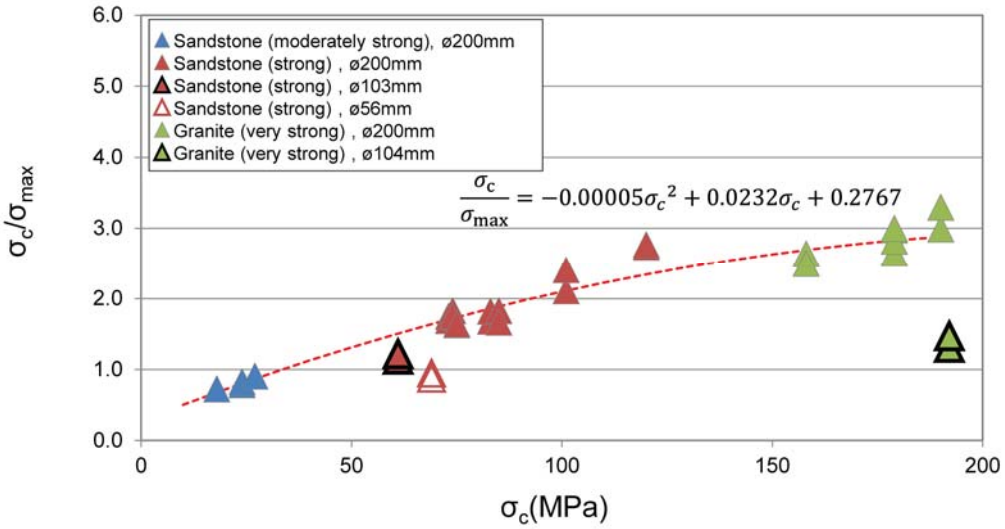

Figure 7.10 Unsupported tunnel spalling as a function of compressive strength and maximum tangential stress.

7.2.2 Comparison of Model Results with Field Observations

The laboratory results correlate well with observations of 4-5m diameter full scale unsupported tunnels excavated within a rock mass having a Uniaxial Compressive Strength of 250-270 MPa and widely spaced tightly healed geological discontinuities. The onset of stress driven failure for the full scale unsupported tunnel was experienced for intact rock strength to maximum induced tangential stress ratio of approximately

3.5. The mining tunnels were constructed using excellent drilling and blasting techniques. The tunnels were designed with semi-circular walls and a flat floor. Incipient back (roof) failure due to a sub-horizontally oriented main principal stress component can be seen in Figure 7.11.

Figure 7.11 Full scale unsupported semi-circular tunnels showing on-set of brittle failure at the centre of the excavation roof due to high horizontal stress.

7.3 Pillar Crushing Failure

Pillar design and stability analysis is a critical component of a mining engineering design process. Although the fundamental concepts of Factor of Safety as the ratio of pillar strength to average pillar stress and pillar stability have been understood for some time, it is only more recently that the tools have become available to allow more quantitative analyses of pillar strength and stability to be carried out (Villaescusa, 2014).

In basic engineering mechanics terms, stability refers to the stability of equilibrium, or the ability of the overall structure, or an element of that structure such as a mine pillar, to undergo a small change in the equilibrium state of loading without producing a state of unstable equilibrium involving a sudden release of stored strain energy or large deformations (Brady & Brown, 2004). This form of instability may lead to crushing and the total collapse of a pillar and, in some cases, its surrounds. In other cases, the peak load-carrying capacity of a pillar may be exceeded and it may show visible signs of having been over-loaded, but it may retain some load-carrying capacity and

continue to provide support to the mine structure without undergoing unacceptably large deformations (Villaescusa, 2014).

7.3.1 Ratio of Intact Rock Strength to Induced Stress

For the laboratory experiment described here, the ratio of intact rock compressive strength to the average pillar stress adjacent to the tunnels walls was calculated during loading. Figure 7.12 shows the results for the onset of pillar crushing mode of failure. The average pillar stress was obtained by dividing the vertical load by the pillar area. The test result for 103 mm diameter unsupported granite block was not plotted since the vertical load reached to the loading machine capacity before the pillar started to fail (see Chapter 6). The result shows that the strength stress ratio at pillar crushing appears to be also related to uniaxial compressive strength. The relationship is describes as:

$$\frac{\sigma_c}{\sigma_{ave}} = -0.0001{\sigma_c}^2 + 0.0345\sigma_c + 0.4869 \qquad (5.3)$$

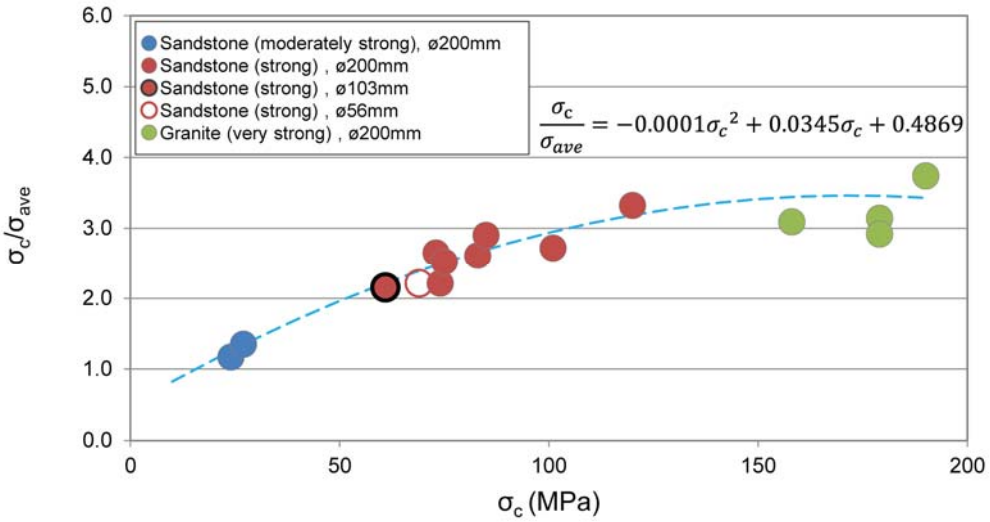

Figure 7.12 On-set of unsupported pillar crushing as a function of compressive strength and average pillar strength.

7.4 Comparison with Past Physical Model Studies

This thesis experiment results were compared with past physical model studies (Chapter 2). Figure 7.13 shows a ratio of intact rock strength to maximum tangential stress at spalling failure plotted in terms of intact rock strength. Although a positive correlation can be seen, the data scattered even among the same materials.

Figure 7.14 plots the strength to stress ratio with respect to excavation diameter. In generally with an increase in an excavation diameter, the strength to stress ratio at spalling failure became higher. As similar with Figure 7.10, an excavation size effect can be seen. The results obtained from this thesis experiment corresponds well with past physical model studies. The data from this and precious experiments suggests that, the strength to stress ratio at spalling can be seen as a material strength independent.

In addition to excavation diameter, the effect of a ratio of pillar width and height is seen in Figure 7.15.

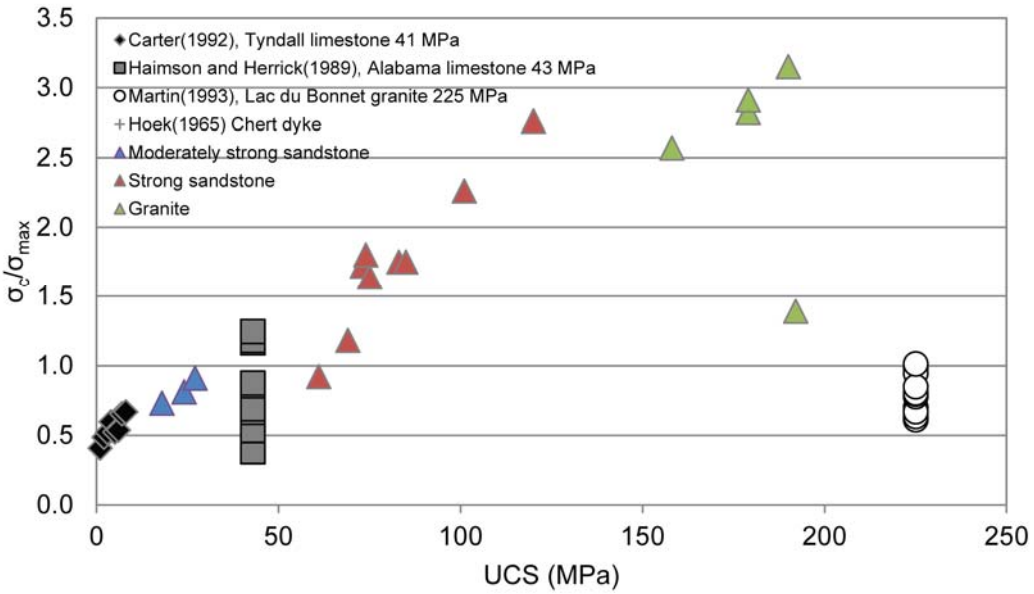

Figure 7.13 A comparison of strength and stress ratio in material strength at spalling with past physical model test results.

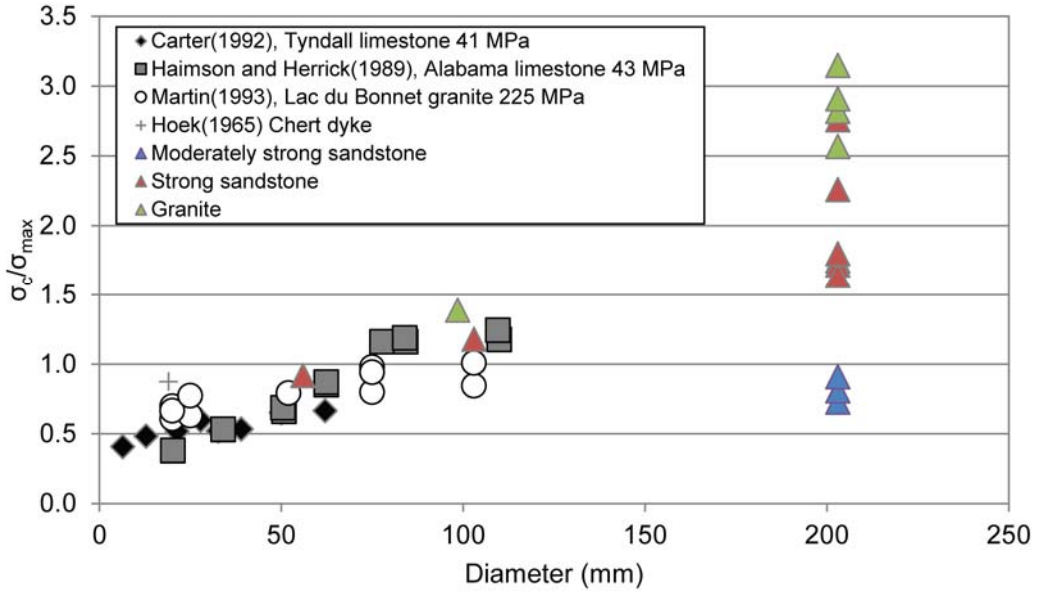

Figure 7.14 A comparison of strength and stress ratio in excavation diameter at spalling with past physical model test results.

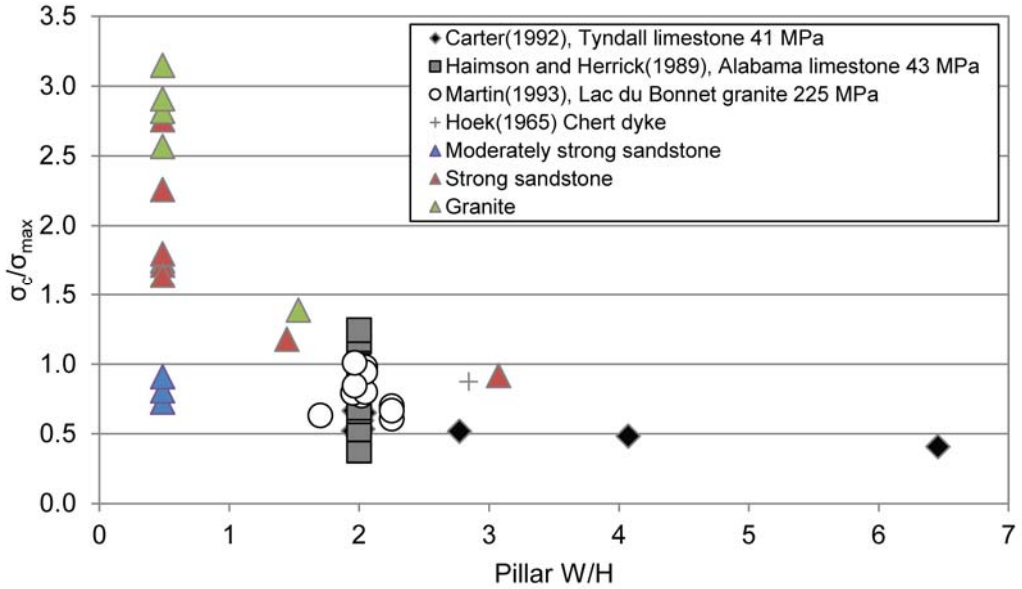

Figure 7.15 A comparison of strength and stress ratio in a ratio of pillar width to height at spalling with past physical model test results.

7.5 Application of Test Results to Pillar Design

Figure 7.16 shows the ratio of compressive strength to the average induced stress values experienced at pillar crushing, where shear failure was commonly experienced. The ratio of compressive strength to the average induced stress for the associated spalling failure for each pillar is also shown. As the strength of the materials decreased, the separation between spalling and pillar crushing events was less defined.

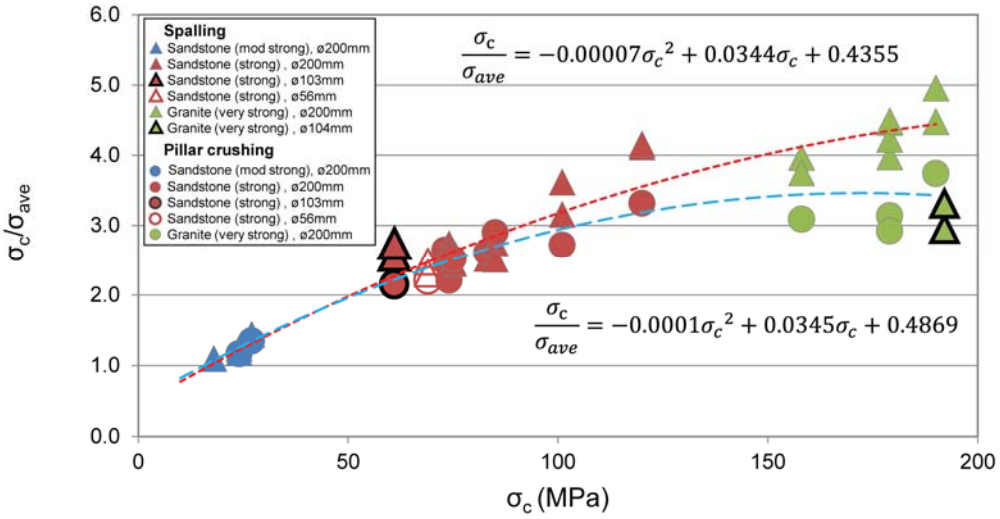

Figure 7.16 Progressive failure of unsupported tunnels as a function of compressive strength and average pillar strength.

7.5.1 Pillar Stability Graph

The results for the scaled-down unsupported pillars were compared with the full scale results from the Pillar Stability Graph database (Lunder, 1994; Villaescusa, 2014). For a range of pillar width to height (0.5 to 3.0) and the three rock types tested, the pillar crushing results from the laboratory testing compares well with the full scale results determined from underground observations (Figure 7.17). A slight gain on strength was detected from the laboratory samples, as they did not have any open geological structures and were tested using a slight amount of confinement that allowed to and maintained a post-peak strength. The laboratory and the field scale results suggest that for hard rock, the critical value for pillar strength is the ratio of σ_c/σ_{ave} regardless of the pillar geometry.

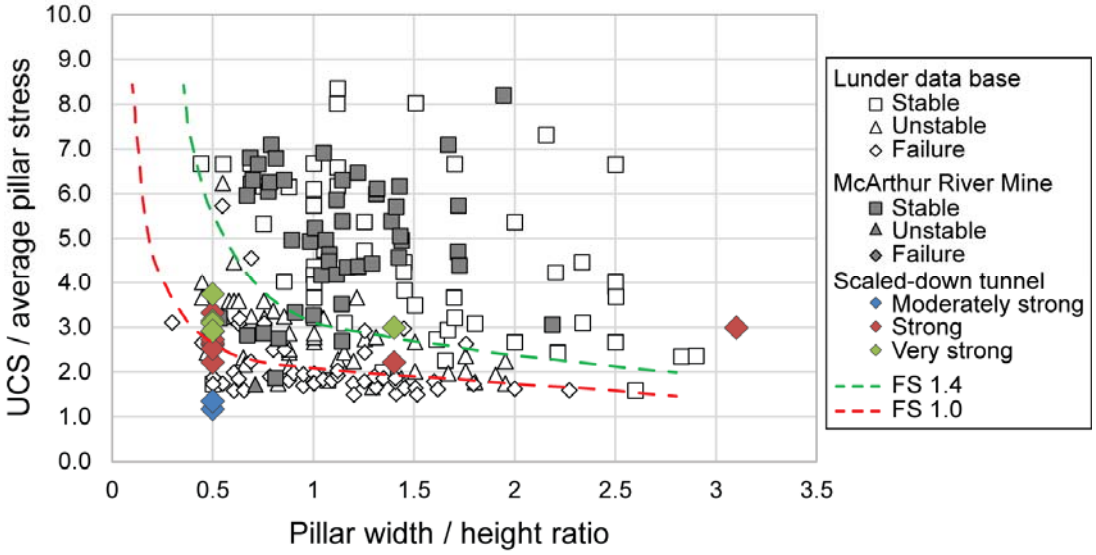

Figure 7.17 Comparison of scaled-down pillar crushing failure results with the full scale Pillar Stability Graph database (after Villaescusa (2014)).

7.5.2 Failure Envelopes Derived from Model Tests

The confining pressures on the tunnel walls were modelled using non-linear finite element modelling with a typical result shown in Figure 7.18. The confining pressure used in the testing is representative of the confining pressure available in the vicinity of most underground excavations.

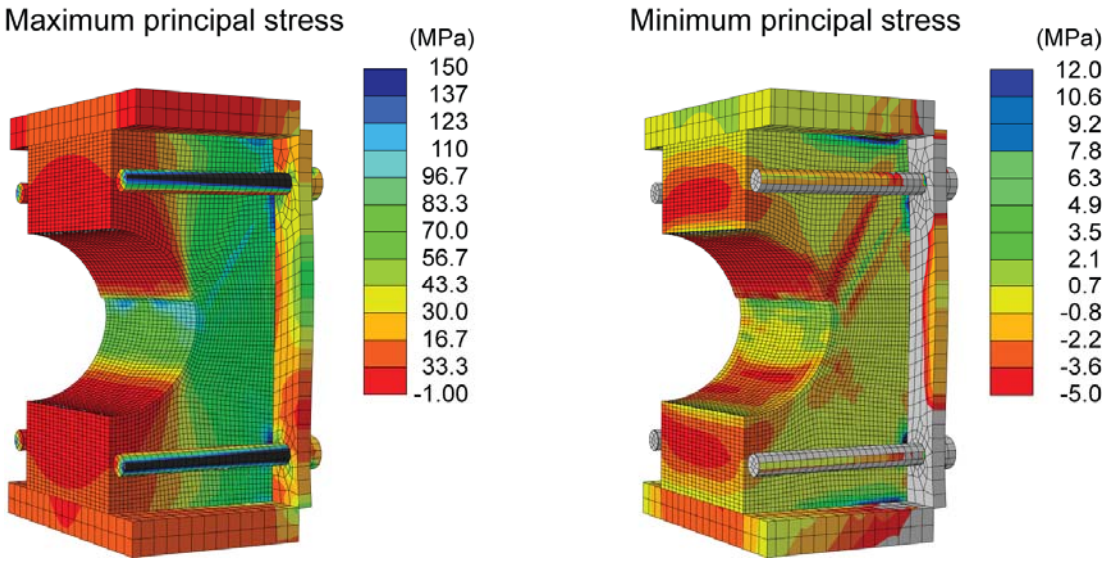

Figure 7.18 Section view of pillar stress distribution. Results from non-linear modelling using the program Abaqus.

In the calculations it was assumed that the lateral stresses were caused by the reaction force of the bolt elongation. The confinement stress of the specimen was estimated by calculating the confinement pressure (Figure 7.19).

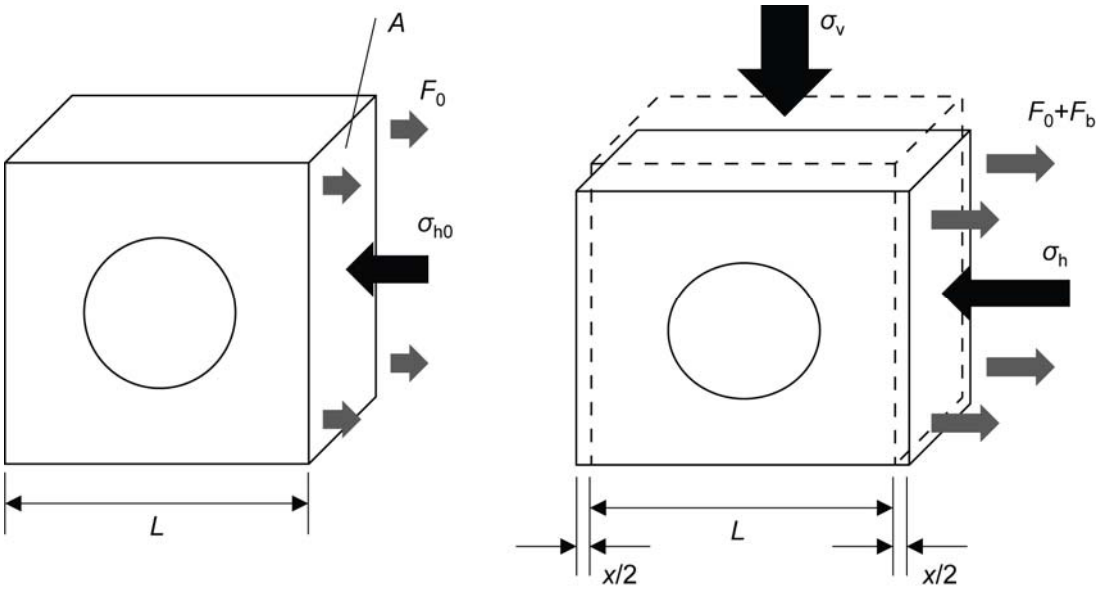

Figure 7.19 Confinement stress provided by lateral steel confinement platens.

The initial lateral stress σ_{h0} was provided by the bolt tensioning which is obtained from:

$$\sigma_{h0} = 4 \times \frac{F_0}{A} \tag{7.4}$$

where F_0 is the initial bolt tension force and A (= W x H) is the area of the plate.

During a test, the specimen deformed subject to the applied vertical loading. The specimens behaved elastically until spalling occurred with the lateral strain obtained by:

$$\varepsilon_h = \sigma_v \times \frac{\nu}{E} \tag{7.5}$$

where σ_v is the vertical loading stress, E and ν are the elastic modulus and Poisson's ratio of the rock material, respectively. The threaded bar elongations (δ) are assumed to be equal to lateral specimen deformation x. That is:

$$\delta = x = \varepsilon_h W \tag{7.6}$$

Then, the bolt force F_b is calculated from:

$$F_b = k\,\delta \tag{7.7}$$

where the specimen original width is W, and k is the stiffness of the bolt. The horizontal stress applied on the specimens σ_h is determined as follows.

$$\sigma_h = 4 \times \frac{F_0 + F_b}{A} \tag{7.8}$$

$$\sigma_h = \sigma_{h0} + 4\frac{k\nu W}{AE}\sigma_v \tag{7.9}$$

Figure 7.20 shows the failure envelope for all the unsupported tunnel tests and the three types of materials used.

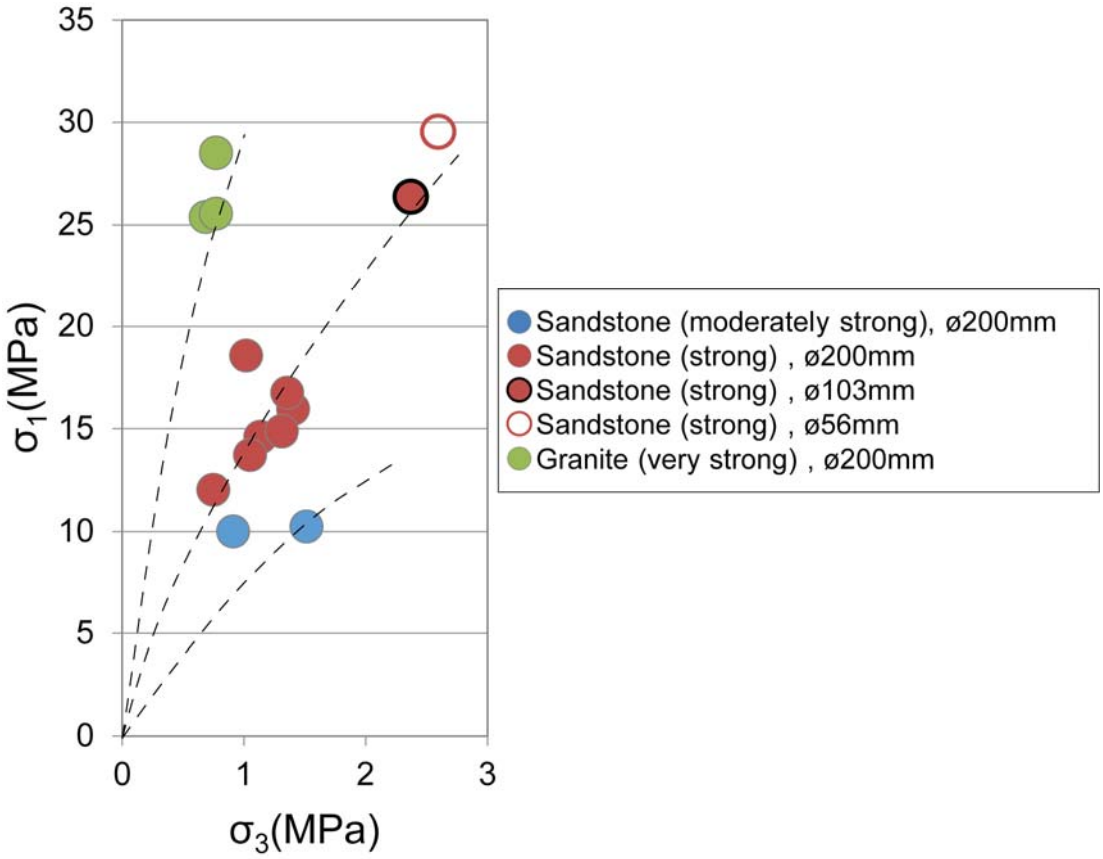

Figure 7.20 Failure envelopes for the scaled-down unsupported tunnels.

7.5.3 Strain at Spalling and Pillar Crushing

The data from the high speed video was used to calculate the strain inside the tunnels at the moment of the spalling failure. Figure 7.21 shows an example of strain calculation. Since the load was applied from the bottom of the specimens, vertical strain were mainly concerned. An excavation convergence at failures was measured from the image and strains were calculated using a front measurement scale.

The relationships for the 200 mm diameter unsupported tunnel tests are shown in Figure 7.22a. Li (2004) investigated that the intact rock critical strain decrease as the intact rock mass strength increase. A similar correlation was determined between strain value at spalling and the uniaxial compressive strength of intact rock used in these experiments. As expected, the strain at pillar crushing was slightly greater than the strain at spalling failure, as shown in Figure 7.22b. The experimental results are also in accordance with field data reported by Hoek (1999). Excavation strain was also

plotted with a ratio of material strength to maximum tangential stress at tunnel boundary. In both failures, the strain decreased with an increase in a strength to stress ratio.

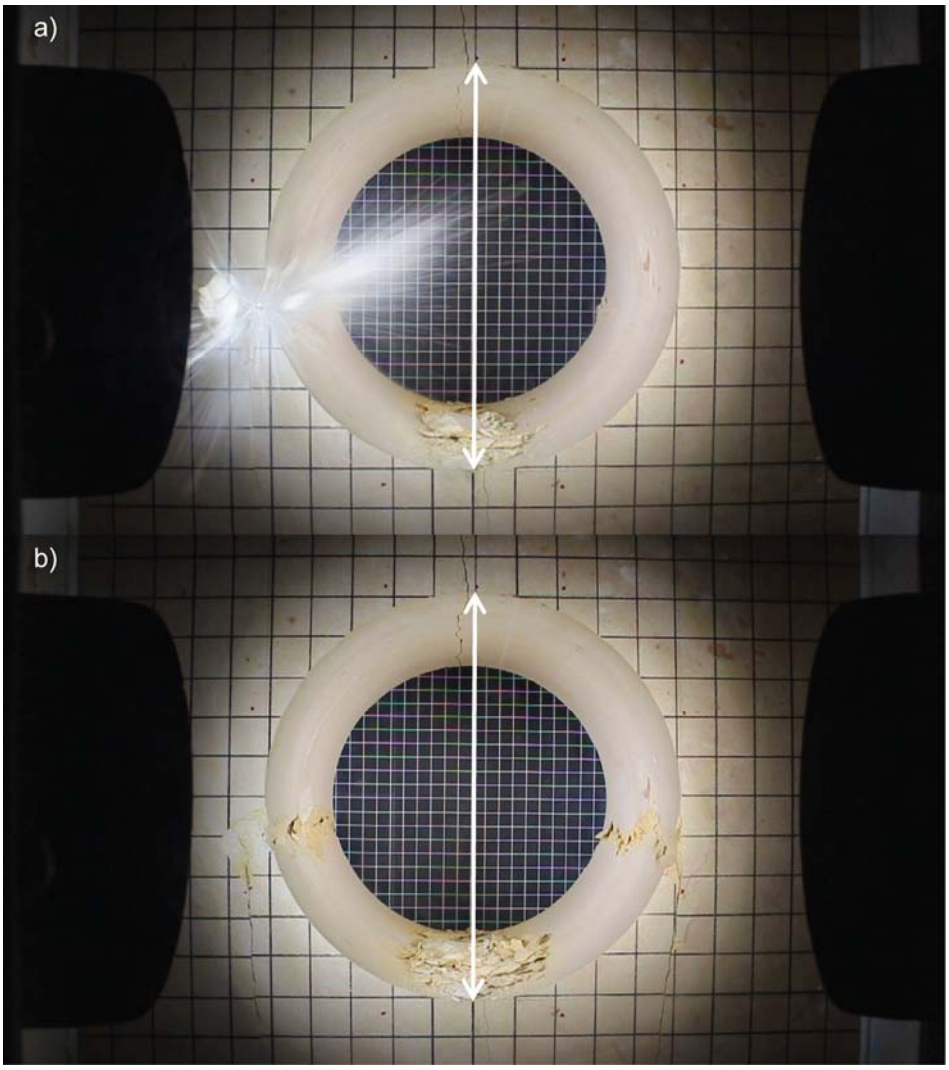

Figure 7.21 An example of strain calculation at a) spalling b) pillar crushing.

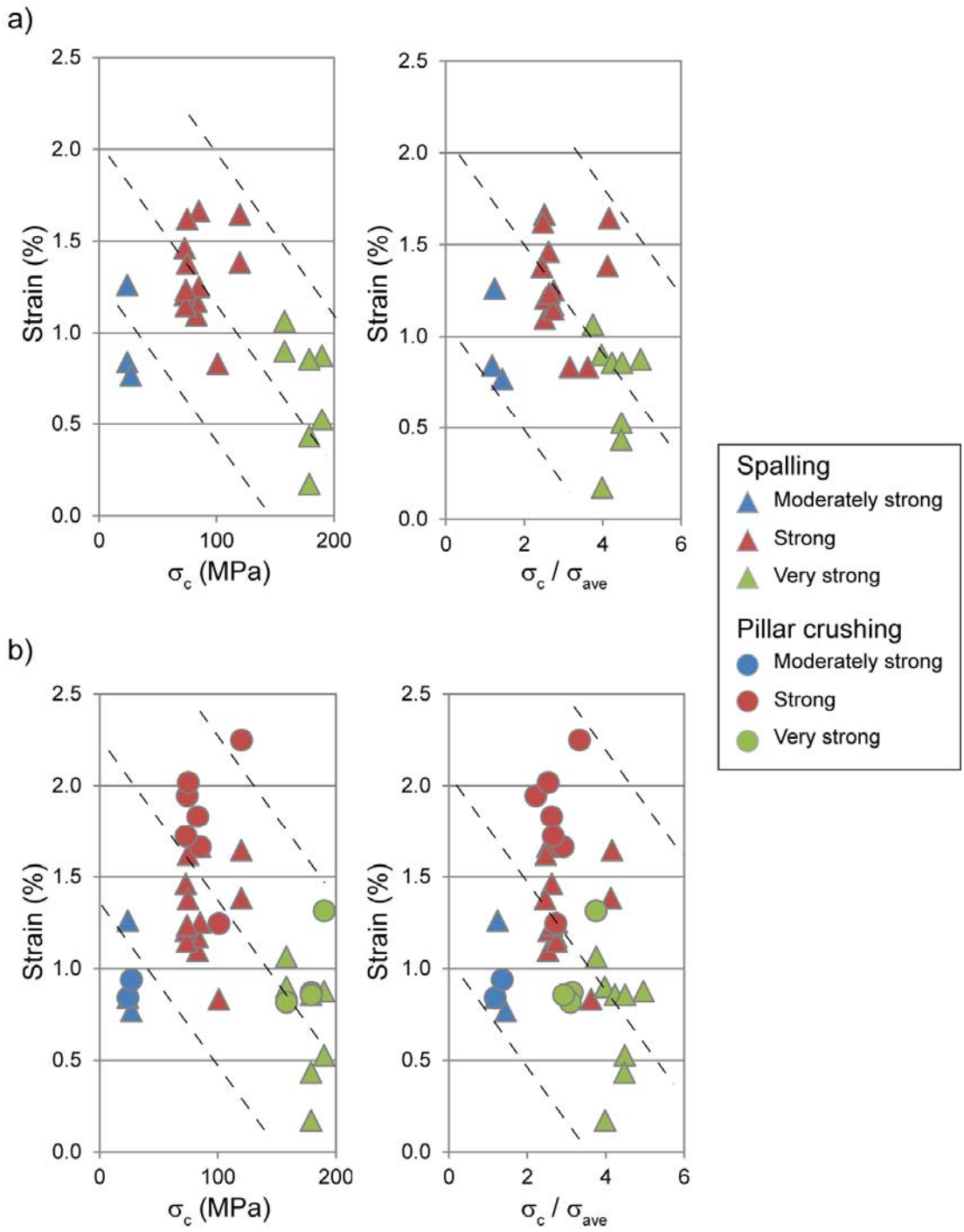

Figure 7.22 a) Strain at the spalling failure for the scaled-down unsupported tunnels, b) a comparison of strain at the spalling failure and pillar crushing for the scaled-down unsupported tunnels.

7.6 Unsupported Tunnel Test Summary

A number of empirical relationships have been determined for the onset of spalling and pillar crushing for unsupported scaled-down tunnels drilled into three different material types. The data suggest that a distinctive ratio of compressive strength to induced stress can be determined for the different stages of progressive failure (i.e., spalling at the tunnel boundaries and pillar crushing adjacent to the tunnels). The relationship appears to be correlated the compressive strength of the materials. The results from laboratory scale tests compare well with data from full scale excavations from a number of mine pillars suggesting that the onset of spalling and pillar crushing are scale independent.

Chapter 8

Ground Support Performance

8.1 Introduction

It is well established that ground support cannot prevent rock mass failure. However, in practice, ground support is used in an attempt to maintain serviceability of excavations after rock mass failure. The author has developed unique techniques to install reinforcement in boreholes drilled radially in the rock block from within the scaled down tunnels to simulate integrated rock bolt mesh and shotcrete support. The laboratory experiments allow assessment and relative comparisons of different scaled-down ground support schemes.

8.2 Ground Support Test Configurations

Various ground support schemes were implemented into the 200 mm diameter strong sandstone tunnels. The details of the materials comprising the ground support elements were described in Chapter 3.

8.2.1 Patterns Tested

For testing purposes, the 200 mm diameter tunnels were assumed to represent a 4 m full size tunnel. Given that a typical full scale pattern would typically consist of 1.2 m rings of bolts. The distance between the rings within the experiments were set to 67 mm. Similarly the rock bolt collar distance (within a ring) in practice can be about 1.5 m, so that the bolts were set at 80 mm apart within the rings of the scaled down tunnel. Similarly a 5 mm thick shotcrete layer is meant to represent a full scale 100 mm thick layer. The length of the bolts was set to 50 mm or equivalent of 1 m in full scale. This is short by industry standards but still acceptable here on the failure investigated was at the surface of the scaled down tunnels. The 200 mm diameter tunnel had limitations on the length of drilling that could be undertaken taking into account the dimensions of the drilling machine and space left for the drill bit. This is not considered serious matter as the failure investigated was related to surface support. Figure 8.1 and Figure 8.2 show square and staggered bolting style patterns respectively. The variety of ground support configurations used in this experiment are summarised in Table 8.1. Ground support application is described in order of the installation sequence. For

example, SC-Mesh-Bolt, means that shotcrete (SC) was sprayed first, followed by mesh and bolts.

The scaled down tunnel had 3 reinforcement rows with bolts installed in 8 directions. Bolts were installed either in a staggered or in a square pattern (see Figure 8.1 and Figure 8.2). As described earlier, the rock bolts were fully encapsulated by adhesive and tightened by a nut with three washers (Figure 8.3). Four different types of mesh style were installed to compare their characteristics and performance. In all cases, one piece of mesh sheet (640 mm x 200 mm) was installed inside of the tunnel and overlapped at the bottom fixed by rock bolts (Figure 8.4). Shotcrete mix was sprayed using a pneumatic spray gun. As standard, a 5 mm thickness of shotcrete layer was applied all over the tunnel surface. When shotcrete was applied twice, the second layer thickness was set as 3 mm. The shotcrete mix was cured in average 7 days until it reached the designed strength (approximately 3.5 MPa).

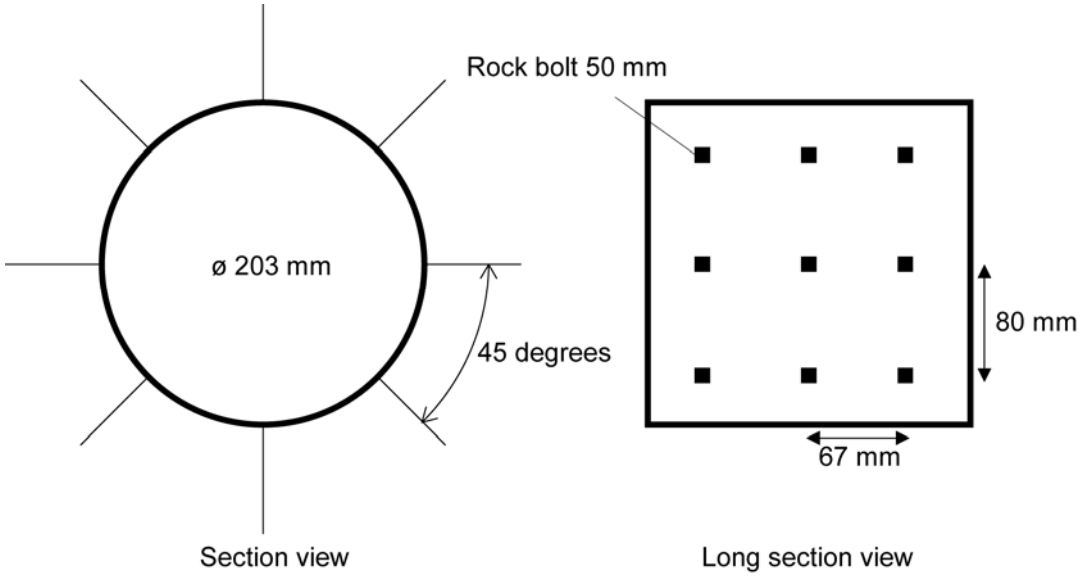

Figure 8.1 Square bolting style pattern.

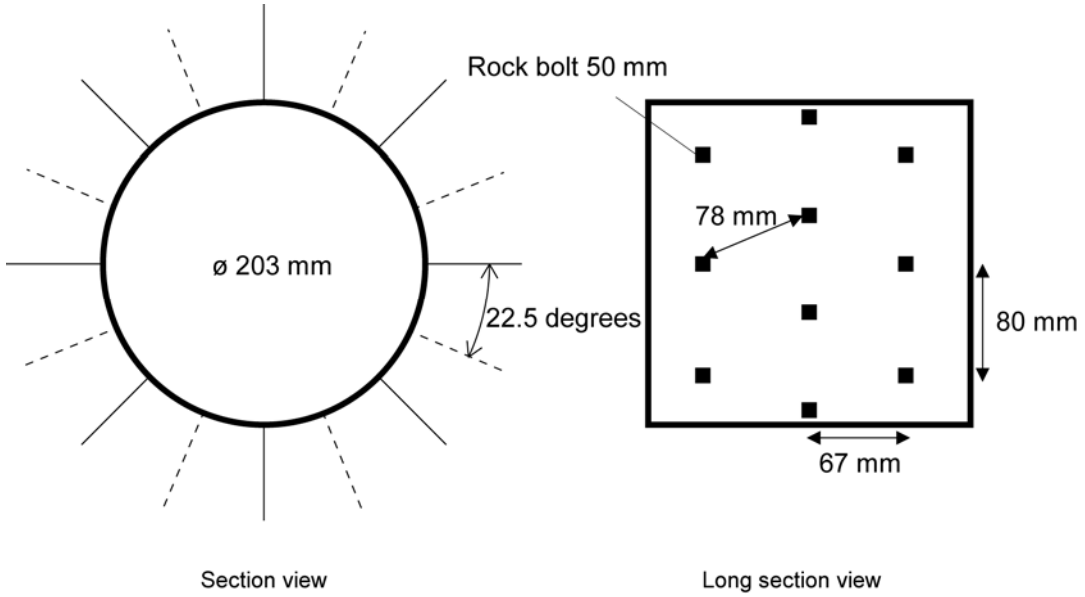

Figure 8.2 Staggered bolting style pattern.

Table 8.1 Ground support configuration summary.

Specimen No.	Ground support scheme tested	Block material UCS (MPa)	Bolting pattern	Mesh type
1	Mesh-Bolt	88	Staggered	Stiff
2	SC-Mesh-Bolt	107	Staggered	Stiff
3	Mesh-Bolt	87	Square	Stiff
4	Mesh-Bolt-SC	85	Square	Stiff
5	Mesh-SC-Bolt	79	Square	Wide
6	Mesh-Bolt-SC	87	Square	Wide
7	Mesh-SC-Bolt	88	Square	Flex
8	Mesh-Bolt-SC	84	Square	Chain
9	Mesh-Bolt	78	Square	Chain
10	SC-Mesh-Bolt	68	Square	Chain
11	SC-Mesh-Bolt	76	Square	Chain
12	SC-Mesh-Bolt*	83	Square	Chain
13	Mesh-SC-Mesh-Bolt	83	Square	Chain (2 layers)
14	SC-Mesh-SC-Mesh-Bolt	88	Square	Chain (2 layers)
15	SC-Mesh-SC-Mesh-Bolt*	91	Square	Chain (2 layers)

* Load was held for 30 minutes prior to any failure for convergence measurement.

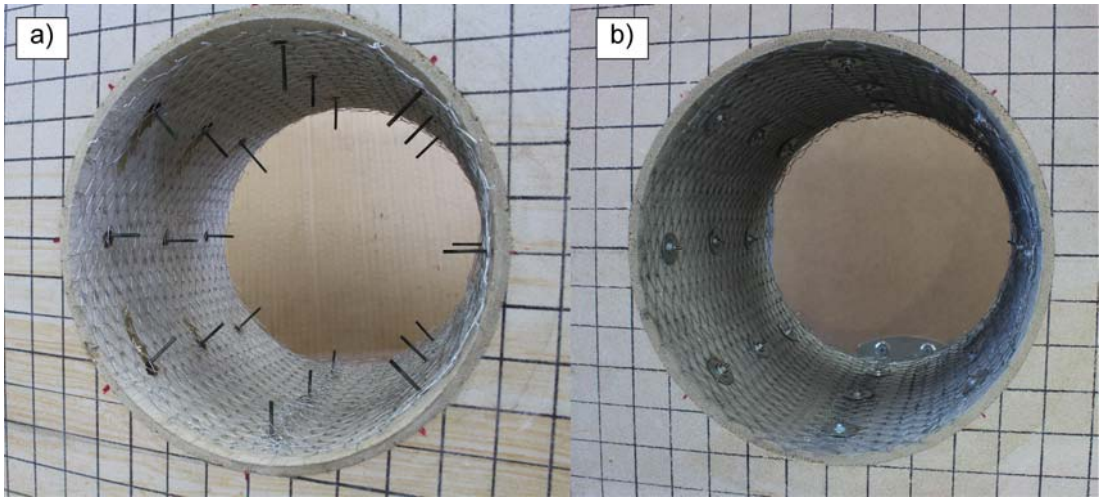

Figure 8.3 An example of rock bolt installation a) full encapsulation b) fixation by nut.

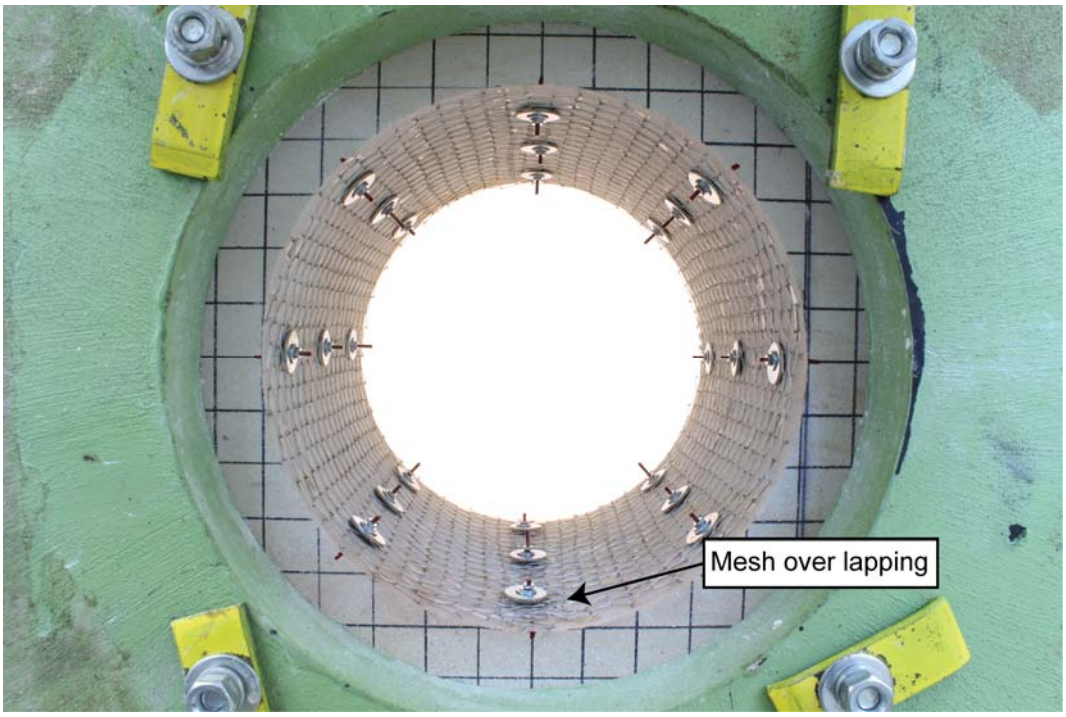

Figure 8.4 Mesh overlap at the tunnel bottom.

8.3 Ground Support Stabilisation

To start the analysis, an unsupported tunnel test result is shown here, and compared with one of the ground support test result in order to examine to the ground support performance. A 200 mm diameter unsupported strong sandstone test result (UCS 76

MPa) was compared with ground support scheme composed of the chain link mesh and rock bolts installed using a square pattern (Specimen No.9) and material strength of 78 MPa .

The chain link mesh was applied onto the tunnel surface and fixed using 50 mm long rock bolts elements.

Figure 8.5 shows the comparison of the tunnel behaviour of the unsupported tunnel with respect to the tunnel supported with chain link mesh and rock bolts. In both cases, material ejection was observed when spalling occurred on the tunnel sidewalls. In unsupported tunnel, damage occurred widely on tunnel sidewalls (Figure 8.5a). When a reinforcement system was installed, failure occurred between rock bolt spacing (Figure 8.5b). With ground support, the material ejection only experienced in one side, with ejection velocity at 4.2 m/s. The ejection velocity of the unsupported rock failure was 9.0 m/s. The benefits of a minimal ground support scheme, such as bolts and mesh was clearly seen. The tunnel showed more controlled behaviour with reinforcement (Figure 8.6). It can be also seen that the ejected material was held by the chain link mesh. The damage region was contained between rock bolts.

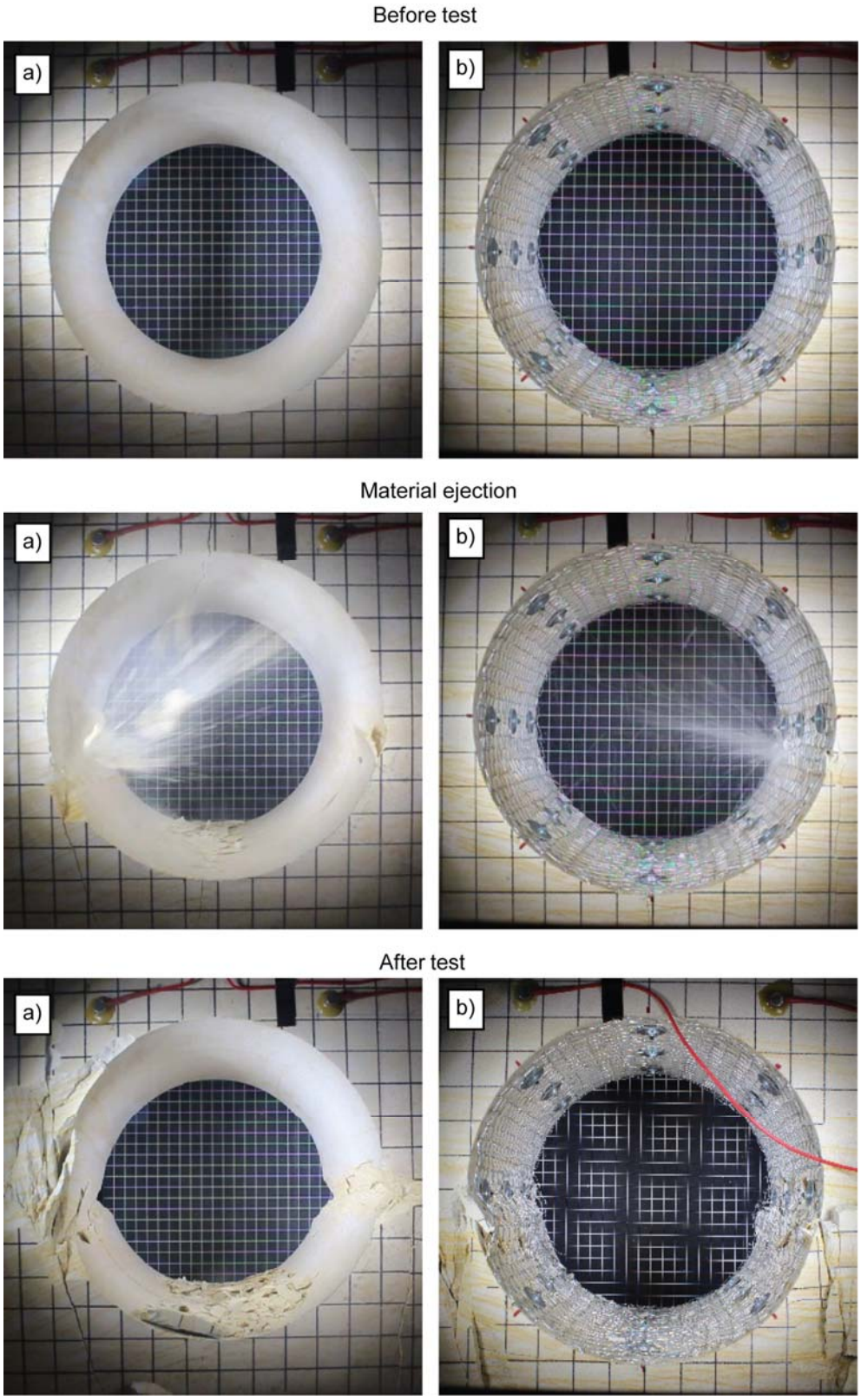

Figure 8.5 Observation of failure mechanism of a) unsupported tunnel b) chain link mesh and rock bolt (square pattern) support (Specimen No.9).

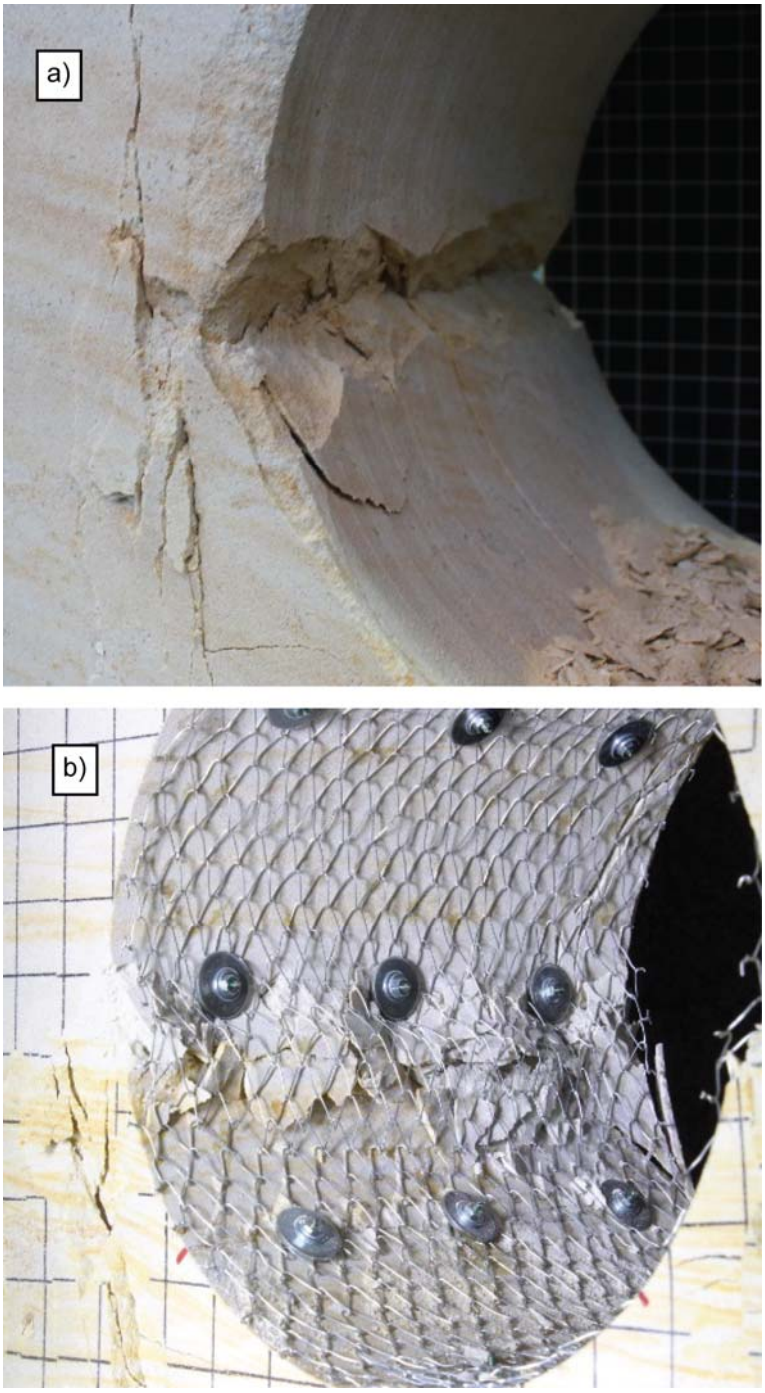

Figure 8.6 Sidewall after failure a) unsupported tunnel b) chain link mesh and rock bolt (square pattern) support (Specimen No.9).

Figure 8.7 shows the load displacement relationship from both the unsupported tunnel test and the reinforced tunnel test with the accumulated AE activities monitored. Both data show a similar trend, seismic activities increased at spalling and they showed a

sharp growth at the onset of pillar crushing. The load bearing capacity increased slightly with the ground support application (Figure 8.7b). Specially after spalling, which occurred at similar loads for both experiments. The reinforced tunnel gained and additional 17 % load compared with the unsupported tunnel. A vertical crack created during pillar crushing intersected into a rock bolt and causing a shear failure (Figure 8.8). Following shear failure immediately a significant load drop off and vertical shear movement was experienced within the pillar.

Table 8.2 shows a ratio of the intact rock strength and the stress at failures for spalling and pillar crushing. Similar to the unsupported tunnel test result analysis, the maximum tangential stress at spalling was calculated using the Kirsch solution. The average pillar stress was used to calculate the stress induced failure at pillar crushing. Since both specimens had a similar strength, spalling occurred at a similar induced stress. The largest difference was seen more obvious at pillar crushing. Reinforcement can be seen to increase the post spalling strength of the specimen.

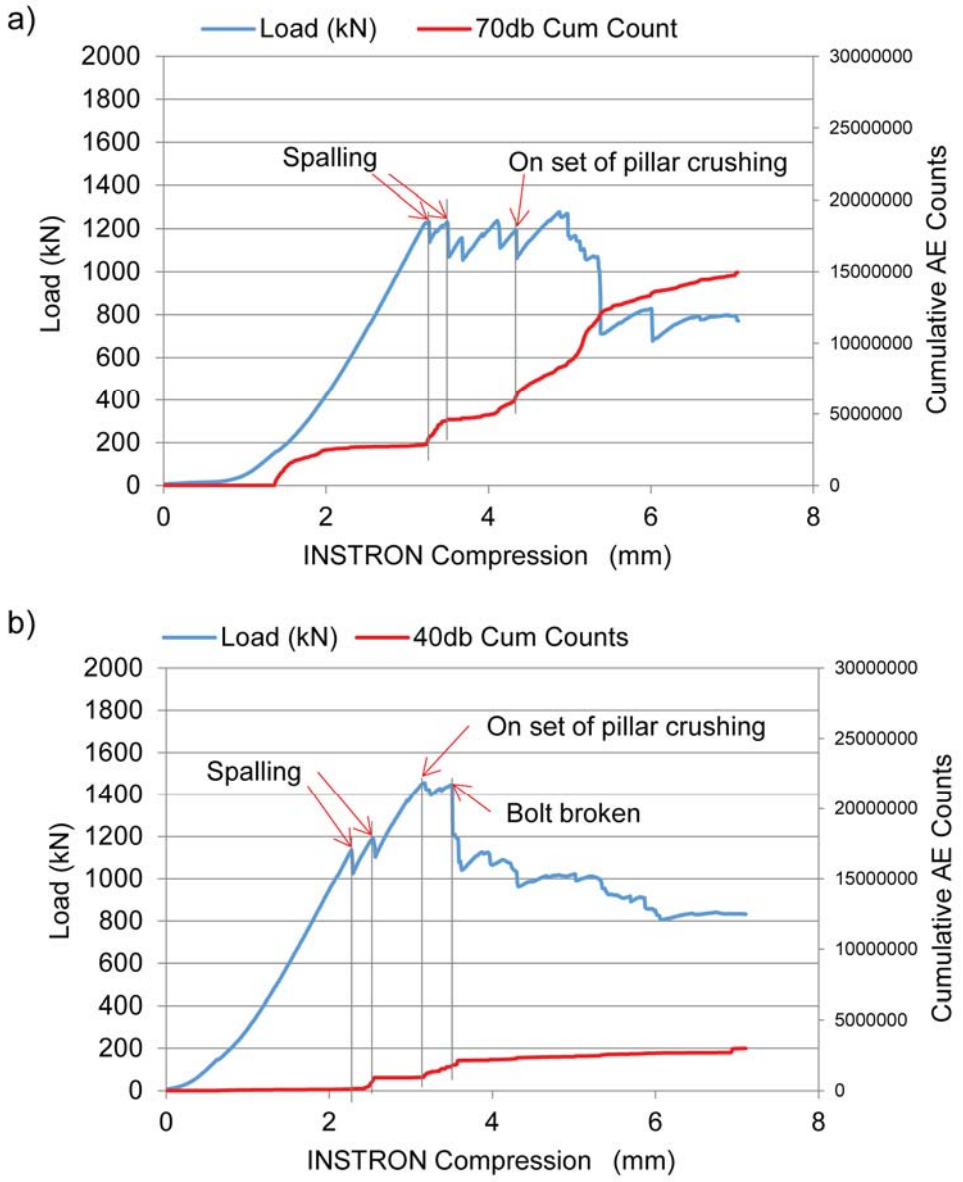

Figure 8.7 Load displacement relationship with recorded AE activities a) unsupported tunnel b) reinforcement and chain link support (Specimen No.9).

Figure 8.8 Rock bolt shear failure (after test).

Table 8.2 Comparison of the stress and strength ratio at failure with unsupported tunnel test result.

Specimen No.	UCS (MPa)	σ_c/σ_{max} at spalling	σ_c/σ_{ave} at pillar crushing	Ejection velocity (m/s)
Unsupported	76	1.6-1.7	2.5	4.2-9.0
Reinforced (No.9)	78	1.8	2.1	4.2

8.4 Comparison for Similar Ground Support Schemes

Ground support tests were repeated to examine the reliability of the test results. Similar ground support schemes were implemented with strong sandstone specimens which had different uniaxial compressive strength.

The ground support scheme consisted of a 5 mm thick shotcrete layer covered by chain link mesh with rock bolts in square pattern (Specimen No. 10 to 12 in Table 8.1). A shotcrete layer was initially sprayed onto a tunnel surface and covered by a 640 mm x 200 mm chain link mesh sheet. After a surface support system installation, 24 rock bolts were installed. Figure 8.9 shows the ground support scheme and the specimen

ready for testing (Specimen No.10). The uniaxial compressive strength for each specimen were 68, 76 and 83 MPa respectively.

During the testing of Specimen No. 12, the loading was held at 1000 kN for 30 min to conduct a convergence measurement. Loading was restarted after the measurement and specimens were loaded until a vertical compression reached 7 mm.

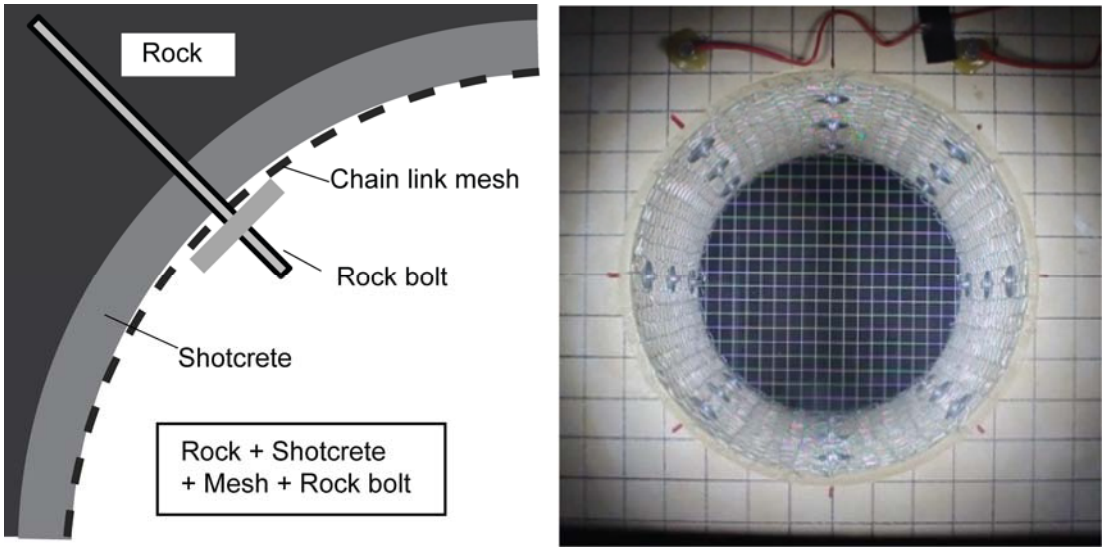

Figure 8.9 Ground support scheme consisting of an initial 5 mm shotcrete layer followed by chain link mesh and rock bolt reinforcement.

Figure 8.10 shows the three specimens during the loading processes. Spalling damage occurred between the rock bolt area and the broken shotcrete slabs were contained within the chain link mesh. Violent ejection was seen in all the cases; however, materials were ejected mostly from the edge of the tunnel walls near from specimen face rather than within the tunnel sidewalls. Measured ejection velocity was 6.0 m/s, 7.4 m/s and 7.1 m/s respectively. Specimen No. 10 (Figure 8.10a) had the lowest rock strength among three tests. When pillar crushing occurred, one rock bolt was broken by shear failure on the left side. In Specimens No.10 and 12, the rock bolts remained in place even after surface and pillar failure occurred (Figure 8.10b and c).

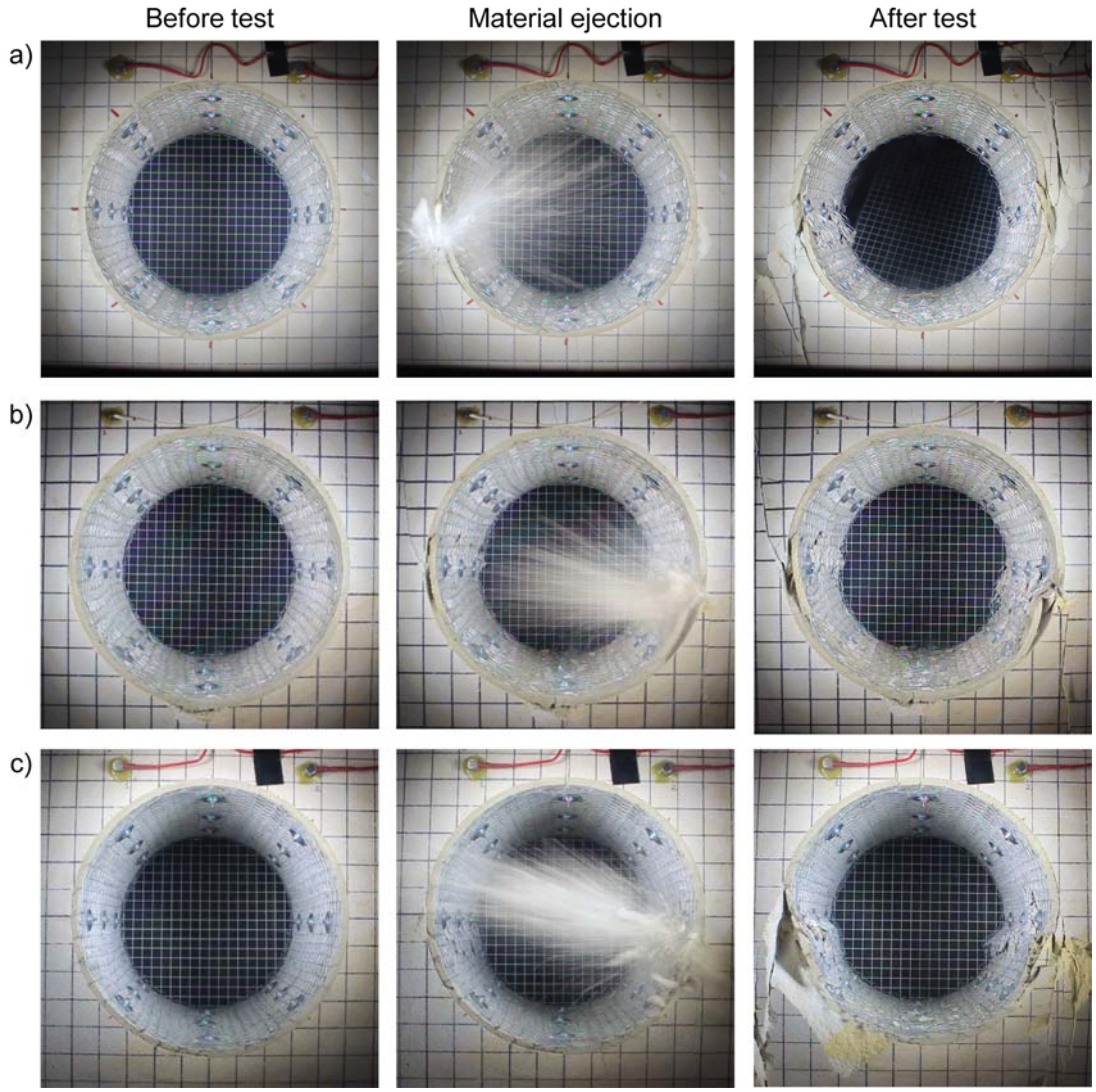

Figure 8.10 Comparison with the same ground support configuration tests, a) 68 MPa (Specimen No.10) b) 76 MPa (Specimen No.11) and c) 83 MPa (Specimen No.12).

Figure 8.11 shows the load displacement curves from the three test results with accumulated AE activities. The data shows that very little Acoustic Emission is experienced up to the spalling failure. This complicates any use of AE data on a prediction of failure. A combined plot of the three load-displacement data is also shown in Figure 8.12. Although Specimen No.10 (Figure 8.11a) had the lowest uniaxial compressive strength among the three specimens, spalling occurred at 1500 kN, which is a similar load level compared with Specimen No.12 (UCS 83 MPa,

Figure 8.11)). The strength and stress ratio for spalling and pillar crushing are shown in Table 8.3. Although slightly different loading performance were seen in the three specimens, the ground support performance was very similar.

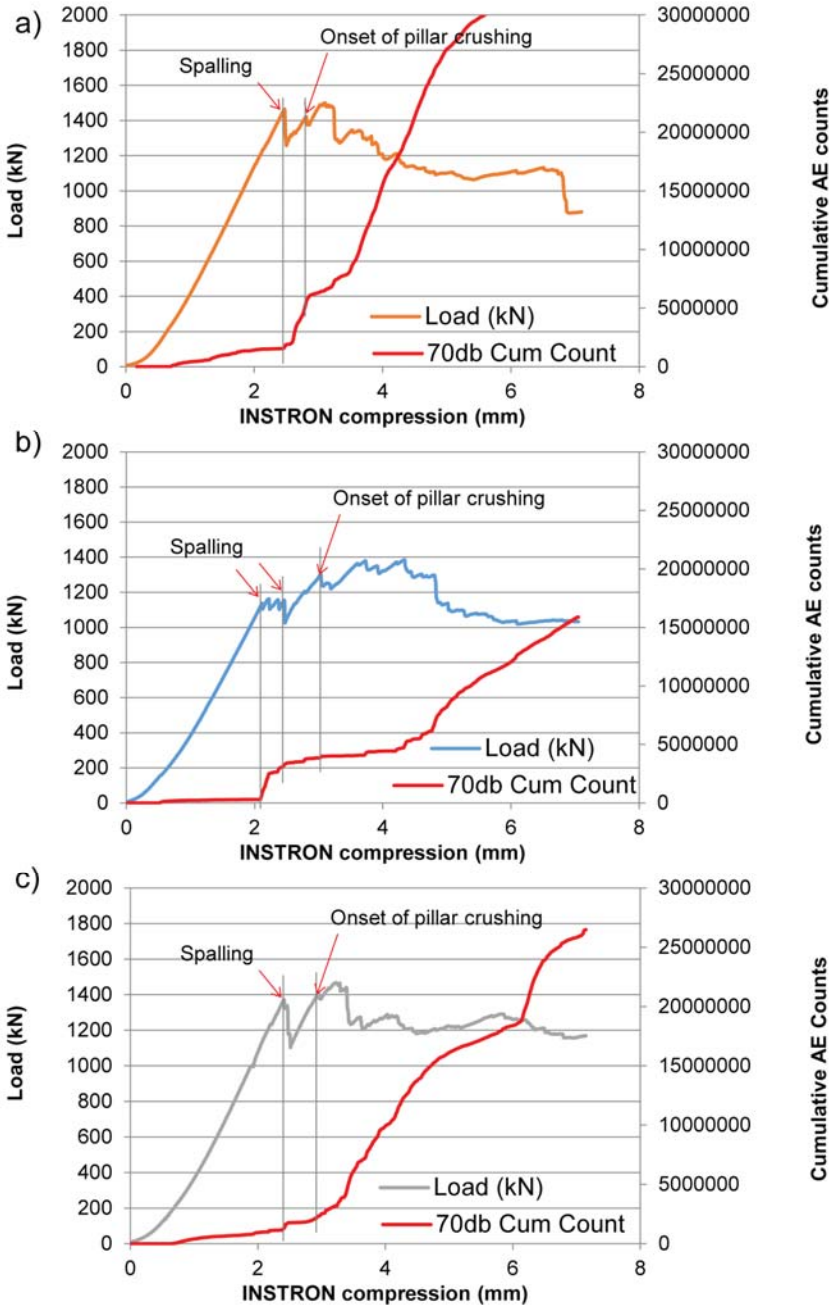

Figure 8.11 Load relationship curve of the same ground configuration test with AE data a) 68 MPa (Specimen No.10) b) 76 MPa (Specimen No.11) and c) 83 MPa (Specimen No.12).

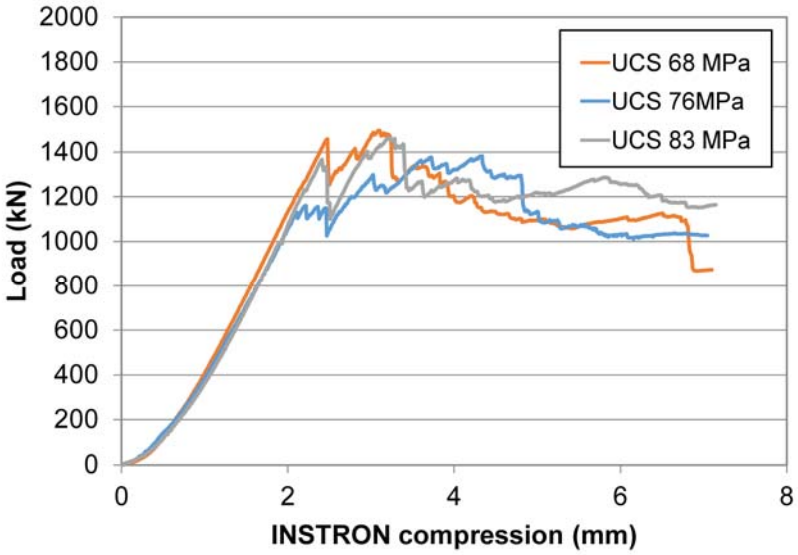

Figure 8.12 Combined load-displacement curve.

Table 8.3 Strength to stress ratio at failure for specimens having the same ground support scheme.

Specimen No.	UCS (MPa)	σ_c/σ_{max} at spalling	σ_c/σ_{ave} at pillar crushing	Ejection velocity (m/s)
10	68	1.2-1.3	1.9	6.0
11	76	1.7-1.8	2.3	1.8-7.4
12	83	1.6-1.7	2.4	7.1

8.5 Comparison of Bolting Pattern

Two different rock bolting patterns were implemented into similar rock strength specimens (Figure 8.13). In both cases, 50 mm long mild steel rock bolts were installed radially in three rows.

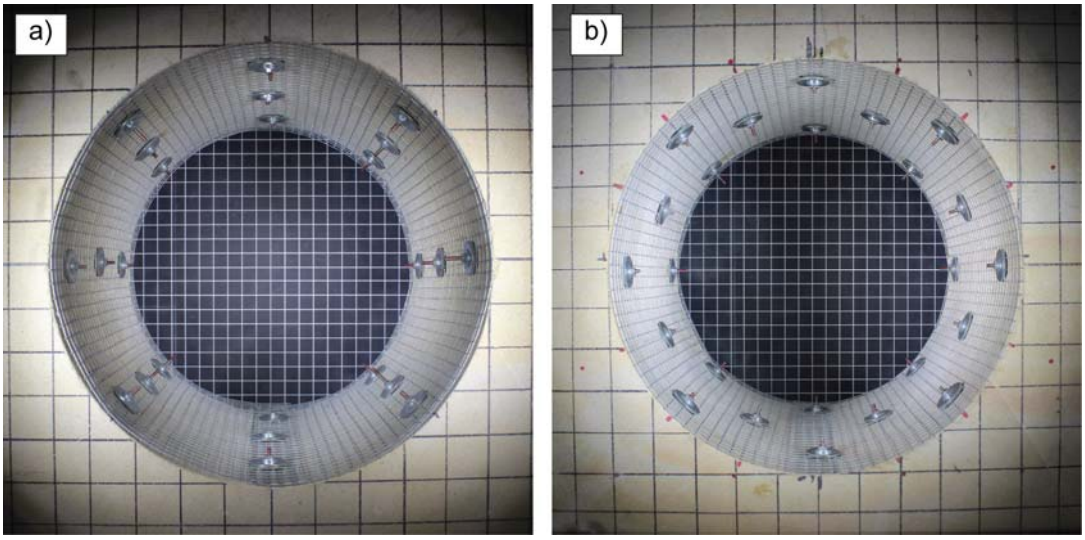

Figure 8.13 Two different bolting pattern a) square pattern (Specimen No.3) b) staggered pattern (Specimen No.1).

In both Specimen No. 1 and 3, a stiff welded mesh type was installed. A total of 24 rock bolts were installed within the square and staggered pattern respectively. The test results were examined to compare the performance of changing bolting pattern (Figure 8.14).

At spalling failure, horizontal cracks propagated in the tunnel walls with resulting broken slabs ejected dynamically. In the case of the square pattern, the horizontal crack propagated along the entire tunnel wall slightly below a row rock bolts (Figure 8.15a). The staggered pattern did not allowed the same level of crack propagation (Figure 8.15b). As can be seen, rock bolts disturbed the crack propagation process (Figure 8.15). Ejected velocity at spalling was 3.3-4.3 m/s for the square bolting pattern and 1.3-3.9 m/s for the staggered bolting pattern. As the tunnel deformed, the stiff welded mesh bulked at the damaged area.

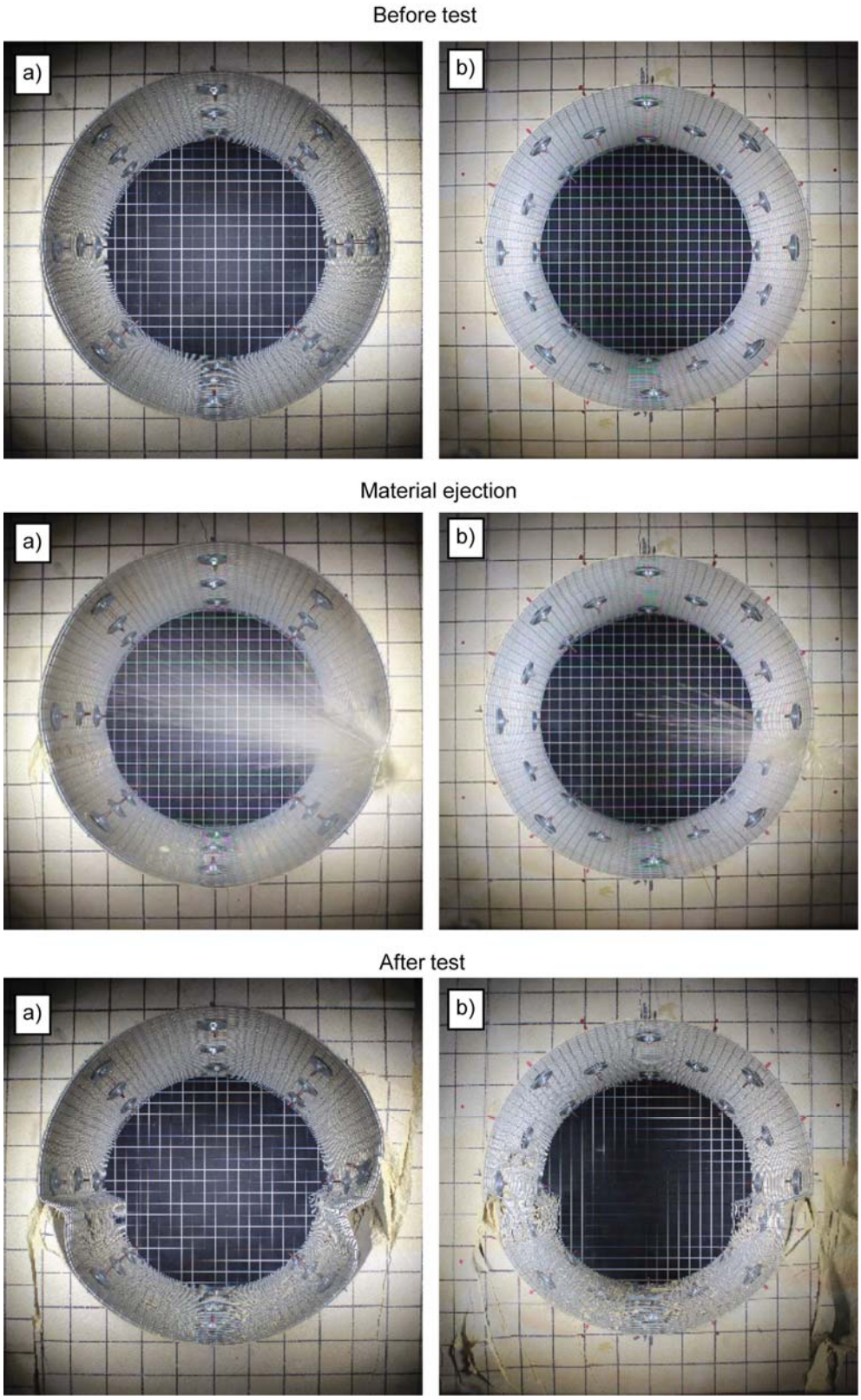

Figure 8.14 Performance comparison with different bolting pattern a) square pattern (Specimen No. 3) b) staggered pattern (Specimen No.1).

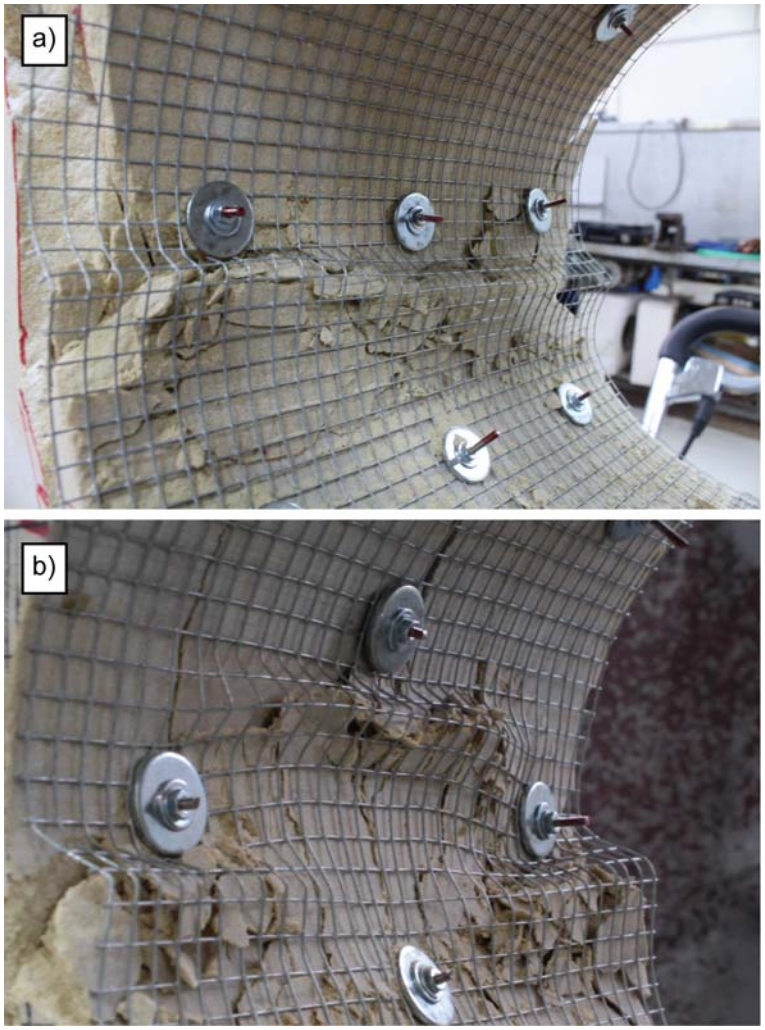

Figure 8.15 Failures on tunnel sidewall a) square bolting pattern b) staggered bolting pattern.

Figure 8.16 shows the load displacement curve for two different bolting patterns. A similar response was determined. However, more violent unloading occurred with the spalling at the square pattern. There was no clear difference in the strength to stress ratio at spalling and pillar crushing failures (Table 8.4).

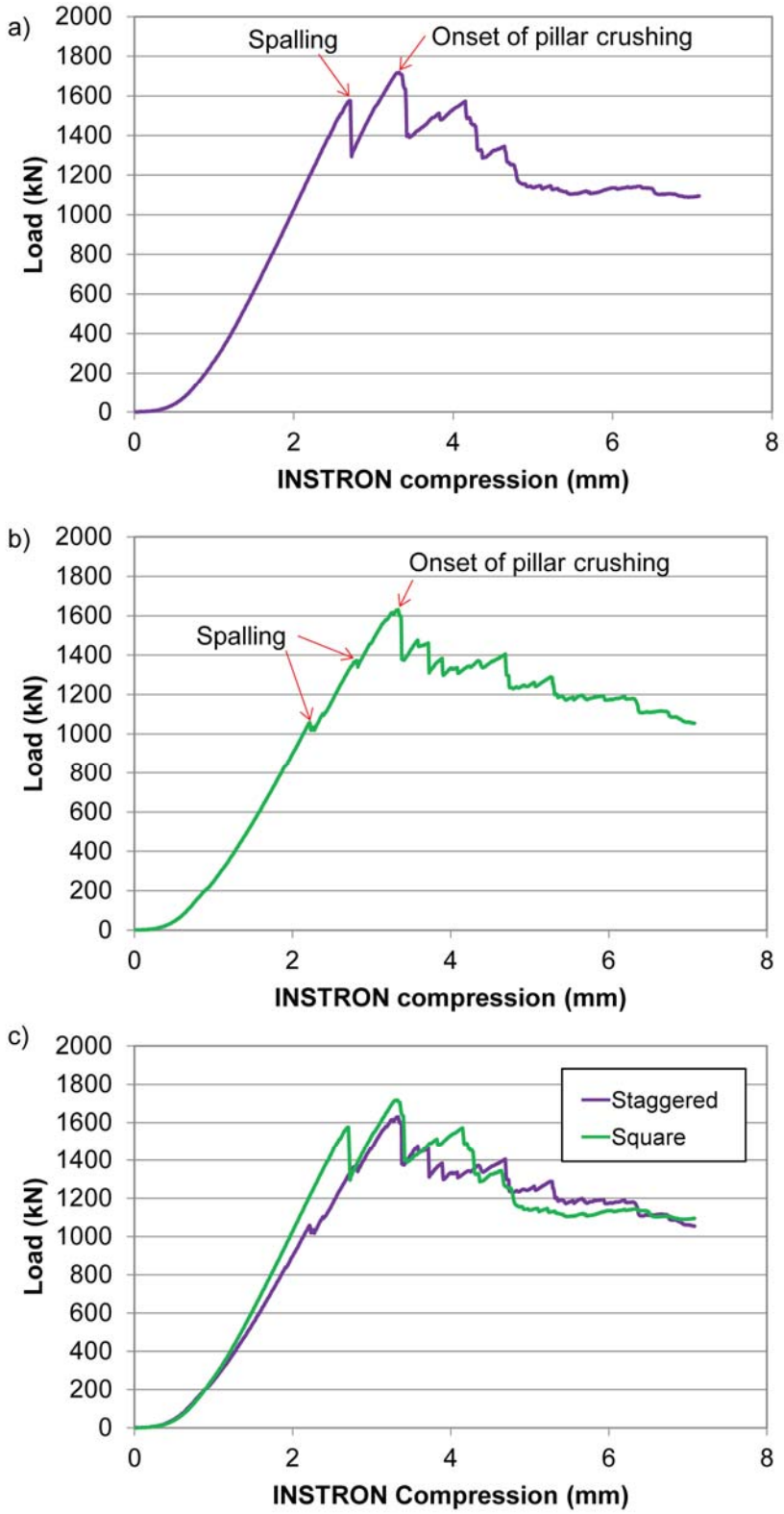

Figure 8.16 Load displacement of a) square pattern (Specimen No. 3) b) staggered pattern (Specimen No.1) c) combined plot.

Table 8.4 Strength to stress ratio at failure of different bolting pattern.

Specimen No.	UCS (MPa)	σ_c/σ_{max} at spalling	σ_c/σ_{ave} at pillar crushing	Ejection velocity (m/s)
3 (square)	87	1.5-1.6	2.0	3.3-4.3
1 (staggered)	88	1.7-2.2	2.2	1.3-3.9

8.6 Comparison of Mesh Materials

As mentioned in Chapter 3, four different types of mesh were used; stiff welded mesh, Wide-aperture stiff mesh, flexible mesh and chain link mesh. Each mesh has a different support characteristic and the performance was compared as a part of an integrated ground support scheme.

8.6.1 Stiff welded vs Chain Link

A combination of mesh and rock bolts (square pattern) were installed in Specimen No.3 and 9 (see Table 8.1). Stiff welded mesh and chain link mesh were applied and fixed by rock bolts onto the tunnel surfaces.

The major difference attributed to the mesh materials was seen in the tunnel sidewalls after failure (Figure 8.17). In Specimen No.3, the stiff welded mesh buckled between the bolting spaces and very little interaction with rock material was observed (Figure 8.17a). On the other hand, when spalling occurred, the chain link mesh deformed holding the detached materials (Figure 8.17b). The flexibility of chain link mesh enabled a continuous retention with a better load transfer to the reinforcement. Internal damage during the loading process was minimised compared with the result using stiff welded mesh.

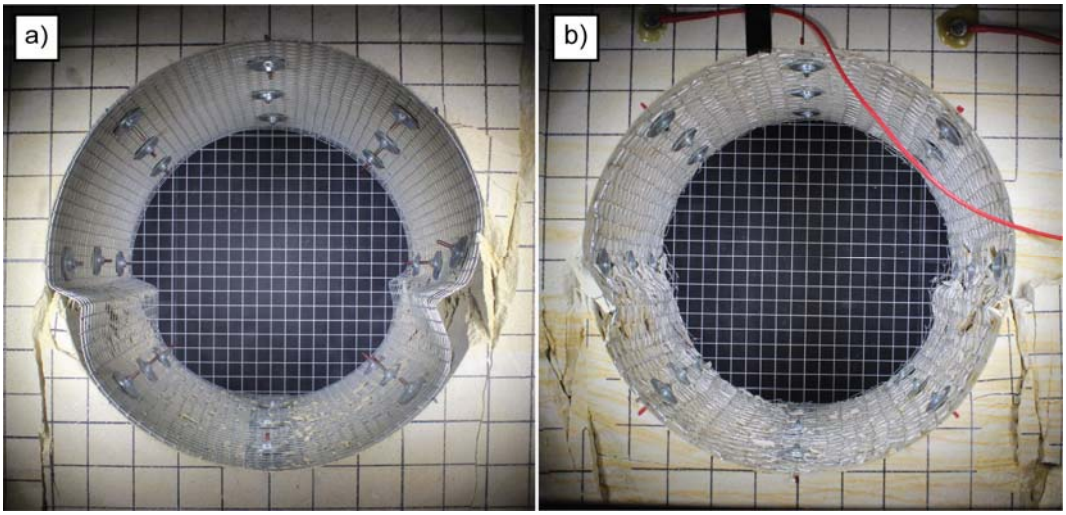

Figure 8.17 Failure on tunnel sidewalls a) stiff welded mesh (Specimen No.3) b) chain link mesh (Specimen No.9).

Figure 8.18 shows the load-displacement curve for the different mesh materials. Although more violent unloading occurred with the stiff welded mesh, there was no clear difference in the strength to stress ratio at spalling and pillar crushing failure (Table 8.5).

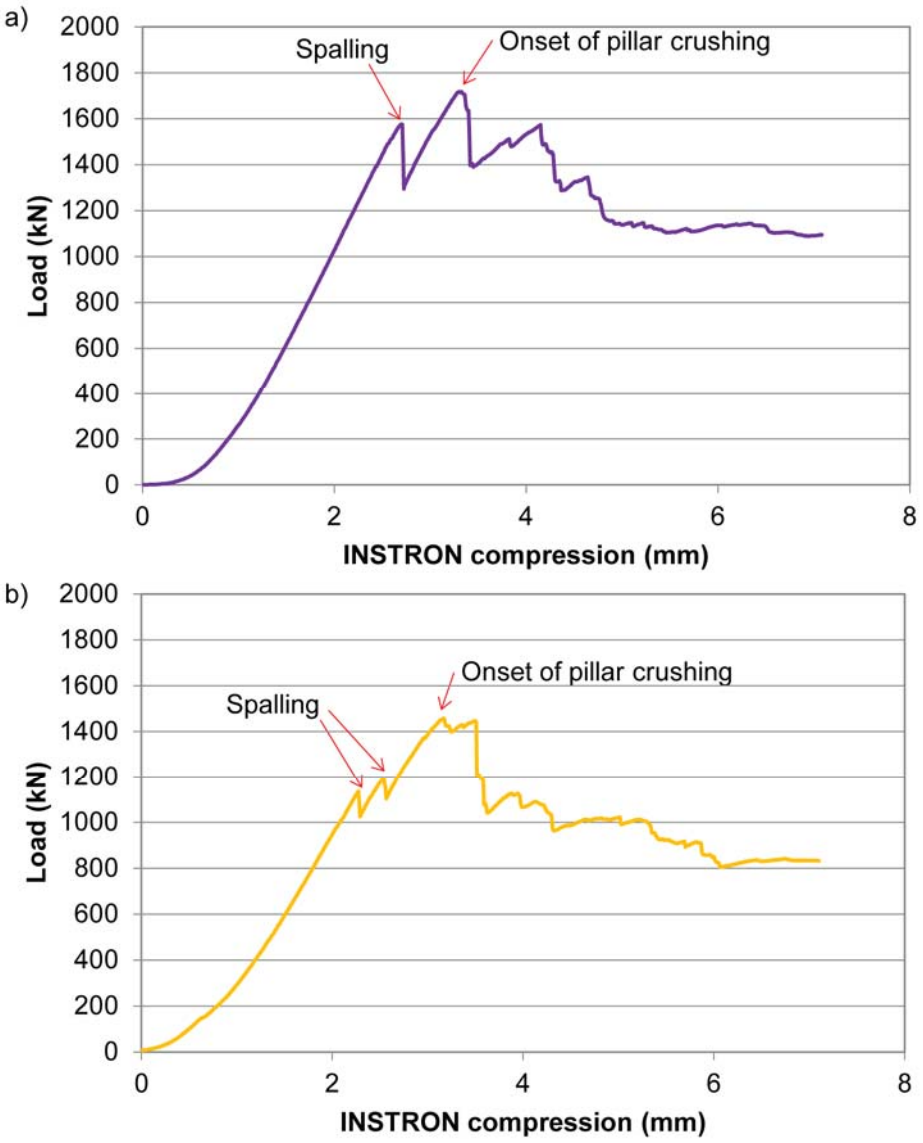

Figure 8.18 Load-displacement curve a) stiff welded mesh b) chain link mesh.

Table 8.5 Strength to stress ratio at failure of different mesh material.

Specimen No.	UCS (MPa)	σ_c/σ_{max} at spalling	σ_c/σ_{ave} at pillar crushing	Ejection velocity (m/s)
3 (stiff welded)	87	1.5-1.6	2.0	3.3-4.3
9 (chain link)	78	1.8	2.1	4.2

8.6.2 Mesh Material Comparisons with a Shotcrete Layer

Furthermore, the mesh performance was also examined in combination with a shotcrete layer.

8.6.2.1 Comparison of Flexible Mesh and Wide-aperture stiff mesh

A 5 mm shotcrete layer was applied over flexible and wide-aperture stiff mesh respectively in specimens No.5 and 7 as shown in Figure 8.19. In both cases, rock bolts were installed in a square pattern after the shotcrete application.

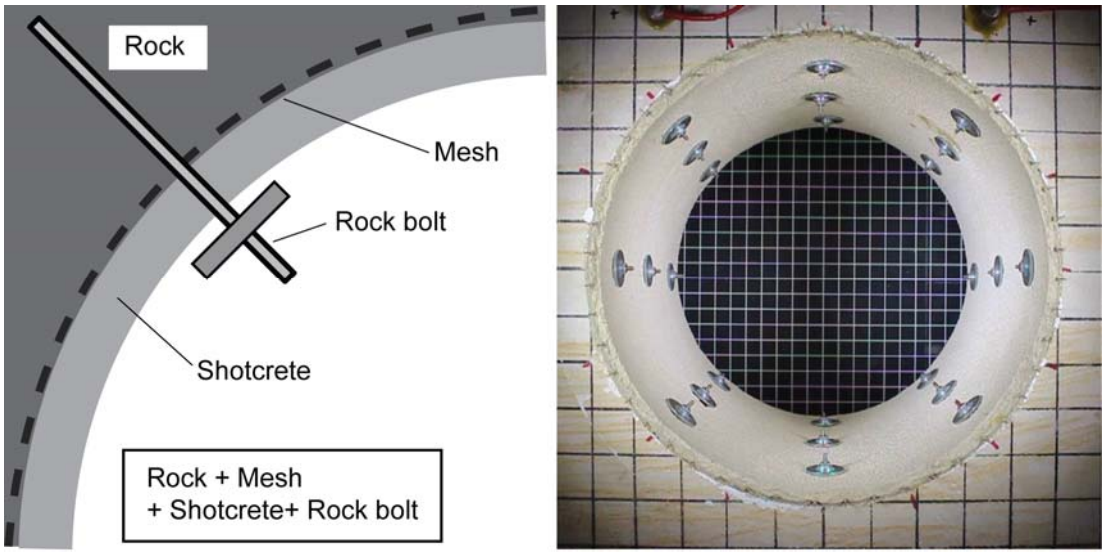

Figure 8.19 Ground scheme consisting of mesh, shotcrete and rock bolt application.

Figure 8.20 shows tunnel failure progress with two different mesh materials. Both test results showed that the stiffness of the mesh embedded within the shotcrete also contribute to the failure. Ejection velocity at spalling were 6.6 m/s with the flexible mesh and 6.1 m/s for wide-aperture stiff mesh. At spalling, the flexible mesh buckled locally between rock bolts (Figure 8.20a). On the other hand, the wide aperture mesh buckled at the welded point and material ejection occurred simultaneously along tunnel side walls (Figure 8.20b). Furthermore the continuous surface failure was driven by mesh during loading. The flexible mesh showed less bucking after failure,

however, both mesh materials induced shotcrete failure and broken materials were ejected and fell off to the tunnel bottom. The experiment showed that shotcrete spalling remains a distinct possibility when mesh reinforced shotcrete is used.

Figure 8.21 shows the load-displacement curve for two mesh material test. As described before, there was no distinctive difference between the two surface support systems (Table 8.6).

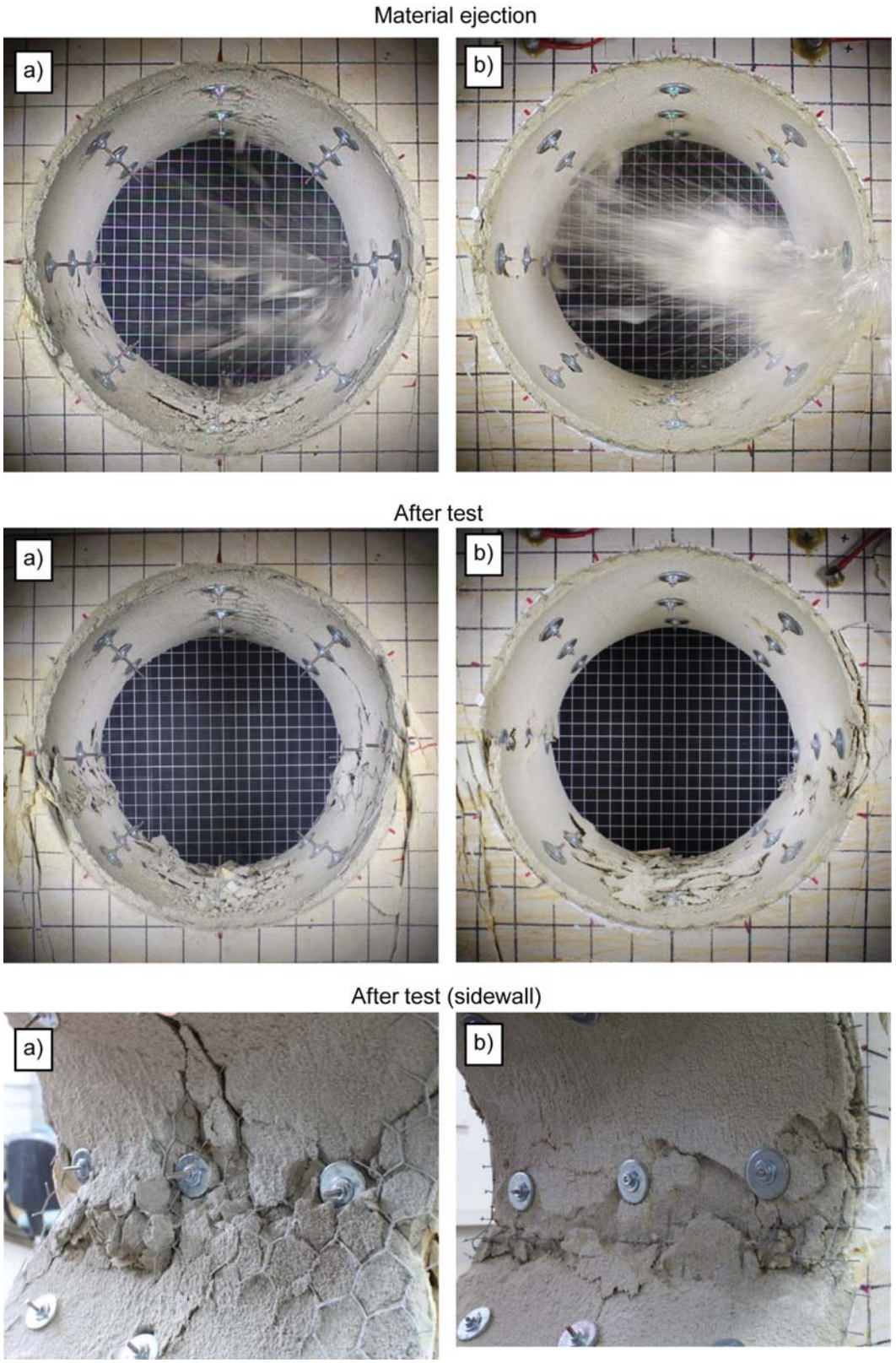

Figure 8.20 Comparison of failure mechanisms a) flexible mesh (Specimen No.5) b) Wide-aperture stiff mesh (Specimen No.7).

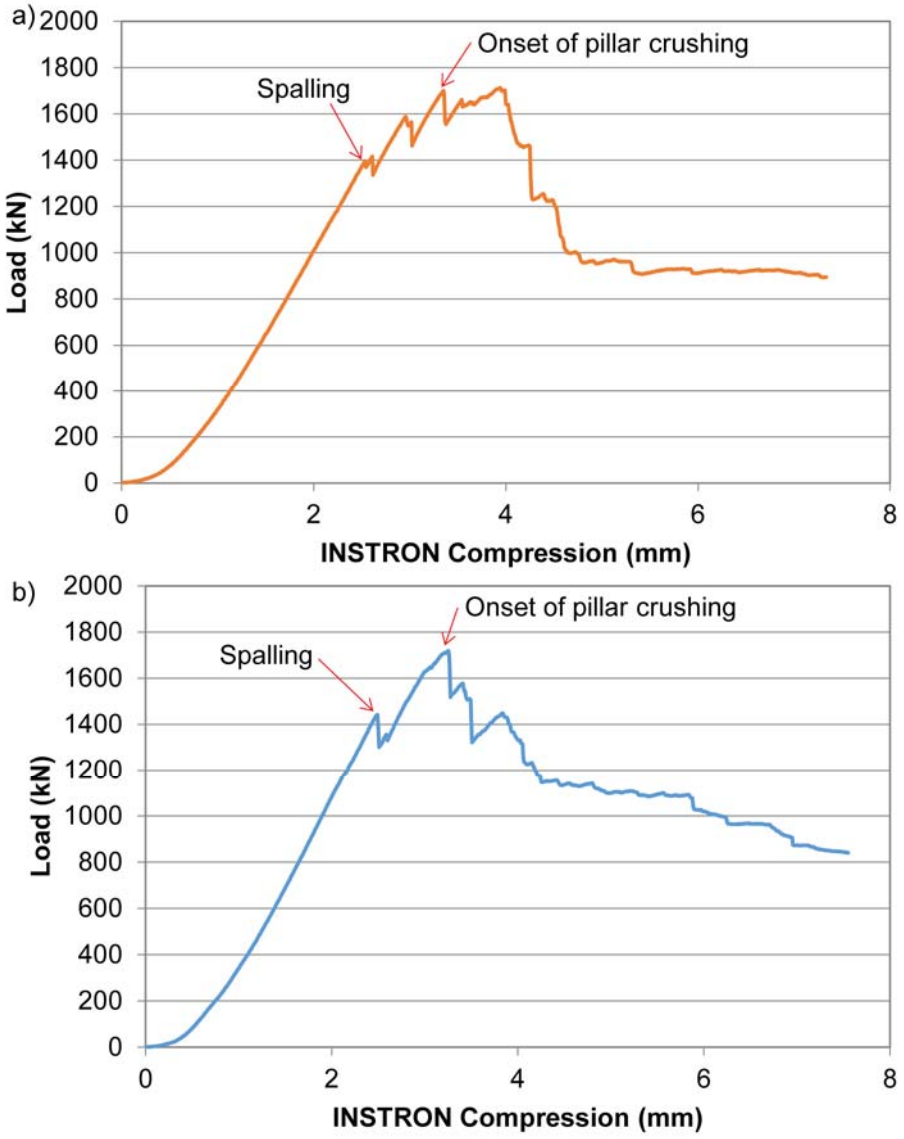

Figure 8.21 Load-displacement curve a) flexible mesh b) Wide-aperture stiff mesh.

Table 8.6 Strength to stress ratio at failure of different mesh material at failures.

Specimen No.	UCS (MPa)	σ_c/σ_{max} at spalling	σ_c/σ_{ave} at pillar crushing	Ejection velocity (m/s)
5 (wide)	79	1.4-1.5	1.8	6.1-6,2
7 (flexible)	88	1.6-1.7	2.1	1.9-6.6

8.6.2.2 Comparison of Stiff Welded Mesh, Wide-aperture stiff mesh and Chain Link Mesh

Mesh material properties were further investigated within a shotcrete application. Stiff welded mesh, Wide-aperture stiff mesh and chain link mesh were installed with rock bolts and a shotcrete layer respectively (Specimen No.4, 6 and 8). Each mesh sheet was placed onto a tunnel surface and fixed by 24 rock bolts using a square pattern. A 5 mm thick shotcrete layer was applied afterwards embedding the mesh (Figure 8.22).

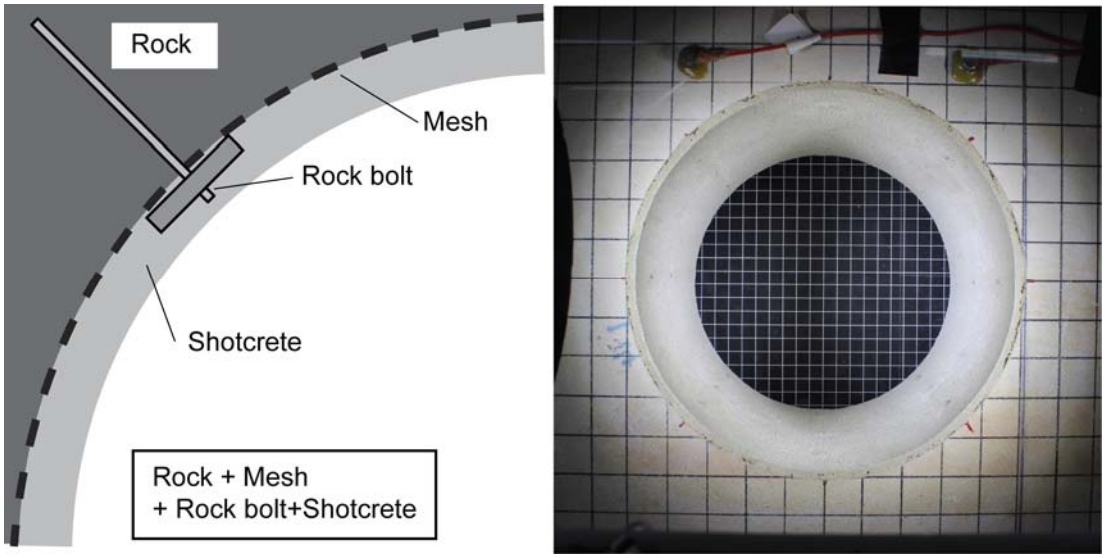

Figure 8.22 Ground support scheme consisting of mesh, rock bolts and shotcrete application.

Figure 8.23 compares the resulting failures mechanisms on a result of the different mesh materials. At spalling, large shotcrete panels were ejected by the stiff welded mesh (Figure 8.23a). Shotcrete panel ejection was also see in underground mine (Figure 8.24). Large slabs were ejected from the excavation surface. Figure 8.23b showed a similar behaviour. Shotcrete panel ejection was driven by the Wide-aperture stiff mesh. Once a shotcrete surface was cracked, broken shotcrete panels were ejected immediately along the entire tunnel wall. Meanwhile with the chain link, thin shotcrete slabs fell off gradually onto the tunnel bottom at spalling (Figure 8.23c). Material ejection was also observed when spalling cracks propagated through the entire sidewall, however, the chain link mesh deformed in accordance with the tunnel

wall convergence. Smaller shotcrete pieces failed at a low progressive and more controlled rate.

Figure 8.25 shows the tunnel sidewalls after failure. The welded mesh buckled underneath the shotcrete layer and this induced further damage on the tunnel surface (Figure 8.25a and b). Since the Wide-aperture stiff mesh was less stiff, it deformed largely in localized area, resulting on less damage area on the tunnel surface. The resulting damage area was smaller with the chain link mesh compared to the welded mesh cases (Figure 8.25c). It clearly shows that the flexibility of chain link mesh minimized the surface support damaged area. Figure 8.26 showed closer looks of the damage on the surface support both of scaled size excavation and full scale excavation. In both cases, chain link mesh was embedded within shotcrete layer and the interaction of surface support materials was seen at failure. Chain link mesh deformed with surface movement. The weight of the debris on the tunnel bottom after failure were measured to evaluate the amount of damage (Table 8.7). Debris mainly consisted of broken shotcrete panels, finer particles and tunnel surface slabs. The result also indicated that the stiffness of the mesh increased the damage on shotcrete. With chain link mesh, the amount of debris was half compared to the debris resulting from stiff welded mesh usage.

Figure 8.27 shows load displacement curve from the three mesh material tests. The three rock specimens have a similar rock strength and a reinforced shotcrete layer using different mesh materials experienced failures at similar rock strength and stress ratio (Table 8.8).

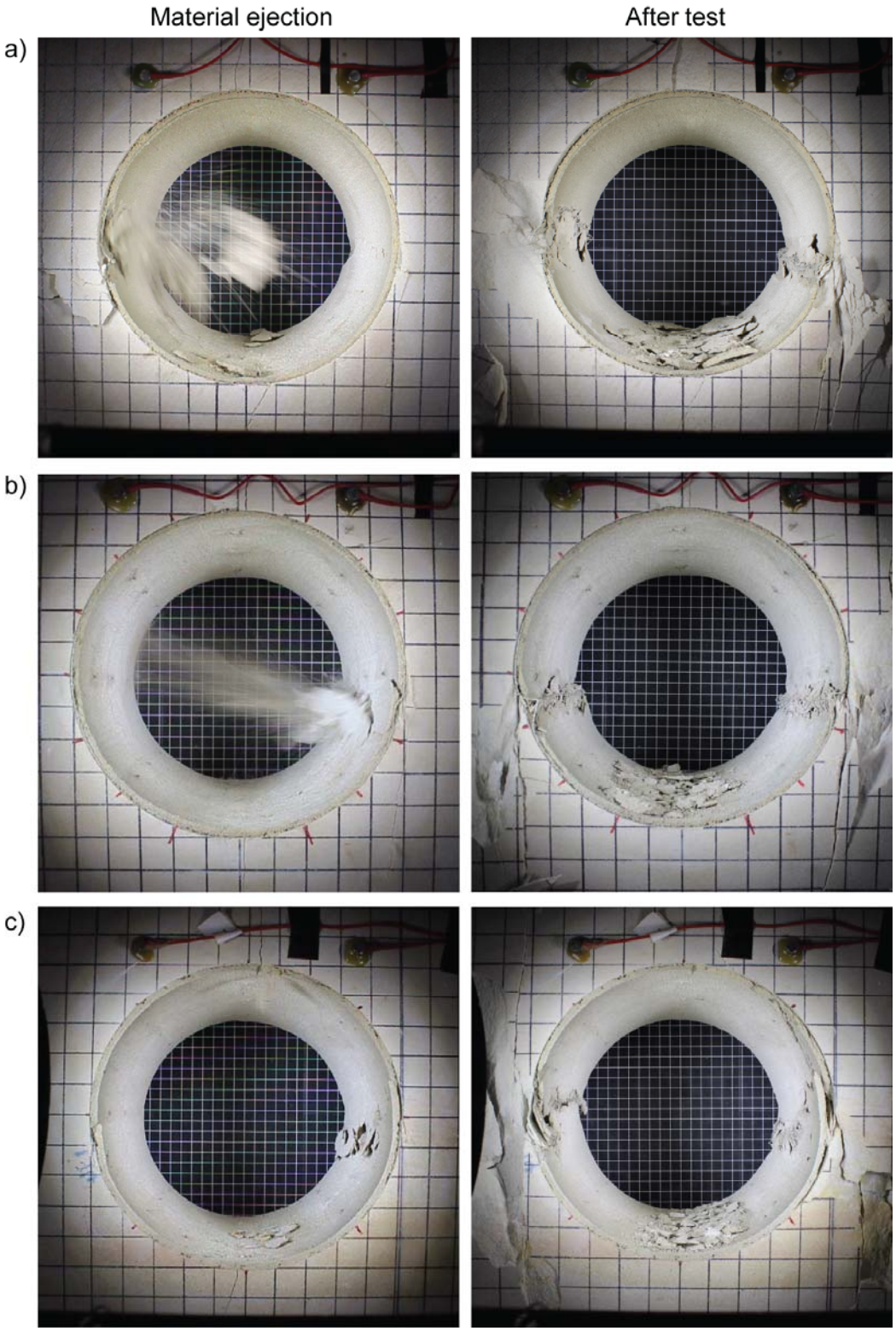

Figure 8.23 Failure on sidewall at spalling and after pillar failure a) stiff welded mesh (Specimen No.4) b) Wide-aperture stiff mesh (Specimen No.6) c) chain link mesh (Specimen No.8).

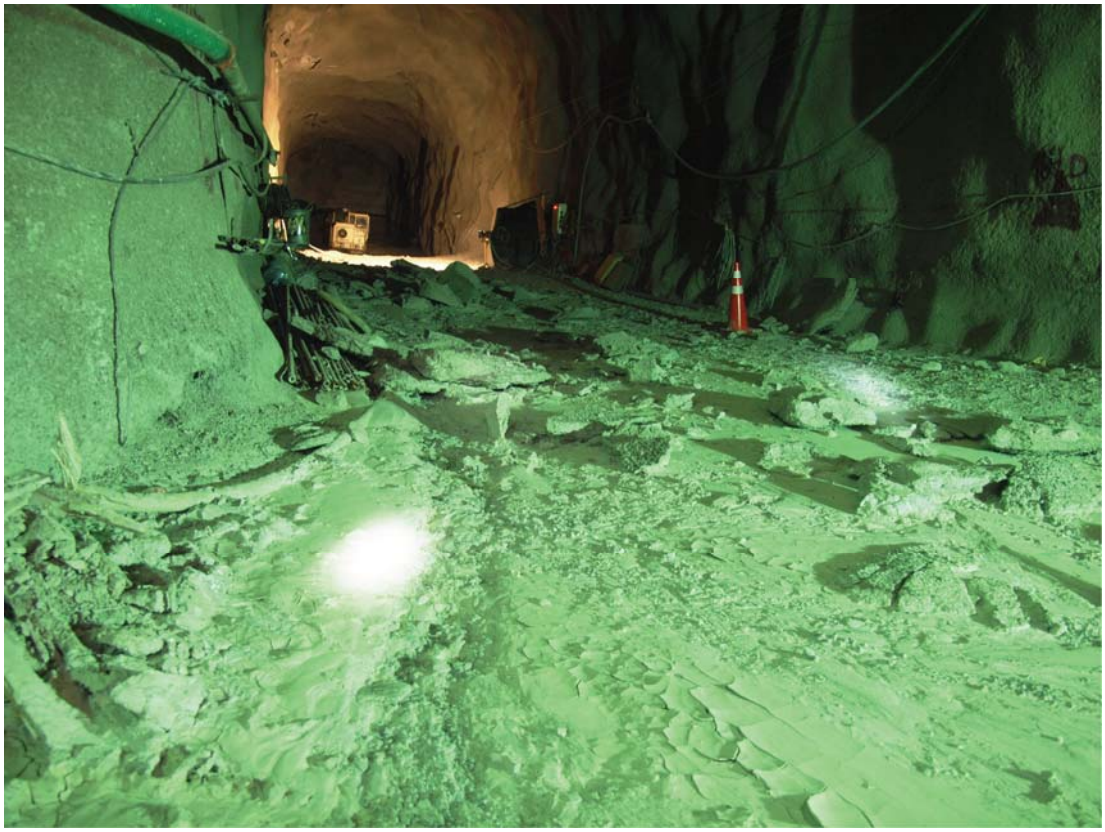

Figure 8.24 Ejected shotcrete materials on the floor at underground mine.

a)

b)

c)

Figure 8.25 Tunnel sidewall after pillar failure a) stiff welded mesh b) Wide-aperture stiff mesh c) chain link mesh.

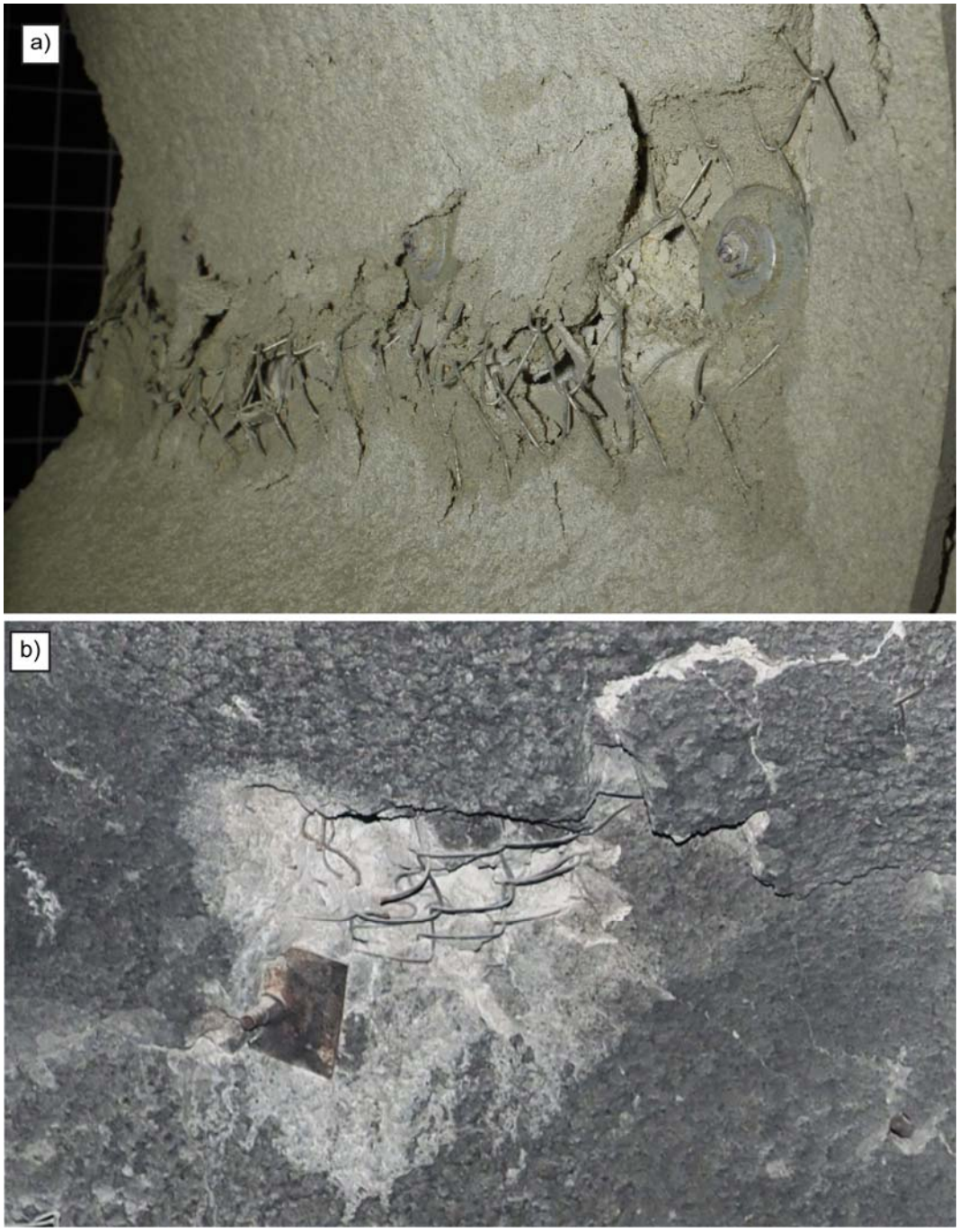

Figure 8.26 Comparison of reinforced shotcrete at failure a) scaled sized specimen b) full scale excavation.

Table 8.7 Debris weight collected after failure with different mesh materials

Mesh type	Stiff welded mesh	Wide-aperture stiff mesh	Chain link mesh
Debris (g)	94	60	49
Ratio (%)	100	64	52

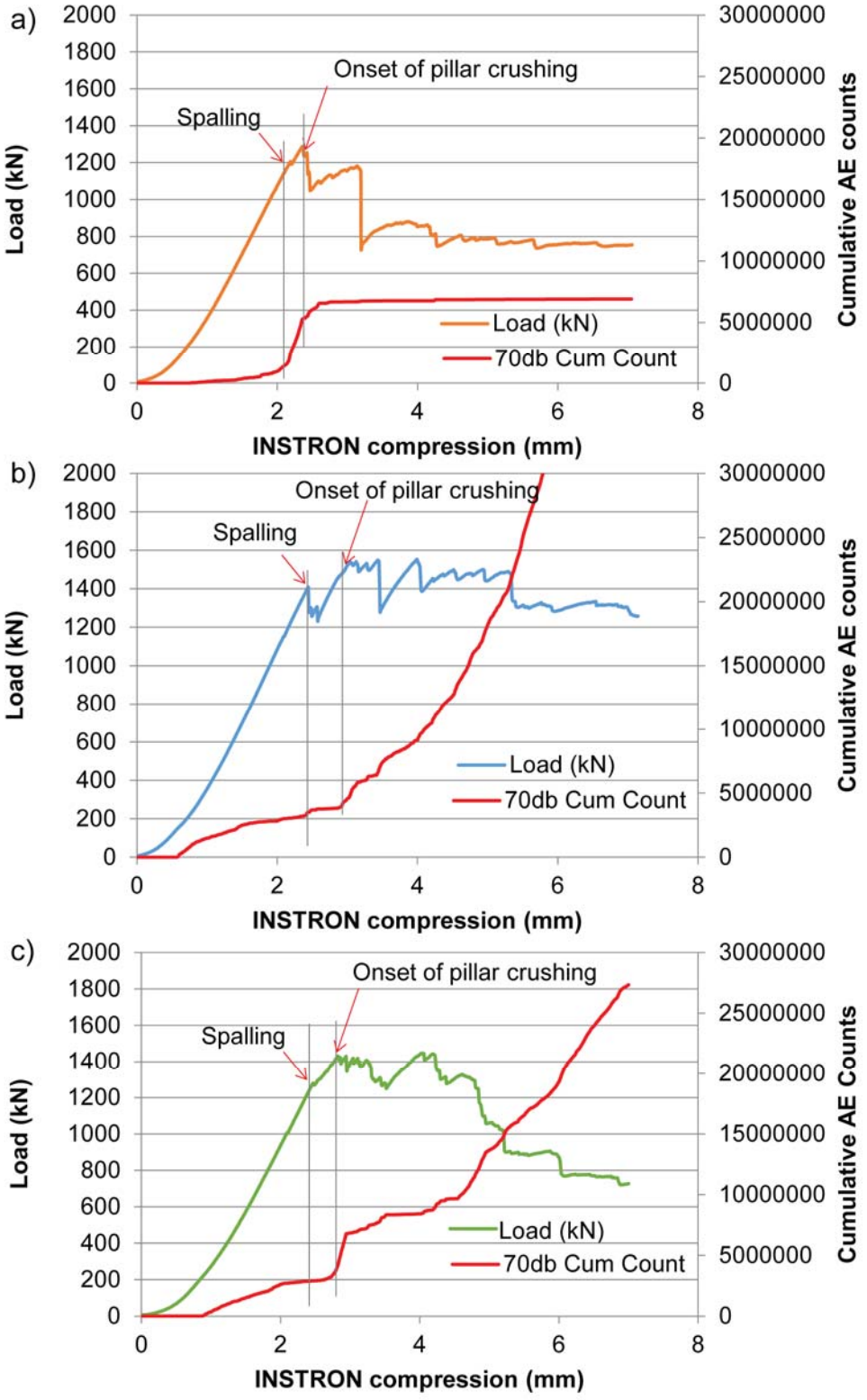

Figure 8.27 Load displacement curve a) stiff welded mesh b) Wide-aperture stiff mesh c) chain link mesh.

Table 8.8 Strength to stress ratio at failure of the three different mesh material at failures.

Specimen No.	UCS (MPa)	σ_c/σ_{max} at spalling	σ_c/σ_{ave} at pillar crushing	Ejection velocity (m/s)
4 (stiff)	85	1.8	3.1	3.0
6 (wide)	87	1.7-1.8	2.3	4.6-7.1
8 (chain)	84	1.6-1.8	2.3	5.6

8.7 Shotcrete Layer

A number of ground support schemes with and without a shotcrete layer were compared to investigate the shotcrete effect as a part of the surface support.

8.7.1 Shotcrete Application Followed by Bolts and Stiff Mesh

Stiff welded mesh with rock bolts were installed in a staggered pattern both onto Specimen No. 1 and 2. Prior to the installation of the mesh on Specimen No.2, a 5 mm thick shotcrete layer was applied. Figure 8.28 shows the failure processes for the two cases in which material ejections and mesh buckling were observed at spalling. Ejection velocity was 1.3-3.9 m/s for Specimen No.1 and 3.3-4.3 m/s for Specimen No.2. A clear difference was observed on the tunnel sidewalls (Figure 8.29). The stiff welded mesh buckled in accordance with the tunnel surface movement as shown in Figure 8.29a. Cracks propagated over the tunnel surface and the broken slabs were held by the mesh. On the other hand, when the shotcrete layer was inserted between the mesh and the tunnel surface, the damage propagated straight along the tunnel wall on the shotcrete layer. Surface damage was concentrated on a limited area (Figure 8.29b).

Figure 8.31 shows load displacement curve from the two tests. Specimen No.2 undertook higher load compared to Specimen No.1. The unloading was greater in the case of the shotcrete failure, while more episodes of spalling were seen without the shotcrete. The behaviour might be because of the higher rock strength of specimen No.2 and no clear difference was seen at the strength to stress ratio at failure (Table 8.9).

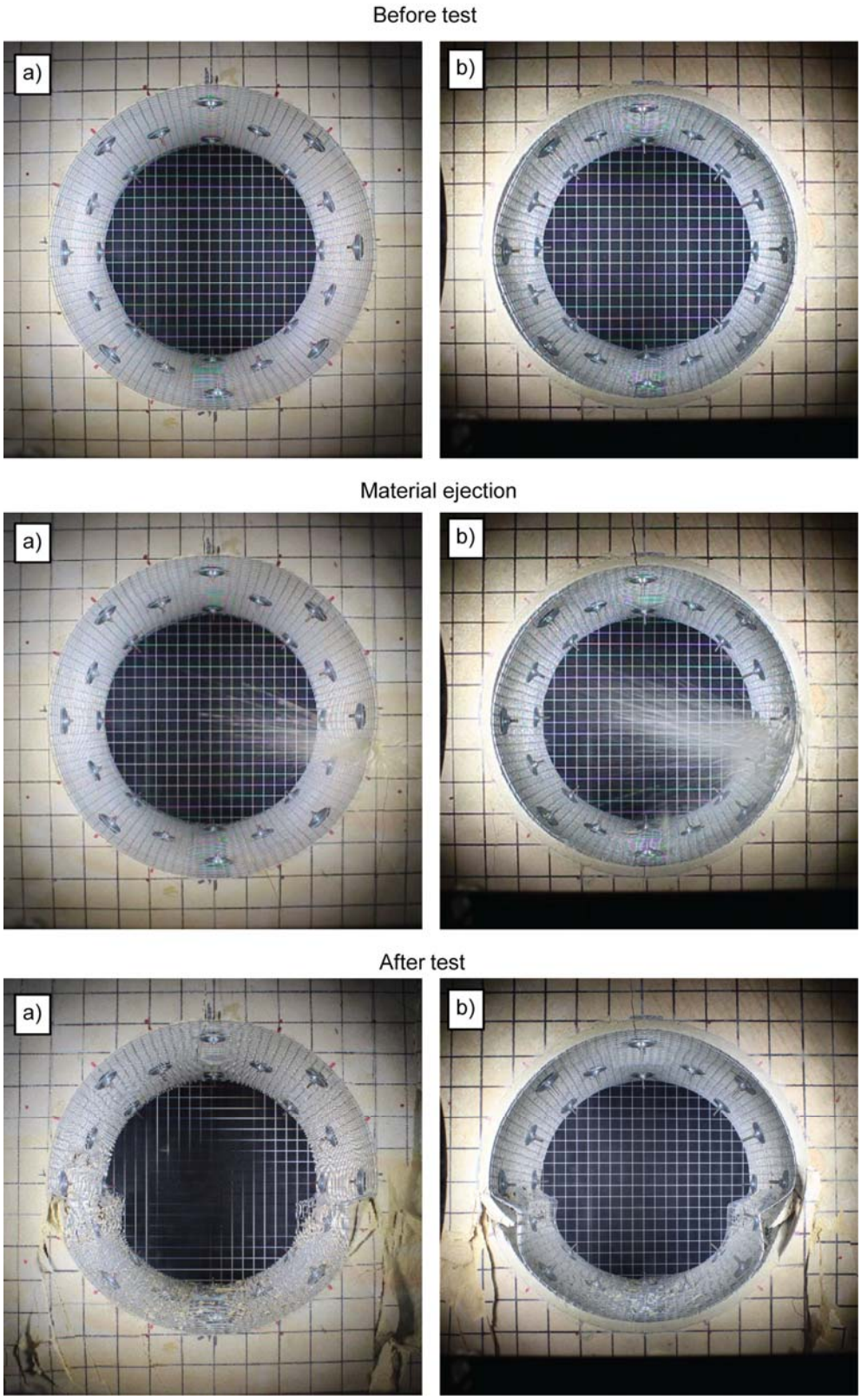

Figure 8.28 Failure progression a) stiff welded mesh and rock bolts (Specimen No.1) b) 5 mm shotcrete layer, stiff welded mesh and rock bolts (Specimen No.2).

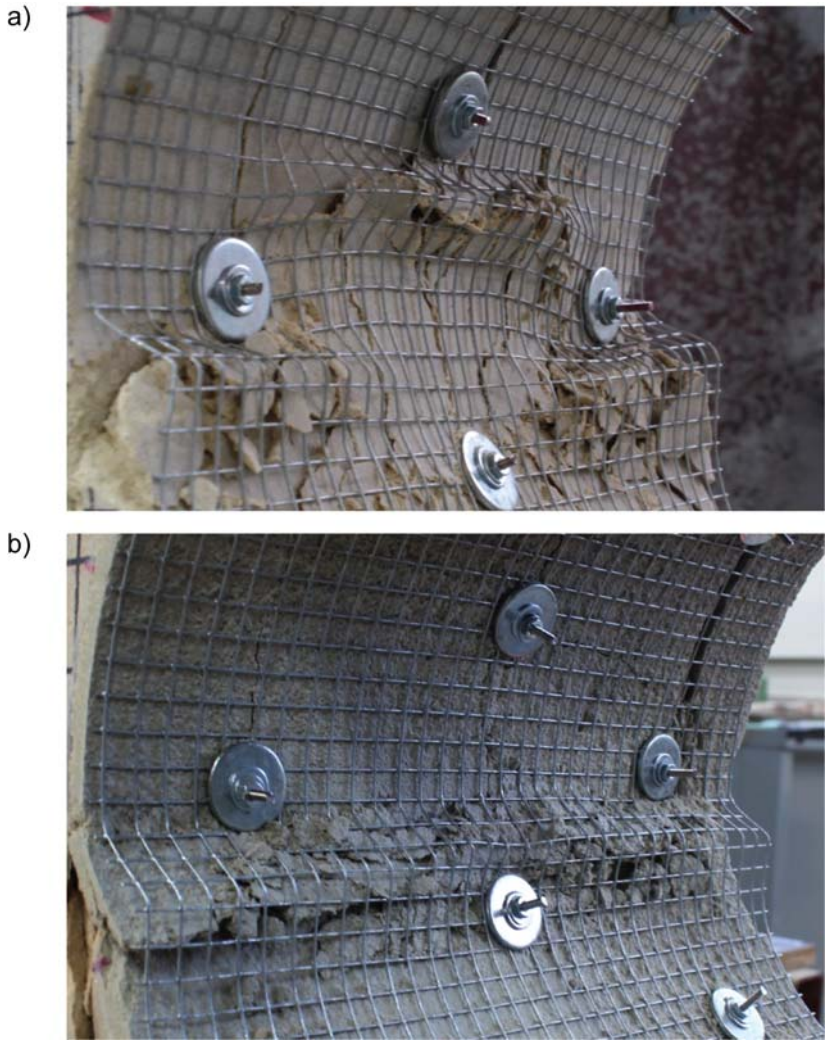

Figure 8.29 Tunnel sidewall after failure a) stiff welded mesh and rock bolts (Specimen No.1) b) 5 mm thick shotcrete layer, stiff welded mesh and rock bolts (Specimen No.2).

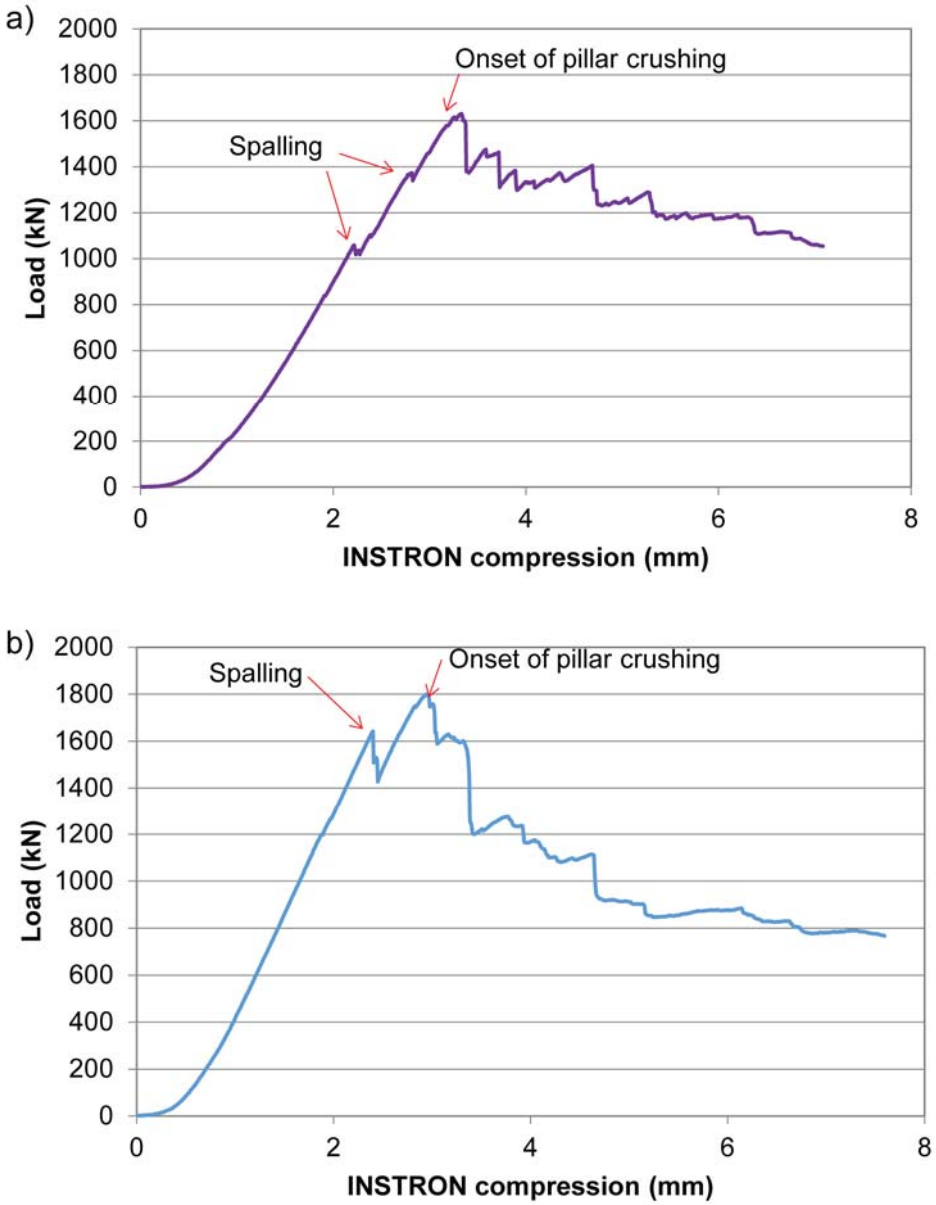

Figure 8.30 Load displacement curve a) stiff welded mesh and rock bolts b) 5 mm thick shotcrete layer, stiff welded mesh and rock bolts.

Table 8.9 Strength to stress ratio at failure of two ground support scheme.

Specimen No.	UCS (MPa)	σ_c/σ_{max} at spalling	σ_c/σ_{ave} at pillar crushing	Ejection velocity (m/s)
1	88	1.7-2.2	2.2	1.3-3.9
2	107	1.7-1.9	2.4	3.5-5.2

8.7.2 Shotcrete Application Followed by Bolts and Chain Link Mesh

The benefit of a shotcrete layer was also seen in a combination with chain link mesh and rock bolts using a bolting in square pattern. Specimen No.9 had a ground support scheme composed of chain link mesh and rock bolts and Specimen No.11 had a 5 mm shotcrete layer between the tunnel surface and the mesh.

Figure 8.31 shows the tunnels sidewalls failure for Specimens No.9 and 11. The chain link mesh deformed in accordance with the tunnel surface damage development (Figure 8.31a). The chain link mesh held the broken rock slabs in place. The damage continuously developed in the tunnel surface during the spalling process. The material ejection occurred constantly and the finer particles were ejected through the chain link mesh. In Figure 8.31b, damage propagated within the shotcrete layer and the chain link mesh held the detached shotcrete plates. After the spalling, the damage on the tunnel panels were restrained by the shotcrete.

Figure 8.32 shows the load displacement curve from the two testing results. Even though the shotcrete layer eased the material ejection, a significant load drop off are seen in both cases at spalling. Table 8.10 shows a similar strength to stress ratio at failures.

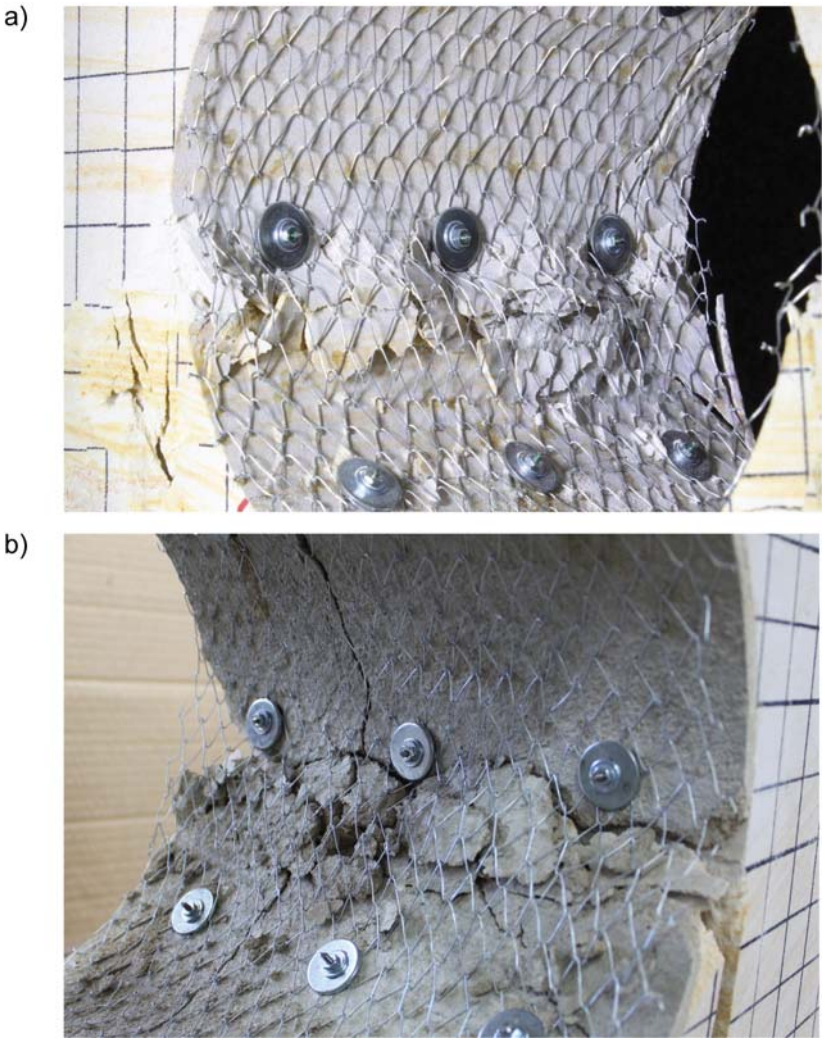

Figure 8.31 Tunnel sidewall after failure a) chain link mesh and rock bolts (Specimen No.9) b) 5 mm shotcrete layer, chain link mesh and rock bolts (Specimen No.11).

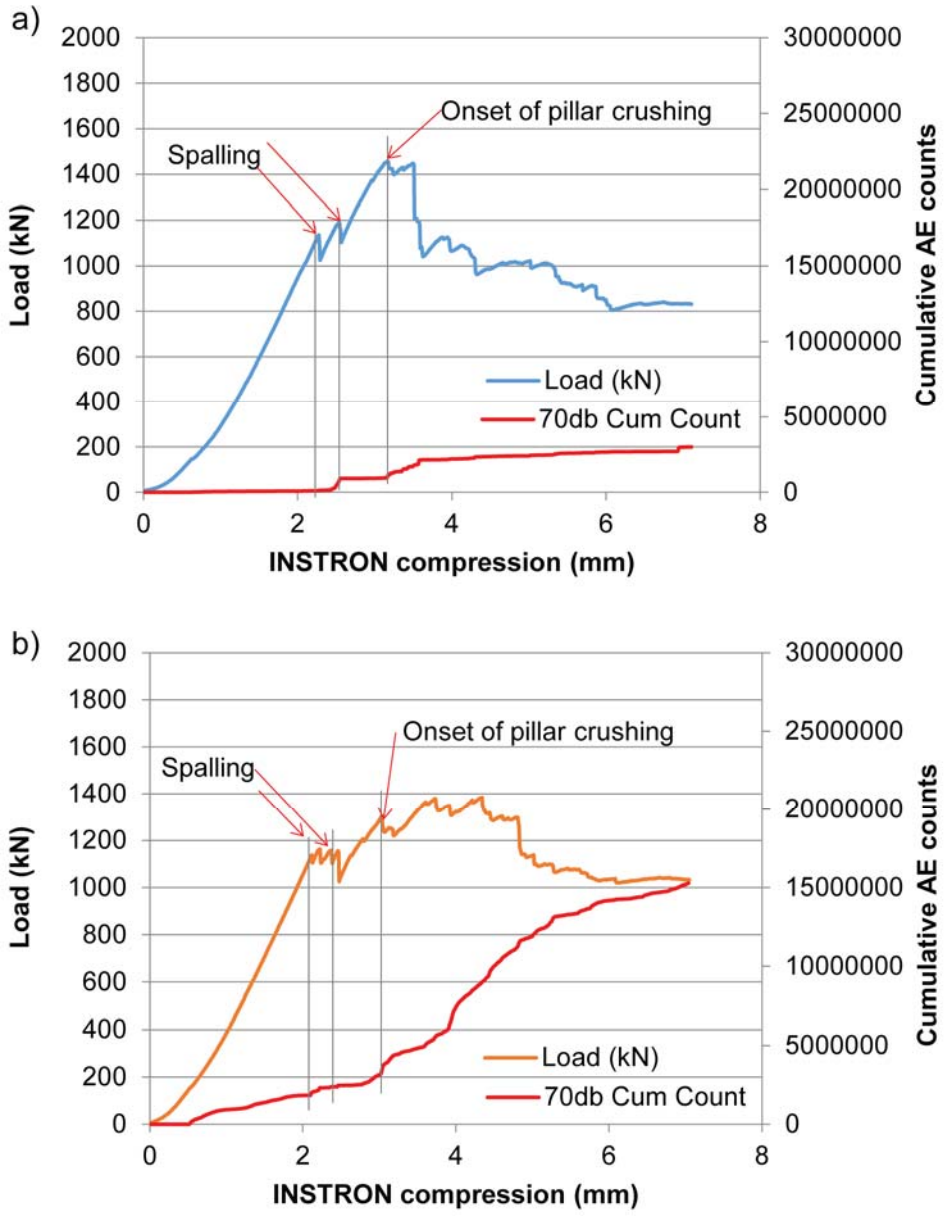

Figure 8.32 Load displacement curve failure a) chain link mesh and rock bolts b) 5 mm shotcrete layer, chain link mesh and rock bolts.

Table 8.10 Strength to stress ratio at failure of shotcrete application comparison.

Specimen No.	UCS (MPa)	σ_c/σ_{max} at spalling	σ_c/σ_{ave} at pillar crushing	Ejection velocity (m/s)
9	78	1.8	2.1	4.2
11	76	1.7-1.8	2.3	1.8-7.4

8.8 Mesh Reinforced vs Mesh Exposed

The sequence of shotcrete and mesh installation was also investigated. A combination of a 5 mm thick shotcrete layer, chain link mesh and 24 rock bolts in square pattern were applied in a different order. For Specimen No.8, the shotcrete was sprayed after the installation of chain link mesh and rock bolts. For Specimen No.11, the chain link mesh was applied after the shotcreting process.

Figure 8.33 shows the failure progressions for the different ground support schemes. For the mesh reinforced shotcrete layer, the crack propagated gradually along the tunnel sidewall (Figure 8.33a). The damaged area was localised and the chain link mesh interlocked with the broken shotcrete panels. The detached shotcrete pieces ejected from the tunnel surface at an ejection velocity of 5.6 m/s. When the chain link mesh was exposed above the shotcrete layer, the crack propagated immediately at spalling and broken panels detached from the tunnel surface (Figure 8.33b). Larger shotcrete panels were held within the mesh and only the finer particles were ejected (velocity 7.4 m/s). The detailed chain link mesh interactions with the shotcrete layer are shown in Figure 8.34. The embedded chain link mesh engaged with shotcrete at failure (Figure 8.34a). For the exposed mesh the broken shotcrete panels were detached from the tunnel surface and buckled with the chain link mesh (Figure 8.34b).

Figure 8.35 shows load displacement curve for the two testing results. The unloading at spalling was less violent in the case of the mesh reinforced case. In both cases, a pillar crushing commenced before reaching a maximum load. The ratio of the strength to stress at failures shows very similar value (Table 8.11).

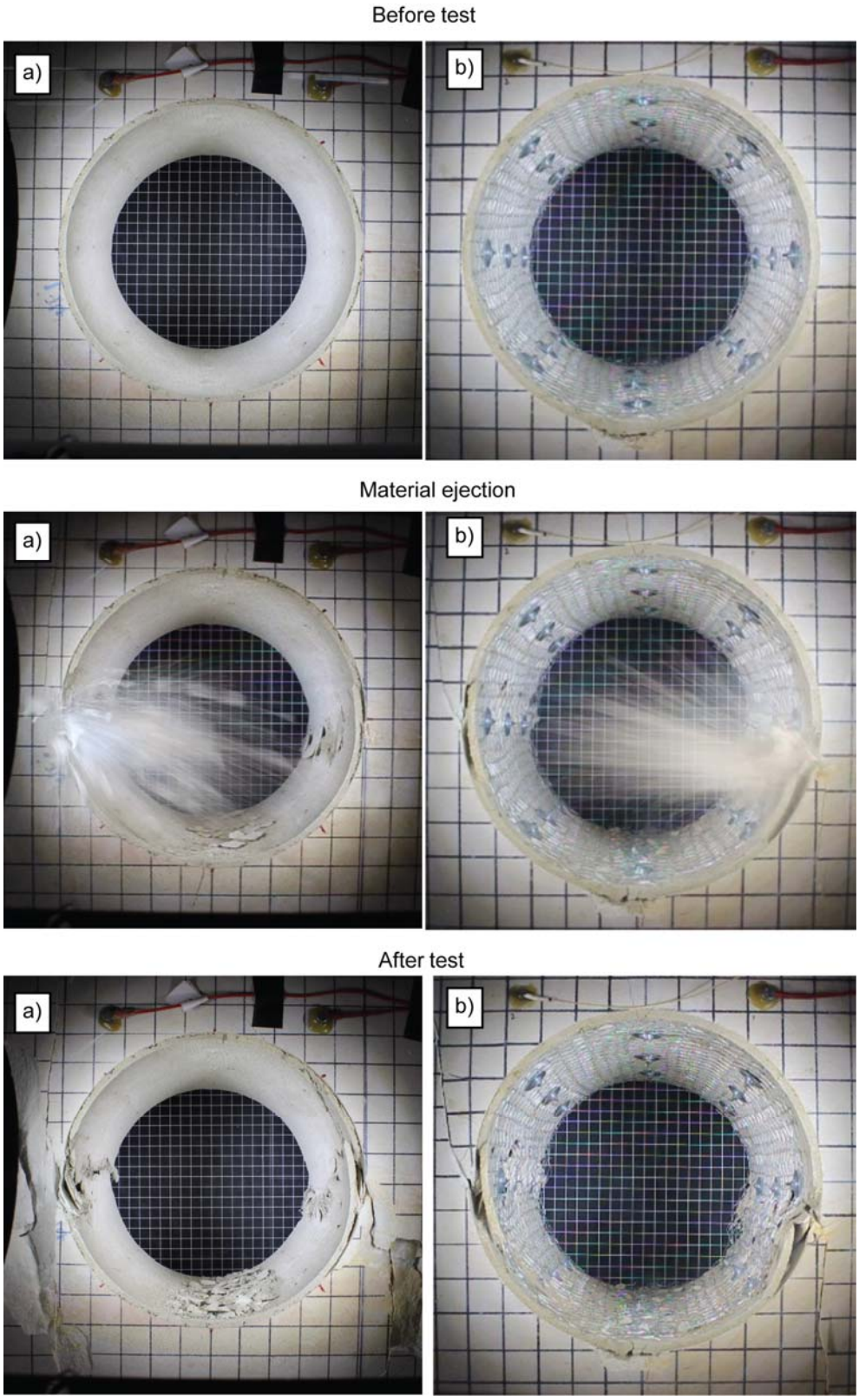

Figure 8.33 Failure mechanism in different mesh position a) mesh exposed (Specimen No.8) b) mesh embedded (Specimen No.11).

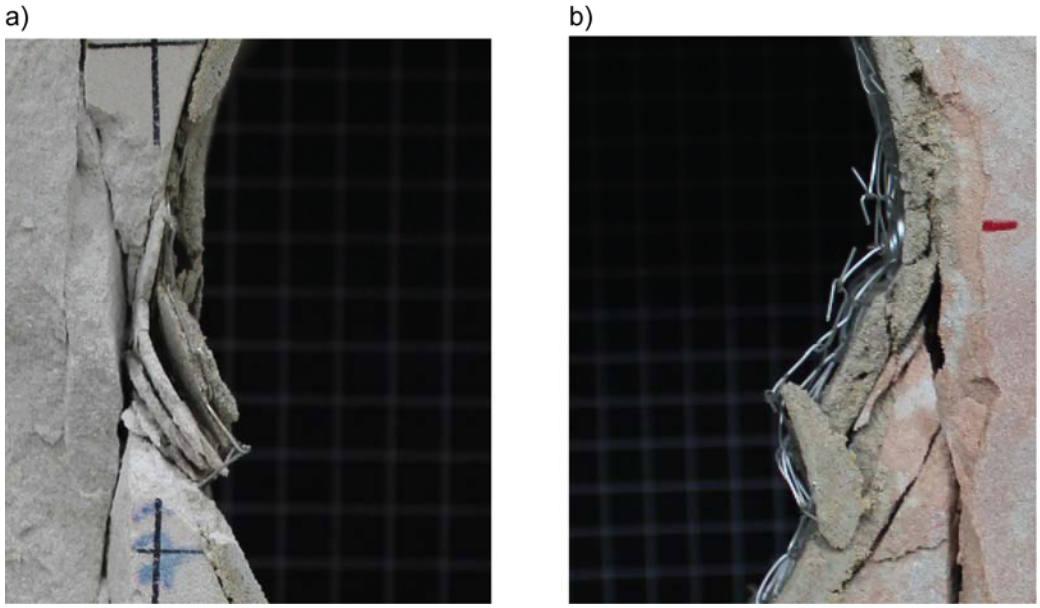

Figure 8.34 Tunnel surface after failure a) mesh reinforced (Specimen No.8) b) mesh exposed (Specimen No.11).

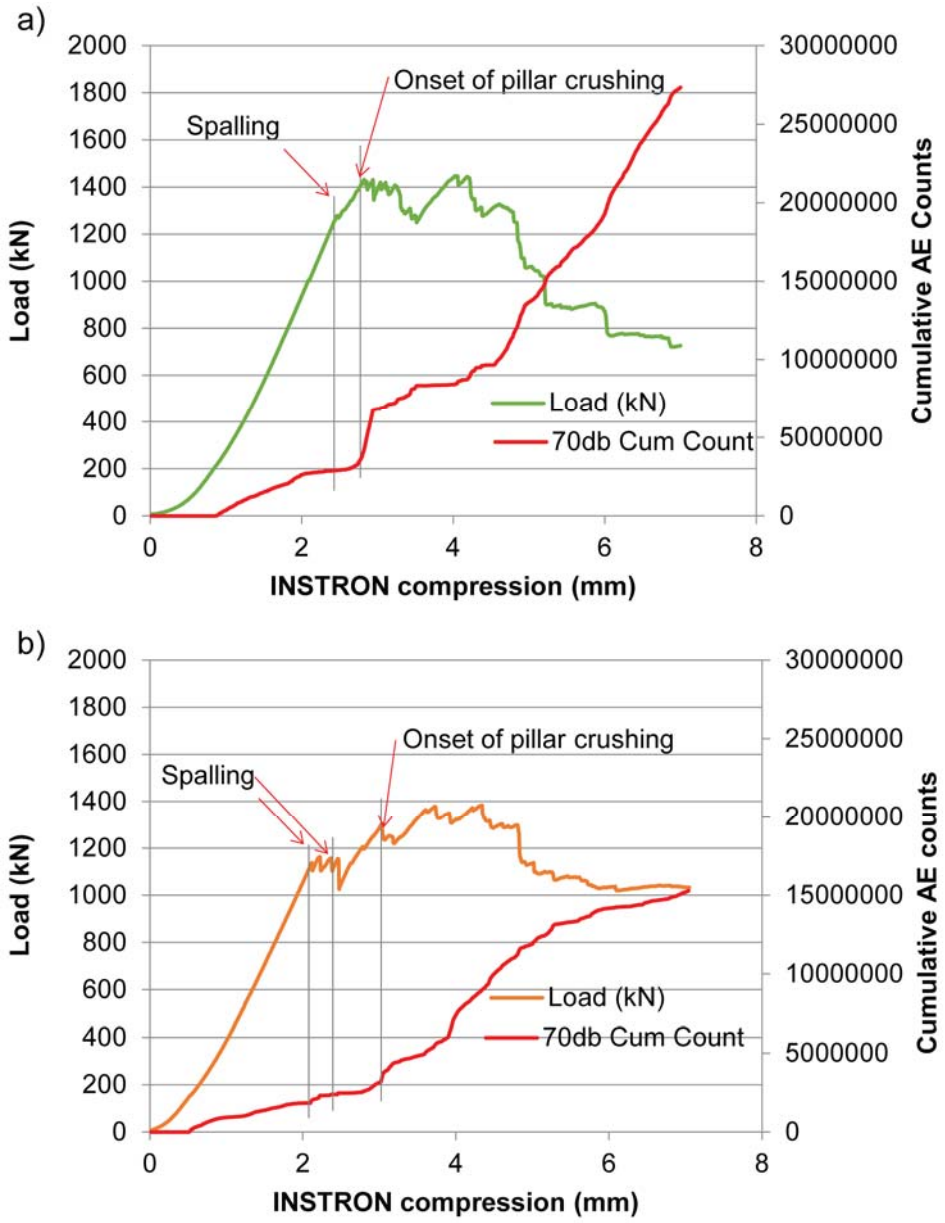

Figure 8.35 Load displacement curve a) mesh reinforced b) mesh exposed.

Table 8.11 Strength to stress ratio at failure of mesh reinforced and mesh exposed.

Specimen No.	UCS (MPa)	σ_c/σ_{max} at spalling	σ_c/σ_{ave} at pillar crushing	Ejection velocity (m/s)
8 (reinforced)	78	1.6-1.8	2.3	5.6
11 (exposed)	76	1.7-1.8	2.3	1.8-7.4

8.9 A Comparison of Ground Support Schemes

A number of ground support schemes involving a combination of shotcrete, chain link mesh and rock bolts in square pattern were compared. The ground support components were installed in different sequence as shown in Figure 8.36. In both Specimen No.8 and 11, a 5 mm thick shotcrete layer and chain link mesh were applied in a different application order (Figure 8.36 a and b). In Specimen No.13, two chain link mesh sheets were used. One reinforcement the shotcrete and another was exposed (Figure 8.36c). Furthermore an additional shotcrete layer and mesh sheet were applied before a rock bolts installation in Specimen No.14 (Figure 8.36d). The thickness of the initial and the second shotcrete layer was designed as 5 mm and 3 mm respectively.

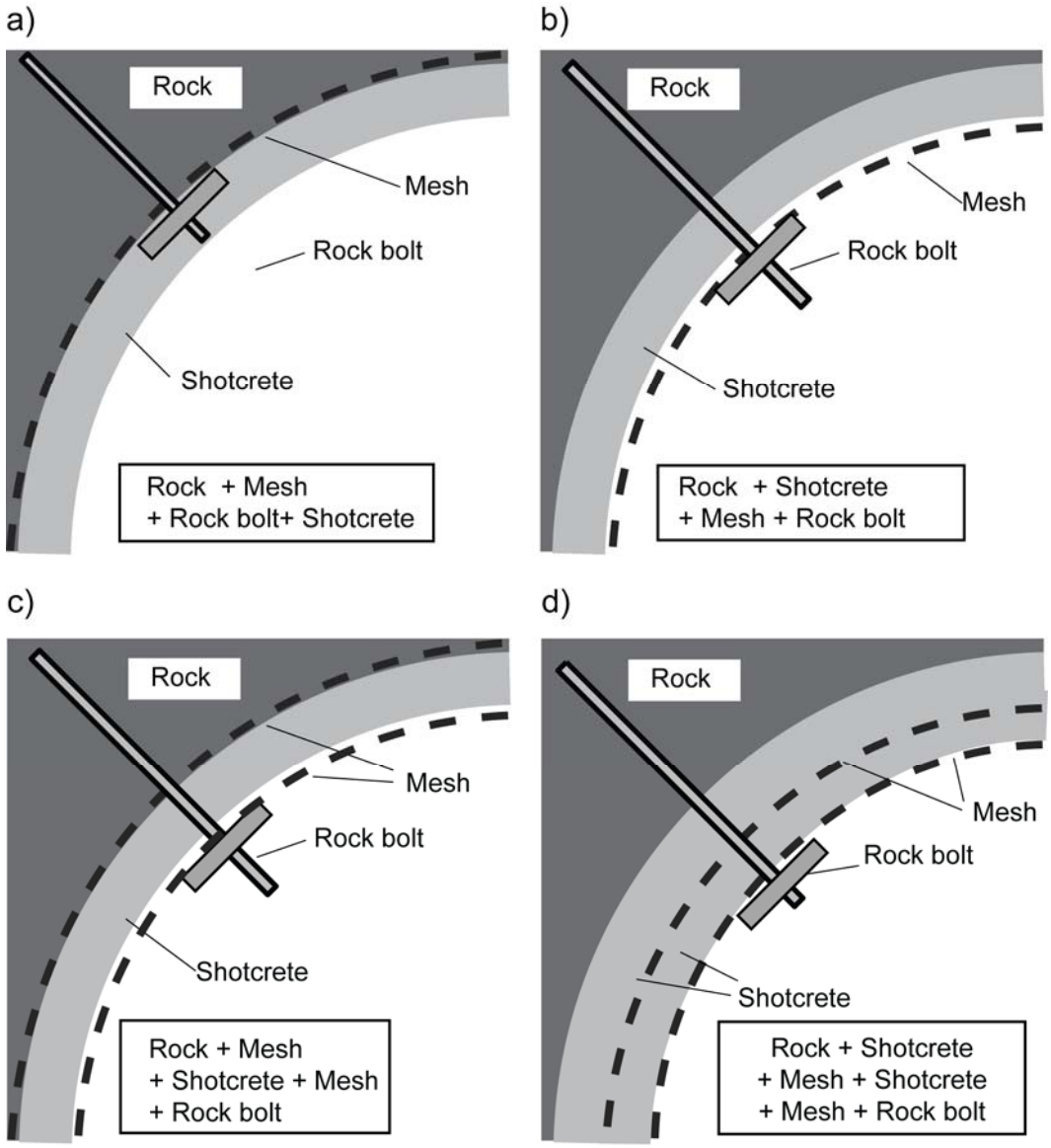

Figure 8.36 A comparison of ground support schemes a) mesh, shotcrete and rock bolt b) shotcrete, mesh and rock bolt c) mesh, shotcrete, mesh and rock bolt d) shotcrete, mesh, shotcrete, mesh and rock bolt.

Material ejections were observed in the all cases and are shown in Figure 8.37. Broken materials including shotcrete panels and particles were ejected violently (Figure 8.37a) while the broken shotcrete panels were contained within mesh when it was exposed. Ejection velocity was 5.6 m/s, 7.4 m/s, 7.2 m/s and 4.1 m/s respectively. The additional layer of embedded mesh did not contribute to the material ejection velocity reduction

(Figure 8.37b and c. However, in the case of Specimen No.14, less material ejection was experienced as shown in Figure 8.37d.

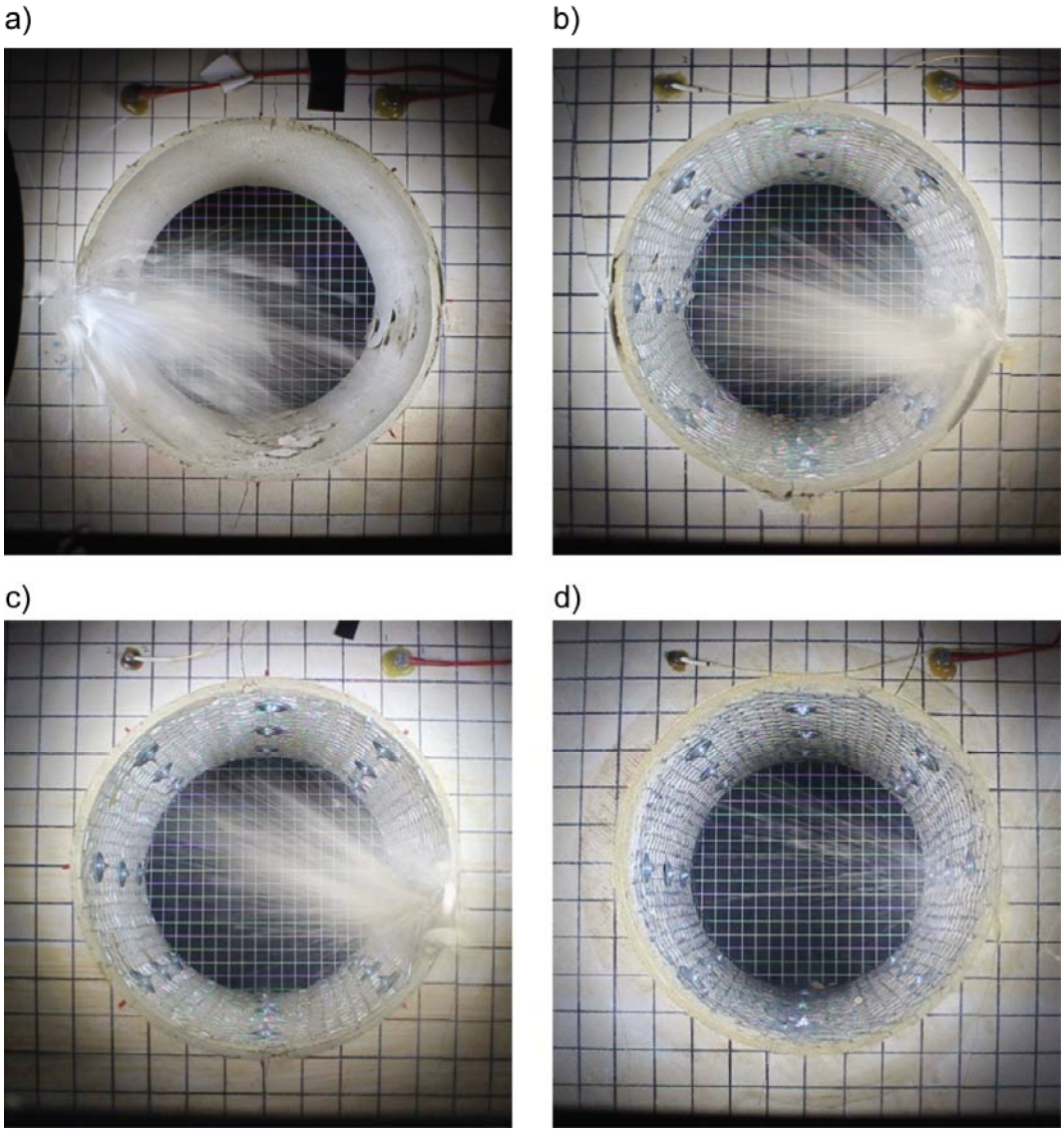

Figure 8.37 Material ejection at spalling failure a) mesh, shotcrete and rock bolt b) shotcrete, mesh and rock bolt c) mesh, shotcrete, mesh and rock bolt d) shotcrete, mesh, shotcrete, mesh and rock bolt.

Figure 8.38 presents the tunnel surfaces after failure. As described before, when the mesh was embedded under a shotcrete layer, the two support elements interacted. When the mesh was exposed it retained the broken shotcrete plates (Figure 8.38a and

b). When a mesh was installed both under and on top of a shotcrete layer (Figure 8.38c), the broken shotcrete plates were connected and also held by the external mesh. Finally when the shotcrete layer was applied twice, the internal damage become smaller compared with other configuration (Figure 8.38d).

The tunnel sidewall damages are shown in Figure 8.39. The embedded mesh was able to localise the damage area, and this was not seen when the mesh was exposed (Figure 8.39a and b). Less cracking and ejection were observed on the shotcrete surface when shotcrete was applied twice (Figure 8.39c and d).

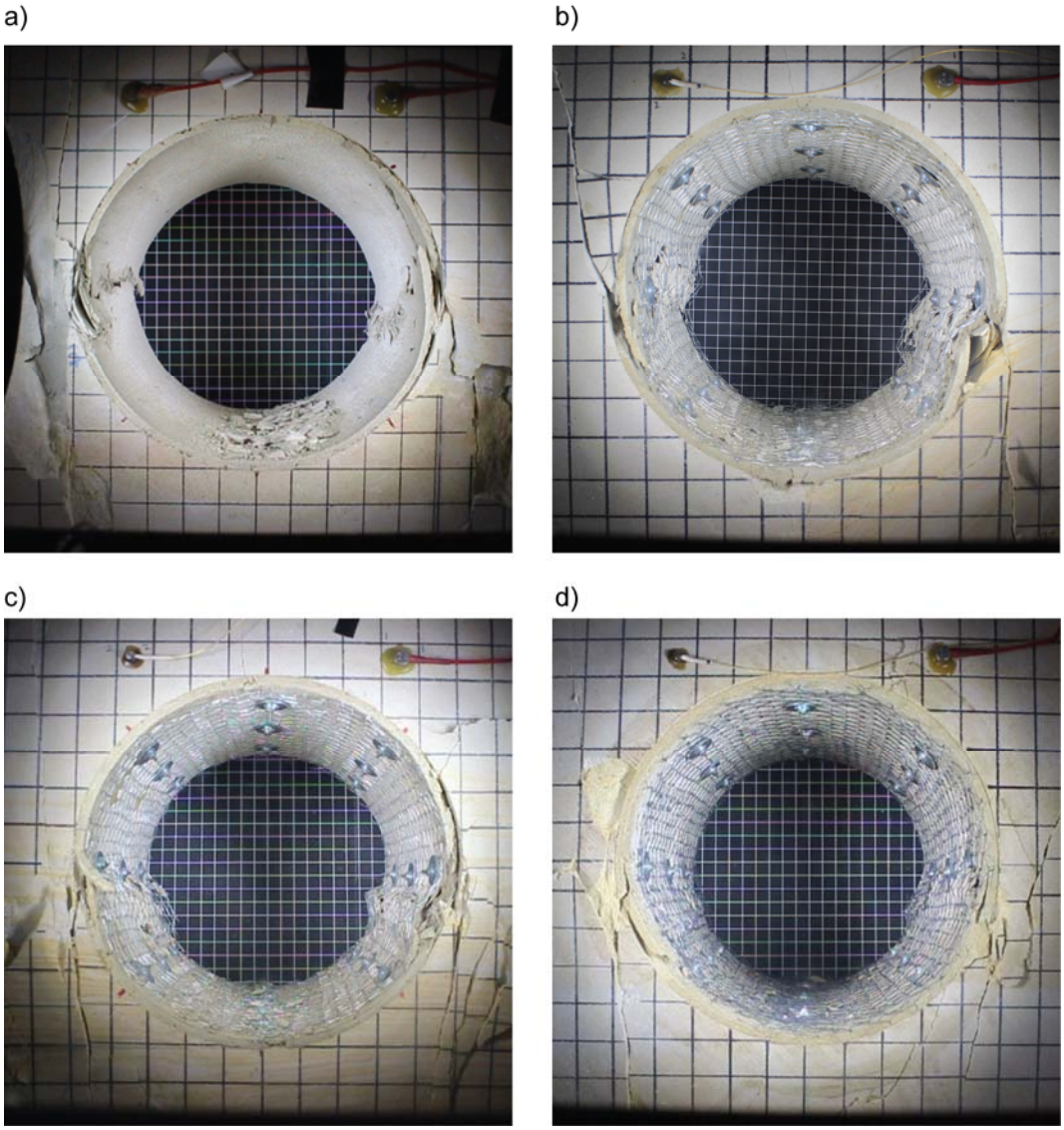

Figure 8.38 Ground support performance following tunnel failure a) mesh, shotcrete and rock bolt b) shotcrete, mesh and rock bolt c) mesh, shotcrete, mesh and rock bolt d) shotcrete, mesh, shotcrete, mesh and rock bolt.

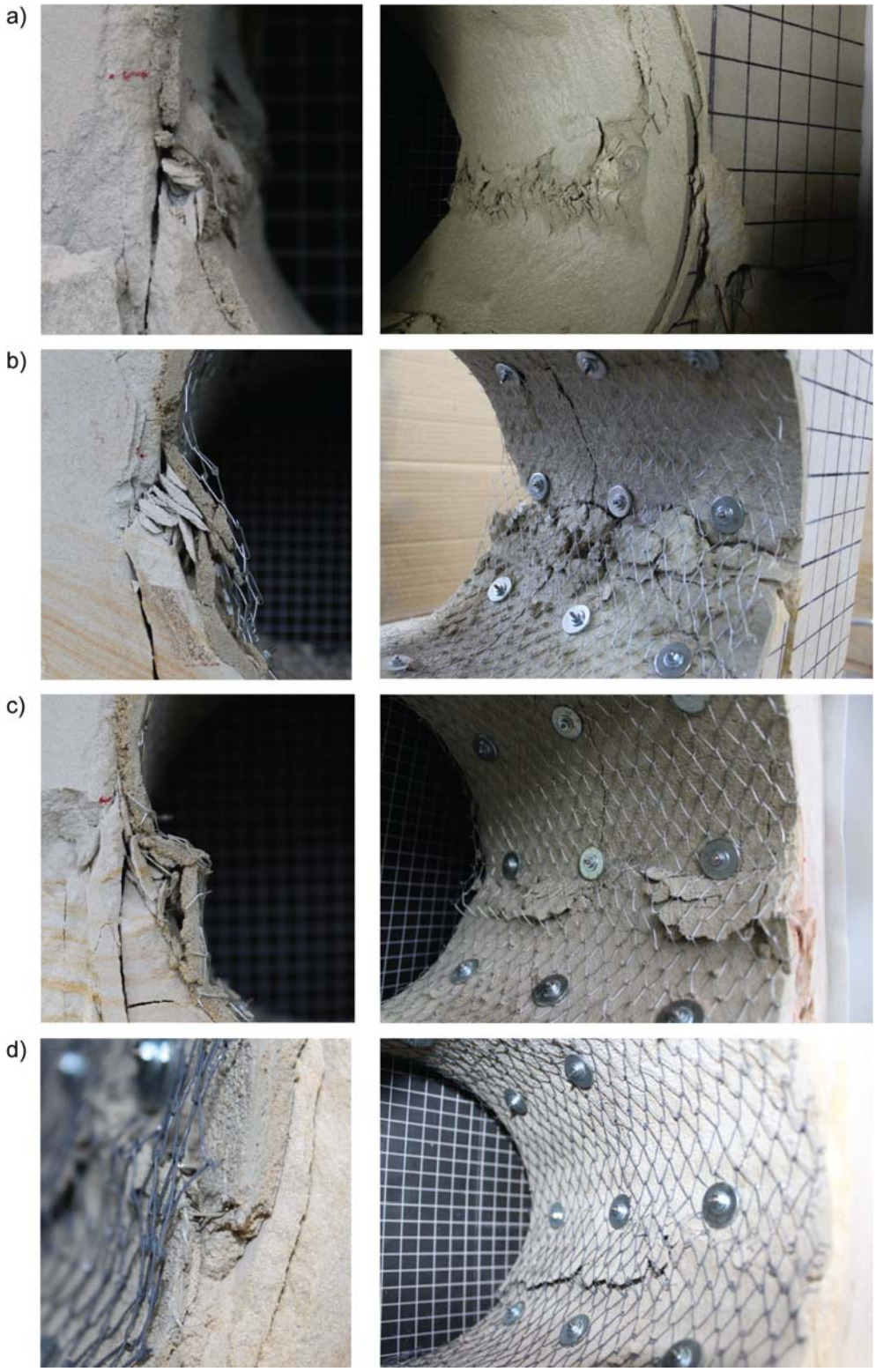

Figure 8.39 Tunnel sidewalls after failure a) mesh reinforced shotcrete b) mesh exposed shotcrete c) mesh embedded and mesh exposed shotcrete d) mesh reinforced shotcrete with mesh exposed.

Figure 8.40 shows the load displacement and the AE activities from the four tests. The uniaxial compressive strength ranged from 76 to 88 MPa. In all cases, the AE activities initiated after tensile crack appearance on top and bottom of the tunnels. A sudden load drop off was experienced at spalling with a subsequent load increase until it reached a peak strength. Although some variation was experienced, the load displacement curves were similar.

The amount of debris collected from the different ground support scheme tests is shown in Table 8.12. As can be seen, the external mesh contributed to reduce the amount of debris. The less the debris falling onto the tunnel floor. The detailed damage volume from each ground support scheme is examined in Chapter 9.

At pillar crushing stage, vertical shear cracks were formed with a significant load drop off (Figure 8.41). It exaggerated internal convergence and more damages were seen on the excavation surface. In case of Specimens No.14, internal damage induced by shear failure on the pillar was also contained within surface support and less damage was experienced.

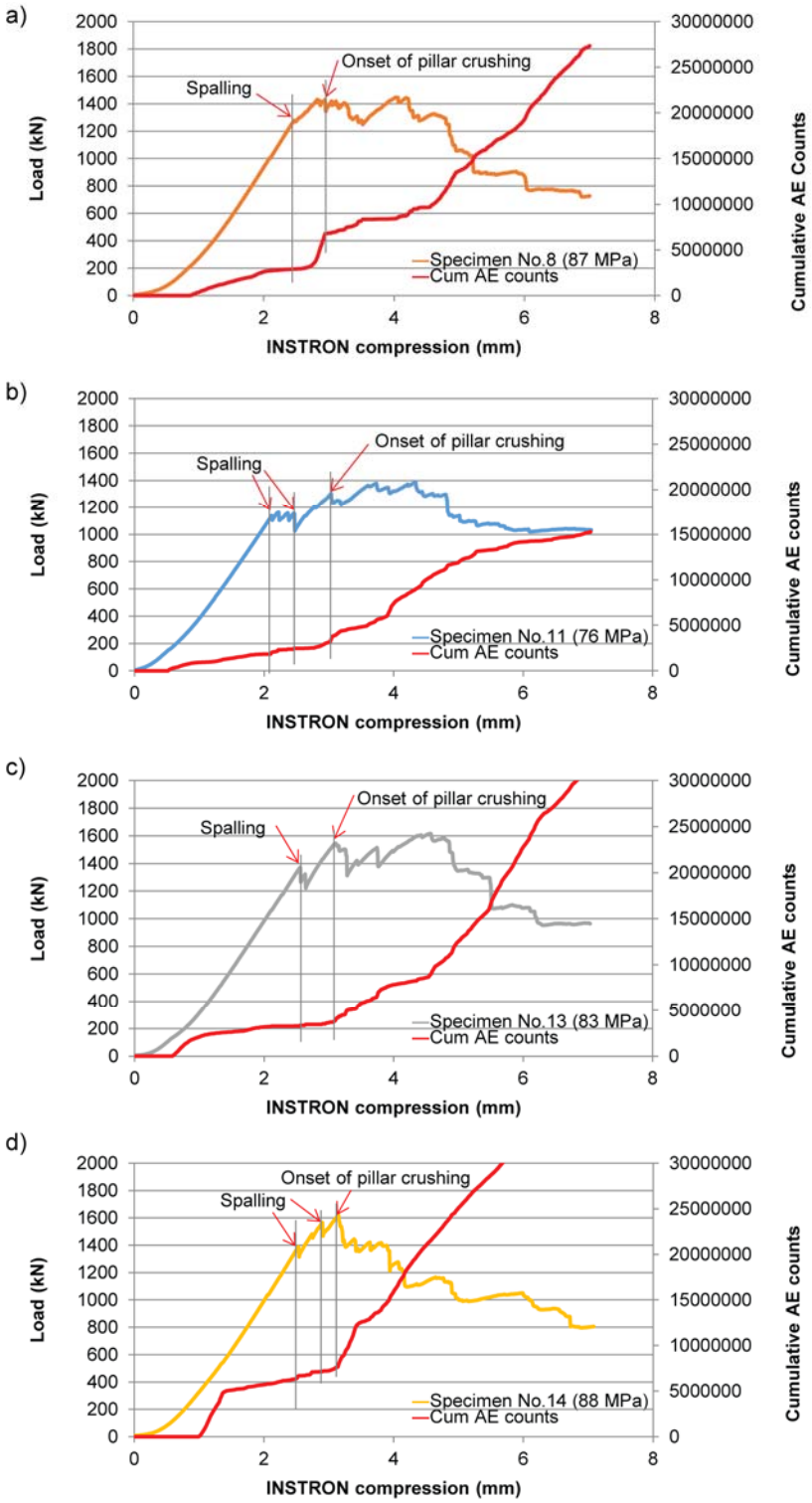

Figure 8.40 Load-displacement curves for different ground configuration tests with AE data a) mesh reinforced shotcrete b) mesh exposed shotcrete c) mesh

embedded and mesh exposed shotcrete d) mesh reinforced shotcrete with mesh exposed.

Figure 8.41 The shear failure on the pillar (Specimen No.14).

Table 8.12 Debris weight collected after failure with different ground support schemes.

Specimen No.	8	11	13	14
Ground support	M-B-S	S-M-B	M-S-M-B	S-M-S-M-B
Debris (g)	49	24	14	6
Ratio (%)	100	49	29	12

8.10 Ejection Velocity and Ground Support

Figure 8.42 shows ejection velocities at spalling of both unsupported and stabilised tunnel tests. The average velocity from both tunnel sidewalls were plotted as a function of the uniaxial compressive strength. As mentioned in Chapter 6, material ejection velocities have an increasing trend with higher uniaxial compressive strength. With surface support systems, ejection velocities were lower compared to that of the unsupported test results.

In Specimen No.1 and 2, rock bolts were installed in staggered pattern which is shown in red circle in Figure 8.42. Average ejection velocities were 2.6 m/s and 4.4 m/s respectively. The ejection velocity became lower compared with a similar ground scheme with square bolting pattern.

Specimens No. 1, 3 and 9 were stabilised using by rock bolts and mesh only, i.e. the tunnel surface was exposed, which is shown in grey triangles in Figure 8.42 . In this experiment, the existence of a shotcrete layer can be seen to increase the ejection velocities. It was assumed that when a shotcrete layer was cracked, finer particles were ejected easily due to the brittleness of the shotcrete materials used in this experiment. This is similar to shotcrete ejection failures experienced in full scale tunnel conditions

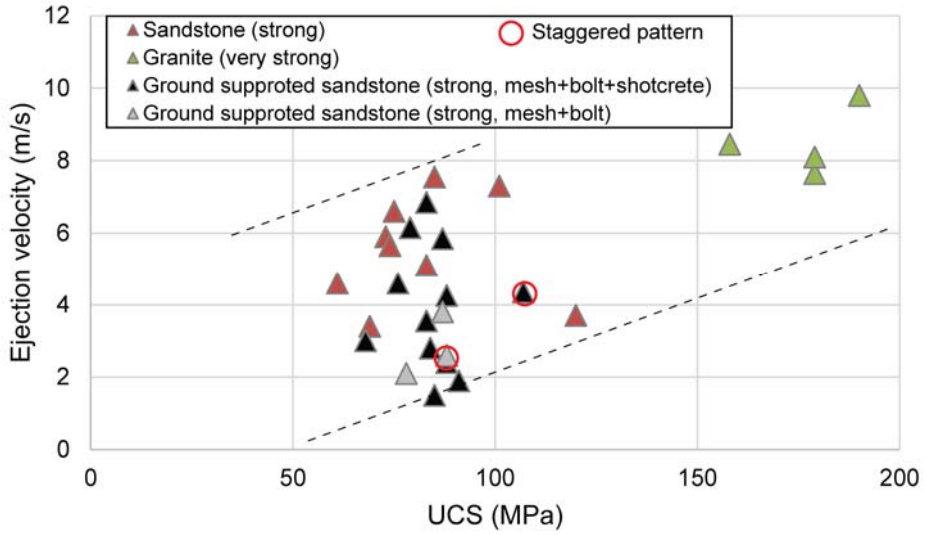

Figure 8.42 Ejection velocity at spalling for unsupported and stabilized tunnel specimens.

8.11 Ground Support and Ratio of Strength to Stress at Failure

The ratio of intact rock strength to the maximum tangential stress at spalling was plotted for the 200 mm diameter unsupported tunnel test results (Figure 8.43). As described in Chapter 7, the ratio at spalling failure showed an increase with uniaxial compressive strength. With ground support, the specimens were able to take additional stress and hence the ratio decreased slightly compared with unsupported test results. A related conclusion is that the ground support schemes contributed to enhance the specimen strength prior spalling.

Figure 8.44 shows the intact rock strength and average pillar stress at pillar crushing. It also indicates that ground support increases the post peak strength of specimen.

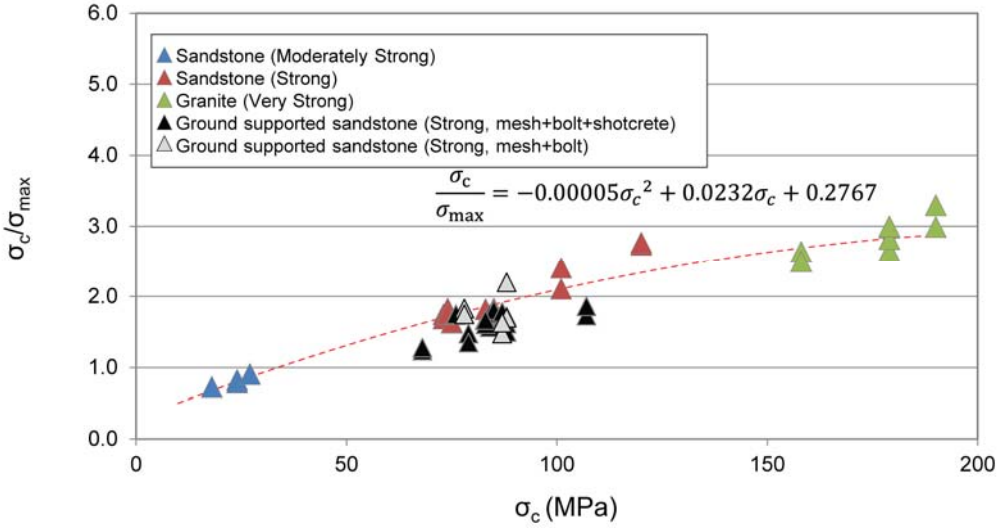

Figure 8.43 Unsupported and stabilised tunnel spalling as a function of compressive strength and maximum tangential stress (200 mm diameter tunnels).

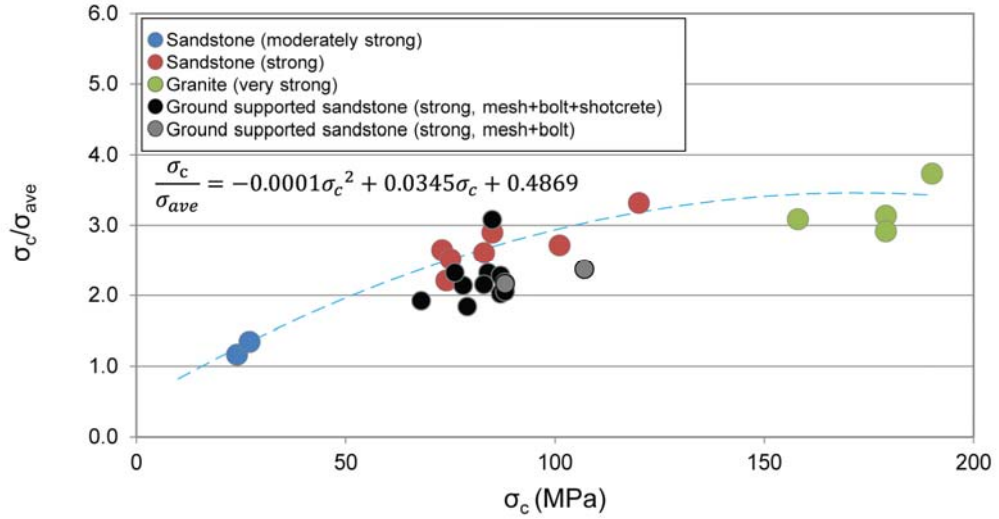

Figure 8.44 Unsupported and stabilised onset of pillar crushing as a function of compressive strength and average pillar strength.

8.12 Ground Support Performance Summary

The performance of ground support elements was investigated as a part of a number of ground support schemes.

Various ground support schemes were examined. The major difference was not seen in the load displacement curves. Mesh under shotcrete helped to enhance the shotcrete connection and adhesion to the tunnel surface. Mesh outside of shotcrete prevented the shotcrete panels falling off from the tunnel surfaces.

Four types of mesh were compared as a part of surface support systems. Under a compressive loading, welded mesh types induced further damages by buckling. Especially when the welded mesh was embedded under a shotcrete layer, it pushed shotcrete panels which exaggerated the damages on the surface support.

Although a shotcrete layer showed brittle failure, the crack propagation developed locally on a shotcrete layer compared with unsupported walls.

Reinforcement by rock bolt increased the residual strength of specimens. Spalling propagated around the rock bolts and the damage on the tunnel surface occurred between bolts. On average, ejection velocities at spalling was reduced and the strength and stress ratio at pillar crushing decreased with reinforcement. Crack propagation process was disturbed and development rate was decreased when the rock bolts were installed on a staggered pattern.

Chapter 9

Excavation Shape Measures

9.1 Laser Scanning Arrangement

Tunnel strain measurements were conducted onto 2 sets of ground support schemes, namely Specimen No.11, 12, 14 and 15 in Table 8.1.

Specimens No.11 and 12 were composed of a 5 mm shotcrete layer, chain link mesh and reinforcement in square pattern. An additional second shotcrete layer and external chain-link mesh were applied onto Specimen No.14 and 15. These ground support schemes were called a single layer and a double layer ground support scheme respectively. Both of single ground supported and double supported tunnel failure progression are provided in Appendix A.

Table 9.1 summaries the strain measurement arrangement and Figure 9.1 and Figure 9.2 shows the strain measurement points within the load-displacement curves. Initial measurement was carried out to all specimens before start of the loading. This data was used as a base point of the excavation shape and strain was calculated as a movement from this base point. For samples No.12 to 15, an additional measurement was undertaken before spalling occurred. From the experience, spalling normally occurred in 200 mm diameter strong sandstone circular excavation when the load exceeded 1000 kN. The loading was stopped and held at 1000 kN to conduct a laser scanning and restarted at the same loading rate. The experiments were continued until a specimen compression by the servo controlled machine reached 7 mm and a final laser scanning was conducted under loading. During the experiment of the Specimen No.15, the servo controlled loading machine stopped working after the strain measurement at 1000 kN. Although tensile crack propagated on the top and bottom of the excavation, there were no other significant damage in the specimen. The specimen was unloaded and reloaded again until failure (Figure 9.2). Strain measurement was undertaken again before the second loading to check the plastic strain existence, however it was negligible.

Table 9.1 Strain measurement arrangement.

Specimen No.	Ground support application	UCS (MPa)	Strain measurement		
			Before loading	Before spalling (1000 kN)	After failure
11	SC-Mesh-Bolt	76	○	-	○
12	SC-Mesh-Bolt	83	○*	○	○
14	SC-Mesh-SC-Mesh-Bolt	88	○	-	○
15	SC-Mesh-SC-Mesh-Bolt	91	○*	○	○

* Measurement was conducted twice.

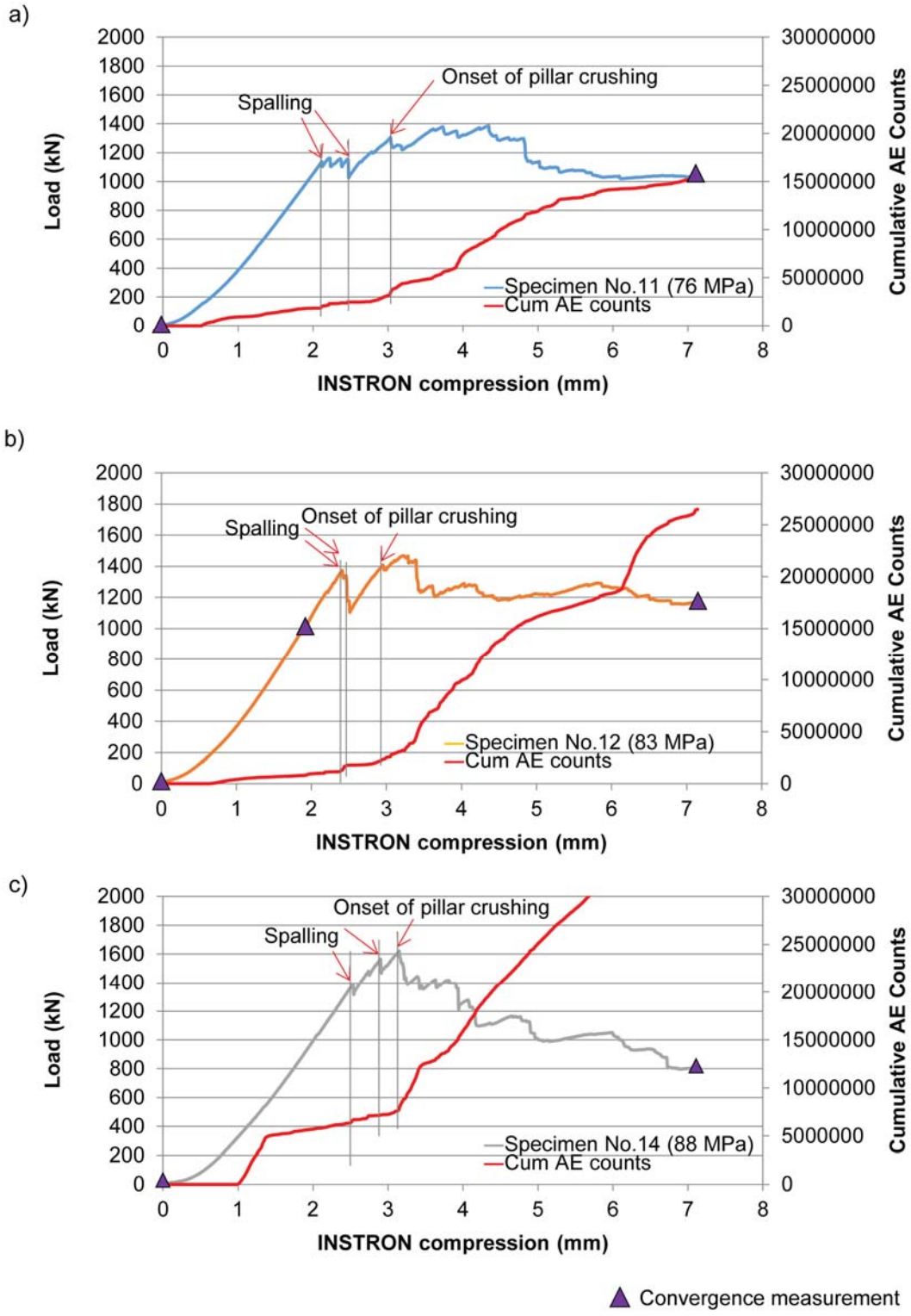

Figure 9.1 Stain measurement point of a) Specimen No.11 b) Specimen No.12 c) Specimen No.14.

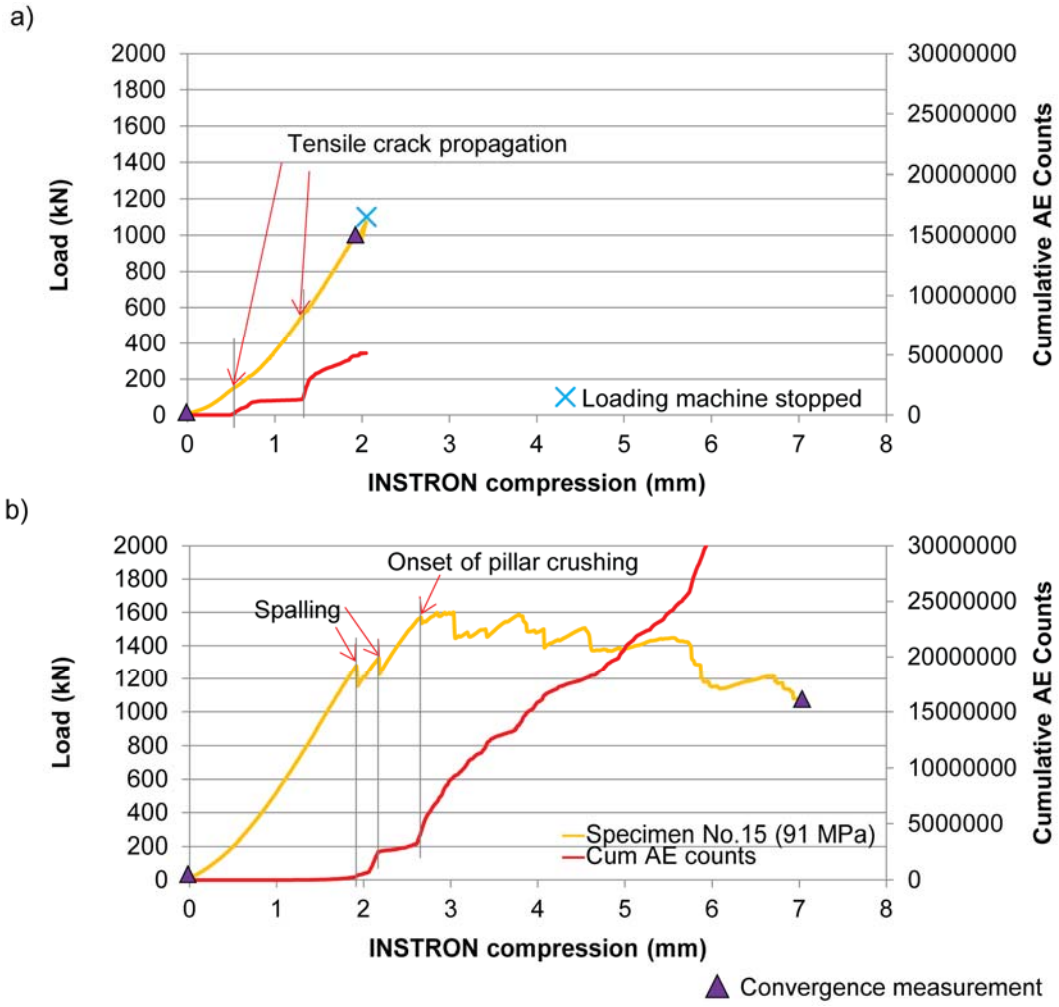

Figure 9.2 Strain measurement point of Specimen No.15 a) the first loading b) the second loading.

9.2 Data Correction

The laser scanner was mounted on the bottom steel plate as shown in Figure 9.3. Since the top plate was fixed and the vertical load was applied from the bottom to specimens, the laser scanner shifted with the bottom plate movement. Therefore the measurement data required connections before a strain calculation could take place.

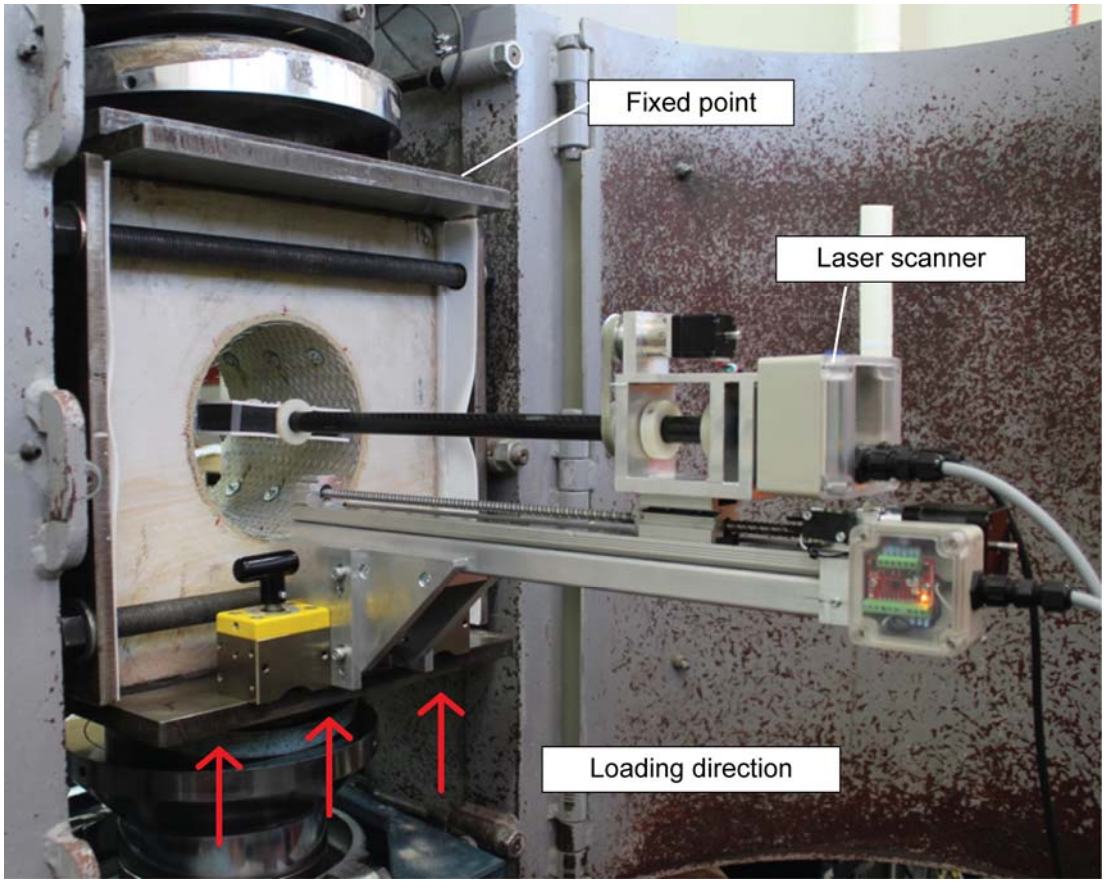

Figure 9.3 Laser scanner settings.

As shown in Figure 9.4, the laser scanner was initially set to be centralised within a circular excavation. As the bottom plate moved, the entire laser scanner system raised and the laser measurement base point deviated from the excavation centre (Figure 9.5). To understand radial strains more accurately, the data was corrected after acquisition. During the measurement, the laser head was rotated around 360 °. The distance from the laser measurement base point to the tunnel surface was recorded with the rotation angle data (Figure 9.6). The data was corrected for changes in the laser measurement base point.

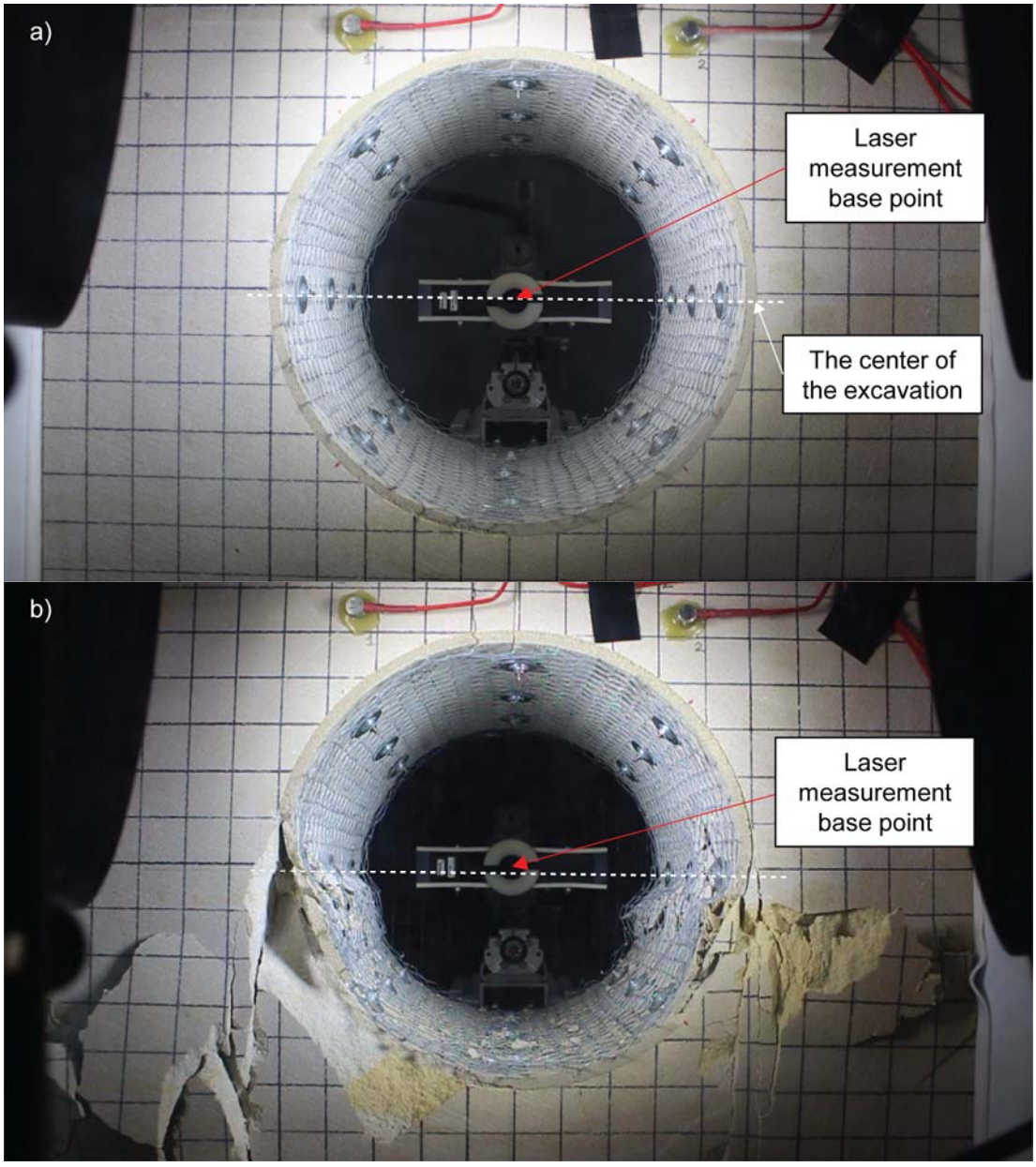

Figure 9.4 Strain measurement by the laser scanner a) before loading b) after failure.

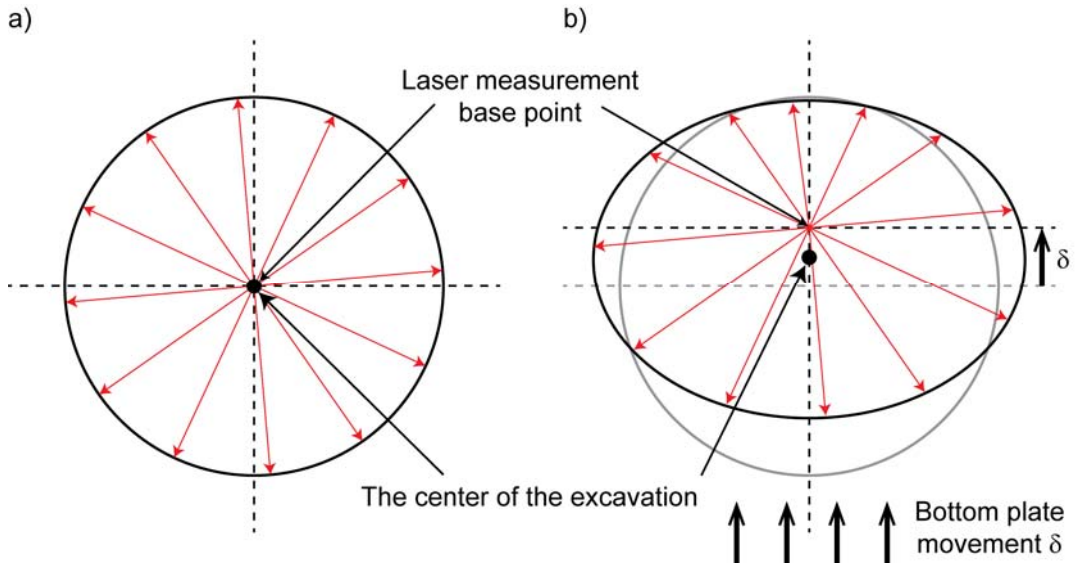

Figure 9.5 Laser scanned data scheme a) measurement before loading b) measurement after loading.

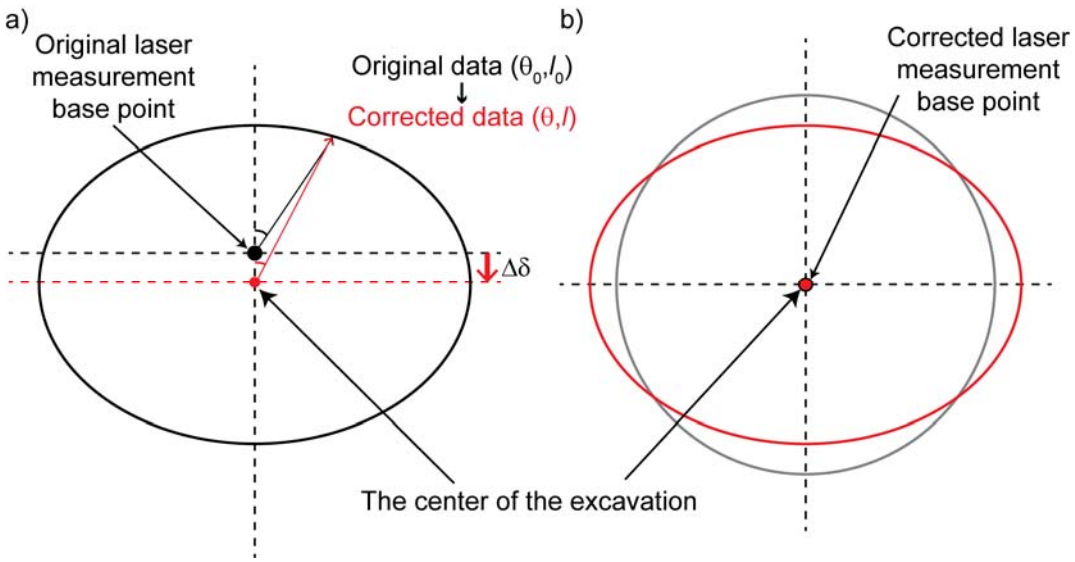

Figure 9.6 Data correction concept a) measurement data correction method b) measurement data after correction.

In this correction, it is assumed that the tunnel deformation occurred radially. The data correction amount was obtained from the load displacement curve. When the loading started, the displacement values showed a moderate increase (Figure 9.7). It is assumed that the initial compression occurred in the rubber sheets rather than the specimen

deformation. After they were compressed, the load increased linearly until reaching the spalling level.

The data correction amount $\Delta\delta$ is decided as a half of the bottom plate movement obtained as the equation below;

$$\Delta\delta = \frac{1}{2}(\delta - \delta_0) \tag{9.1}$$

where δ is the loading machine compression and δ_0 is the initial displacement determined from the load displacement curve.

Therefore, the corrected data (θ, l) can be obtained using following equations.

$$l = \sqrt{(l_0 \sin\theta_0)^2 + (l_0 \cos\theta_0 + \Delta\delta)^2} \tag{9.2}$$

$$\theta = \tan^{-1}\left(\frac{l_0 \sin\theta_0}{l_0 \cos\theta_0 + \Delta\delta}\right) \tag{9.3}$$

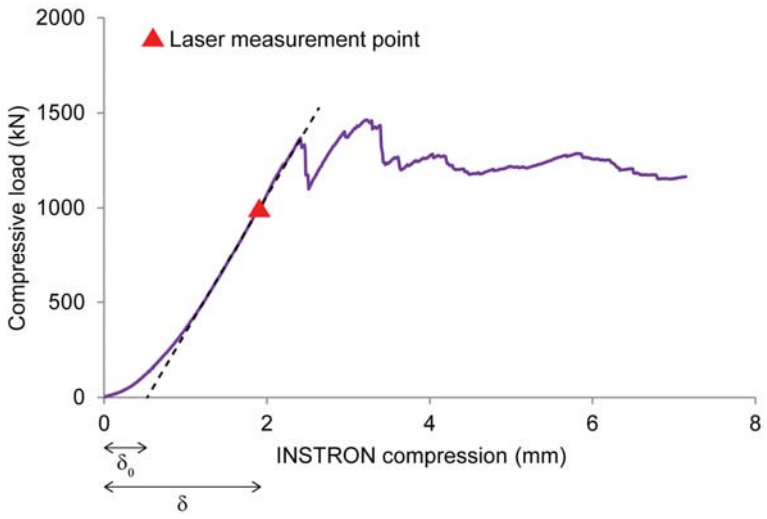

Figure 9.7 Data correction values from load displacement curve

9.3 Initial Measurement

In all cases, a laser scanning was conducted before the loading started. This data was used as a basepoint for subsequent strain calculations. The scanned data was plotted in

3D view with excavation surface in Figure 9.8. In all cases, a chain link mesh was applied onto a shotcrete surface and they were fixed by reinforcement. The scanned data reflected the excavation surface condition very well with the rows of reinforcement clearly seen. Figure 9.9 shows an example of excavation surface view plotted by a laser scanning result. The chain link mesh and reinforcement materials are clearly identified.

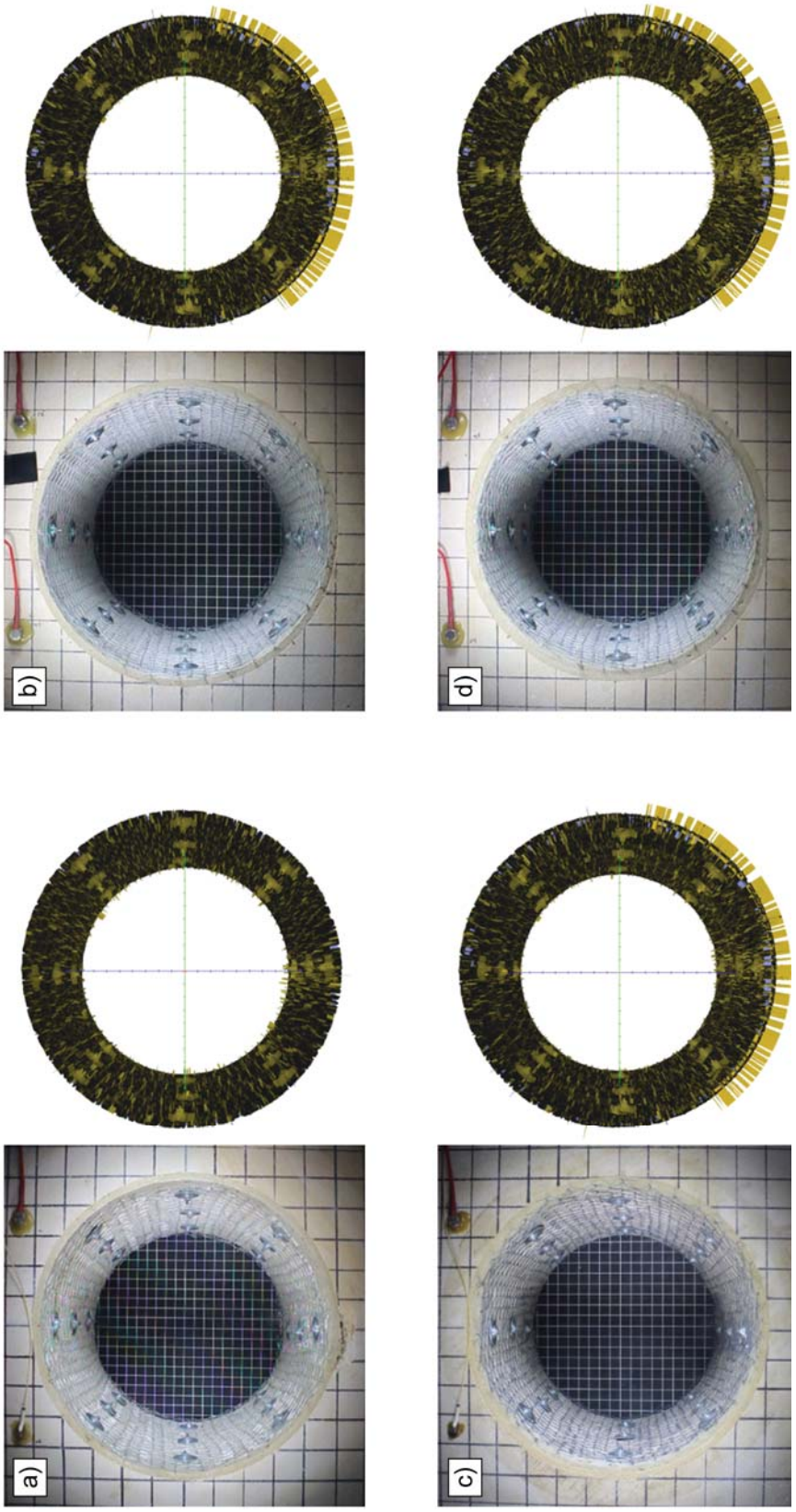

Figure 9.8 Excavation surface and 3D views by laser scanning before testing a) Specimen No.11 b) Specimen No.12 c) Specimen No. 14 d) Specimen No.15.

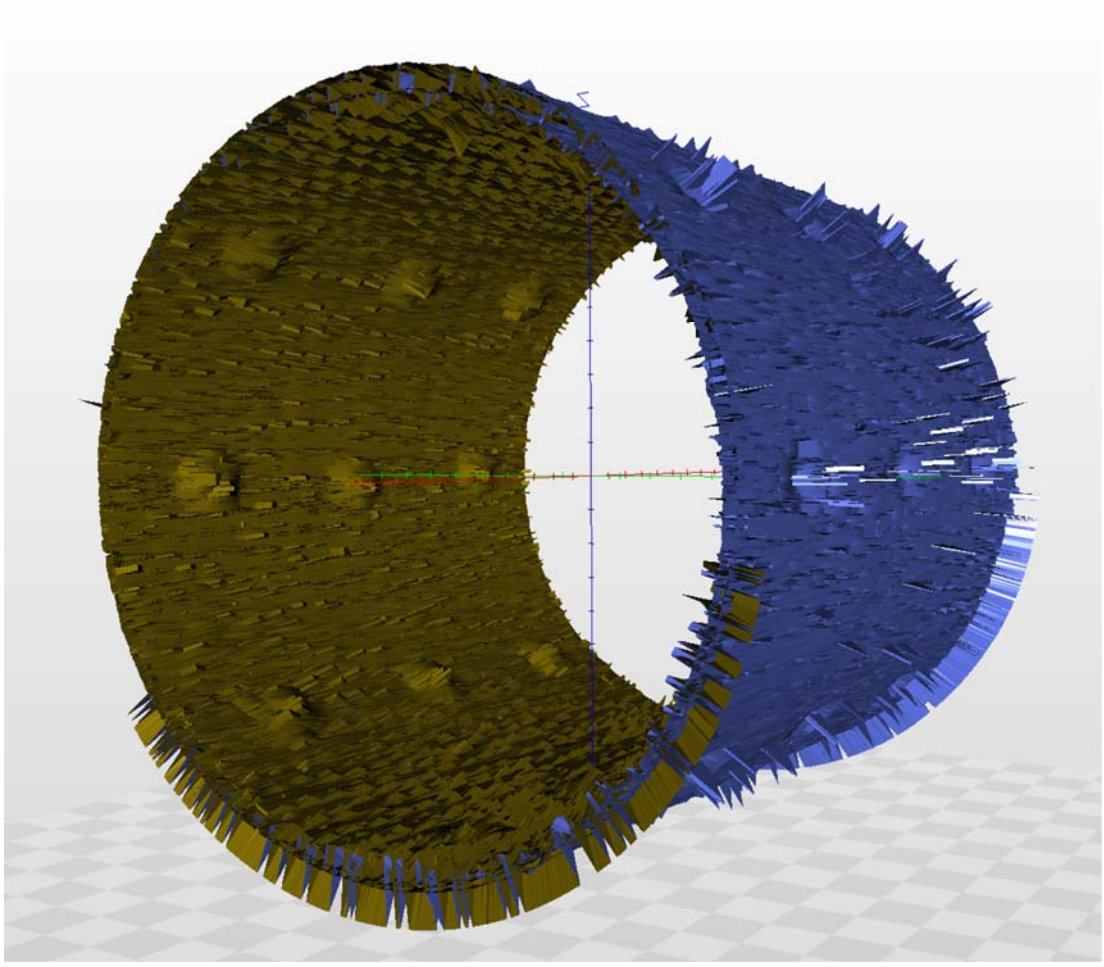

Figure 9.9 Example of an inside sight of 3D view.

9.4 Excavation Behaviour before Spalling

A laser scanning was conducted before spalling occurred in Sample No.12 and 15. The loading was held for 30 min and restarted again after the measurements were completed.

9.4.1 Kirsch Solution

A stress distribution around a circular excavations in the elastic condition is well described by Hoek and Brown (1980). Even though the specimens used in their experiments did not have enough pillar width to strictly comply elastic theory, the stress distribution was confirmed as to be close to an elastic condition, as indicated by the numerical modelling (see Chapter 7).

Assuming tunnel elasticity, the deformation can be calculated using the Kirsch solution as below.

$$u_r = \frac{p_1+p_2}{4G} + \frac{p_1-p_2}{4G}(3-4\nu)\cos 2\theta \qquad (9.4)$$

Where u_r is tunnel deformation, p_1 and p_2 are applied load ($p_1 > p_2$), θ is deformation angle and G and ν are Young's modulus and Poisson's ratio respectively. Figure 9.10 shows an example of deformed shape of the 200 mm diameter circular tunnel under 1000 kN compression. A circular tunnel shape become an ellipse under uniaxial compression.

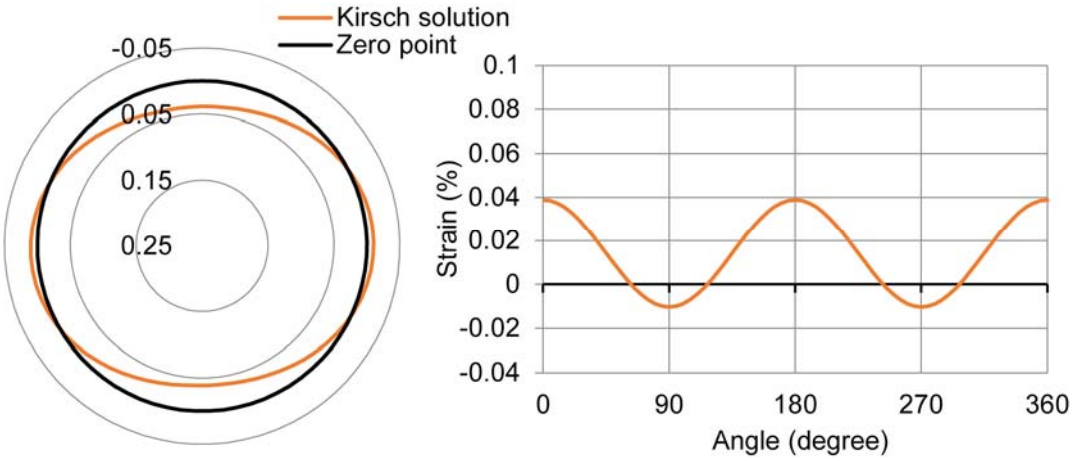

Figure 9.10 An example of elastic deformation calculated by the Kirsch solution.

9.4.2 Strain before Spalling

Figure 9.11 shows the excavation behaviour before spalling (1000 kN) for Specimens No.12 and 15. In both cases, tensile cracks had already propagated in the vertical direction from both the top and bottom of the excavations. There was no other damage seen on the excavation surface or adjacent pillars. Figure 9.12 shows 3D view before spalling occurred.

The strain was obtained by calculating a difference from the initial laser scanning results. Figure 9.13 shows the average strain for two configurations. The scanning was conducted for every 0.072 degrees, however, the data shown in the Figure 9.13 was

shown for every degree to simplify the results. In both cases, excavation deformed into an ellipse shape which is similar with the Kirsch solution shown the earlier in Figure 9.10. It can be said that the excavation behaved in an elastic manner at this stage of the loading. The spikes were due to laser reflection with the chain link mesh and reinforcement and also due to roughness of the excavation surface.

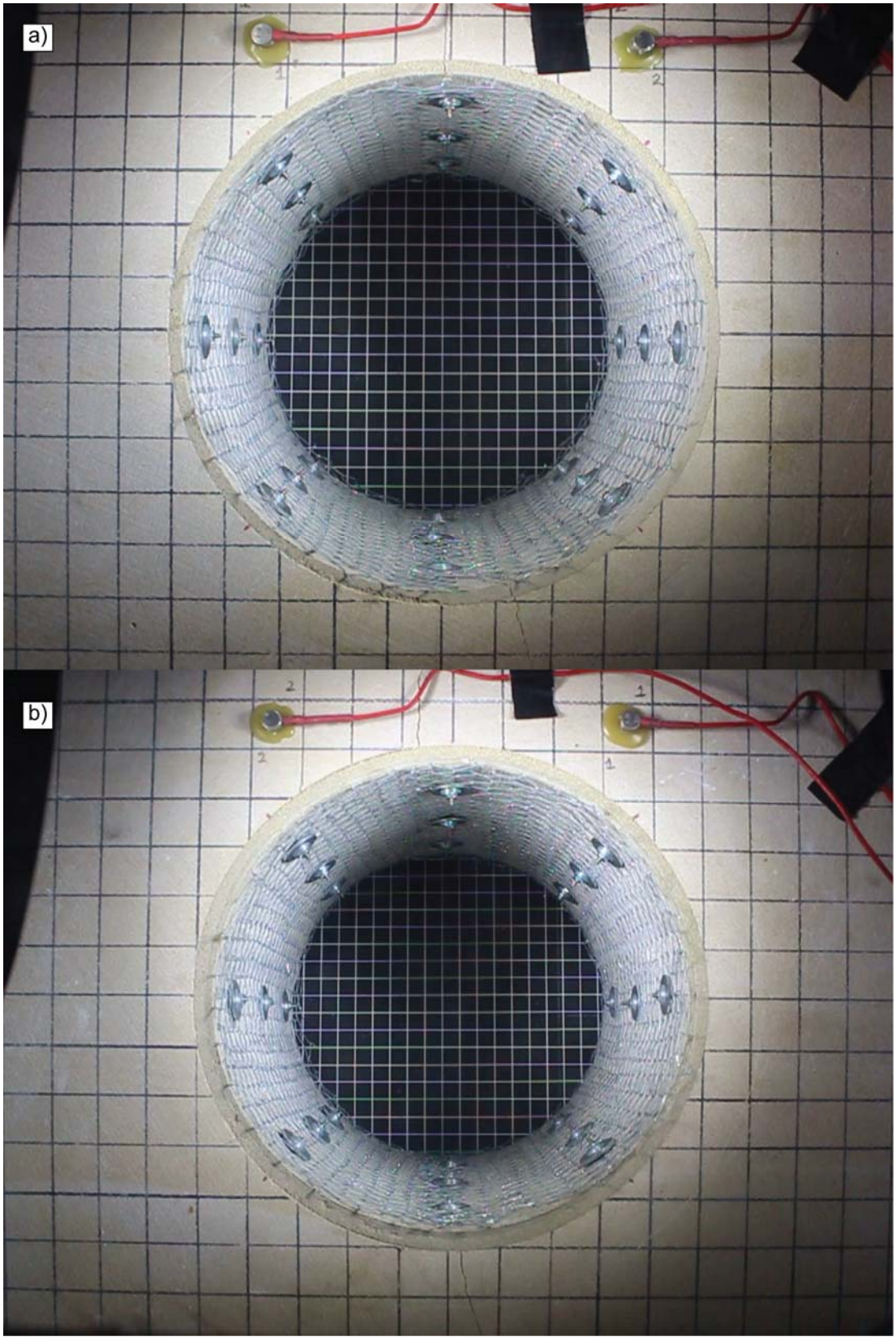

Figure 9.11 Specimens before spalling a) Specimen No.12 b) Specimen No.15.

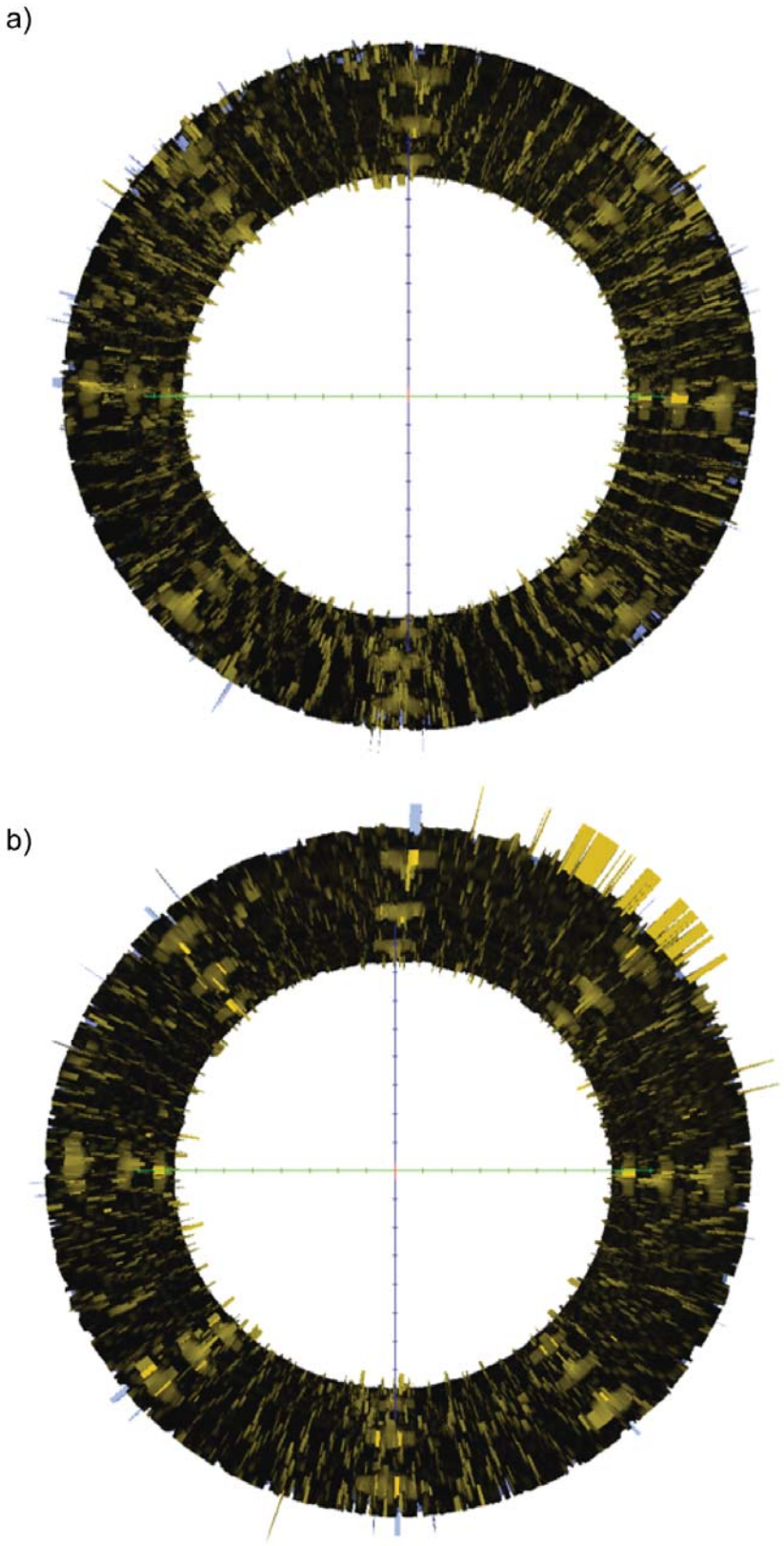

Figure 9.12 Three dimensional views before spalling.

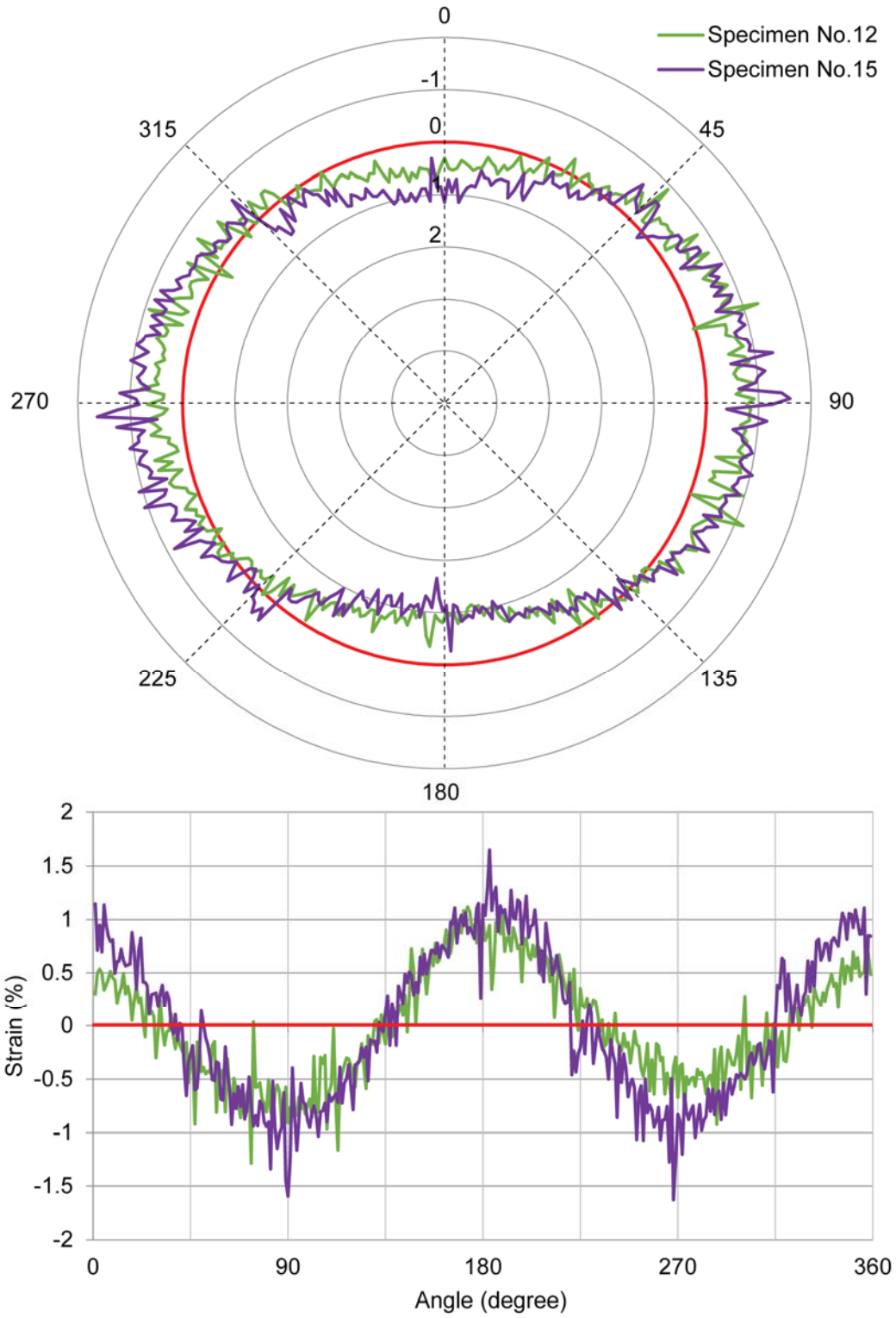

Figure 9.13 Average strain profile before spalling.

9.5 Excavation Behaviour after Failure

The last laser scanning was conducted after spalling and pillar crushing were observed.

9.5.1 Three Dimensional View

The excavation surfaces after failure and 3D views from the laser scanning are shown in Figure 9.14 to Figure 9.17. More damage was experienced on Samples No.11 and 12 (Figure 9.14 and Figure 9.15) compared with Samples No. 14 and 15 (Figure 9.16 and Figure 9.17). The details of two different surface support behaviour was described in Chapter 8. The observed damage on the excavation was scanned and projected on 3D view very well.

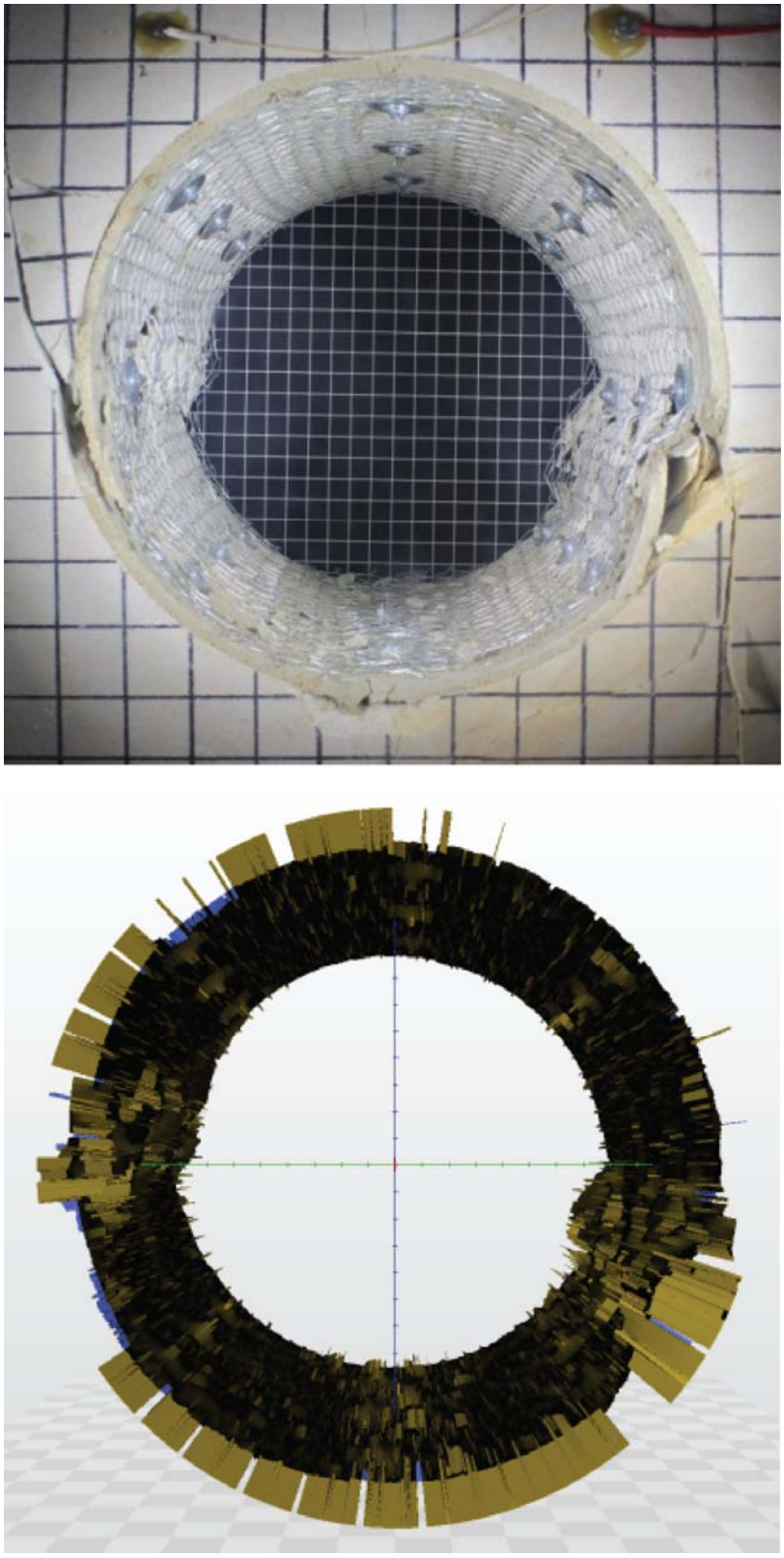

Figure 9.14 Comparison of 3D view and excavation surface after failure of Specimen No.11.

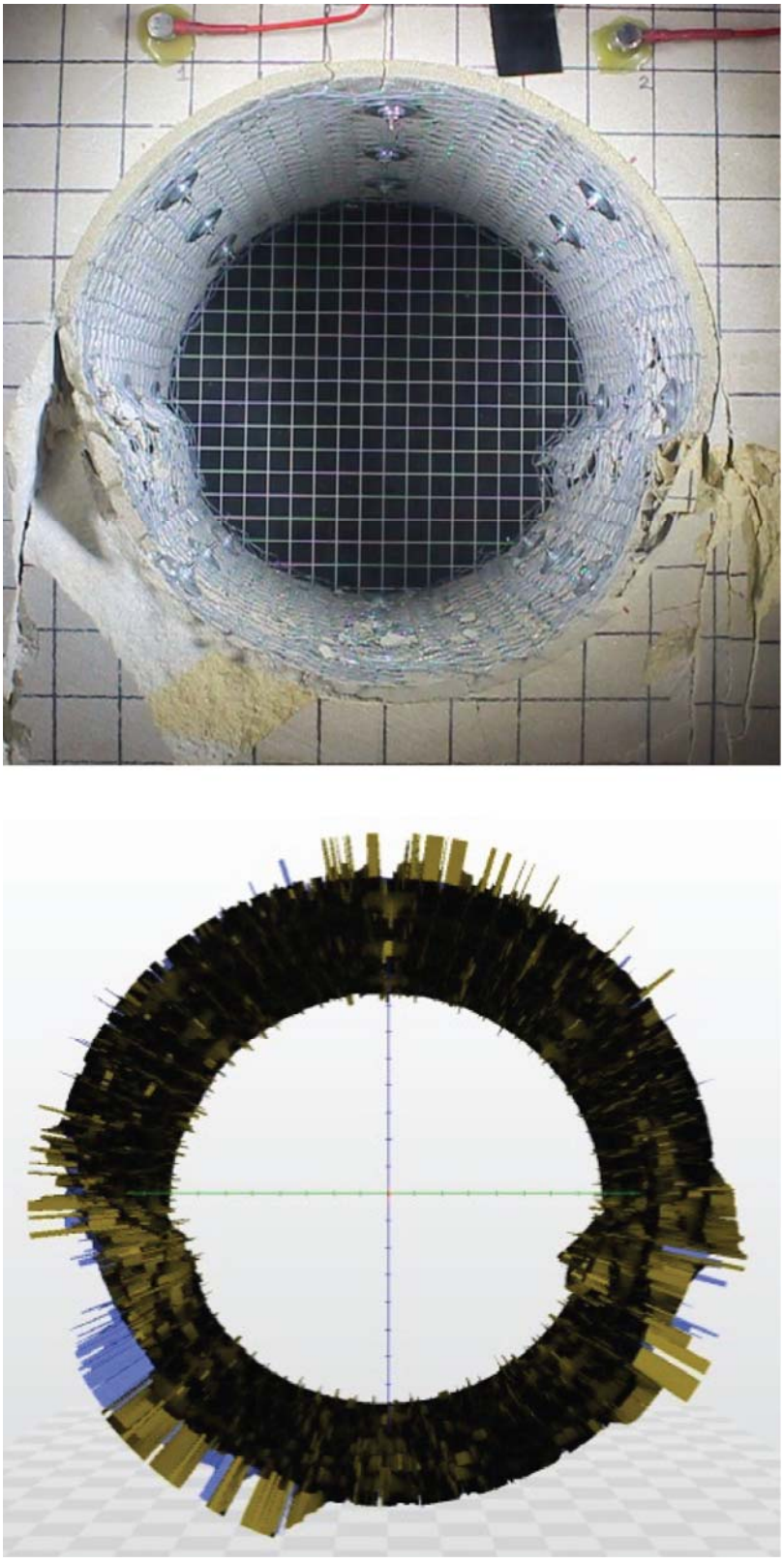

Figure 9.15 Comparison of 3D view and excavation surface after failure of Specimen No.12.

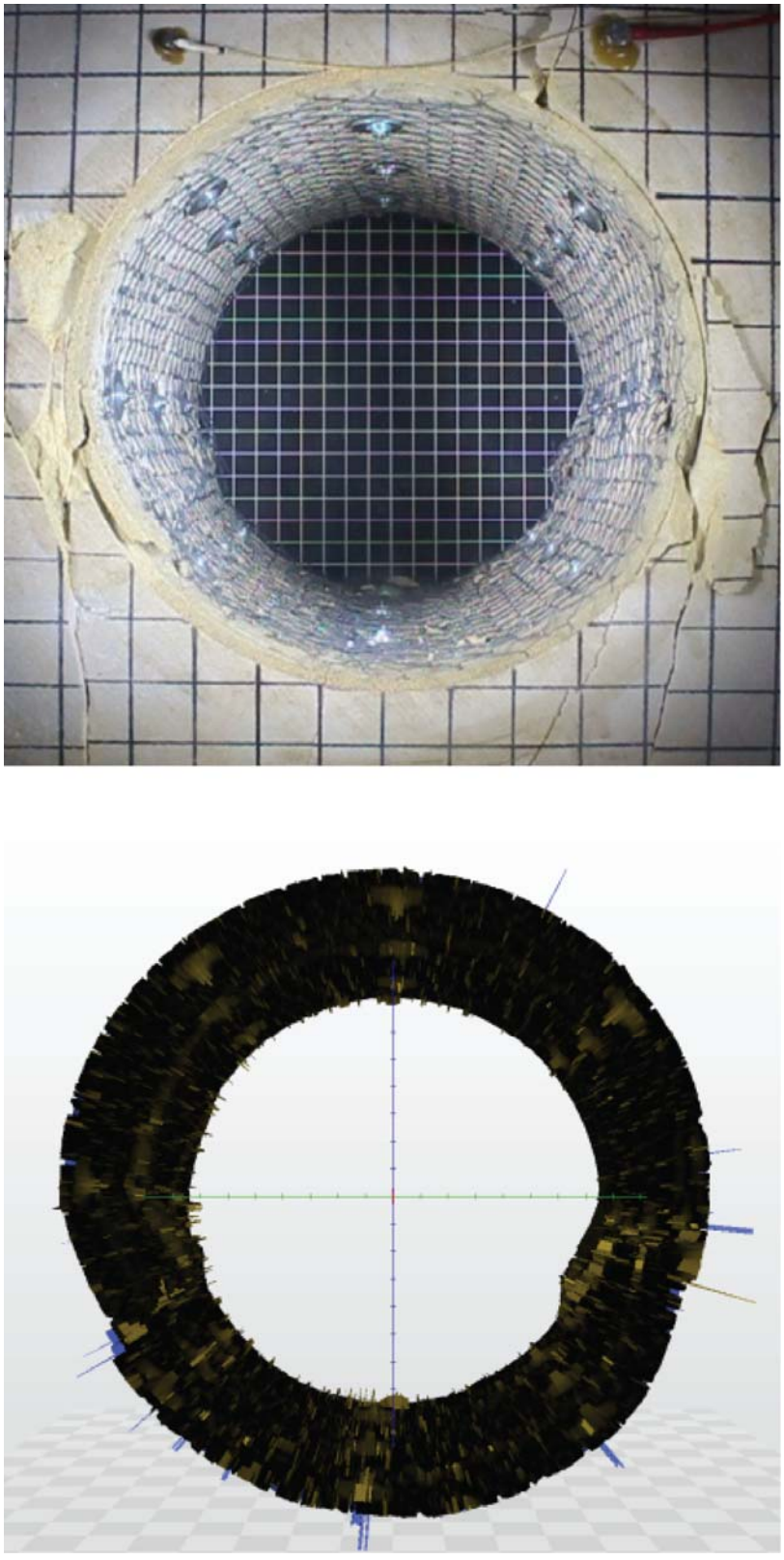

Figure 9.16 Comparison of 3D view and excavation surface after failure of Specimen No.14.

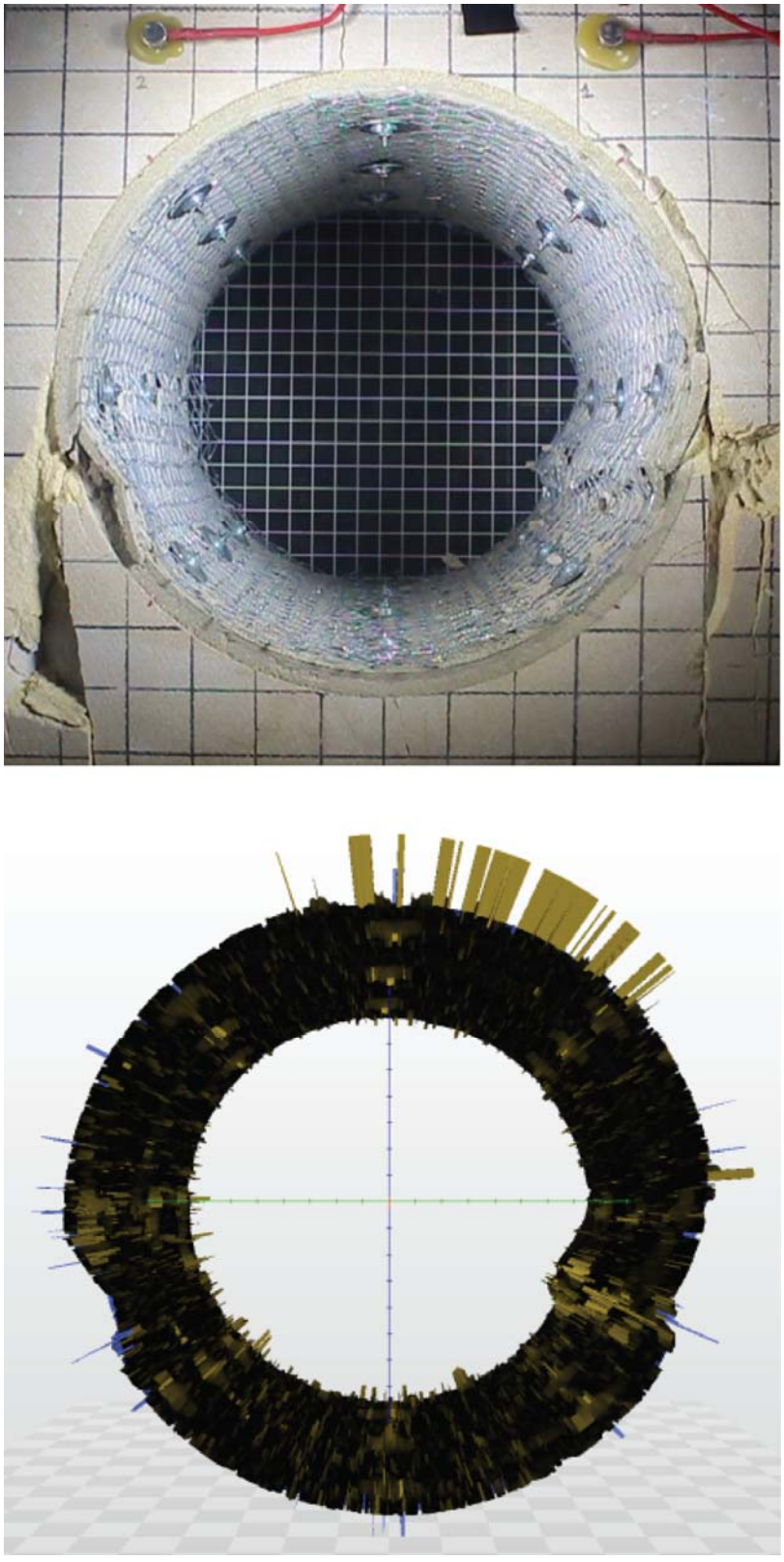

Figure 9.17 Comparison of 3D view and excavation surface after failure of Specimen No.15.

9.5.2 Strain Data

Figure 9.18 shows the calculated strain after failure for the four specimens. The strain profiles of all the scans were plotted and the average value is represented as a red line. The reinforcement positions were marked in red dash lines. In all the cases, damage was concentrated on both sides of the tunnel walls between the reinforcement spacing, i.e. 90 to 135 and 225 to 315 degrees. Generally, the maximum strain values were 15% in all the cases. The data shows that for Specimens No.14 and 15 an additional 3 mm thickness of shotcrete layer was applied, and the actual deformation was smaller than Specimens No.11 and 12.

Figure 9.19 shows the combined average strain profiles after failure. Vertical convergence of approximately 4 % and 5 % was experienced on the top and bottom of the excavation respectively. The convergence was restrained at the horizontal level (90 and 180 degree) by the reinforcement system. In case of the Specimen No.11, the reinforcement at 180 degree failed and the shotcrete panel was detached from the excavation surface with broken reinforcement system.

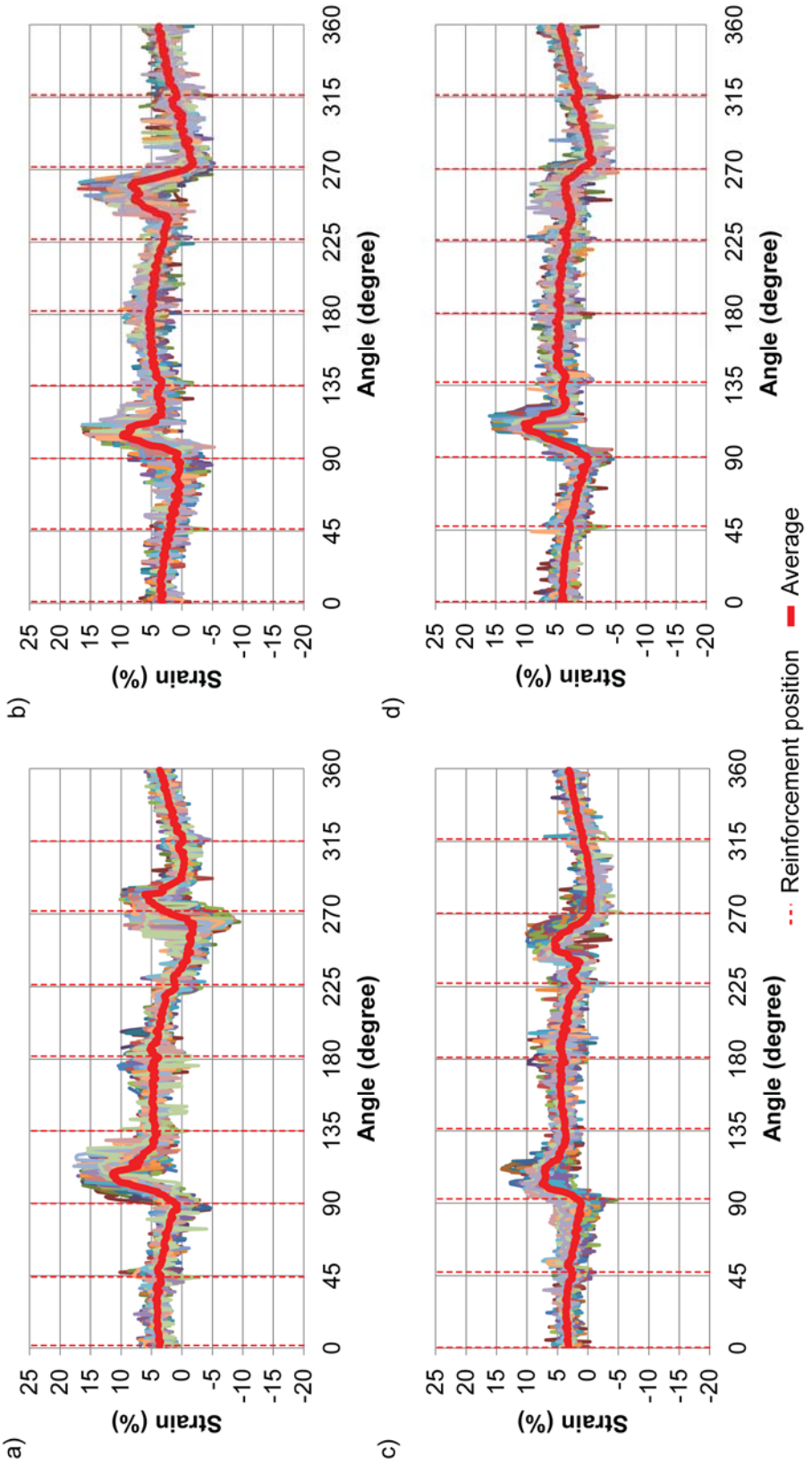

Figure 9.18 Strain profiles after failure a) Specimen No.11 b) Specimen No.12 c) Specimen No.14 d) Specimen No.15

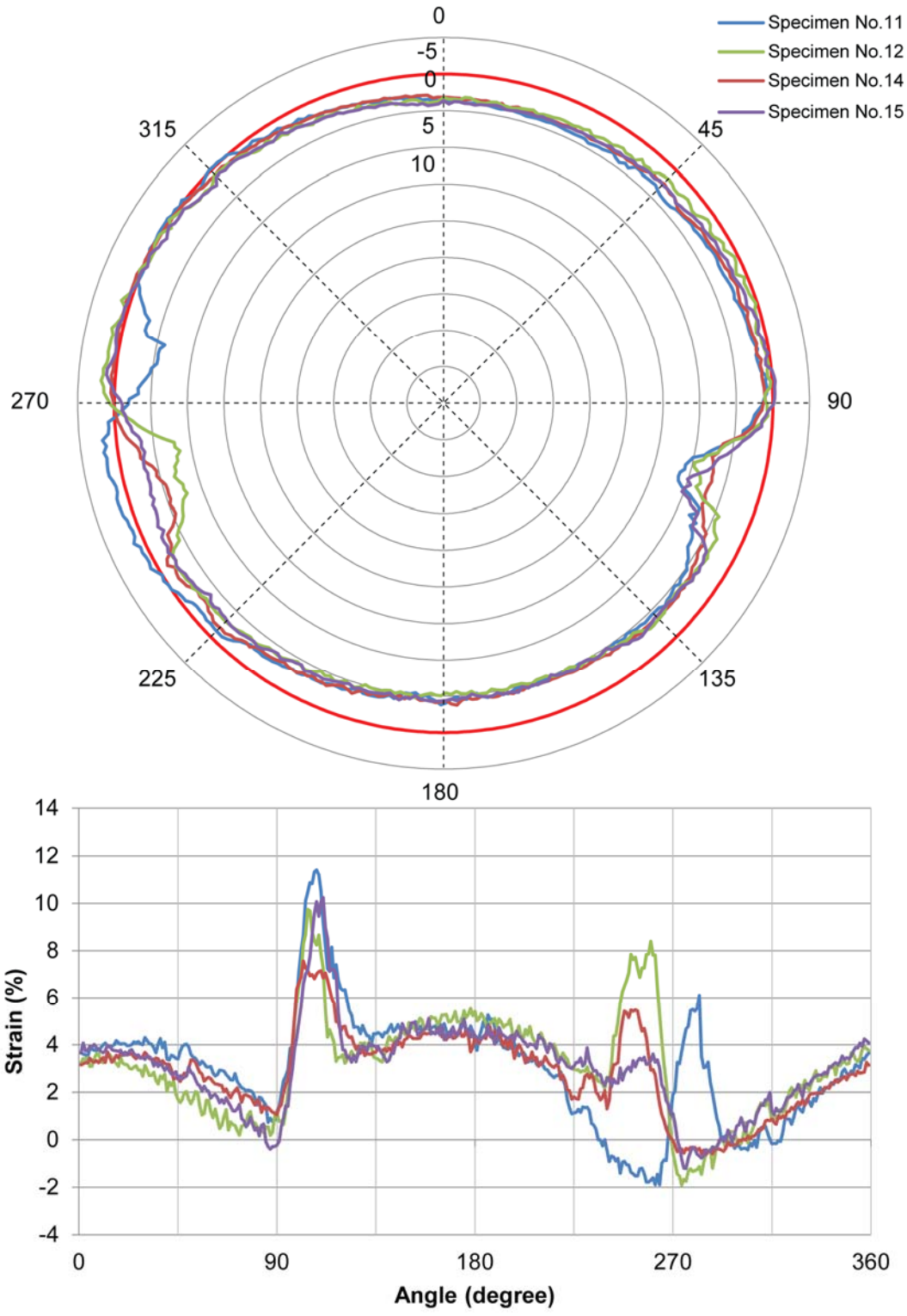

Figure 9.19 Combined average strain profile after failure.

9.5.3 Closure at Failure

Figure 9.20 shows excavation closures after failure. It is very clear that damages were experienced between reinforcement spacing (45 to 90 and 90 to 135 degrees). In case of Specimens No.11 and No.15, damage profile was asymmetry as shown in Figure 9.14 and Figure 9.17. Therefore, damaged was concentrated between 90 to 130 degrees. Both Specimens No.12 and No.14 had a similar symmetry damage profiles and more closure was experienced in case of single layer. Maximum of 8 mm closure in Specimen No.12 and 7 mm in Specimen No.14, i.e. both are equal to 4 % convergence were experienced.

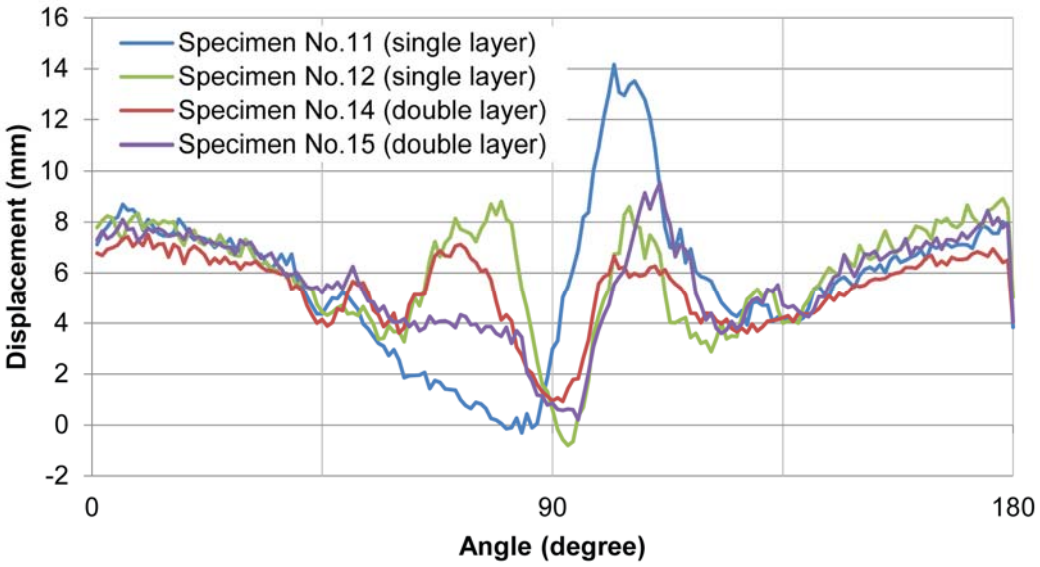

Figure 9.20 Excavation closure after failure.

9.5.4 Results Variability

Figure 9.21 and Figure 9.22 shows the excavation surface after failure. More damage was seen with a single layer surface support compared with a double layer surface support. In addition to horizontal cracks, vertical cracks were also propagated and the shotcrete panels were crushed into small pieces (Figure 9.21). On the other hand Figure 9.22 shows more controlled failure with less cracking away from main failure geometry.

A normal distribution of strain was plotted in Figure 9.23. It shows the dispersion of each scan results with respect to from the average strain value which in defined by the zero value. With a double layer, the failure profiles were less disperse compared with a single layer surface support. The normal deviation is summarized in Table 9.2.

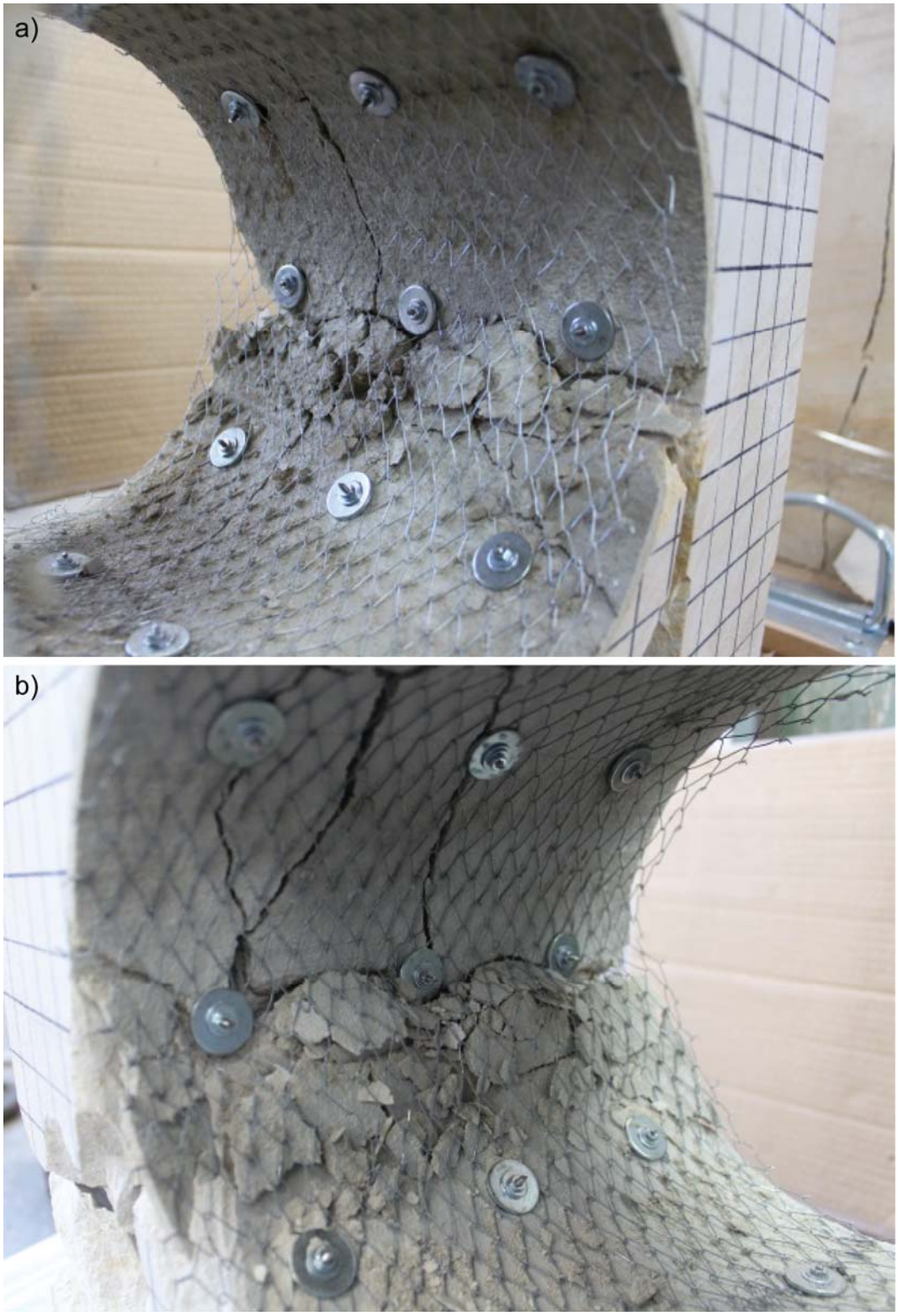

Figure 9.21 Excavation surface with a single layer after failure a) Specimen No.11 b) Specimen No.12.

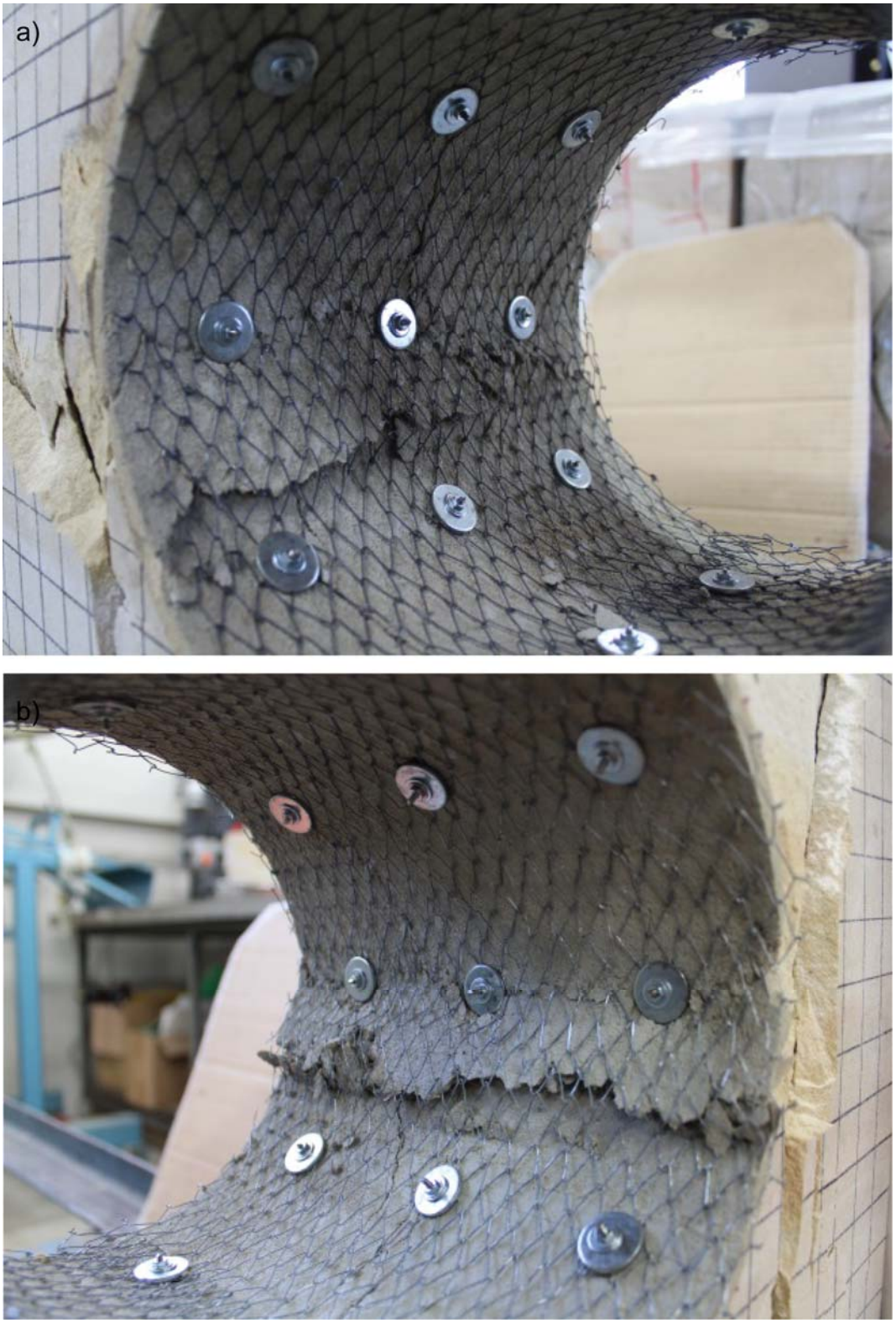

Figure 9.22 Excavation surface with a double layer after failure a) Specimen No.14 b) Specimen No.15.

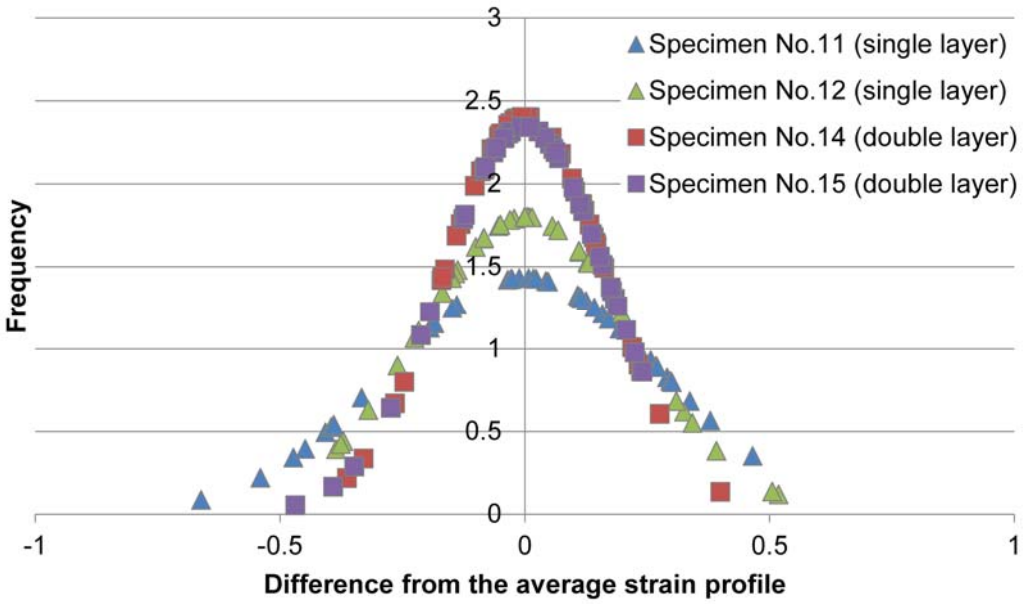

Figure 9.23 Normal distribution of strain profiles.

Table 9.2 Normal deviation of strain profiles.

Specimen No.	Normal deviation
11	0.279
12	0.222
14	0.166
15	0.170

9.5.5 Damaged Volume

Figure 9.24 and Table 9.3 shows the calculated damage volume after failure. The data clearly shows that a double layer surface support helped to reduce the excavation surface damage. This difference was also seen in Figure 9.14 to Figure 9.17.

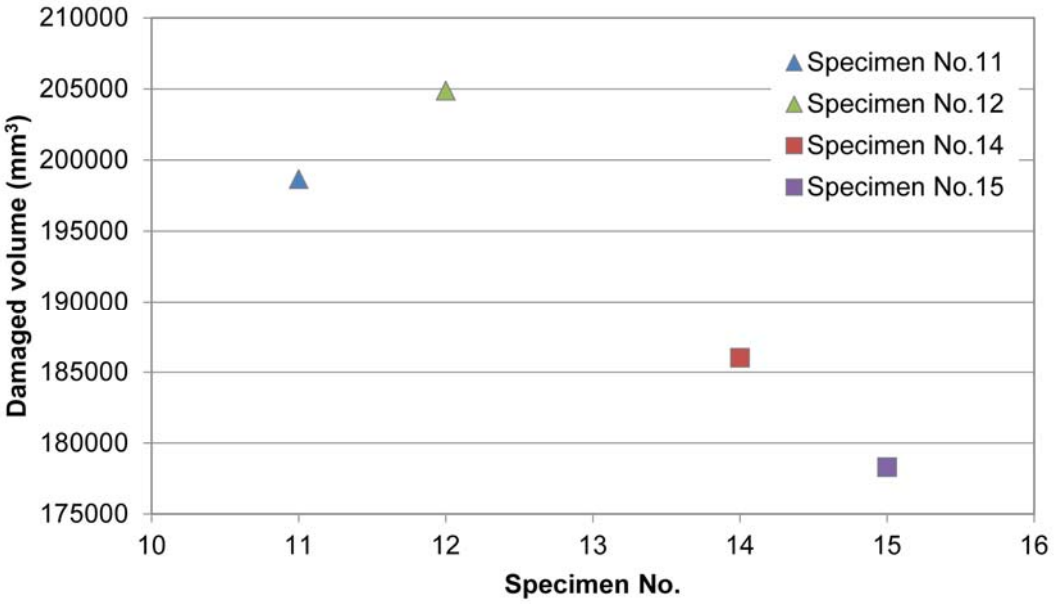

Figure 9.24 Damage volume after failure.

Table 9.3 Damaged volume summary after failure.

Specimen No.	Damage volume (mm^3)	Relative percentage (%)
11	198672	97
12	204880	100
14	186026	91
15	178318	87

9.6 Tunnel Deformation Summary

Laser scanning was conducted onto Specimens No.11, 12, 14 and 15 to monitor the excavation behaviour under loading. The two different ground support schemes were compared and examined in terms of internal damage. The measurement was undertaken before and after loading and before spalling occurred. The measurement results showed that the excavation behaved in an elastic manner before spalling occurred. After pillar crushing occurred, damages were experienced between reinforcement and a chain link mesh held broken materials in both surface support cases. The strain after failure reached approximately 15% with both ground support

schemes, however, the additional surface support layer significantly reduced the damage volumes and showed more controlled behaviour.

Chapter 10

Conclusions and Recommendations

10.1 Conclusions

The behaviour of excavations and surface support performance under progressive loading were studied in detail using scaled down tunnel experiments. The main finding are summarised in the following sections.

10.1.1 Observed Failure Mechanisms

Under progressive compression, various failure mechanisms were experienced around the tunnel walls. Damage on the excavation surfaces appeared before the stress reached the materials intact rock strength value. Spalling and violent ejection occurred when cracks propagated along entire excavation walls. Seismic activities showed no indication prior to spalling, but increase markedly during spalling.

Following spalling on both tunnel walls, shear failure was experienced within the adjacent specimen pillars. The load displacement curve showed a slight unloading during spalling, but the excavation continued taking load. The load displacement curves showed a peak value at the initiation of pillar crushing and then decreased with continuous damage until the end of the experiments. Cracks were propagated parallel to the loading direction and shear failure was also seen.

10.1.2 The Ratio of Strength to Induced Stress at Failure

Stress level that cause failure around circular excavation are a function of the intact rock strength material. The ratio of intact rock strength to induced stress at failure showed an increase with material strength. Spalling occurred as a result of extensile crack generation in compression, and corresponds well with previous research result (Li, 2004) and underground observations.

10.1.3 Rock Behaviour at Failure

At spalling, violent ejection was observed for high strength materials including strong sandstone and granite. For unsupported tunnels, ejection velocities become higher with material strength increase.

10.1.4 Comparison with a Full Scale Sized Tunnel

Scaled down tunnel results were compared with full scaled sized excavation. The results from laboratory scale tests compare well with data from full scale excavations from a number of pillar s suggesting that the ratio of strength to induced stress at the onset of spalling and pillar crushing are scale independent.

10.1.5 Ground Support Performance

The performance of various ground support schemes was investigated. Compared with unsupported tunnels of similar strength, the ground support schemes enhanced the stability, provided a control to excavation deformation and reduced the severity of damage. Different surface mesh support elements were compared as a part of ground support performance evaluation. Similar to underground observations, the chain link mesh showed more compatibility with surface movement compared with welded mesh. The shotcrete layer showed a good contact with excavation surface and failure occurred as distinctive plates within shotcrete layer.

10.1.6 Integrated Surface Support Performance under High Stress

As an integrated system, mesh reinforced shotcrete provided an immediate response to an excavation deformation. When crack initiate within the excavation sidewalls, the embedded mesh interlocks with the shotcrete layer and the detached slabs are retained by the mesh which transfers load to the reinforcing elements. However, detached materials can be ejected violently after spalling. On the other hand, when mesh was applied over a shotcrete layer, cracks were spread immediately and failed into small pieces in a brittle manner. No interaction was experienced between mesh and a shotcrete layer, however the detached shotcrete panels were contained within mesh layer and less materials were ejected at spalling. Finally, when the mesh was applied both underneath and over a shotcrete layer, both surface support material interaction and material retention was achieved at failure. and furthermore, internal damage was eased with additional shotcrete layer application.

10.2 Recommendations and Future Work

This research work consisted of a relative comparison of integrated surface support system performance and further work under stress induced failure.

The research has shown that higher strength materials are more likely to fail violently. Furthermore, stress induced failure on excavation surface could occur without any seismic indication. Therefore surface support with high energy dissipation capacities needs to be installed at condition where a stress induced failure would be expected.

The laboratory test indicated that the surface support installation sequences resulted in a different surface support performance. Therefore surface support capacities should be evaluated as an integrated system rather than individual components.

In the future, the results from the experiments can be used to calibrate numerical modellings to further optimise ground support schemes. Additional laboratory testing including high energy dissipation miniature bolts would allow better control of excavation deformation.

References

Andersson, J. C., & Martin, C. D. (2009). The Äspö pillar stability experiment: Part I—Experiment design. *International Journal of Rock Mechanics and Mining Sciences, 46*(5), 865-878. doi: http://dx.doi.org/10.1016/j.ijrmms.2009.02.010

Barla, G. (2014). TBM tunneling in deep underground excavation in hard rock with spalling behaviour. *Proceedings of the 43rd Geomechanics Colloquim*, 25-39.

Barton, N., Lien, R., & Lunde, J. (1974). Engineering classification of rock masses for the design of tunnel support. *Rock mechanics, 6*(4), 189-236. doi: 10.1007/BF01239496

Bieniawski, Z. T. (1967). Mechanism of brittle fracture of rock: Part I—theory of the fracture process. *International Journal of Rock Mechanics and Mining Sciences & Geomechanics Abstracts, 4*(4), 395-406.

Brady, B. H. G., & Brown, E. T. (2004). *Rock mechanics: for underground mining* (3rd ed.). Dordrecht, Netherlands: Kluwer.

Broch, E., & Sørheim, S. (1984). Experiences from the planning, construction and supporting of a road tunnel subjected to heavy rockbursting. *Rock Mechanics and Rock Engineering, 17*(1), 15-35. doi: 10.1007/BF01088368

Brown, E. T. (1981). *Rock characterization, testing & monitoring : ISRM suggested methods*. Oxford: Published for the Commission on Testing Methods, International Society for Rock Mechanics by Pergamon Press.

Cai, M., & Kaiser, P. K. (2014). In-situ Rock Spalling Strength near Excavation Boundaries. *Rock Mechanics and Rock Engineering, 47*(2), 659-675. doi: 10.1007/s00603-013-0437-0

Carter, B. J. (1992). Size and stress gradient effects on fracture around cavities. *Rock Mechanics and Rock Engineering, 25*(3), 167-186. doi: 10.1007/BF01019710

Christiansson, R., Hakala, M., Kemppainen, K., Siren, T., & Martin, C. D. (2012). *Findings From Large Scale In-situ Experiments to Establish the Initiation of Spalling*. Paper presented at the ISRM International Symposium-EUROCK 2012, Stockholm, Sweden.

Diederichs, M. S. (1999). *Instability of hard rockmass: the role of tensile damage and relaxation.* (Ph.D. Thesis), University of Waterloo.

Diederichs, M. S. (2003). Rock Fracture and Collapse Under Low Confinement Conditions. *Rock Mechanics and Rock Engineering, 36*(5), 339-381.

Diederichs, M. S. (2007). The 2003 Canadian Geotechnical Colloquium: Mechanistic interpretation and practical application of damage and spalling prediction criteria for deep tunnelling. *Canadian Geotechnical Journal, 44*(9), 1082-1116.

Diederichs, M. S., Kaiser, P. K., & Eberhardt, E. (2004). Damage initiation and propagation in hard rock during tunnelling and the influence of near-face stress rotation. *International Journal of Rock Mechanics and Mining Sciences, 41*(5), 785-812. doi: http://dx.doi.org/10.1016/j.ijrmms.2004.02.003

Drover, C., & Villaescusa, E. (2015). *Performance of Shotcrete Support Following Dynamic Loading of Mining Excavations.* Paper presented at the Shotcrete for Underground Support XII, Singapore.

Fairhurst, C. (1964). On the validity of the 'Brazilian' test for brittle materials. *International Journal of Rock Mechanics and Mining Sciences & Geomechanics Abstracts, 1*(4), 535-546. doi: http://dx.doi.org/10.1016/0148-9062(64)90060-9

Ghazvinian, E., Diederichs, M. S., Labrie, D., & Martin, C. D. (2015). An Investigation on the Fabric Type Dependency of the Crack Damage Thresholds in Brittle Rocks. *Geotechnical and Geological Engineering, 33*(6), 1409-1429. doi: 10.1007/s10706-015-9909-1

Ghazvinian, E., Diederichs, M. S., Martin, C. D., Hakala, M., Gorski, B., Perras, M., & Jacobsson, L. (2012). Prediction thresholds for crack initiation and propagation in crystalline rocks *ISRM Comission on Spall Prediction, Report on Testing Procedures*: International Society of Rock Mechanics.

Griffith, A. A. (1921). *The Phenomena of Rupture and Flow in Solids* (Vol. 221).

Haimson, B. C., & Herrick, C. G. (1989). *Borehole breakouts and in situ stress.* Paper presented at the Proceedings, 12th Annual Energy-Sources Technology Conference and Exhibition, Drilling Symposium. American Society of Mechanical Engineers, New York.

Hoek, E. (1965). *Rock Fracture Under Static Stress Conditions*: National Mechanical Engineering Research Institute, Council for Scientific and Industrial Research.

Hoek, E. (1999). Support for very weak rock associated with faults and shear zones. In E. Villaescusa, C. R. Windosor & A. G. Thompson (Eds.), *Rock Support & Reinforcement Practice in Mining* (pp. 19-32). Rotterdam: Balkema.

Hoek, E., & Brown, E. T. (1980). *Underground excavations in rock*. London: Institution of Mining and Metallurgy.

Hoek, E., Kaiser, P. K., & Bawden, W. F. (Eds.). (1995). *Support of Underground Excavations in Hard Rock*. Rotterdam: Balkema.

Hutchinson, D. J., & Diederichs, M. S. (1996). *Cablebolting in underground mines*. British Columbia, Canada: BiTech Publishers.

Knill, J. L., Cratchley, C. R., Early, K. R., Gallois, R. W., Humphreys, J. D., Newbery, J., . . . Thurrell, R. G. (1970). Geological Society Engineering Group Working Party report on the logging of rock cores for engineering purposes. *Quarterly Journal of Engineering Geology and Hydrogeology, 3*(1), 1-24.

Lajtai, E., & Dzik, E. (1996). Searching for the damage threshold in intact rock. *Rock Mechanics: Tools and Techniques, Aubertin, Hassani & Mitri (eds.), Balkema, 1*, 701-708.

Li, J. (2004). *Critical Strain of Intact Rock and Rock Masses.* (Ph.D. Thesis), Curtin University of Technology.

Lunder, P. J. (1994). *Hard rock pillar strength estimation: An applied empirical approach.* (MSc), University of British Columbia, British Columbia, Canada.

Martin, C. D. (1993). *The strength of massive Lac du Bonnet granite around underground openings.* (PhD. thesis), University of Manitoba Manitoba.

Martin, C. D. (1997). Seventeenth Canadian Geotechnical Colloquium: The effect of cohesion loss and stress path on brittle rock strength. *Canadian Geotechnical Journal, 34*(5), 698-725.

Martin, C. D., & Christiansson, R. (2009). Estimating the potential for spalling around a deep nuclear waste repository in crystalline rock. *International Journal of Rock Mechanics and Mining Sciences, 46*(2), 219-228. doi: http://dx.doi.org/10.1016/j.ijrmms.2008.03.001

Mathews, K. E., Hoek, E., Wyllie, D. C., & Stewart, S. B. V. (1980). Prediction of Stable Excavation Spans for Mining at Depths Below 1,000 Meters in Hard Rock. Ottwa, Ontario, Canada: Golder Associates Report to Canada Centre for Mining and Energy Technology (CANMET), Department of Energy and Resources.

Morton, E. C. (2009). *Static testing of large scale ground support panels.* (Thesis (M Sc)), Curtin University of Technology.

Morton, E. C., Thompson, A. G., & Villaescusa, E. (2009). *The performance of mesh, shotcrete and membranes for surface ground support.* Paper presented at the Rock Engineering in Difficult Conditions, Proceedings of the Third Canada-US Rock Mechanics Symposium and 20th Canadian Rock Mechanics Symposium, Tront, Ontario, Canada.

Murell, S. A. F. (1958). The strength of coal under triaxial compression. In W. H. Walton (Ed.), *Mechanical properties of non-metallic brittle materials* (pp. 123-145). London: Butterworths Scientific Publications.

Nicksiar, M., & Martin, C. D. (2013). Crack initiation stress in low porosity crystalline and sedimentary rocks. *Engineering Geology, 154*, 64-76. doi: http://dx.doi.org/10.1016/j.enggeo.2012.12.007

Ortlepp, W. (1997). *Rock fracture and rockbursts : an illustrative study*. Johannesburg: South African Institute of Mining and Metallurgy.

Ortlepp, W. D. (1993). High Ground Displacement Velocities Associated with Rockburst Damage. *Rockbursts and Seismicity in Mines 93*, 101-106.

Ortlepp, W. D., & Stacey, T. R. (1994). Rockburst mechanisms in tunnels and shafts. *Tunnelling and Underground Space Technology, 9*(1), 59-65. doi: http://dx.doi.org/10.1016/0886-7798(94)90010-8

Player, J. R., Morton, E. C., Thompson, A. G., & Villaescusa, E. (2008). *Static and dynamic testing of steel wire mesh for mining applications of rock surface support.* Paper presented at the The Sixth International Symposium on Ground Support in Mining and Civil Engineering Construction.

Rojat, F., Labiouse, V., Kaiser, P. K., & Descoeudres, F. (2009). Brittle Rock Failure in the Steg Lateral Adit of the Lötschberg Base Tunnel. *Rock Mechanics and Rock Engineering, 42*(2), 341-359. doi: 10.1007/s00603-008-0015-z

Thompson, A. G., Villaescusa, E., & Windsor, C. R. (2012). Ground Support Terminology and Classification: An Update. *Geotechnical and Geological Engineering, 30*(3), 553-580.

Thompson, A. G., Villaescusa, E., & Windsor, C. R. (2012). Ground Support Terminology and Classification: An Update. *Geotechnical and Geological Engineering, 30*(3), 553-580.

Villaescusa, E. (1999). *Laboratory testing of weld mesh for rock support.* Paper presented at the International Symposium on Rock Reinforcement Practice in Mining, Kalgoorlie.

Villaescusa, E. (2014). *Geotechnical Design for Sublevel Open Stoping*. Florida, USA: CRC Press.

Villaescusa, E., Azua, J. M., Player, J. R., & Morton, E. C. (2012, October 8019). *A database of static and dynamic energy absorption of mesh for rock support.* Paper presented at the Proceedings of the 2012 Australian Mining Technology Conference, Perth, Australia.

Villaescusa, E., & Schubert, C. J. (1999). Monitoring the performance of rock reinforcement. *Geotechnical and Geological Engineering, 17*(3-4), 321-333.

Villaescusa, E., Thompson, A. G., & Player, J. (2015). Dynamic Testing of Ground Support Systems. Report No. 312 (pp. 146): Minerals and Energy Research Institute of Western Australia.

Villaescusa, E., Thompson, A. G., Player, J. R., & Morton, E. C. (2010). Dynamic Testing of Ground Control Systems. Report No. 287 (pp. 187): Minerals and Energy Research Institute of Western Australia.

Appendix – A:

Circular Excavation Failure under Compression

A1 Unsupported Tunnel Result…….....218
A2 Ground Supported Tunnel Result (Single Layer, Specimen No.10)……229
A3 Ground Supported Tunnel Result (Double Layer, Specimen No.15)…..…..240

A1 Unsupported Tunnel

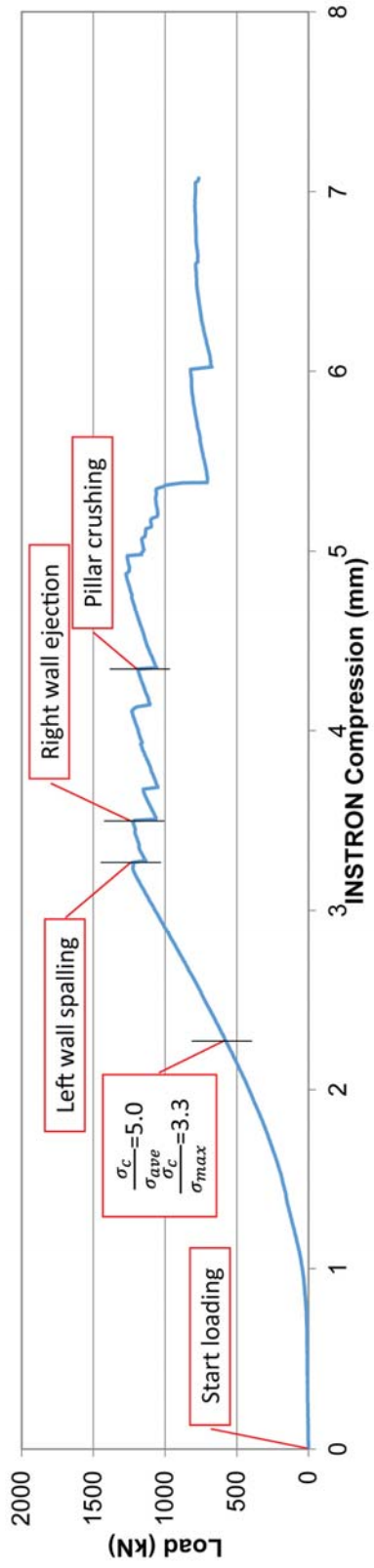

	Start loading (0:00)	$\frac{\sigma_c}{\sigma_{ave}}$=5 (4:37)	Left wall spalling (6:32)	Right wall ejection (7:00)	Pillar crushing (8:41)
Load (kN)	0	600	1227	1214	1191
INSTRON Compression (mm)	0	2.31	3.27	3.50	4.34
$\frac{\sigma_c}{\sigma_{max}}$	-	3.33	1.63	1.65	1.68
$\frac{\sigma_c}{\sigma_{ave}}$	-	5.00	2.45	2.47	2.52
	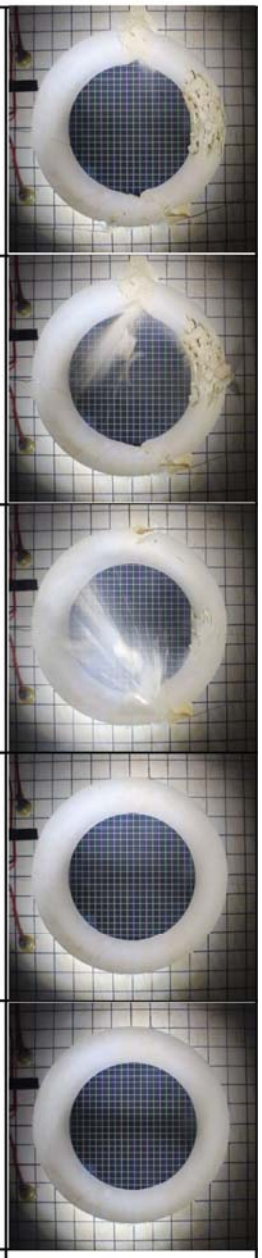				

Load displacement curve with tunnel behaviour.

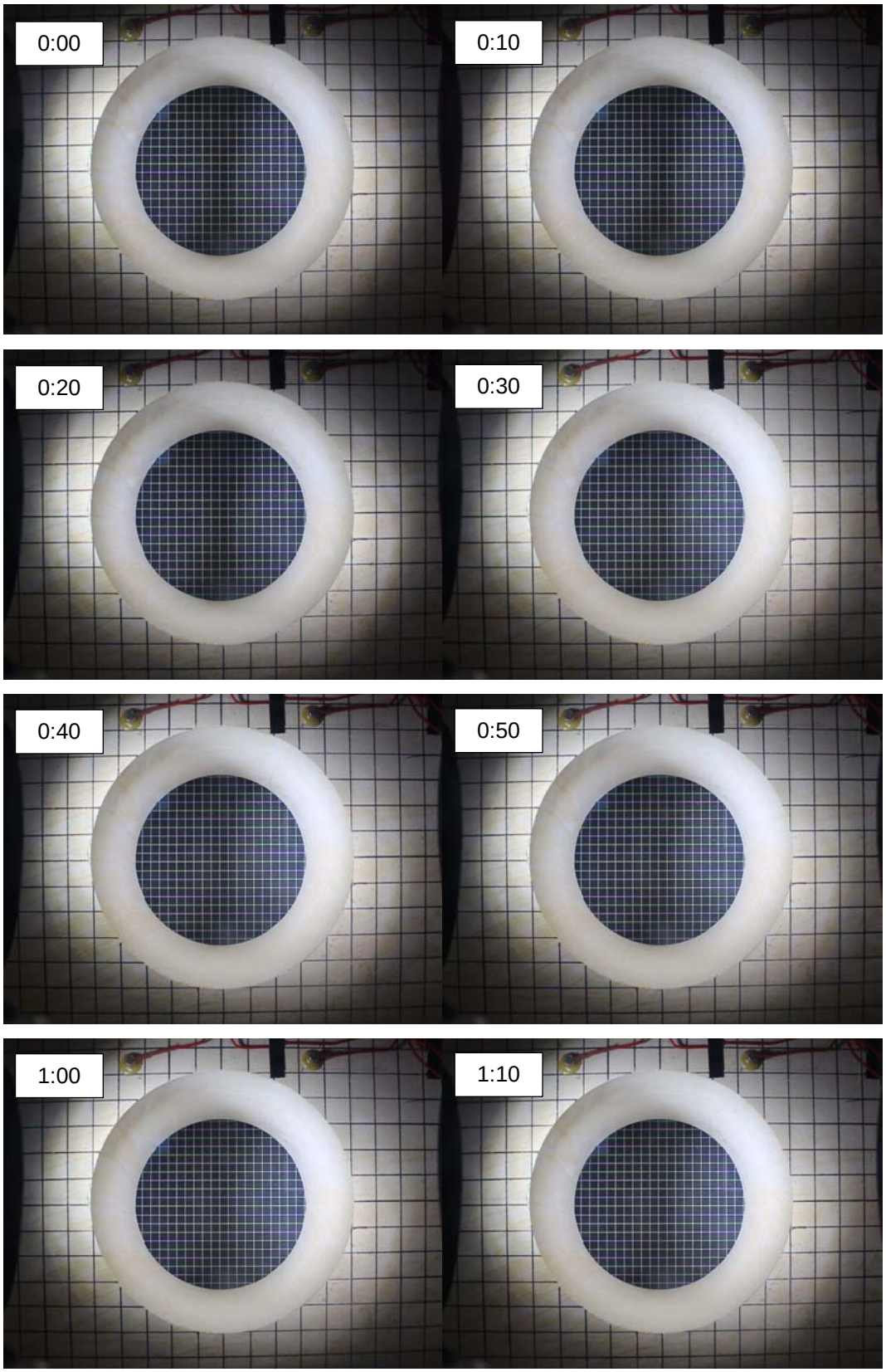
0:00
0:10
0:20
0:30
0:40
0:50
1:00
1:10

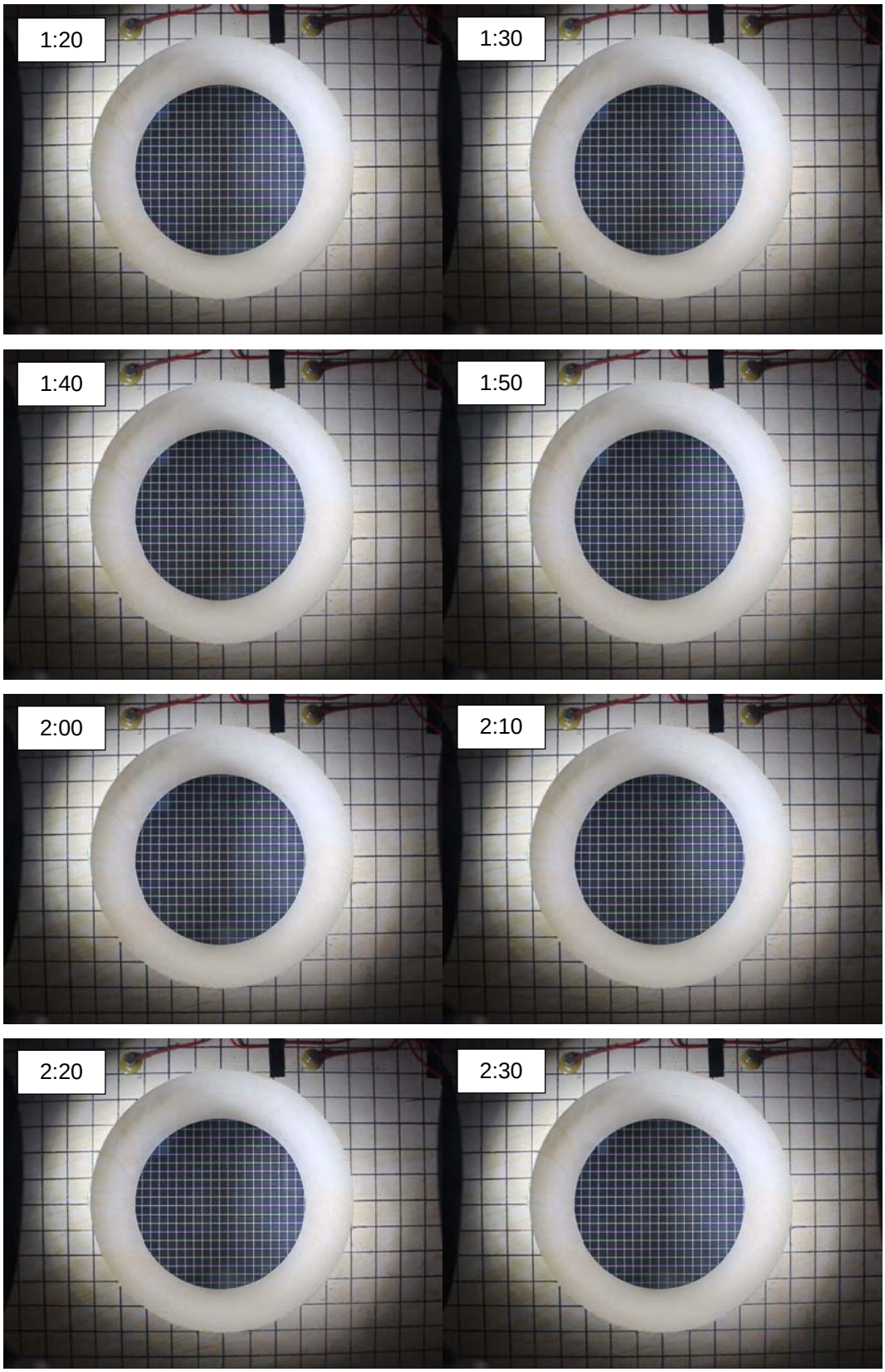
1:20
1:30
1:40
1:50
2:00
2:10
2:20
2:30

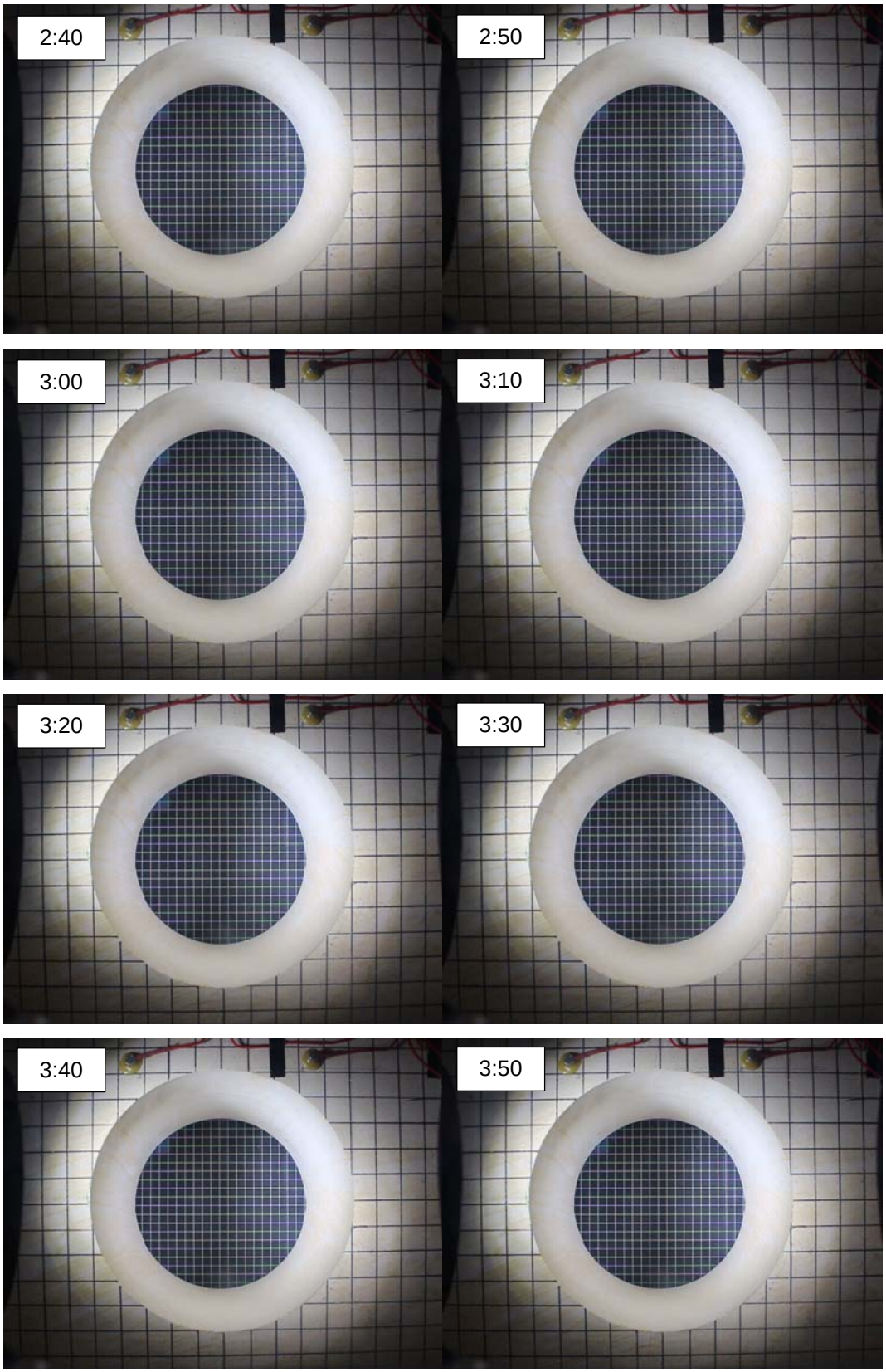
2:40
2:50
3:00
3:10
3:20
3:30
3:40
3:50

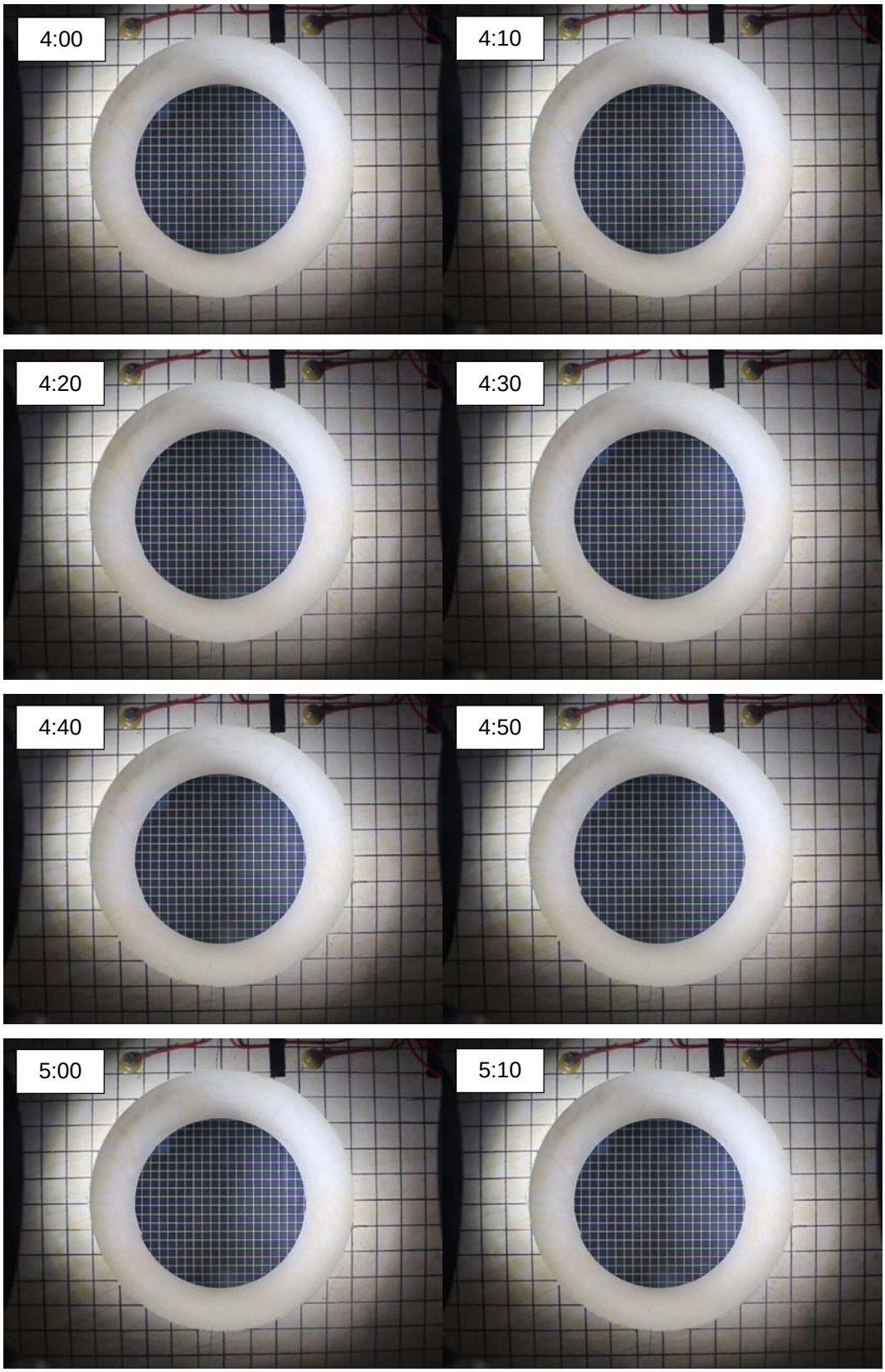
4:00
4:10
4:20
4:30
4:40
4:50
5:00
5:10

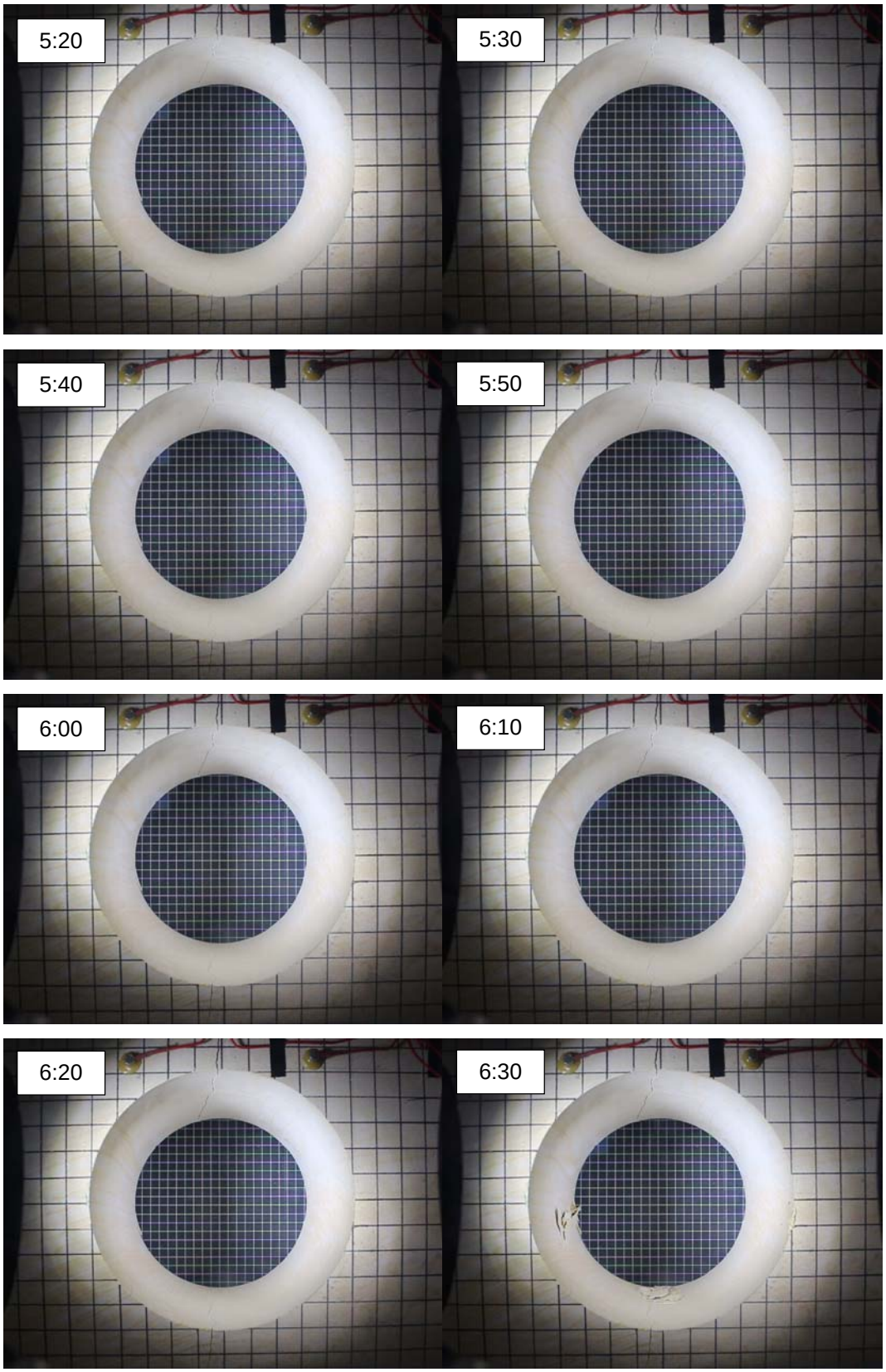
5:20
5:30
5:40
5:50
6:00
6:10
6:20
6:30

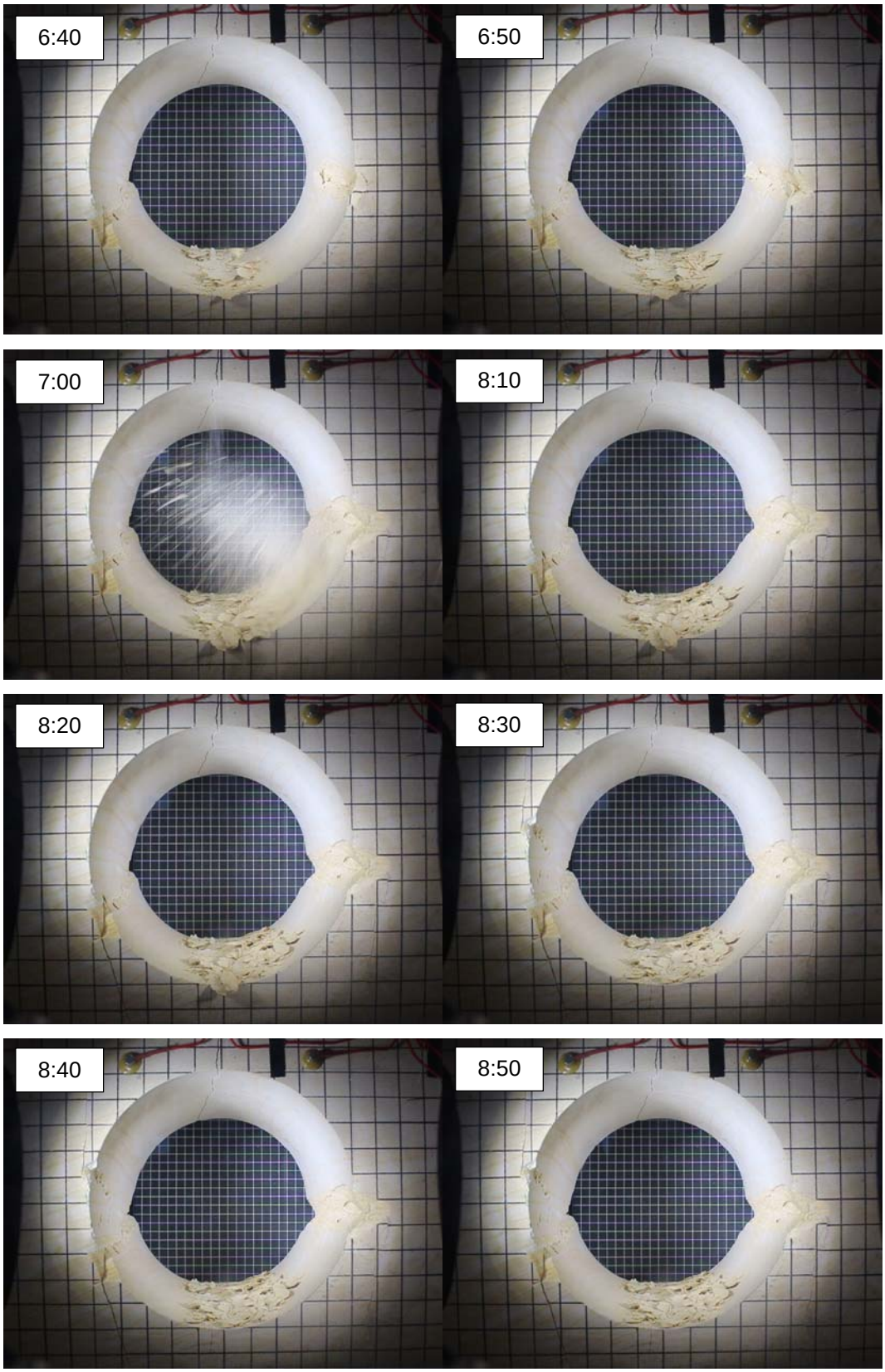
6:40
6:50
7:00
8:10
8:20
8:30
8:40
8:50

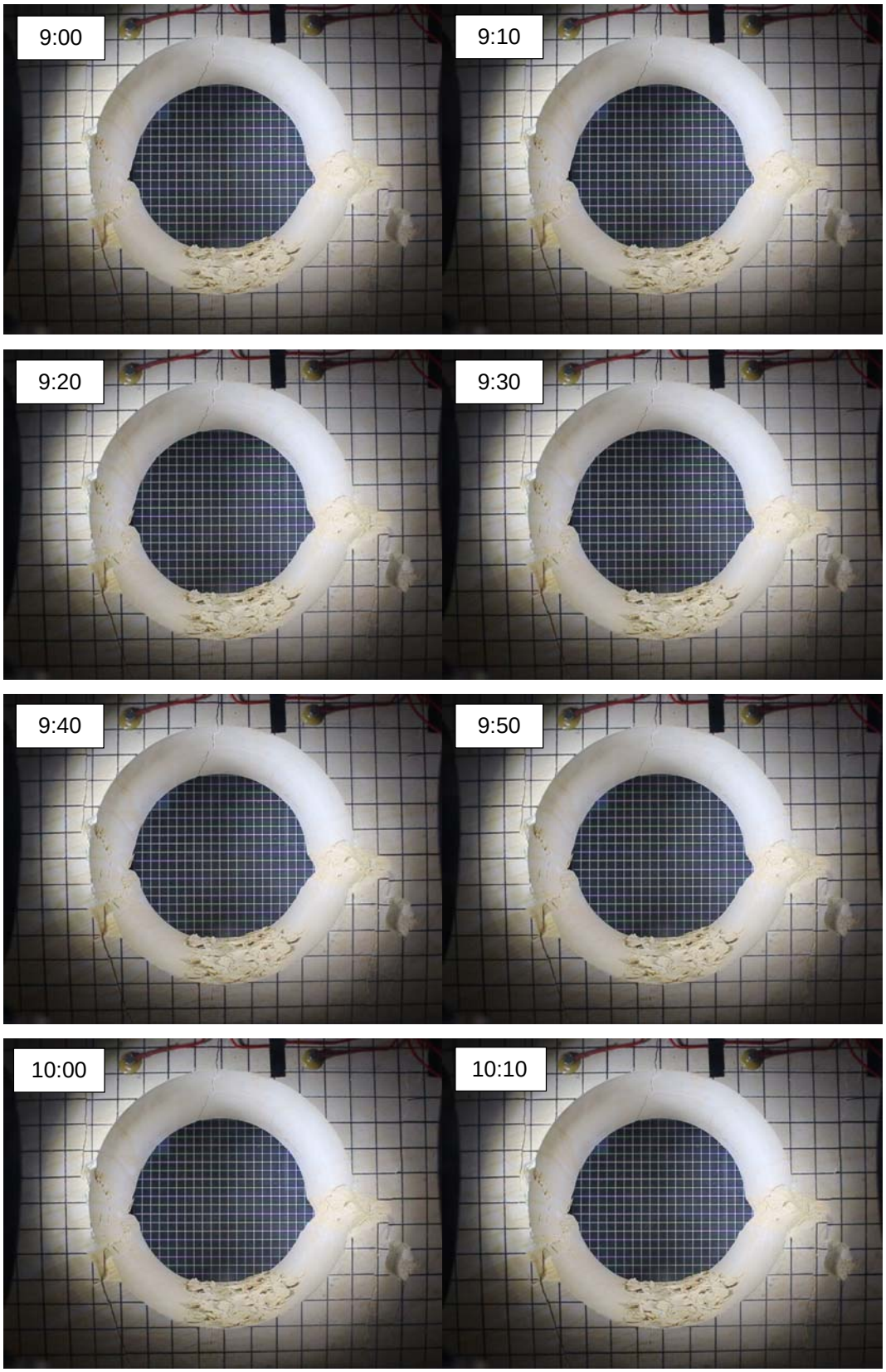
9:00
9:10
9:20
9:30
9:40
9:50
10:00
10:10

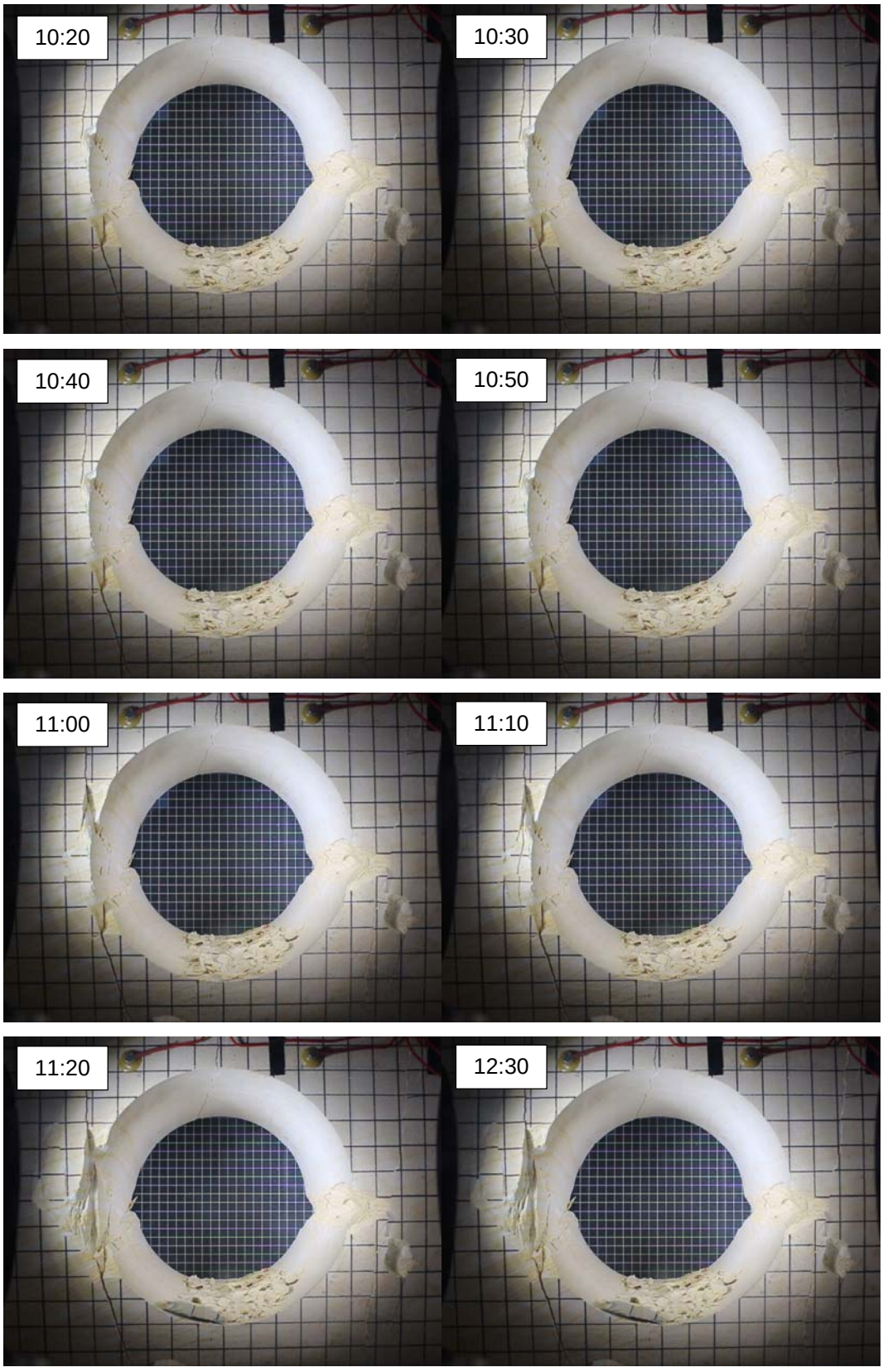
10:20
10:30
10:40
10:50
11:00
11:10
11:20
12:30

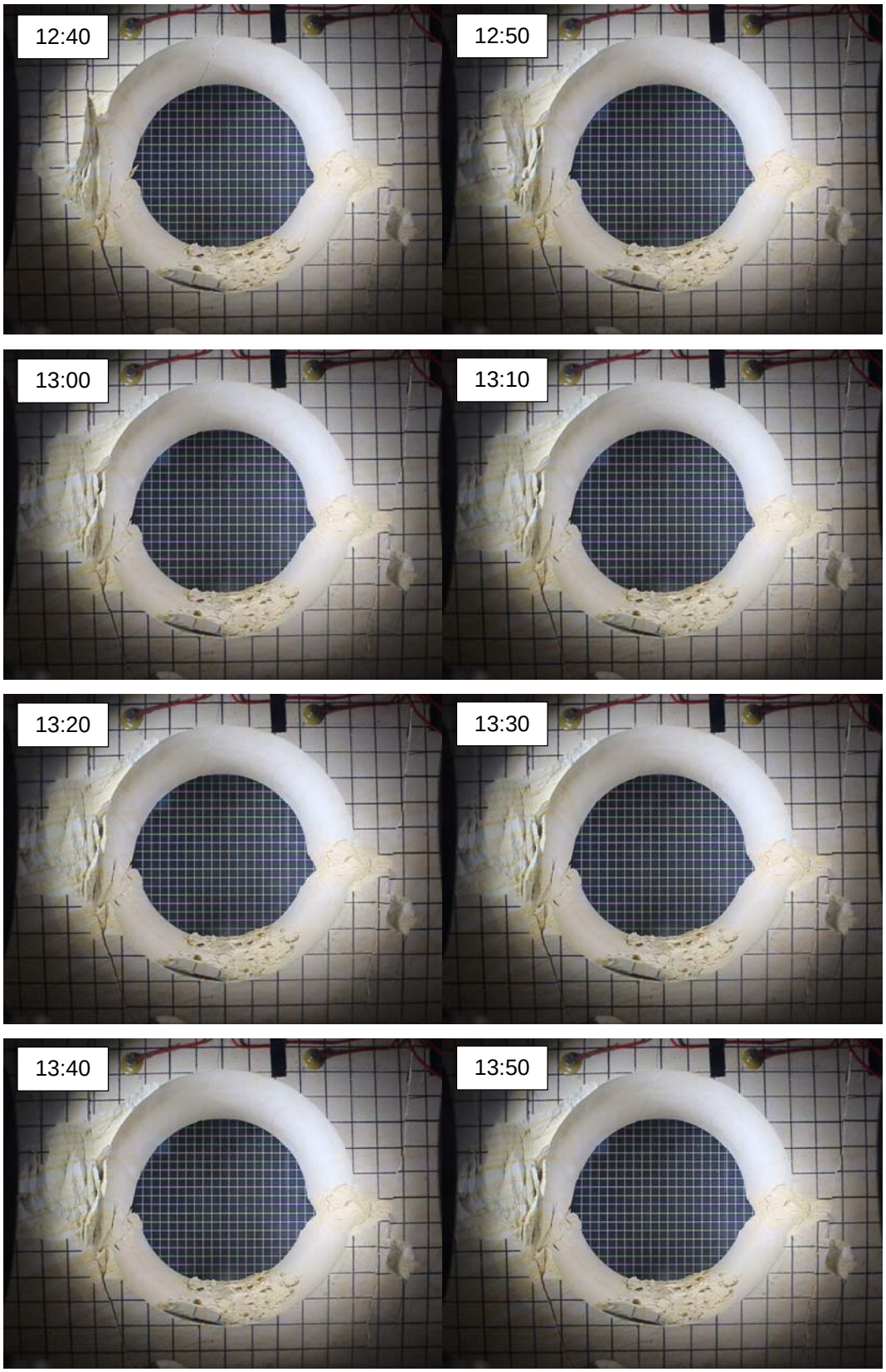
12:40
12:50
13:00
13:10
13:20
13:30
13:40
13:50

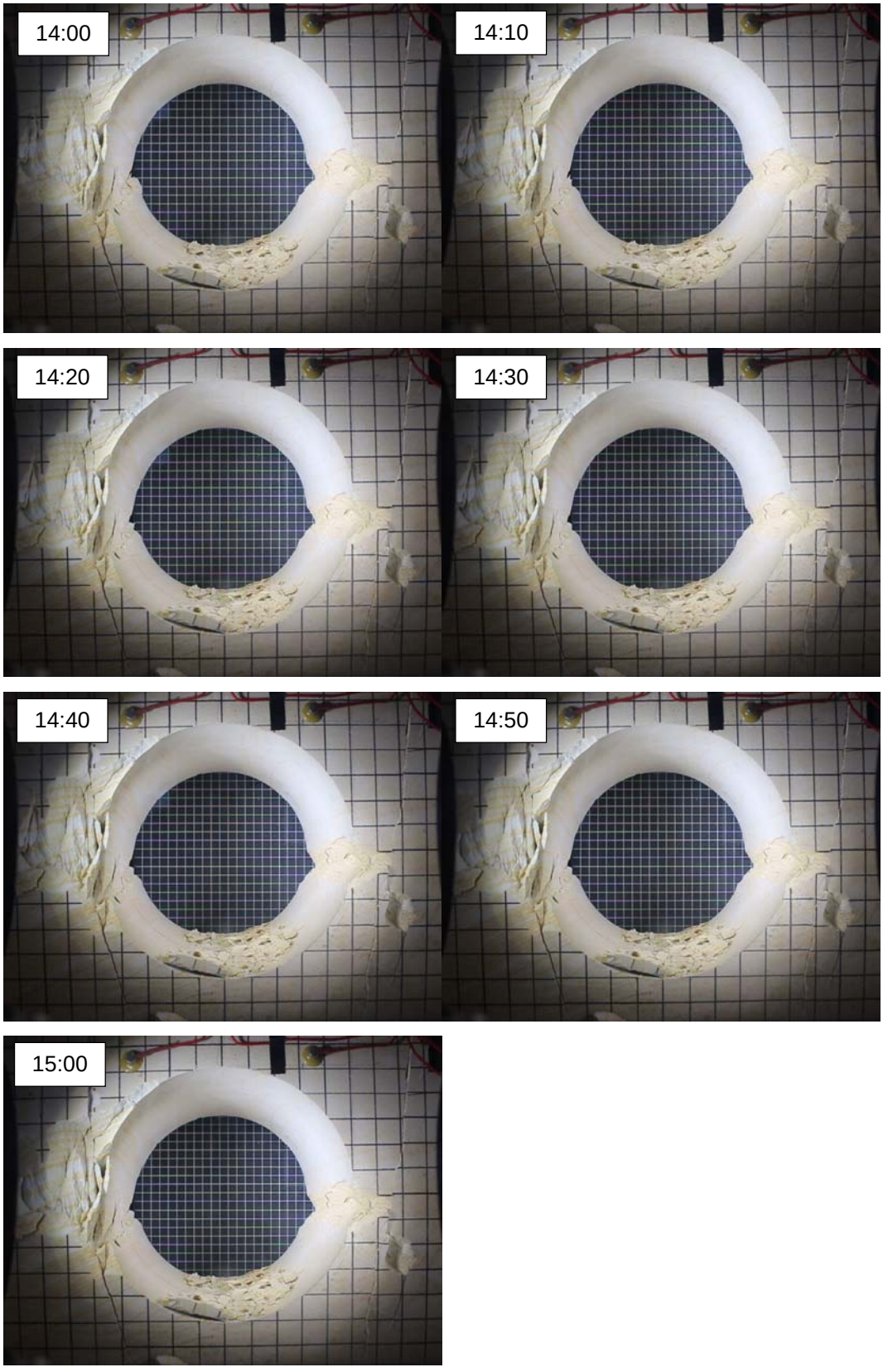
14:00
14:10
14:20
14:30
14:40
14:50
15:00

A2 Ground Supported Tunnel (Single Layer, Specimen No.10)

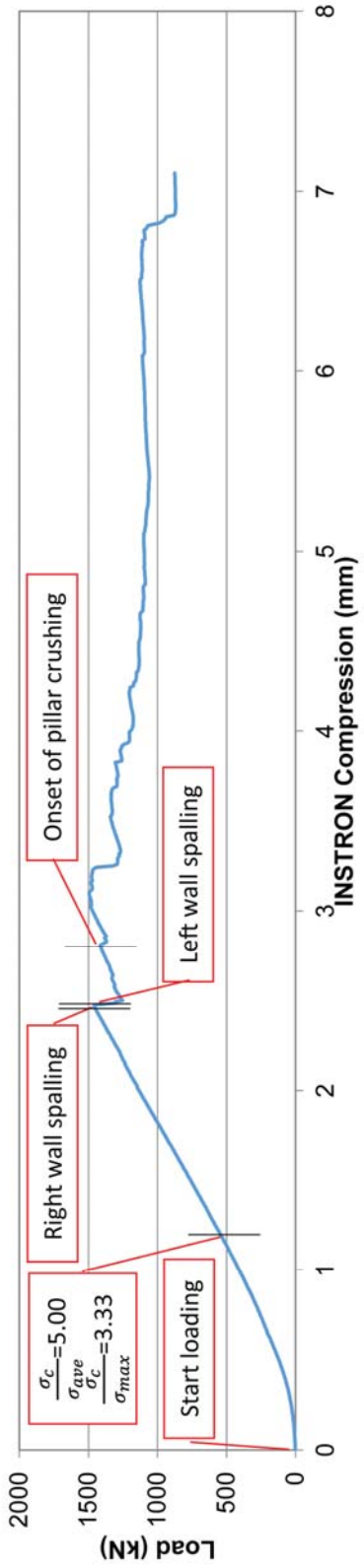

	Start loading (0:00)	$\frac{\sigma_c}{\sigma_{ave}}$=5 (2:24)	Right wall spalling (4:56)	Left wall spalling (4:57)	Pillar crushing (5:38)
Load (kN)	0	544	1459	1412	1418
INSTRON Compression (mm)	0	1.20	2.47	2.48	2.82
$\frac{\sigma_c}{\sigma_{max}}$	-	3.33	1.24	1.28	1.28
$\frac{\sigma_c}{\sigma_{ave}}$	-	5.00	1.86	1.92	1.92
	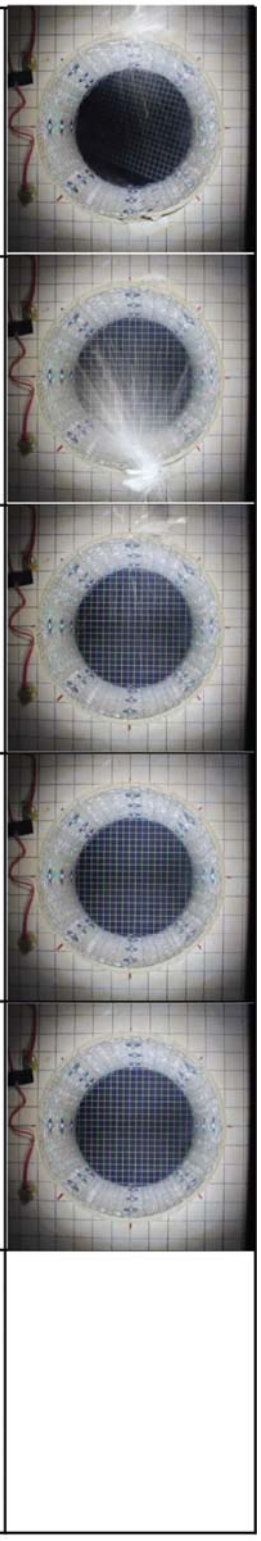				

Load displacement curve with tunnel behaviour.

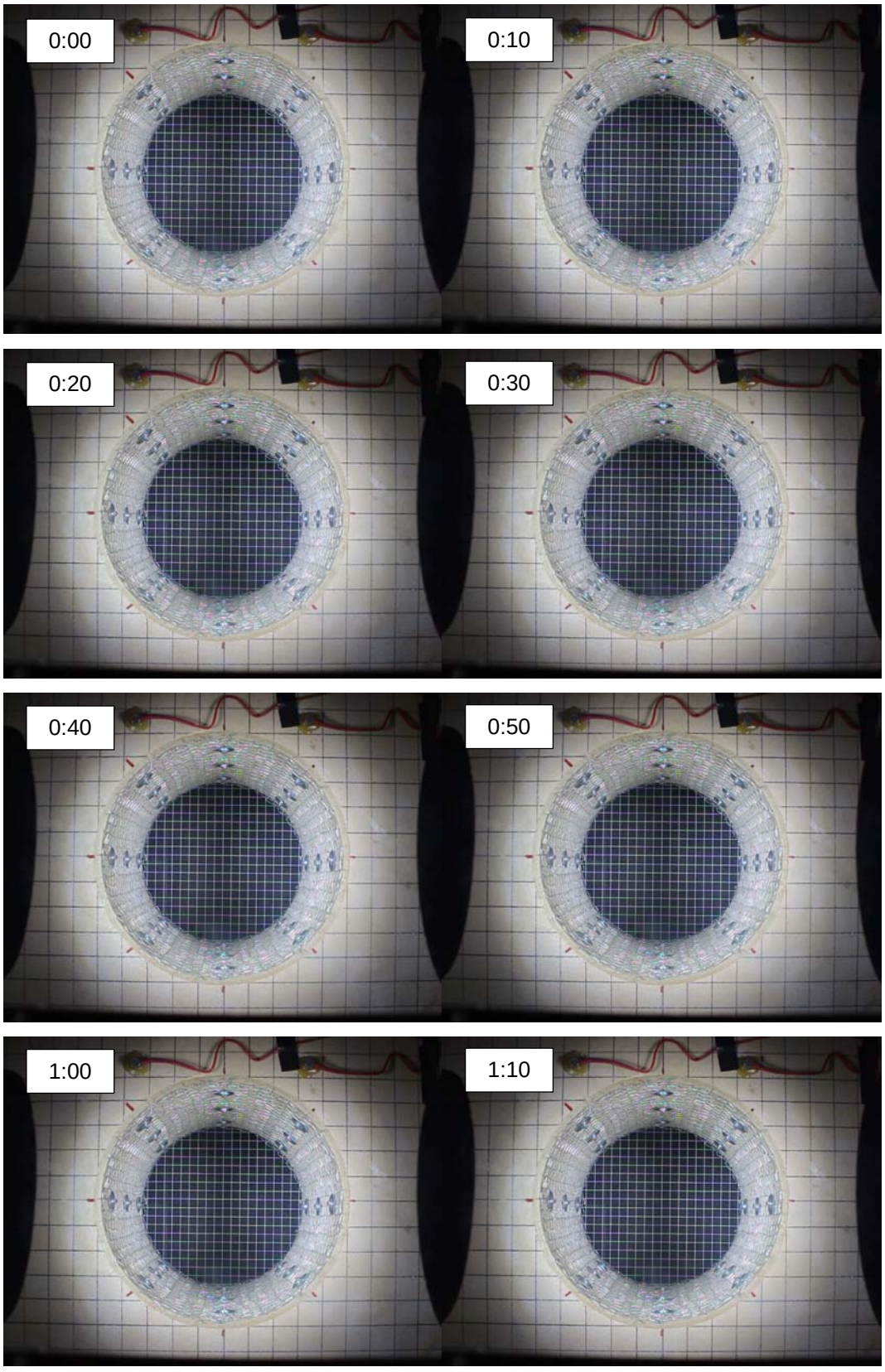
0:00
0:10
0:20
0:30
0:40
0:50
1:00
1:10

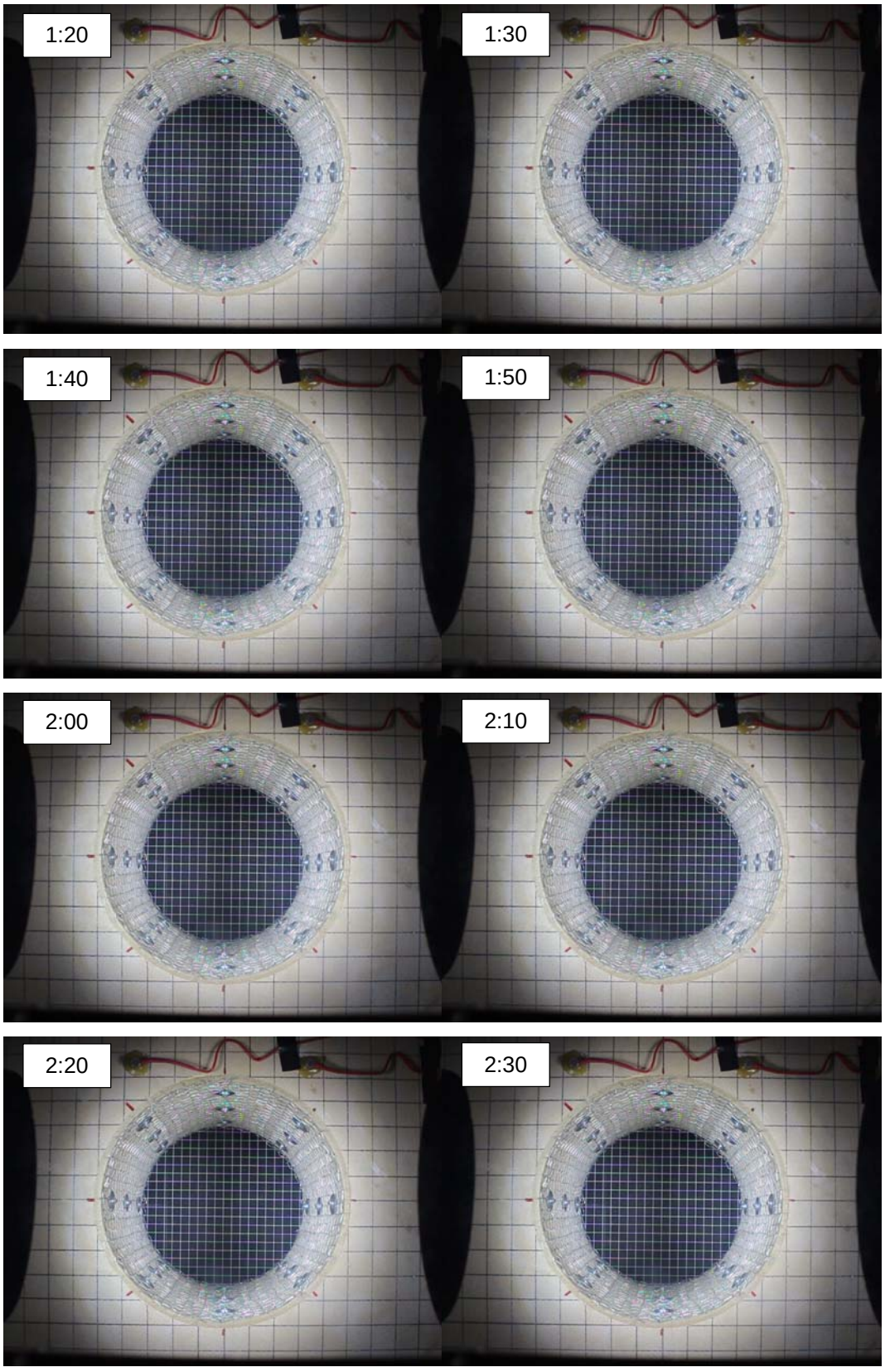
1:20
1:30
1:40
1:50
2:00
2:10
2:20
2:30

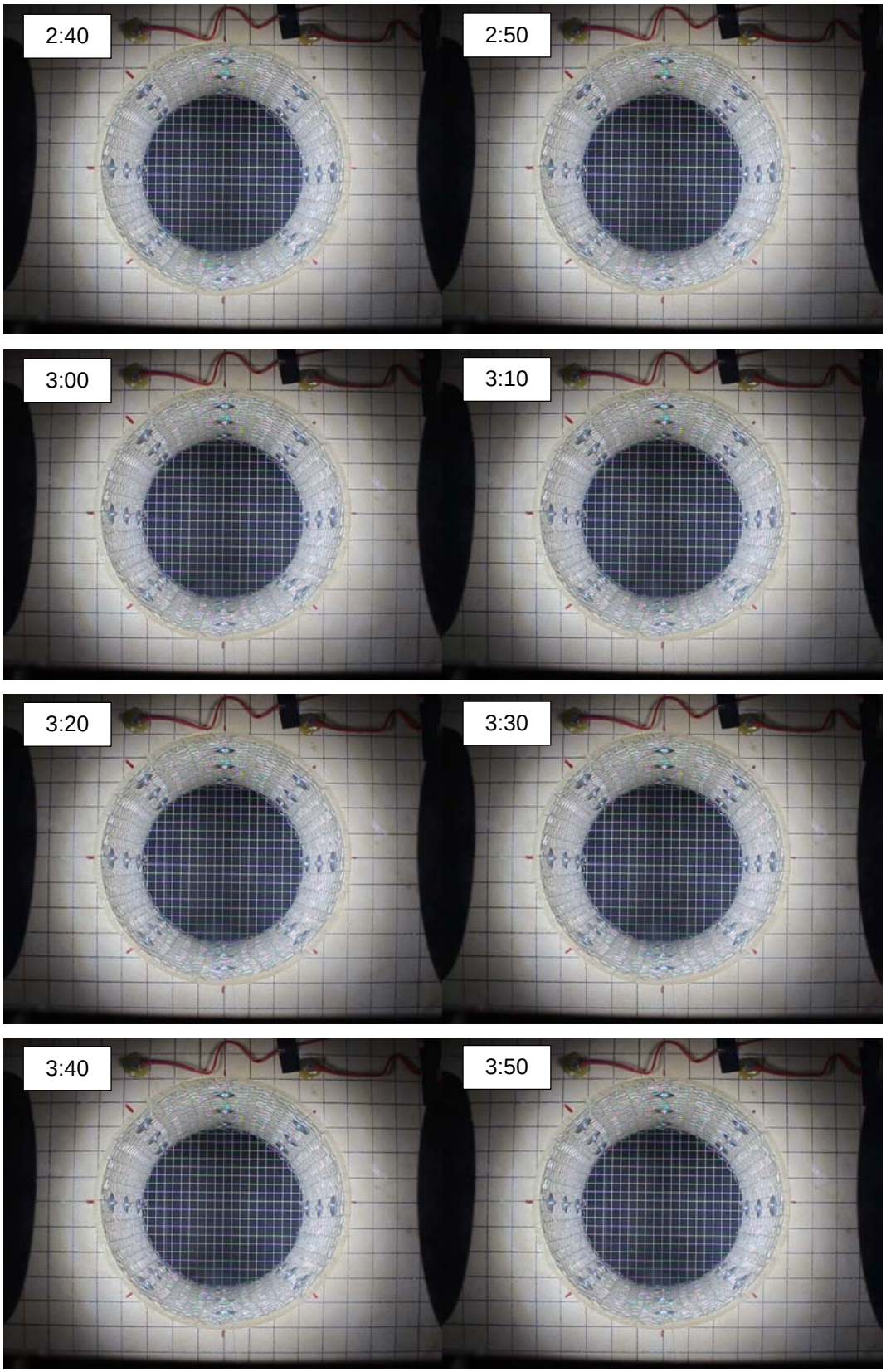
2:40
2:50
3:00
3:10
3:20
3:30
3:40
3:50

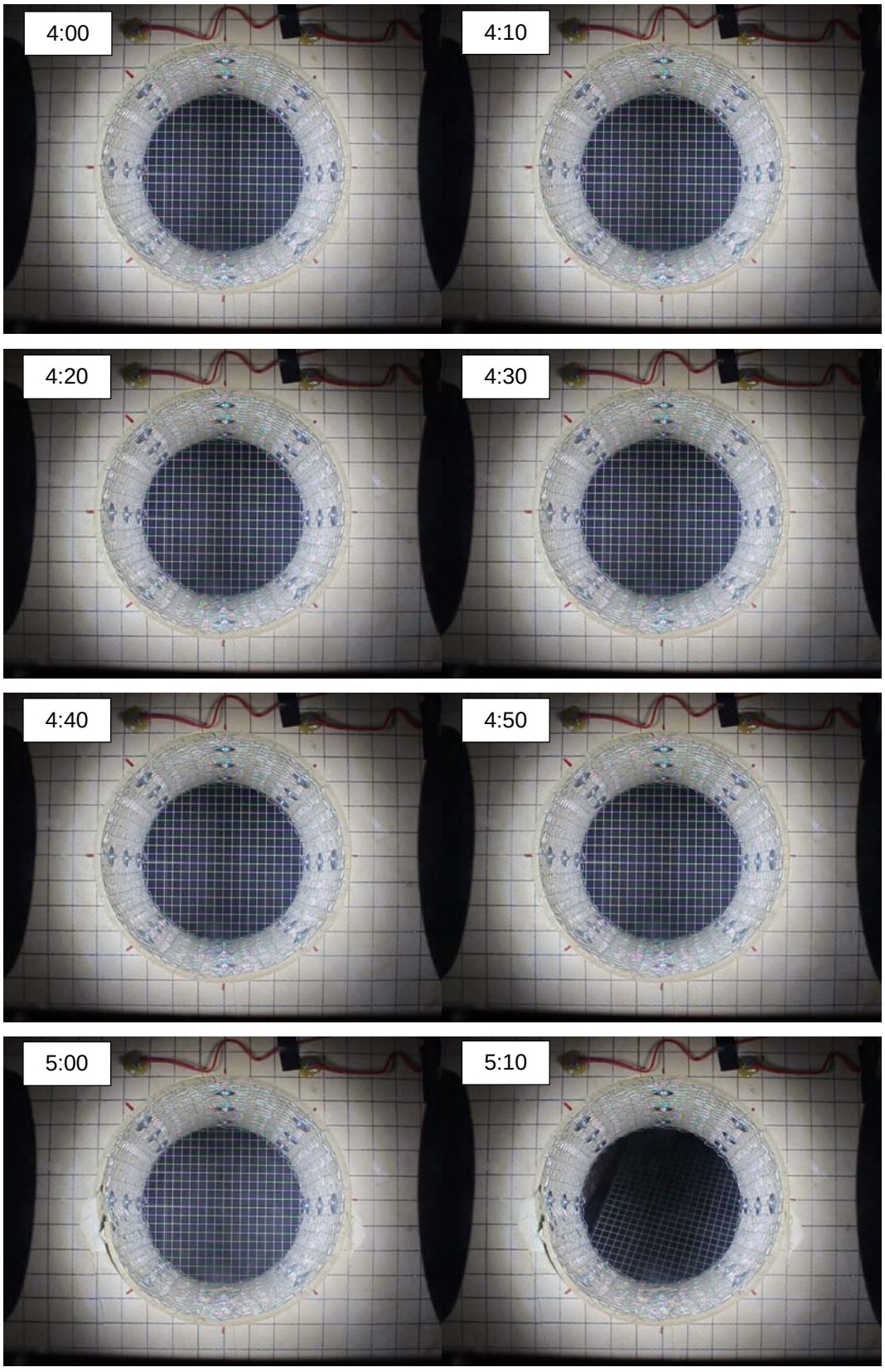
4:00
4:10
4:20
4:30
4:40
4:50
5:00
5:10

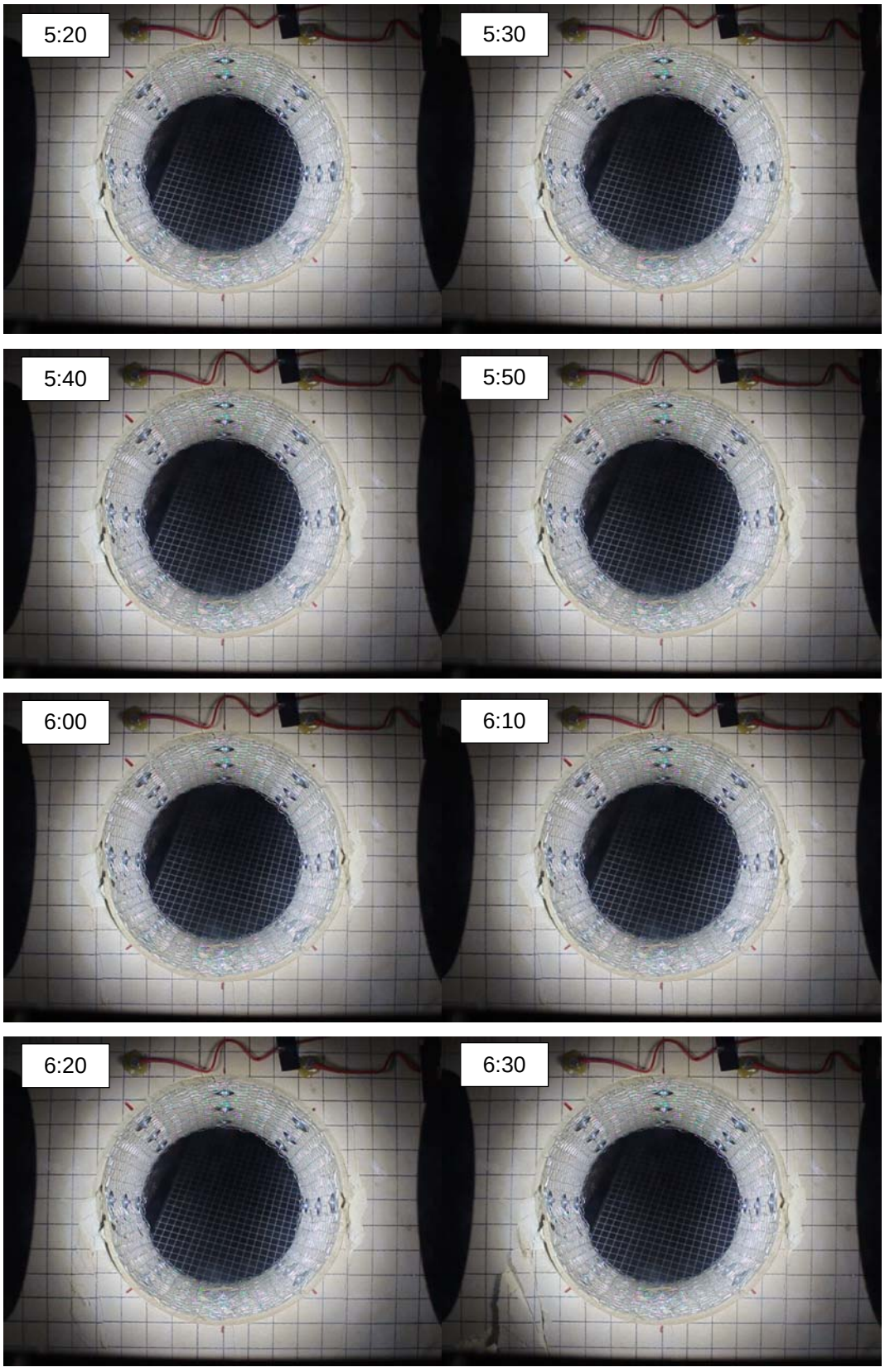
5:20
5:30
5:40
5:50
6:00
6:10
6:20
6:30

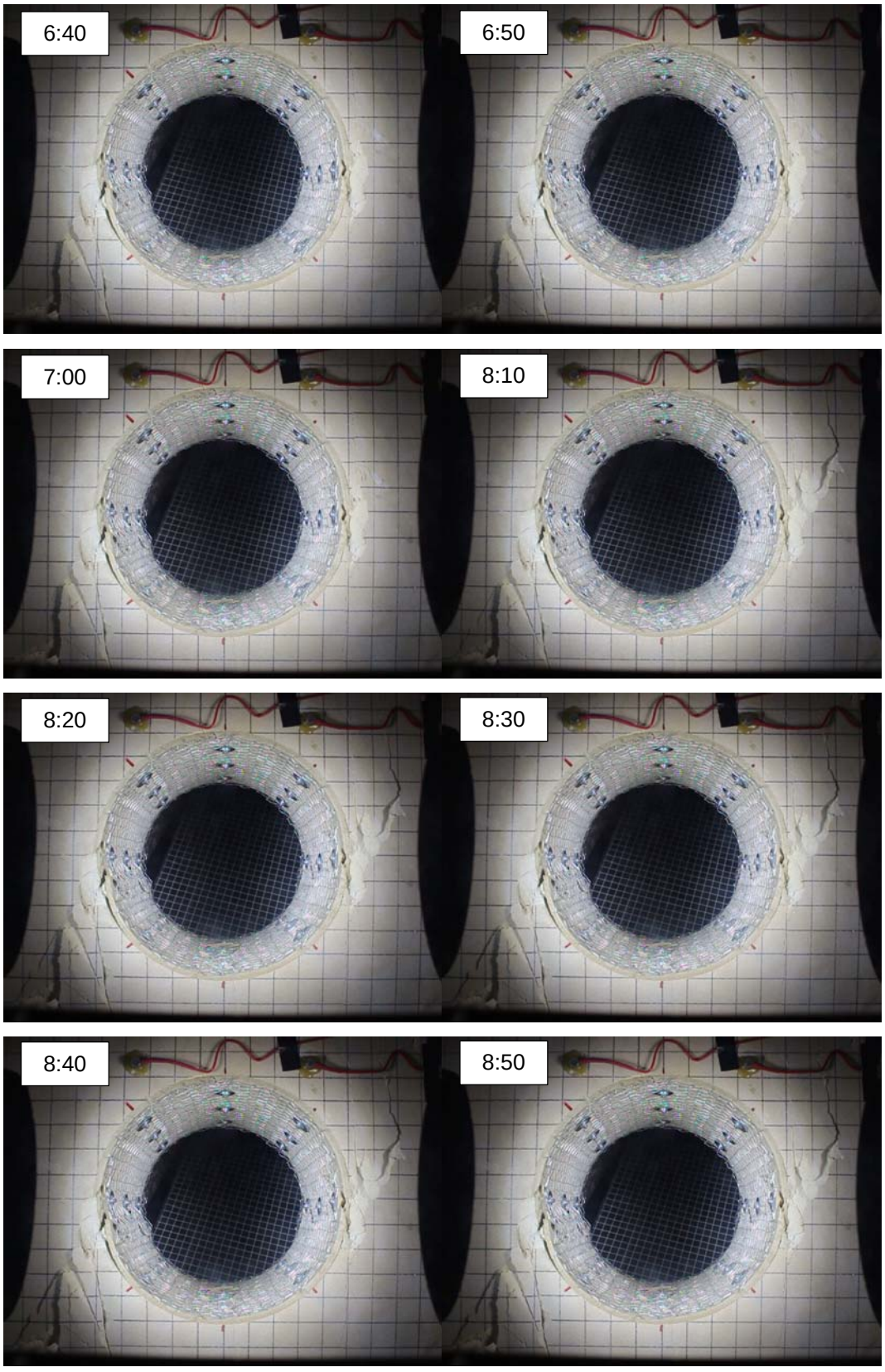
6:40
6:50
7:00
8:10
8:20
8:30
8:40
8:50

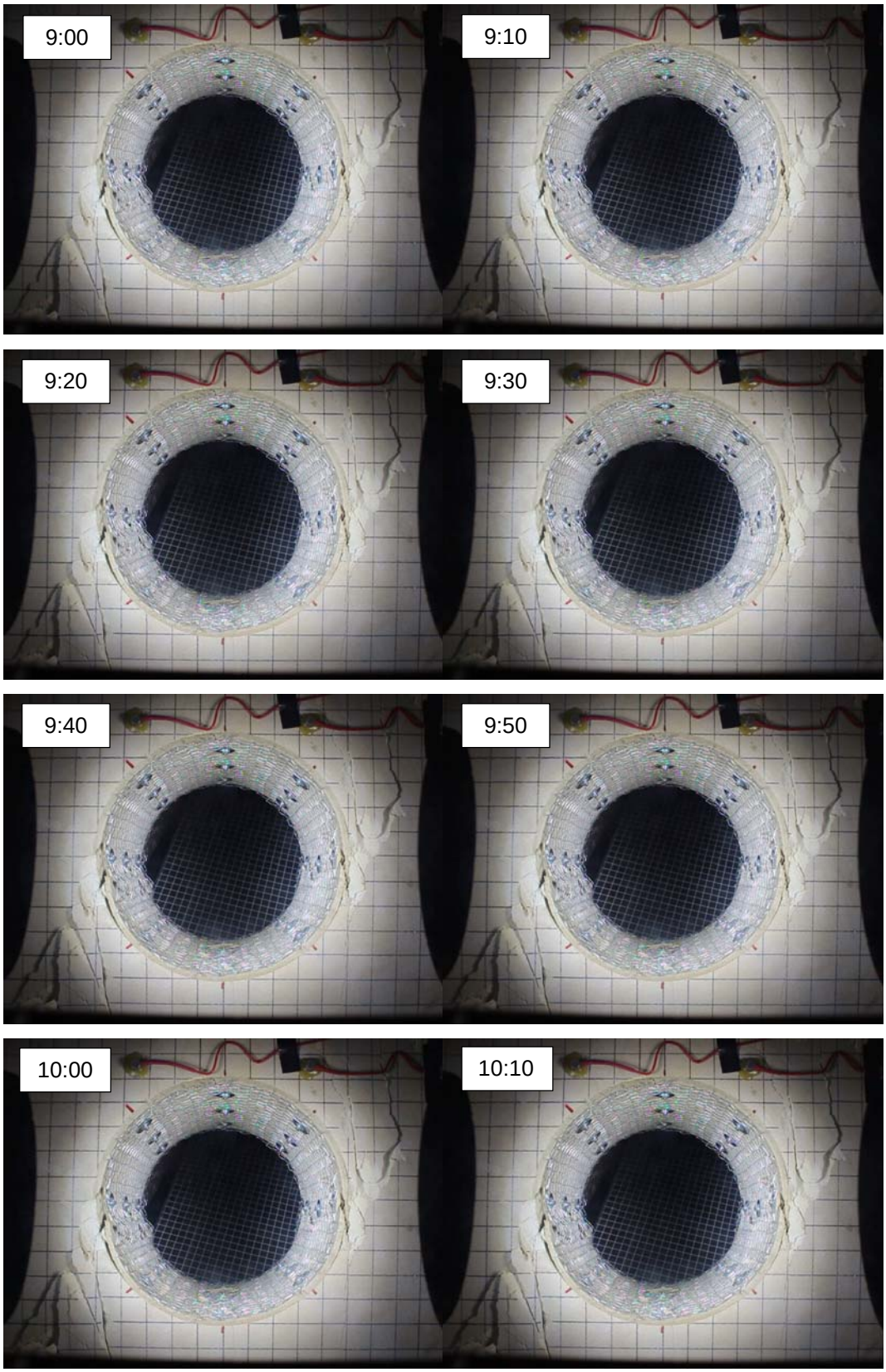
9:00
9:10
9:20
9:30
9:40
9:50
10:00
10:10

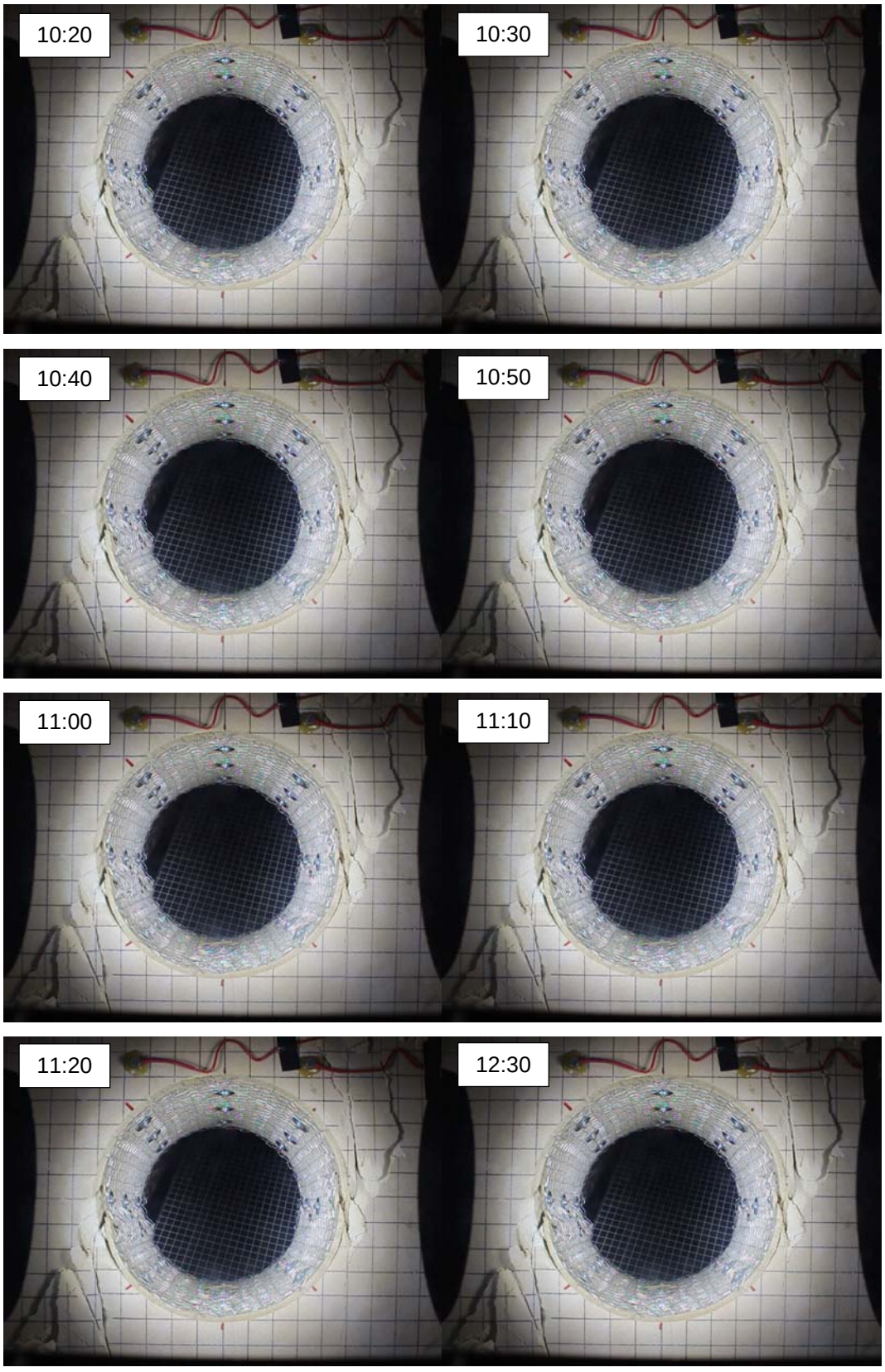
10:20
10:30
10:40
10:50
11:00
11:10
11:20
12:30

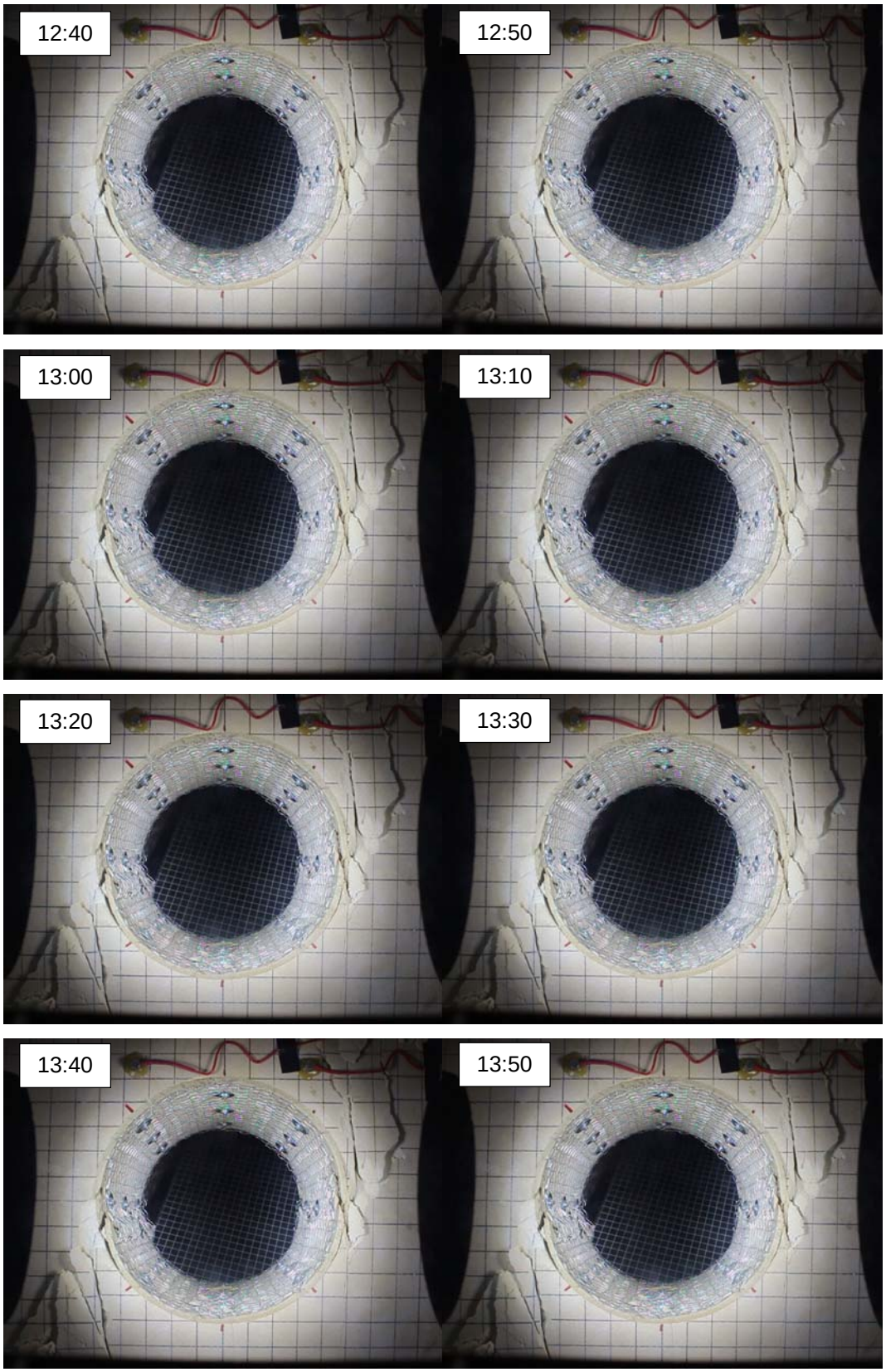
12:40
12:50
13:00
13:10
13:20
13:30
13:40
13:50

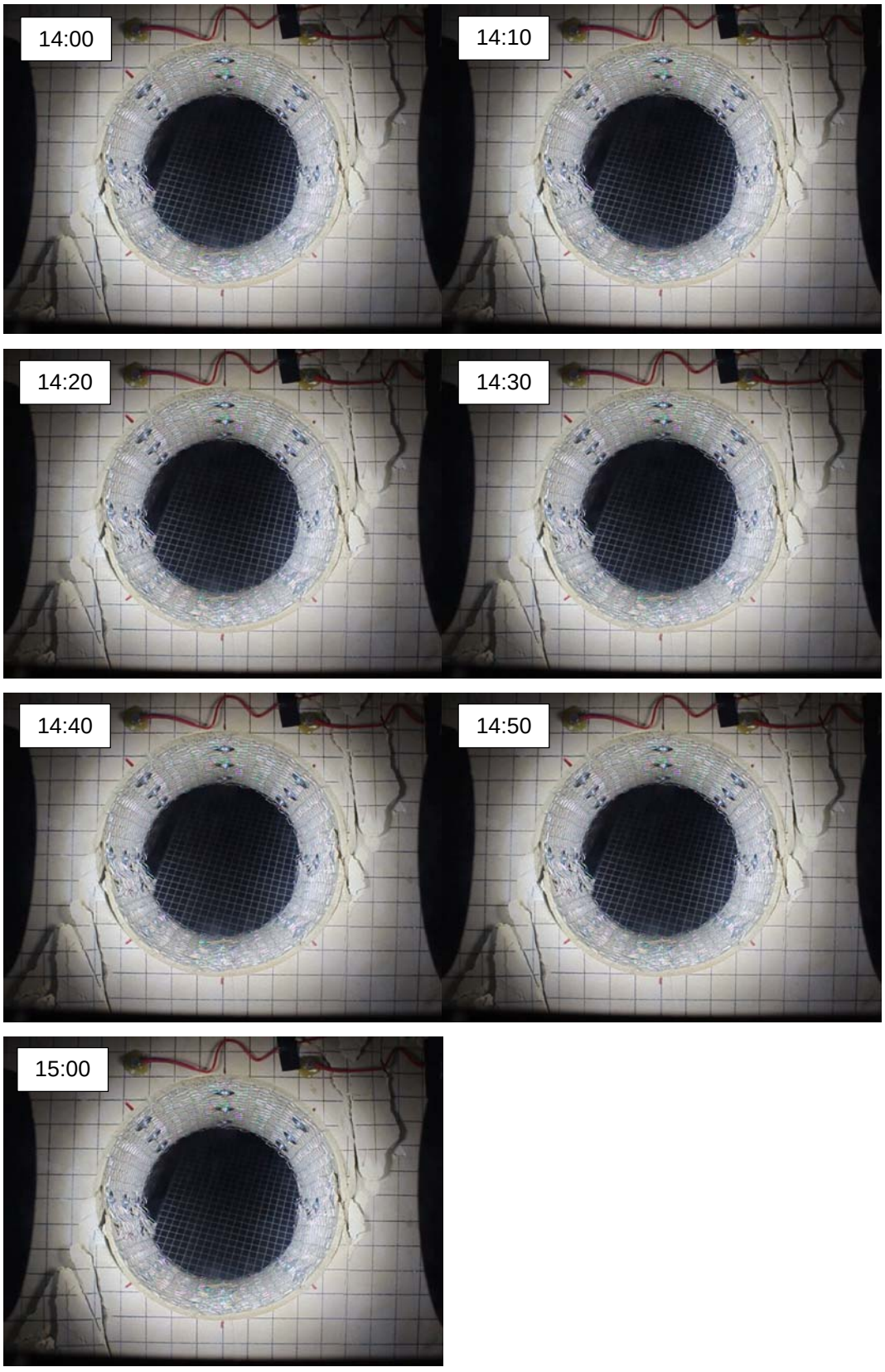
14:00
14:10
14:20
14:30
14:40
14:50
15:00

A3 Ground Supported Tunnel (Double Layer, Specimen No.15)

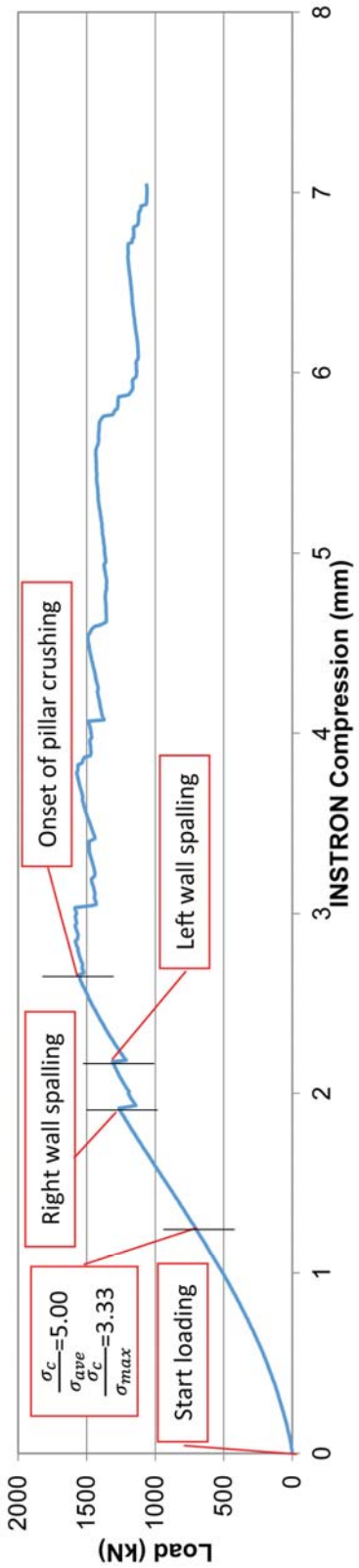

	Start loading (0:00)	$\frac{\sigma_c}{\sigma_{ave}}$=5 (2:33)	Right wall spalling (3:50)	Left wall spalling (4:20)	Pillar crushing (5:18)
Load (kN)	0	728	1267	1314	1559
INSTRON Compression (mm)	0	1.28	1.92	2.17	2.66
$\frac{\sigma_c}{\sigma_{max}}$	-	3.33	1.91	1.85	1.56
$\frac{\sigma_c}{\sigma_{ave}}$	-	5.00	2.87	2.77	2.33
	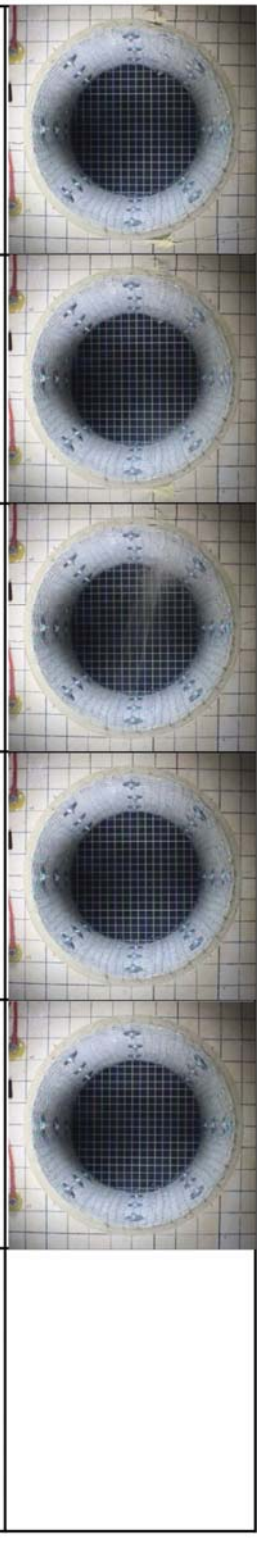				

Load displacement curve with tunnel behaviour.

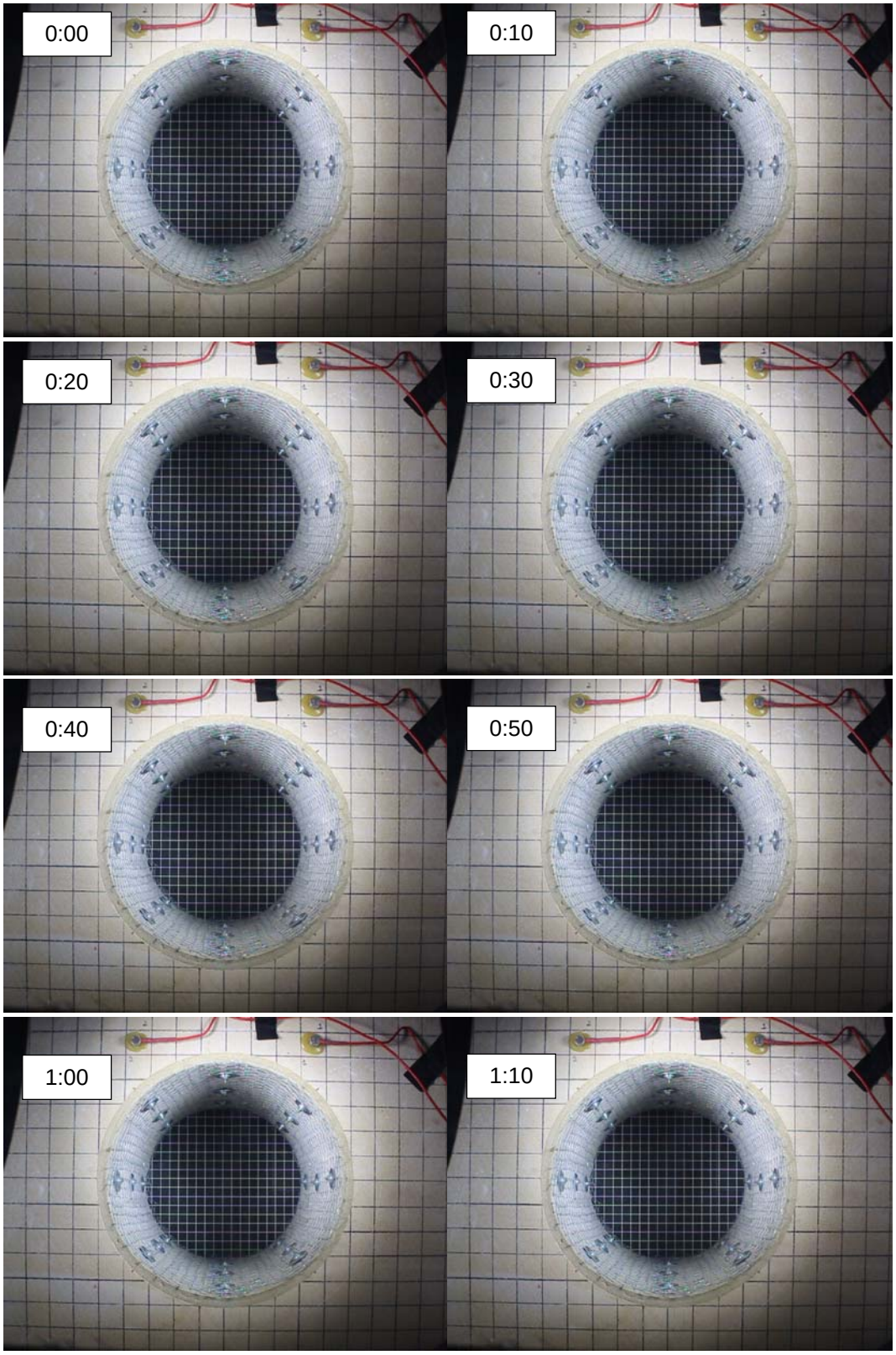
0:00
0:10
0:20
0:30
0:40
0:50
1:00
1:10

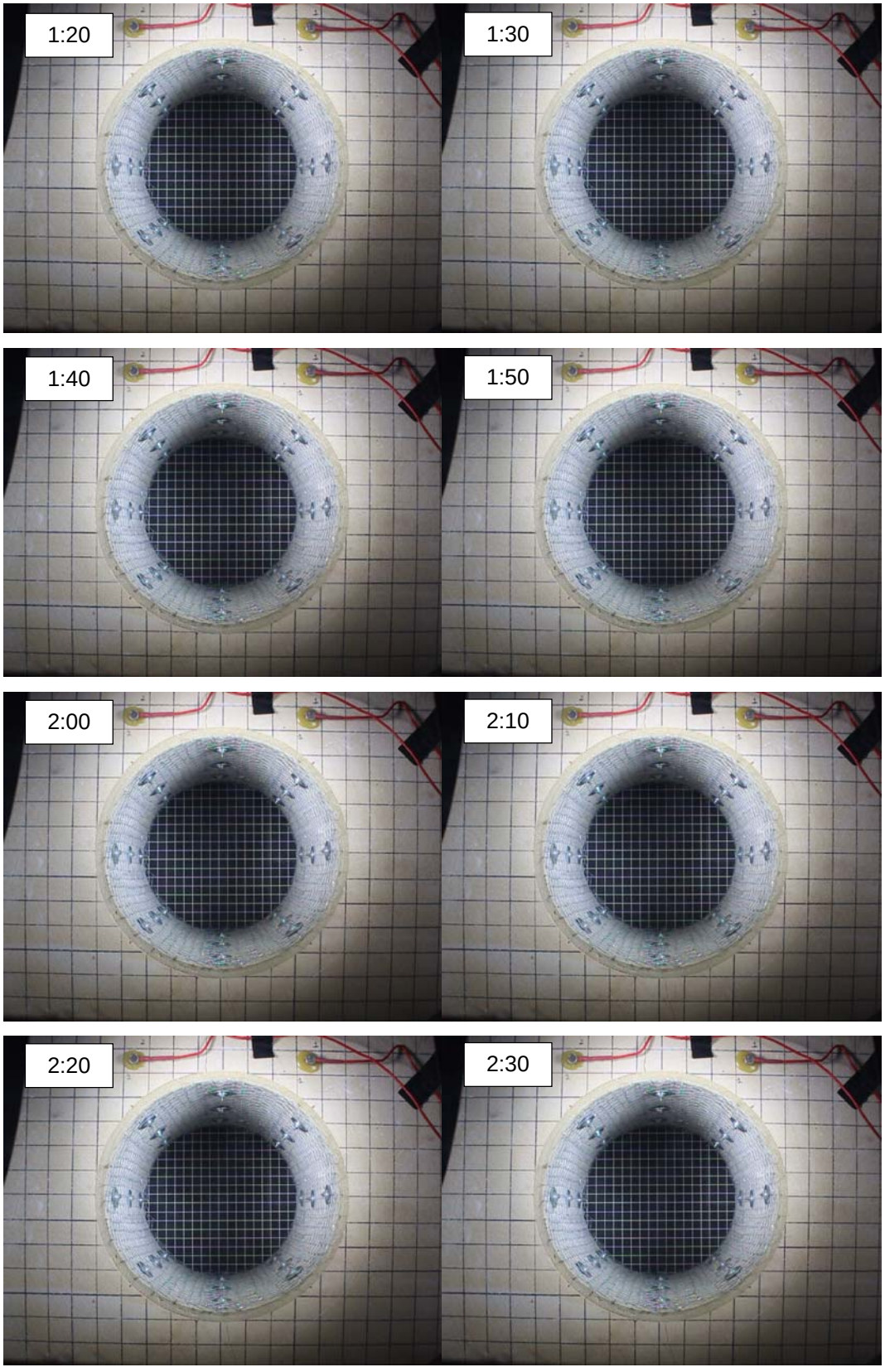
1:20
1:30
1:40
1:50
2:00
2:10
2:20
2:30

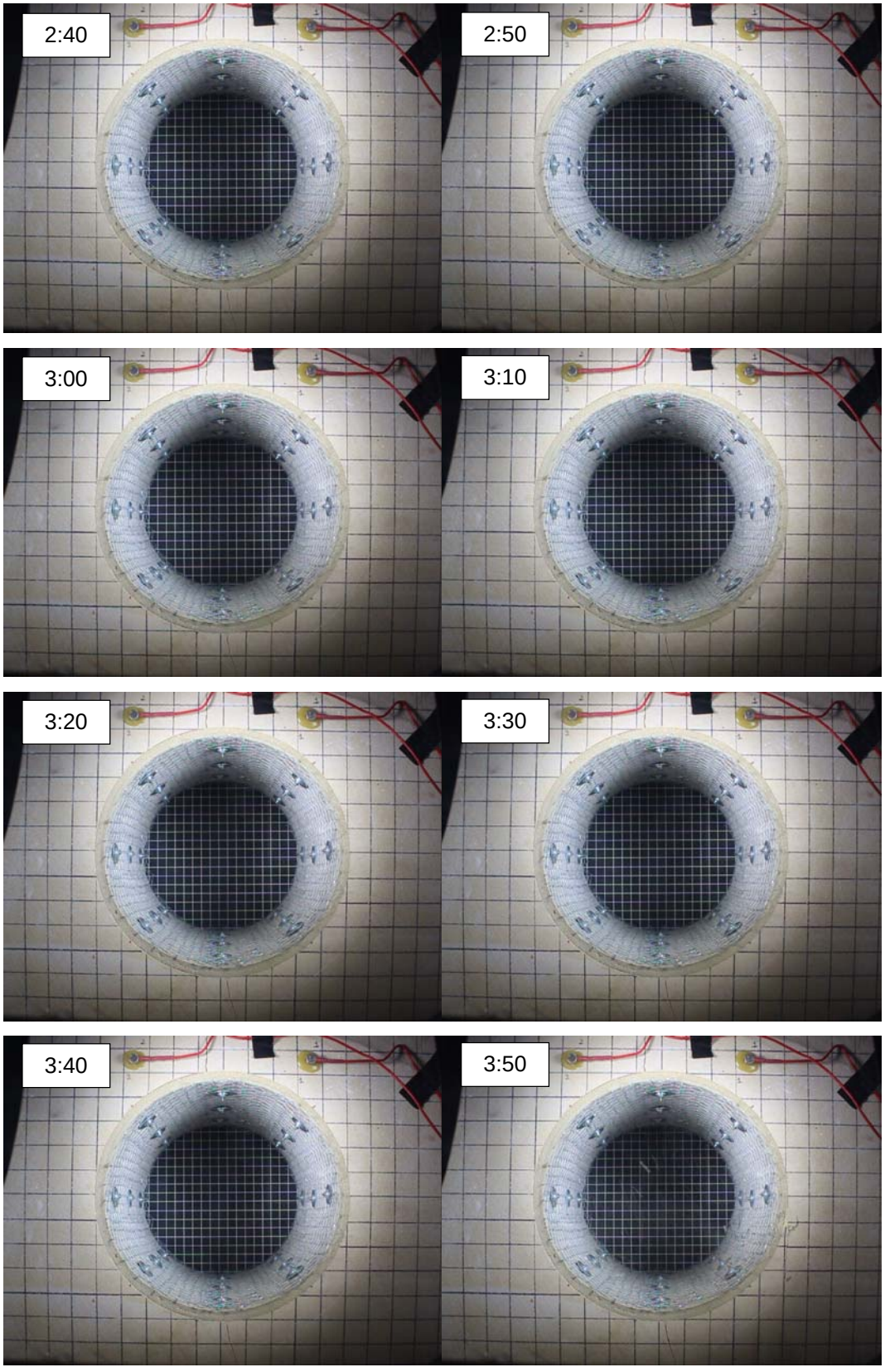
2:40
2:50
3:00
3:10
3:20
3:30
3:40
3:50

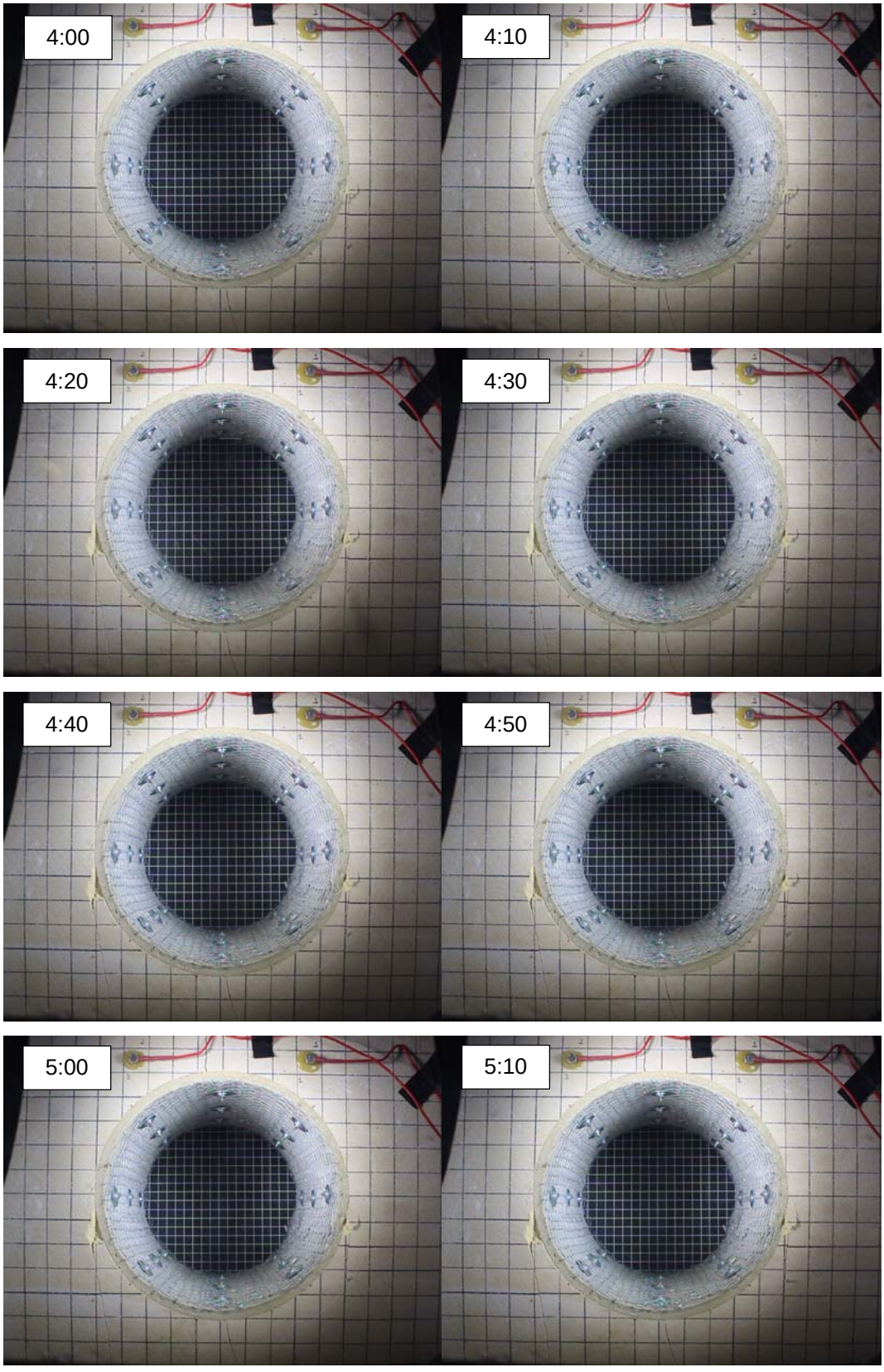
4:00
4:10
4:20
4:30
4:40
4:50
5:00
5:10

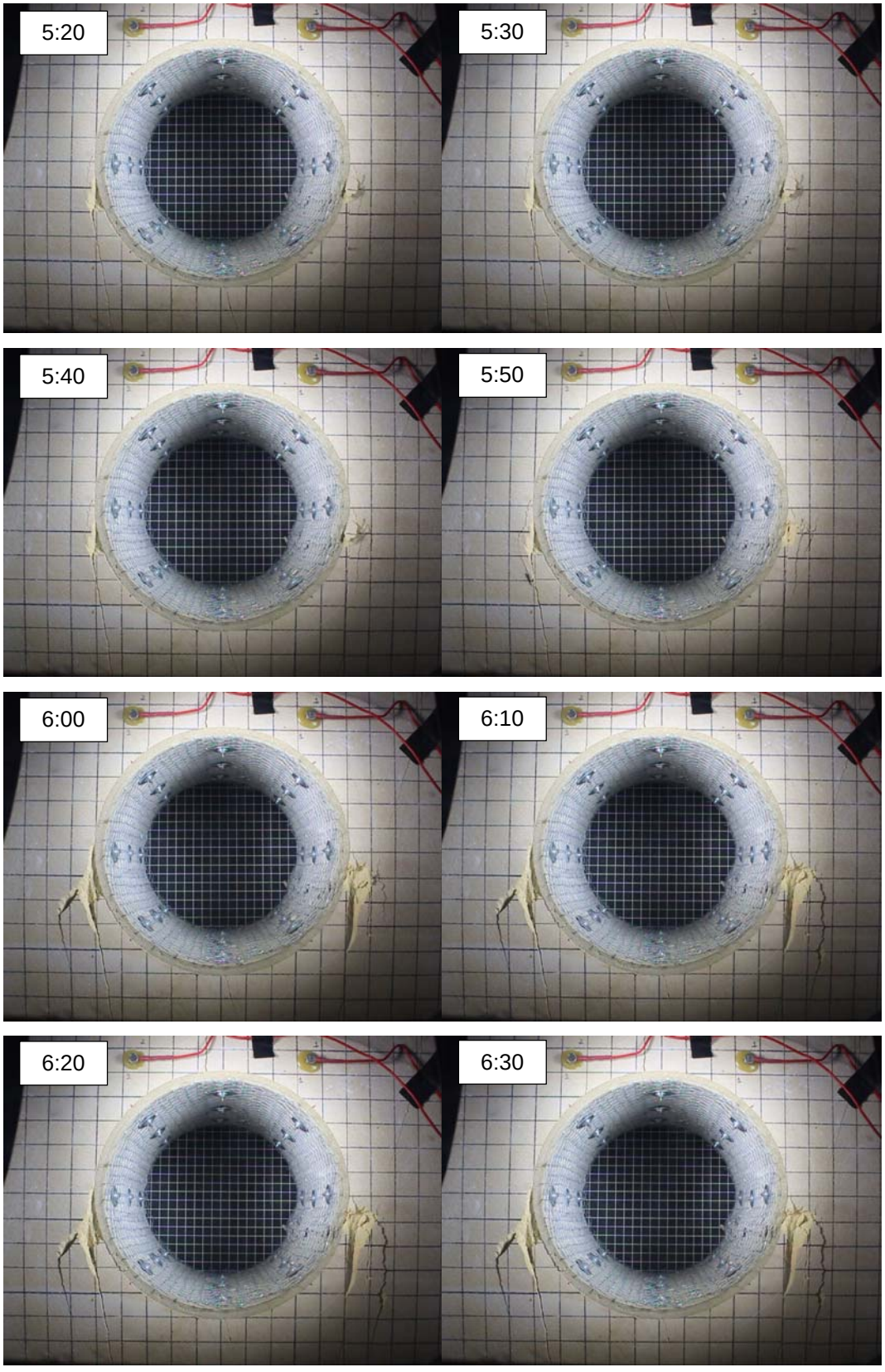
5:20
5:30
5:40
5:50
6:00
6:10
6:20
6:30

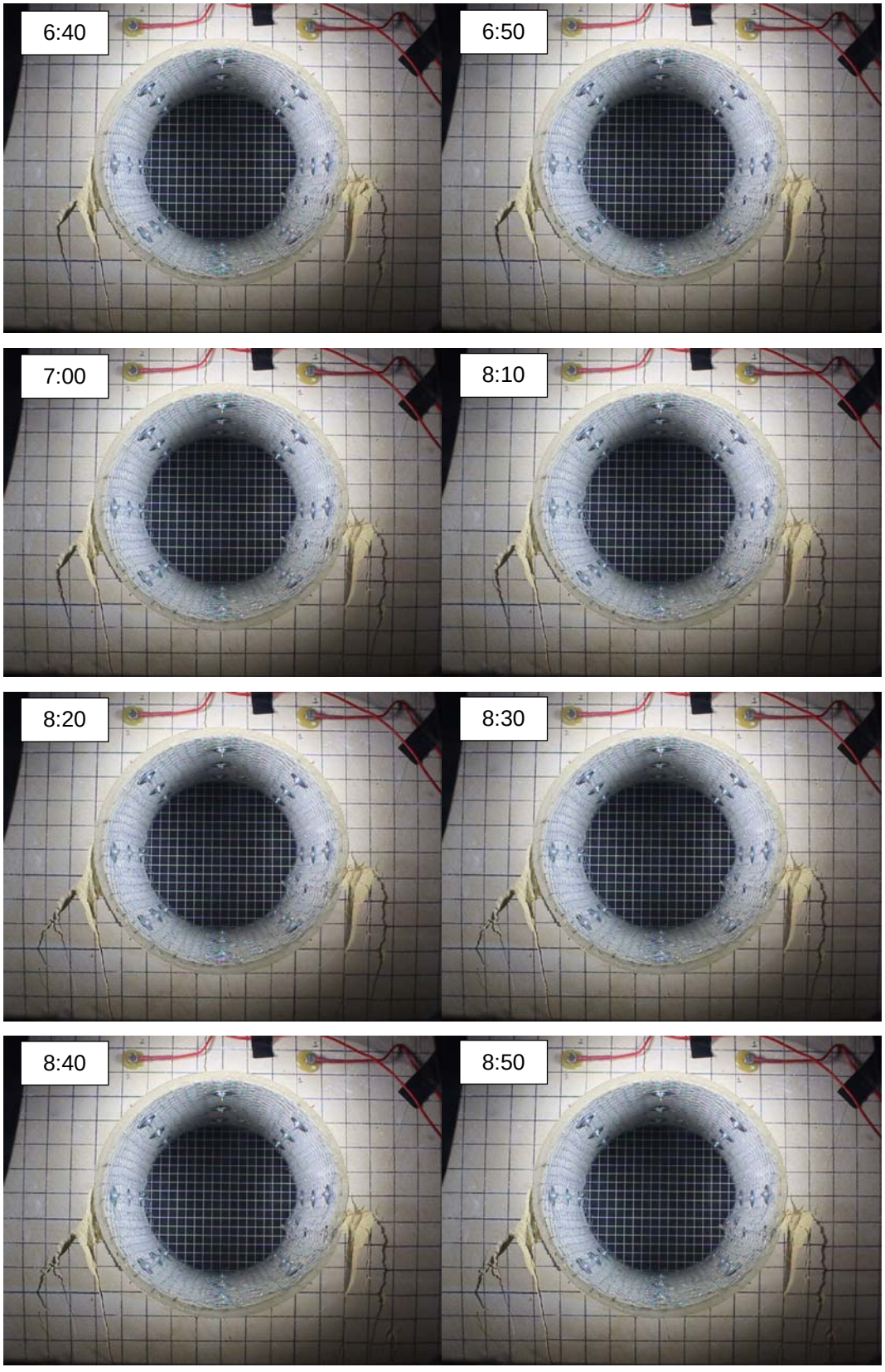
6:40
6:50
7:00
8:10
8:20
8:30
8:40
8:50

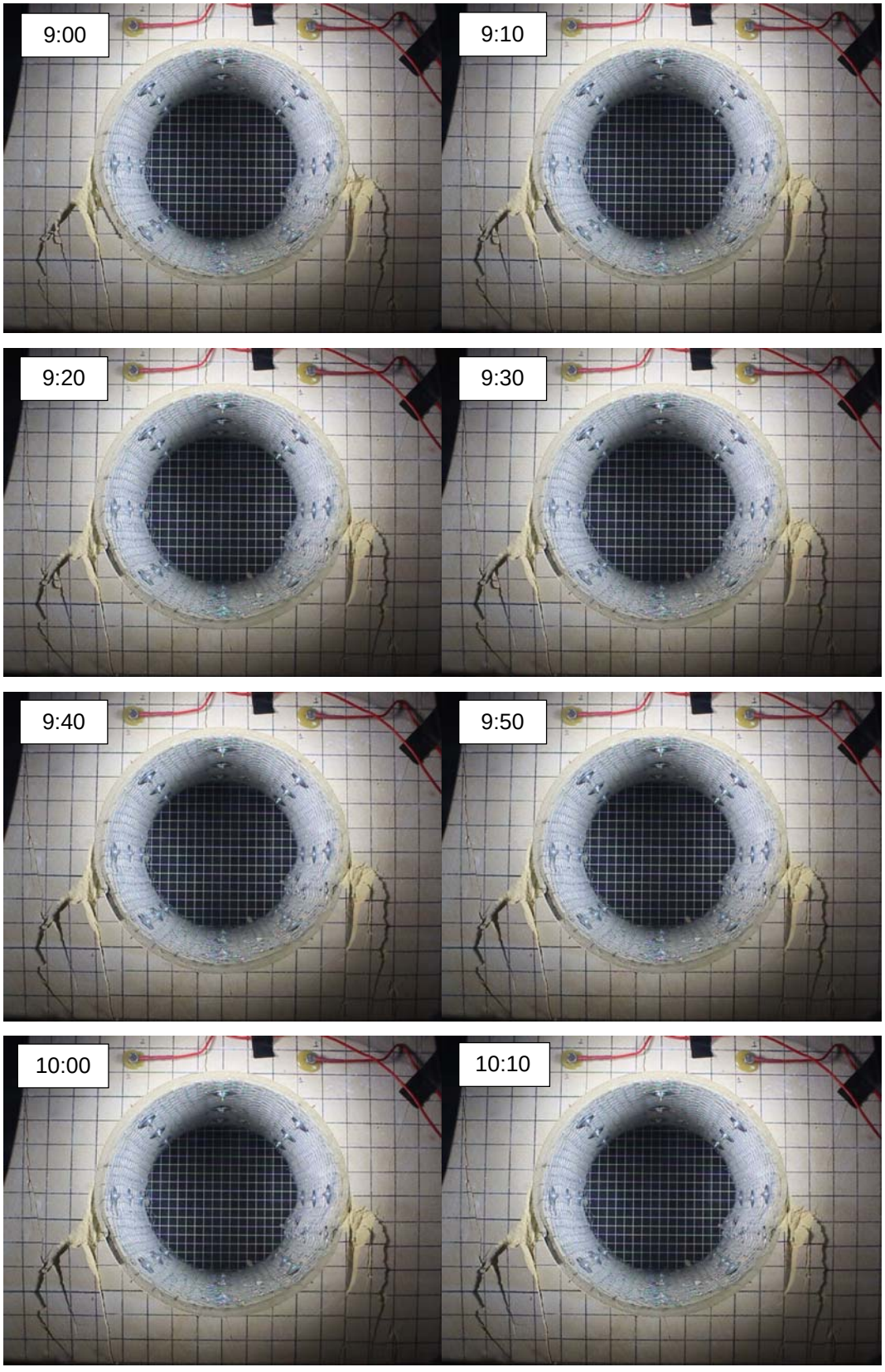
9:00
9:10
9:20
9:30
9:40
9:50
10:00
10:10

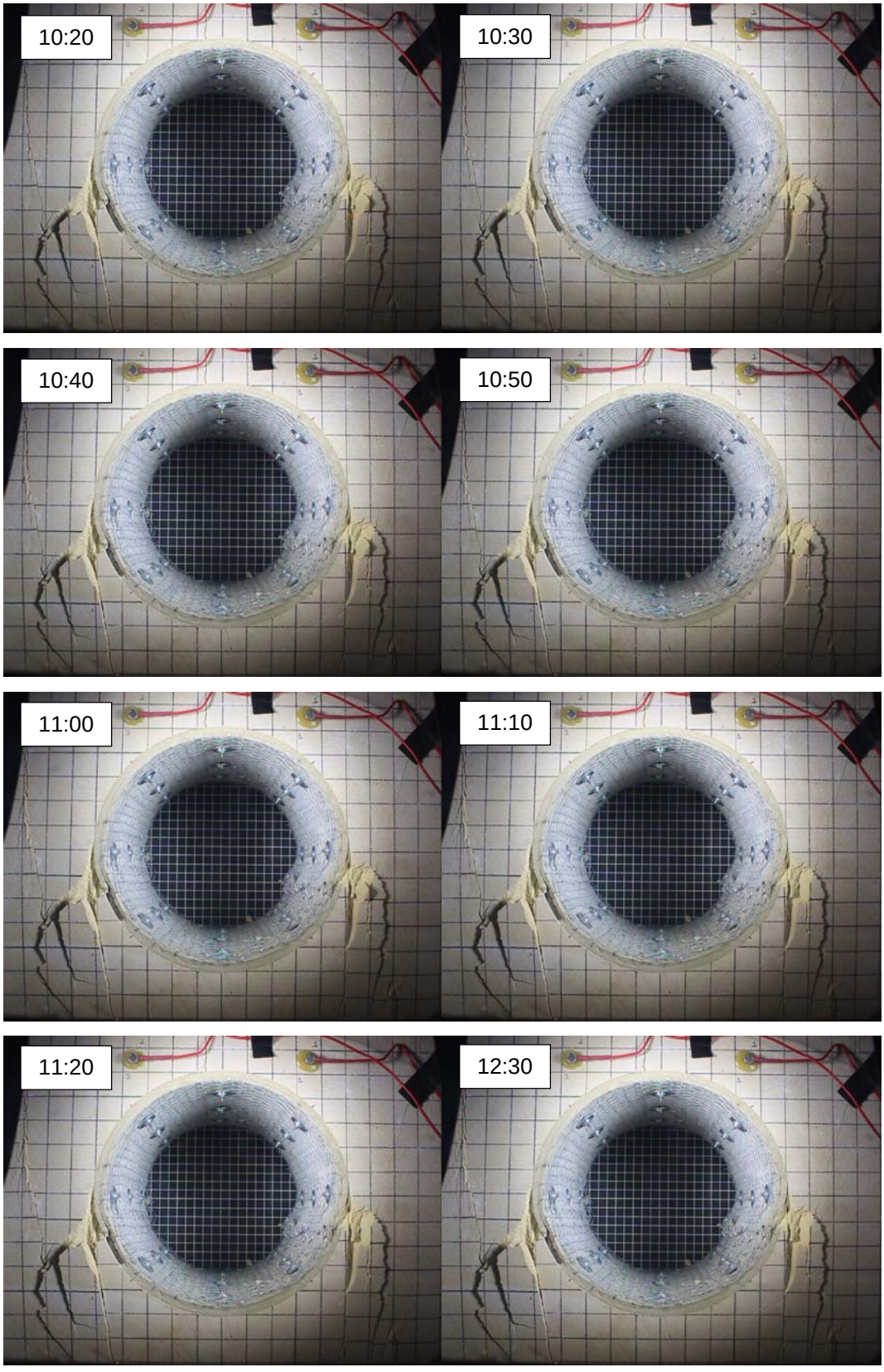
10:20
10:30
10:40
10:50
11:00
11:10
11:20
12:30

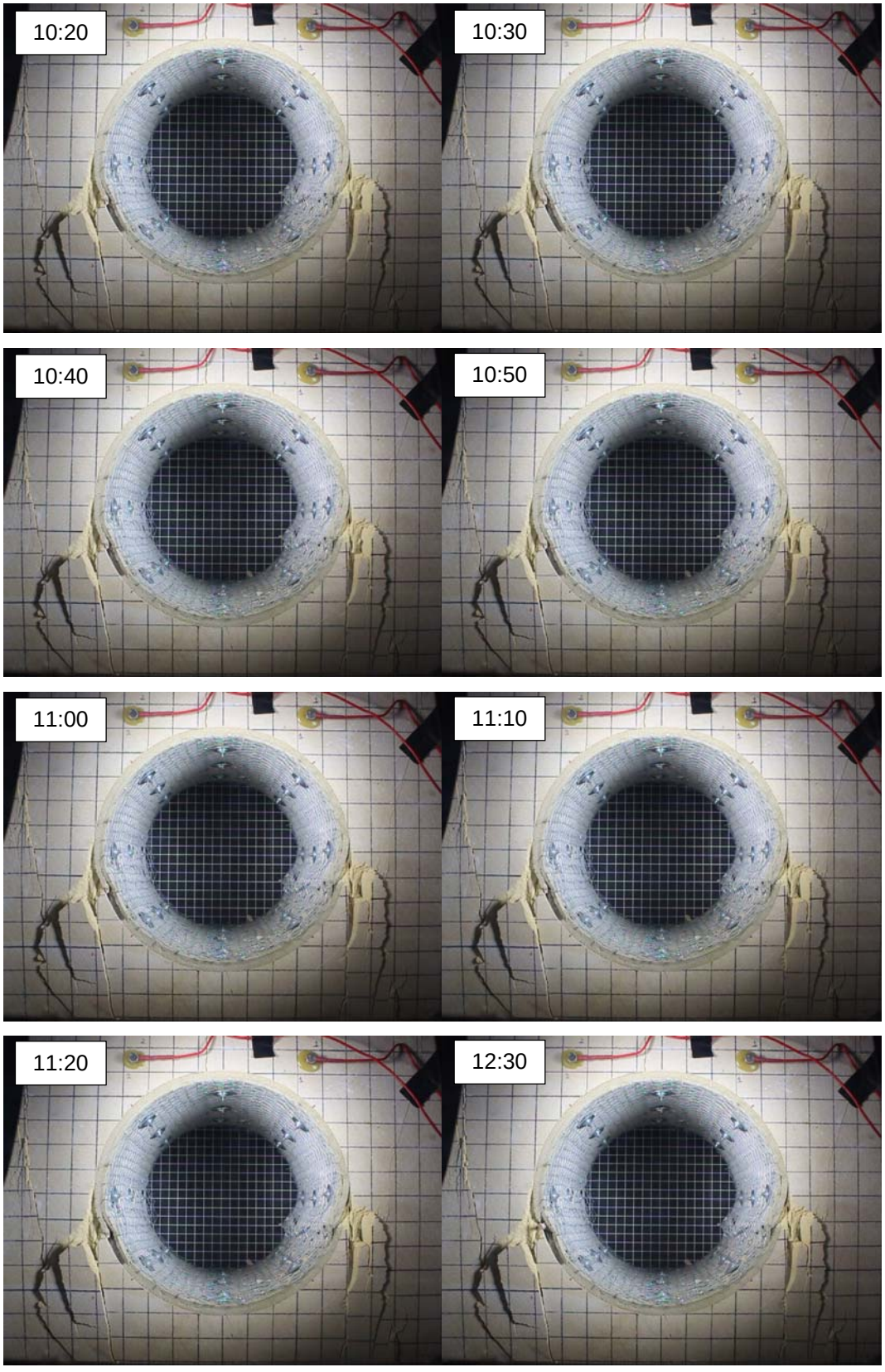
10:20
10:30
10:40
10:50
11:00
11:10
11:20
12:30

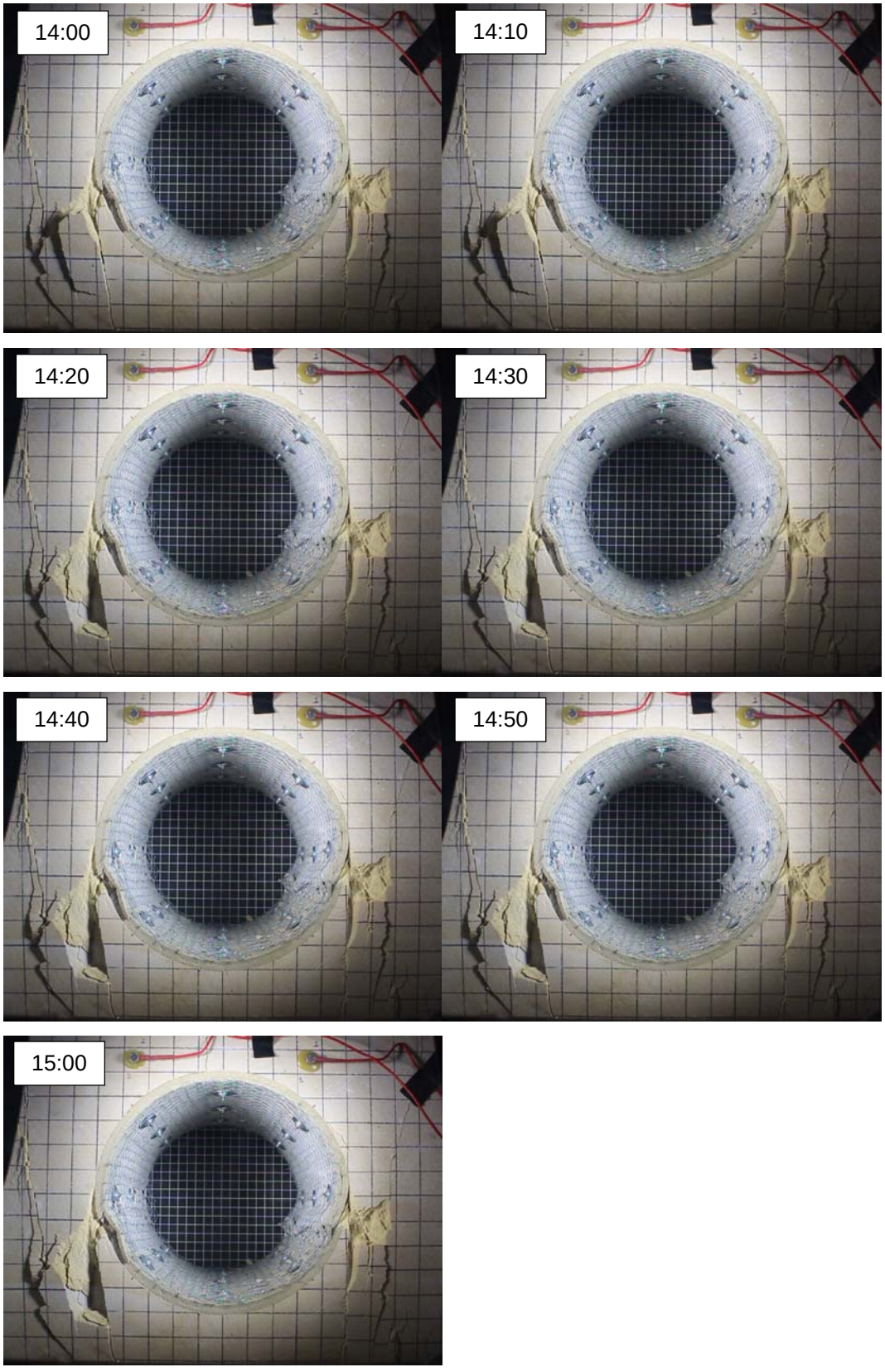
14:00
14:10
14:20
14:30
14:40
14:50
15:00